KU Leuven
Biomedical Sciences Group
Faculty of Medicine
Department of Imagine and Pathology
Division of Nuclear Medicine & Molecular Imaging

MAXIMUM A POSTERIORI RECONSTRUCTION FOR DIGITAL BREAST TOMOSYNTHESIS

Koen MICHIELSEN

Jury:

Promoter:	Prof. Dr. Ir. Johan Nuyts
Co-promoter:	Prof. Dr. Ir. Hilde Bosmans
Chair:	Prof. Dr. Philippe Demaerel
Secretary:	Prof. Dr. Chantal Van Ongeval
Jury members:	Prof. Dr. Ir. Frederik Maes
	Dr. Thomas Mertelmeier
	Prof. Dr. Ioannis Sechopoulos
	Prof. Dr. Jan Sijbers

Dissertation presented in
partial fulfilment of the
requirements for the
degree of Doctor in
Biomedical Sciences

January 2016

I may not have gone where I intended to go,
but I think I have ended up where I needed to be.

– Douglas Adams

Acknowledgments

Het voelt wat vreemd, om nu, na vijf jaar, in dit dankwoord de laatste paragrafen van mijn manuscript neer te schrijven en herinneringen op te halen aan de voorbije jaren. Daarbij kan ik gelukkig vaststellen dat de vele goede herinneringen zeker opwegen tegen de momenten dat het wat minder ging. Vooral omdat er op die momenten altijd wel iemand was om mijn motivatie terug aan te wakkeren. Daarom wil ik hier ook iedereen bedanken met wiens steun ik dit doctoraat tot een goed einde heb kunnen brengen.

Hilde, bedankt om me in contact te brengen met Johan nadat ik je had verteld dat ik wilde stoppen als stralingsfysicus en me liever wou concentreren op onderzoek, en mij zo de kans te geven om dit doctoraat te kunnen starten. Ook daarna was je steun als copromotor van dit werk belangrijk en kon ik dankzij onze discussies mijn werk beter in een ruimere context plaatsen.

Johan, bedankt om altijd klaar te staan met advies en ideeën, en om steeds de juiste vragen te stellen om zo de bron van een probleem te kunnen vinden. Als promotor was jouw steun onmisbaar. Ik ben dan ook dankbaar voor alle tijd die je hebt genomen voor het nalezen van mijn teksten en voor alle suggesties die het werk uiteindelijk veel sterker maakten.

I would also like to express my gratitude to prof. dr. Philippe Demaerel for chairing the public defense, prof. dr. Steven Dymarkowski for coordinating the reading committee, and the members of my jury: prof. dr. ir. Frederik Maes, dr. Thomas Mertelmeier, prof. dr. Ioannis Sechopoulos, prof. dr. Jan Sijbers, and prof. dr. Chantal Van Ongeval. Thank you for taking the time to read and evaluate this work, and for your suggestions which allowed me to better present my work.

Anna, Ahmad, Esmaeel, Georg, Kathleen, Lin, Matthew, Tao, and last but not least, Katrien, thank you for all interesting conversations over the years, both on actual research problems and on weird facts from the latest QI episode.

To Elena, Emmy, and Lesley, who also worked on breast imaging and observer performance, thank you for sharing your experiences and commiserations on our shared problems. Special thanks to Lesley for sharing all her phantom data, and the practical help in setting up my observer experiments.

To Nick, thank you for being an endless source of knowledge on the evaluation and characterization of x-ray systems, for the discussions and ideas on model observers, and the occasional bit of help on figuring out the English language.

To Xochitl, thank you for listening to me complain about all the problems I encountered, and then encouraging me to continue anyway.

To all colleagues in the medical imaging research center at Gasthuisberg, past and present, thank you for all the small things that made it a place I will miss, and for being willing victims in my observer experiments.

Aan de dames van de dienst mammografie, Ann en Kristin in het bijzonder, bedankt dat ik altijd bij jullie terecht kon voor koffie, een babbel, en vaak ook een stuk taart, lang nadat ik het mammo QA team had verlaten.

Ik wil ook mijn vrienden bedanken, voor alle uitstappen en spelavonden, en om me er regelmatig aan te herinneren dat er ook nog een wereld buiten de universiteit bestaat. Ik hoop dat het nu voor jullie ook iets duidelijker is wat ik hier de voorbije jaren allemaal heb gedaan.

Mijn kleine zusje mag ik hier ook niet vergeten, omdat ze nu eenmaal fantastisch is ;)

En tot slot wil ik mijn ouders bedanken, ma en pa, zonder jullie steun zou ik nooit zover geraakt zijn. Het is niet mogelijk om hier in een korte paragraaf op te lijsten waarvoor ik jullie dankbaar ben. Daarom heel simpel en heel gemeend: bedankt voor alles.

Koen.

Contents

Summary

Digital breast tomosynthesis is a recent three dimensional imaging modality that allows visualization of the breast as a stack of parallel slices. When compared to projection mammography, tomosynthesis is preferred for visualizing mass lesions while mammography is preferred for microcalcifications. In clinical evaluations, the diagnostic accuracy of tomosynthesis is at least as good as that of mammography, and both modalities combined outperform mammography used alone. Technical evaluations show that iterative reconstruction methods perform better than filtered backprojection reconstruction, which was used in most of the clinical evaluations. Therefore, the goal of this work was to design and evaluate a maximum a posteriori reconstruction algorithm for digital breast tomosynthesis with a focus on the visualization of microcalcifications.

The first step was to implement a sequence of preprocessing steps to account for the typical assumptions of mono-energetic and scatter-free data acquisition used in iterative reconstruction. With this precorrection, reconstructed attenuation values of adipose breast tissue was found to be close to the expected theoretical value. A further examination of the difference between scatter precorrection and model based scatter correction during reconstruction was performed by evaluating the contrast to noise ratio of simulated masses in patient data. Results showed that the application of either correction method resulted in a similar contrast to noise ratio, which meant precorrection was preferred due to the lower computational cost.

The second part of the work concentrates on developing a maximum a posteriori reconstruction algorithm for breast tomosynthesis. To improve visualization of microcalcifications, a resolution model based on the motion of the x-ray source during image acquisition was combined with a grouped coordinate ascent algorithm that sequentially updated planes parallel to the detector, each with their own position dependent parameters for the resolution model. This new method was evaluated in reconstructions of a simulated power law background containing microcalcifications and resulted in higher contrast to noise ratio when compared to iterative reconstruction without resolution model and improved detectability in a free search observer experiment when compared to filtered backprojection.

One drawback of the plane-by-plane updates in this method was the need for careful initialization of the reconstruction volume in order to avoid severe limited angle artifacts. To remedy this problem and to further accelerate convergence, multigrid updates were implemented, and an update scheme was selected that combined the least amount of artifacts and the best convergence after a fixed computational cost. A further comparison was made with a popular alternative update method using ordered subsets rather than plane-by-plane updates, and found that when using an optimal multigrid sequence, both update methods resulted in similar performance.

The final parts of this work focused on the evaluation of reconstruction methods. A channelized Hotelling observer was designed to detect groups of five microcalcifications in a background of acrylic spheres, and was applied to optimize the detectability of these microcalcifications as a function of the smoothing prior. The model observer correlated well with human observer evaluations of the same data, and found that detectability only varied slightly over a large range of strengths for the quadratic and combined quadratic and total variation priors. Therefore, it was not possible to pick an optimal smoothness based only on this criterion. On the other hand, with this information, the smoothing in the reconstruction could be set according to radiologist preference without worrying about calcification detectability.

This model observer was then applied together with evaluations by a group of expert and non-expert human observers to compare three reconstruction algorithms for breast tomosynthesis. These were the iterative reconstruction developed in this work, the existing filtered backprojection of the Siemens Mammomat Inspiration system, and a new super-resolution filtered backprojection with post-reconstruction denoising. The evaluation consisted of a four-alternative forced-choice experiment to determine microcalcification and mass detectability in phantom data, and a visual grading study on patient data. Both new reconstruction methods showed improved performance on the lesion detection task compared to the system filtered backprojection, but resulted in significantly different overall appreciation of image quality in the visual grading study. From these results and the feedback from the radiologists that participated in the study, we can conclude that the new super-resolution filtered backprojection can replace the original system reconstruction in the clinic. Although the new iterative reconstruction improved the detectability of microcalcifications significantly, the unfamiliar properties of the images were not received as positive by the radiologists. Therefore further development of the iterative reconstruction should focus on artifact reduction and improving image contrast, and should use frequent clinical input in order to obtain a more familiar look and feel (noise pattern, contrast, . . .) for the radiologists.

Samenvatting

Digitale borsttomosynthese is een recente driedimensionale beeldvormingstechniek die de borst toont als een reeks evenwijdige dwarsdoorsnedes. In vergelijking met projectiemammografie, worden massa's beter in beeld gebracht door tomosynthese, terwijl microcalcificaties beter in beeld gebracht worden door mammografie. Klinische evaluaties tonen aan dat de diagnostische nauwkeurigheid van tomosynthese minstens even goed is als die van mammografie, en dat de combinatie van beide modaliteiten beter scoort dan mammografie alleen. Uit technische evaluaties blijkt dan weer dat iteratieve reconstructiemethodes beter presteren dan de gefilterde terugprojectie die werd gebruikt in de meeste klinische evaluaties. Daarom is het doel van dit werk het ontwerpen en evalueren van een maximum a posteriori reconstructie algoritme voor digitale borsttomosynthese, met een focus op de visualisatie van microcalcificaties.

De eerste stap bestond uit een reeks correcties om de typische aanname van een mono-energetische meting zonder strooistraling in iteratieve reconstructie in rekening te brengen. Dankzij deze correcties liggen de gereconstrueerde attenuatiewaarden van vetrijk borstweefsel dicht bij de verwachte theoretische waarden. Een verdere vergelijking tussen het corrigeren van de gemeten data voor strooistraling en het opnemen van deze correctie in het reconstructiemodel werd uitgevoerd door de contrast-ruisverhouding van gesimuleerde massa's in patintendata te meten. De resultaten van deze vergelijking toonden aan dat de gemeten contrast-ruisverhoudingen voor beide correctiemethodes bijna gelijk waren, waardoor de eenvoudigere correctie van de projectiedata werd verkozen.

Het tweede deel van het werk concentreerde zich op het ontwikkelen van een 'maximum a posteriori' reconstructie algoritme voor borsttomosynthese. Om microcalcificaties beter in beeld te brengen werd een model van de systeemresolutie ontwikkeld dat de beweging van de röntgenbron tijdens de beeldopname in rekening brengt. Dit model werd vervolgens gecombineerd met een 'grouped coordinate ascent' algoritme dat de dwarsdoorsnedes sequentieel bijwerkt met behulp van de positie-afhankelijke parameters van het resolutiemodel. Deze nieuwe methode werd geëvalueerd in reconstructies van een gesimuleerde 'power law' achtergrond waarin microcalcificaties werden geplaatst. Daarbij werd aangetoond dat een reconstructie met het resolutiemodel de contrast-ruisverhouding van de microcalcificaties verhoogt in vergelijking met een reconstructie zonder resolutiemodel en dat de detecteerbaarheid van dezelfde microcalcificaties in een observatie-experiment verbeterde in vergelijking met reconstructie door gefilterde terugprojectie.

Een nadeel van de sequentiële updates bij deze methode is de noodzaak om het reconstructievolume zorgvuldig te initialiseren om zo de artefacten veroorzaakt door de onvolledige tomografie te vermijden. Om dit probleem op te lossen en om de convergentie te versnellen, werd een multigrid update schema gekozen dat bij een vaste berekeningskost resulteerde in de minste artefacten en de beste convergentie. Deze methode werd ook vergeleken met een populair alternatief waarbij de updates sequentieel worden uitgevoerd voor de verschillende projectiehoeken in plaats van sequentieel voor de dwarsdoorsnedes. Hierbij bleek dat beide methodes vergelijkbaar presteerden.

De laatste delen van dit werk spitsten zich toe op de evaluatie van reconstructiemethodes. Daarvoor werd een modelwaarnemer ('channelized Hotelling observer') ontwikkeld die in staat is om groepen van vijf microcalcificaties te detecteren in een achtergrond bestaande uit bollen van acrylaat. Deze modelwaarnemer werd vervolgens gebruikt om de detecteerbaarheid van de microcalcificaties te evalueren in functie van de parameters van de ruisonderdrukking in het reconstructie-algoritme. De resultaten verkregen met behulp van de modelwaarnemer correleerden goed met die van de menselijk waarnemers en toonden aan dat de detecteerbaarheid slechts weinig varieert over een groot bereid van de sterkte van de ruisonderdrukking met kwadratische of een combinatie van kwadratische en 'total variation' functies. Daarom was het niet mogelijk om dit criterium te gebruiken om een optimale sterkte voor de ruisonderdrukking te kiezen. Anderzijds betekent dit ook dat de sterkte kan worden aangepast aan de voorkeur van de radiologen zonder dat men zich zorgen hoeft te maken over de detecteerbaarheid van microcalcificaties.

Tot slot werd deze modelwaarnemer samen met evaluaties van een groep ervaren en niet ervaren menselijke waarnemers gebruikt om drie reconstructiemethodes voor borsttomosynthese te vergelijken, namelijk de iteratieve reconstructie ontwikkeld in dit werk, de bestaande gefilterde terugprojectie van het Siemens Mammomat Inspiration toestel, en een nieuwe superresolutie gefilterde terugprojectie met bijkomende ruisonderdrukking. De evaluatie bestond uit een detectie-experiment met vier keuzemogelijkheden om de detecteerbaarheid van microcalcificaties en massa's te bepalen, en een visuele beoordeling van een reeks patiëntenbeelden. Beide nieuwe reconstructiemethodes verbeterden de detecteerbaarheid van letsels in vergelijking met de bestaande gefilterde terugprojectie, maar kregen een significant verschillende beoordeling betreffende de algemene beeldkwaliteit in de visuele evaluatie door radiologen. Uit deze resultaten en uit de feedback van de radiologen die deelnamen aan de studie, kunnen we concluderen dat de nieuwe super-resolutie gefilterde terugprojectie de originele reconstructie kan vervangen in de kliniek. Hoewel de nieuwe iteratieve reconstructie de detectie van microcalcificaties meetbaar verbeterd heeft, werden de ongebruikelijke visuele eigenschappen van de beelden minder goed onthaald door de radiologen. Verder onderzoek op iteratieve reconstructie moet zich daarom richten op het reduceren van artefacten en het verbeteren van het contrast, en daarbij wou het nuttig zijn om regelmatig beroep te doen op advies vanuit de kliniek om zo beelden met een meer vertrouwd uitzicht (ruispatroon, contrast, . . .) te verkrijgen.

Chapter 1

Introduction

Breast cancer is the most prevalent cancer for European women for both incidence and mortality, and its incidence is highest for Belgian women in particular [1]. Due to this high prevalence and the reduction in mortality after early detection [2], [3], population screening is organized in many countries. This typically consists of a two-view mammography examination repeated every two years for women between 50 and 70 years old. However, some lesions, like masses in dense breasts [4], [5], are difficult to detect due to the interference from overlapping normal tissue structures (anatomical noise) in the mammogram.

A three dimensional imaging technique, like tomosynthesis as described by Grant [6], would be able to solve this problem by removing interference from overlapping dense tissue. Because of the requirement for good contrast and detail visibility, it is only since the availability of flat-panel detectors with sufficiently fast readout and adequate resolution that this technique can be applied to mammography. A first practical implementation was evaluated by Niklason et al. [7] and the first commercial digital breast tomosynthesis (DBT) systems are available since 2008 (Hologic Selenia Dimensions) and 2009 (Siemens Mammomat Inspiration). Both systems are in clinical use in UZ Leuven.

1.1 Breast Tomosynthesis

Most breast tomosynthesis systems are built as modifications of regular digital mammography systems. Figure 1.1 shows the schematic of a typical setup. The major components consist of an x-ray source, which is stationary for digital mammography and moves over an arc for breast tomosynthesis. This motion can be implemented as step-and-shoot, where the x-ray tube remains stationary during exposures and then moves to the next position, or by using a continuous tube motion, where the x-ray tube keeps moving during each x-ray pulse of the acquisition. Next, there is the compression plate

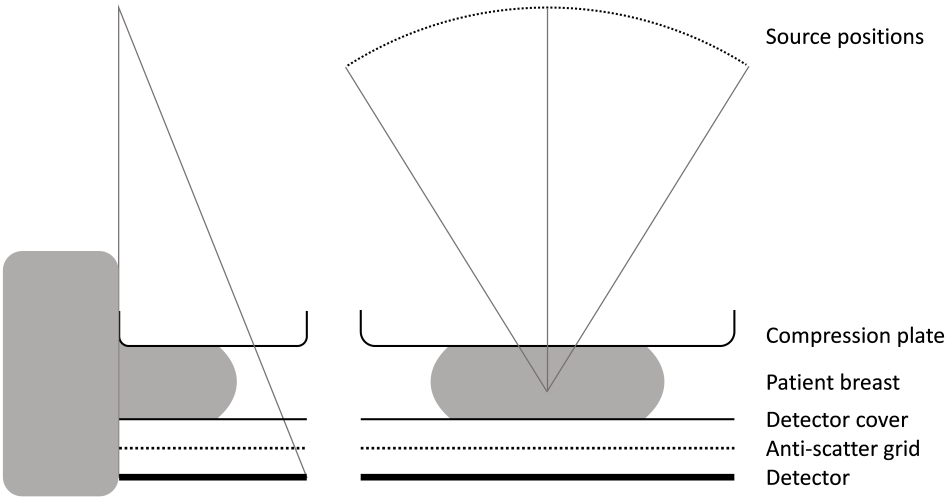

Figure 1.1: Side and frontal views of a typical digital mammography and breast tomosynthesis system setup (not to scale).

which immobilizes the patient's breast against the detector cover. Inside the detector assembly, there is a removable anti-scatter grid, which is present for regular mammography acquisitions, but removed for tomosynthesis acquisitions since it is usually focused on the fixed location of the x-ray source for mammography. The single current exception is the General Electric (GE) SenoClaire 3D which does use a grid in tomosynthesis mode [8]. The final major component is the x-ray detector, which can be either a selenium [9], [10] or silicon [11] based energy integrating detector, or a photon counting detector [12]. The review of Sechopoulos [13] provides more details on the characteristics of DBT systems currently in clinical use or under development. All patient and phantom data used in this work were acquired on a Siemens Mammomat Inspiration system, which is further described in section 1.3.

1.1.1 Clinical Evaluations

The two most obvious differences one can see when comparing clinical images from digital mammography and breast tomosynthesis, are illustrated in figures 1.2 and 1.3. The first figure shows a spiculated mass which is very subtle in the projection view on the left, and immediately obvious in the reconstructed DBT slice on the right. This superior visualization of low contrast mass lesions is also reported in literature [14], [15], and can be considered the greatest strength of breast tomosynthesis. The second figure presents the same comparison for a cluster of microcalcifications. In this example most of the finer details which are visible in the digital mammogram

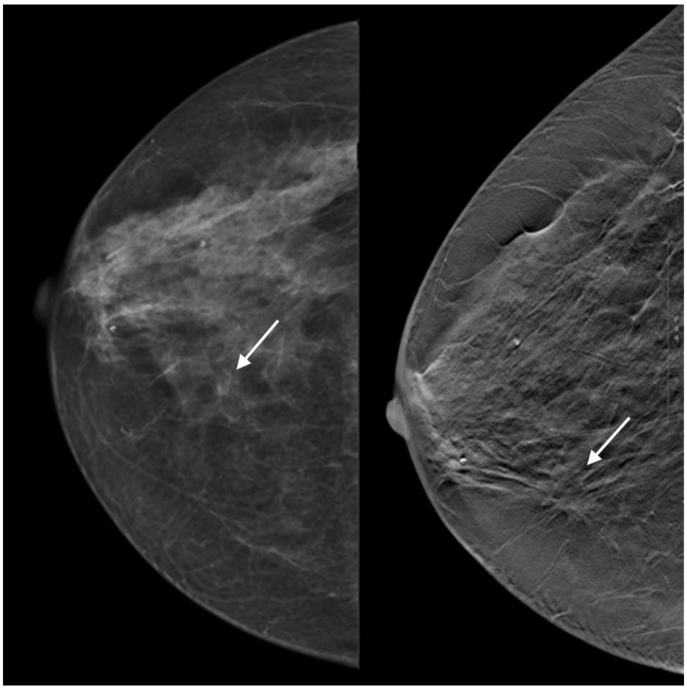

Figure 1.2: Visualization of a spiculated mass in digital mammography (left) and breast tomosynthesis (right).

on the left, are lost in the tomosynthesis reconstruction on the right. This loss of information seems to have only a slight effect on the performance in a detection task [16], but will occasionally result in a different classification of the same cluster in digital mammography and tomosynthesis [17]. More examples of the clinical use of breast tomosynthesis can be found in the works of Park et al. [14], Baker and Lo [18], Uematsu [19], and Peppard et al. [20].

Numerous studies comparing the clinical performance of digital mammography to breast tomosynthesis, or to the combination of digital mammography and breast tomosynthesis, have been published in the last couple of years. A non-exhaustive search finds that out of 18 published studies, 10 were performed on Hologic systems, three on GE systems, three on Siemens systems and two on a Philips (previously Sectra) system. Table 1.1 gives an overview of the references, grouped by the comparison made in the study and the DBT system that was used. Most of these studies were performed on a Hologic Selenia Dimensions system since it was the first DBT system to be approved for clinical use by the American Food and Drug Administration (FDA).

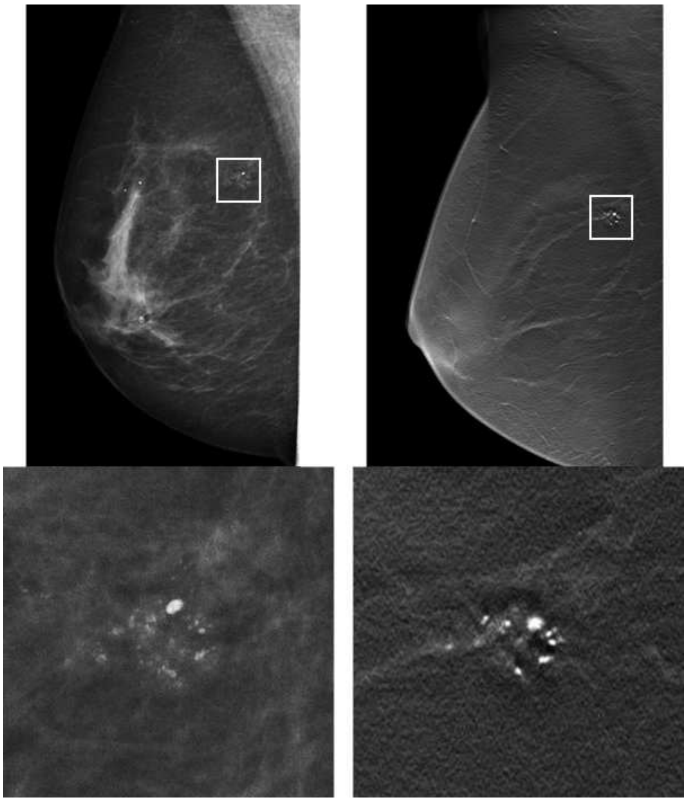

Figure 1.3: Visualization of a microcalcification group in digital mammography (left) and breast tomosynthesis (right).

	Hologic	GE	Siemens	Philips
DM vs DBT	[21]	[22]	[23], [24]	[25], [26]
DM vs DBT+DM	[27]–[33]	[34]		
DM vs DBT vs DBT+DM	[15], [35]	[36]	[37]	

Table 1.1: Overview of studies comparing digital mammography (DM) and digital breast tomosynthesis (DBT) for different manufacturers.

The general consensus from these works seems to be that breast tomosynthesis is non-inferior to digital mammography, which was reported in six of the ten publications making this comparison [21], [22], [25], [35]–[37]. Of the three remaining studies, one was based on a subjective evaluation of image quality [15], and another mentioned that the difference found in their multireader, multicase receiver operating characteristic (ROC) evaluation was only seen for the less experienced radiologists [26], which left only two studies on Siemens systems [23], [24] that found that one-view DBT (mediolateral oblique (MLO)) resulted in better diagnostic performance than two-view digital mammography (craniocaudal (CC) and MLO). However, when performing a meta-analysis of the results in part of these works, Lei et al. [38] do find a significant improvement in sensitivity and specificity for the diagnosis of benign and malignant lesions in the breast.

The remaining studies evaluate the addition of tomosynthesis to digital mammography (not necessarily at the same time or on the same system) against digital mammography on its own. Except for the two studies on GE systems [34], [36] which did not find any differences, all comparisons find that adding tomosynthesis to mammography increases diagnostic accuracy and reduces the recall rate. These overall conclusions are also found in the review by Houssami and Skaane [39].

1.1.2 Reconstruction Methods

The shift-and-add method shown in figure 1.4 is an intuitive way to understand how tomosynthesis reconstruction suppresses interference from overlapping tissue structures. The two objects in planes A and B are projected on top of each other in the central view, which corresponds to the regular digital mammography. In the tomosynthesis acquisition, multiple views are acquired at different angles such that the projections of the objects are slightly shifted relative to one another. For each plane there is a corresponding set of shifts for the different projections such that the addition of the shifted projection images produces a reconstructed image where an object from that specific plane is in focus, while objects from other planes are blurred in the background. This is illustrated on the right hand side of figure 1.4 for planes A and B.

In practice, the shift-and-add method and its equivalent for a general geometry, unfiltered backprojection, are not used for reconstructing clinical data since they are inferior to more advanced methods such as filtered backprojection (FBP), the simultaneous algebraic reconstruction technique (SART), or maximum likelihood (ML) reconstruction [40], [41].

Currently, most image reconstruction in x-ray computed tomography is performed by FBP, although iterative methods are quickly gaining in use [42]. The filtered backprojection is based on analytic inversion of the Radon transform, and gives the true solution for an ideal acquisition (i.e. contin-

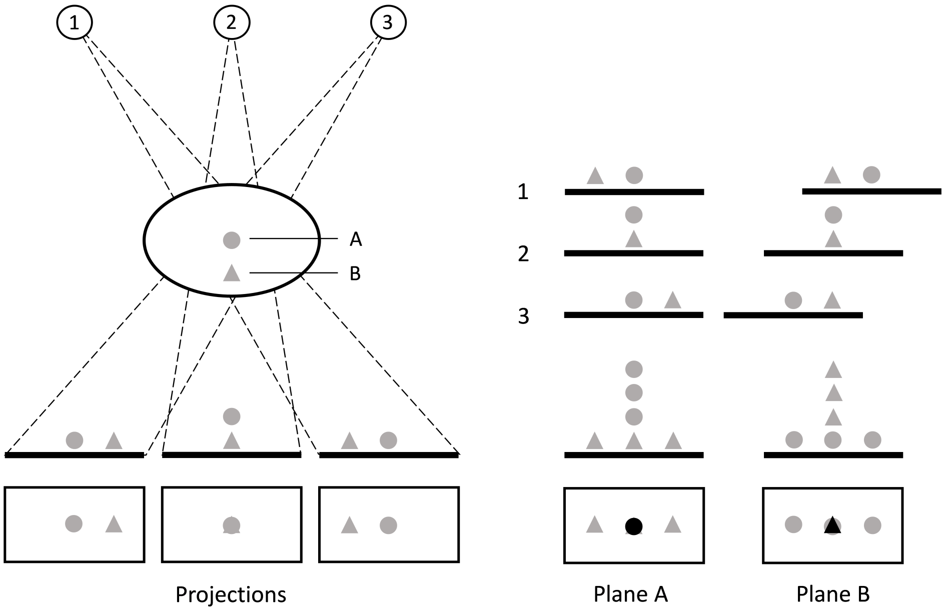

Figure 1.4: Shift and add method.

uous measurements over at least 180°, no scatter, monochromatic x-rays, etc.). In reality these conditions are never met. For DBT in particular, the acquisition is far away from ideal conditions: the sampled angular range is between 10° and 50° which means that insufficient information is obtained for exact reconstruction, and the projection images are degenerated by scattered x-rays, which reduce the contrast and introduce additional noise in the projection data. The scatter fractions in the data can range from 20% to over 60% [43]. In theory, an infinite number of tissue distributions can explain the acquired measurement, so in order to drive the reconstruction algorithm towards the true 3D tissue distribution, it is essential to propose good constraints. In iterative reconstruction, this can be done with prior distributions, which limit the set of possible solutions to ensure that the obtained reconstructions have diagnostic value.

With this in mind, it is understandable that most DBT vendors opt for iterative reconstruction, with only Hologic and Siemens opting for FBP [13]. Although most manufacturers are not very open about the details of the reconstruction methods used in their products, the iterative methods on which they are based are well known. Rather than attempt a direct inversion as in FBP, the reconstruction is formulated as an optimization problem which includes a forward model of the acquisition, and relies on numerical (iterative) rather than analytic inversion. The cost function is typically either the sum of squared differences, which is minimized by SART [44] or

POCS [45], or the likelihood, which can for example be maximized by the ML convex algorithm presented by Lange and Fessler [46] and introduced in DBT by Wu et al. [47]. The reconstruction methods that will be introduced in this work will extend the ML algorithm for transmission tomography (MLTR) developed in our research group [48] by including resolution effects in the forward model and modifying the update sequence to accelerate convergence. The derivation of the basic MLTR algorithm is presented in section 1.2.

Phantom based comparisons of the backprojection, filtered backprojection, SART, and ML convex reconstruction methods [40], [41], [49] showed that a simple backprojection gets the best contrast-to-noise ratio (CNR) for masses due to the low noise, but suffers from artifacts, lack of sharpness, and interplane blurring. FBP improved on BP for high contrast calcifications, but masses were poorly visualized, while ML convex resulted in a balanced image quality superior to both BP and FBP. When comparing ML convex and FBP for multiple acquisition geometries, ML convex resulted in a more consistent performance for resolution, CNR, and interplane artifacts, although FBP can compete when using properly designed filters for specific system geometries. Evaluating SART and ML convex together showed comparable image quality, but for the examined implementation, SART needed only one iteration after initialization, while ML convex needed seven to obtain a good reconstruction. The general conclusion from these studies is that at least for technical measures of image quality, iterative reconstruction in the form of SART or ML convex are preferred over filtered backprojection.

1.2 Maximum Likelihood Reconstruction

1.2.1 Algorithm Derivation

Although the shift-and-add method explained in section 1.1 provides an intuitive insight in the image formation for breast tomosynthesis, the resulting image quality is not adequate for diagnostic purposes. The reconstruction methods introduced in this work are based on the Maximum Likelihood for Transmission tomography (MLTR) algorithm [48]. Therefore we present its basic derivation here.

The general goal of maximum likelihood reconstruction is to find the most likely attenuation distribution $\vec{\mu}$, with μ_j the attenuation in voxel j, that explains the measured data $\vec{y}$, with y_i the measured pixel value for projection line i, or in short, find $\arg\max_{\vec{\mu}} P\left(\vec{\mu}|\vec{y}\right)$. This is a difficult inverse problem, but can be rewritten as a forward problem by using Bayes' rule:

$$P\left(\vec{\mu}|\vec{y}\right) = \frac{P\left(\vec{y}|\vec{\mu}\right) P\left(\vec{\mu}\right)}{P\left(\vec{y}\right)}. \tag{1.1}$$

Performing a logarithmic transformation does not change the optimum because the logarithm is a monotonic function, and the factor $P(\vec{y})$ can be ignored as it depends only on the measurement, which remains constant in the optimization process. With these transformations we find the form of the optimization problem that we will solve in equation 1.3:

$$\ln P(\vec{\mu}|\vec{y}) \propto \ln P(\vec{y}|\vec{\mu}) + \ln P(\vec{\mu}) \tag{1.2}$$

$$\arg\max_{\vec{\mu}} P(\vec{\mu}|\vec{y}) = \arg\max_{\vec{\mu}} \ \ln P(\vec{y}|\vec{\mu}) + \ln P(\vec{\mu}). \tag{1.3}$$

If we assume that the noise on the measured data follows the Poisson distribution, and that this noise is independent for each projection line i, then $P(\vec{y}|\vec{\mu})$ is given by the probability mass function of the Poisson distribution:

$$\begin{aligned} P(\vec{y}|\vec{\mu}) &= \prod_i P(y_i|\vec{\mu}) \\ &= \prod_i P(y_i|\hat{y}_i(\vec{\mu})) \\ &= \prod_i \frac{\hat{y}_i^{y_i} e^{-\hat{y}_i}}{y_i!}, \end{aligned} \tag{1.4}$$

where measurement y_i is the random variable, and $\hat{y}_i$ is the expected value for measurement y_i, which can be calculated as a function of the attenuation distribution $\vec{\mu}$. After performing the logarithmic transformation, we can ignore the constant term $\ln y_i!$ in the optimization:

$$\ln P(\vec{y}|\vec{\mu}) = \sum_i y_i \ln \hat{y}_i - \hat{y}_i - \ln y_i!, \tag{1.5}$$

$$\ln P(\vec{y}|\vec{\mu}) \propto L(\vec{\mu}) = \sum_i y_i \ln \hat{y}_i - \hat{y}_i. \tag{1.6}$$

In the case of the MLTR algorithm, the forward model $\hat{y}_i$ is a basic mono-energetic transmission acquisition without scattered radiation:

$$\hat{y}_i(\vec{\mu}) = b_i e^{-\sum_j l_{ij}\mu_j}, \tag{1.7}$$

with l_{ij} the intersection length between projection line i and voxel j, and b_i the unattenuated value for projection line i. In this forward model, all variables except for the attenuation distribution are assumed to be known before starting the reconstruction.

The second term in the optimization problem in equation (1.3) only depends on the attenuation distribution $\vec{\mu}$, and contains the prior information about the image which is known independently of measurement $\vec{y}$. One typical use is to include the assumption of image smoothness in the form of a quadratic penalty function on the intensity differences between neighboring voxels, as presented in the work of Hebert and Leahy [50]. It is restricted to neighboring voxels by symmetric weights $w_{jk} = w_{kj}$ with $w_{jj} = 0$, and includes a global weight β to balance the prior P_s with the image fidelity term $\ln P\left(\vec{y}|\vec{\mu}\right)$:

$$\ln P\left(\vec{\mu}\right) = \beta P_s\left(\vec{\mu}\right) = -\frac{\beta}{4}\sum_{j,k} w_{jk}\left(\mu_j - \mu_k\right)^2 \tag{1.8}$$

We can now combine the results in equations (1.6) and (1.8) in the posterior log likelihood $\mathcal{L}$:

$$\mathcal{L}\left(\vec{\mu}\right) = L\left(\vec{\mu}\right) + \beta P_s\left(\vec{\mu}\right), \tag{1.9}$$

which is, in full:

$$\mathcal{L}\left(\vec{\mu}\right) = \sum_i y_i \ln\left(b_i e^{-\sum_j l_{ij}\mu_j}\right) - b_i e^{-\sum_j l_{ij}\mu_j} - \frac{\beta}{4}\sum_{j,k} w_{jk}\left(\mu_j - \mu_k\right)^2. \tag{1.10}$$

In order to maximize the posterior likelihood $\mathcal{L}$, we use two other functions: the second order Taylor approximation $T_2\left(\vec{\mu}^n, \Delta\vec{\mu}\right)$ at the current attenuation estimate $\vec{\mu}^n$, and surrogate function $T_S\left(\vec{\mu}^n, \Delta\vec{\mu}\right)$, which should be chosen in such a way that maximization of T_S guarantees an increase of T_2. In practice this means that $T_S\left(\vec{\mu}^n, \Delta\vec{\mu}\right) \leq T_2\left(\vec{\mu}^n, \Delta\vec{\mu}\right)$, and that T_S should not contain any mixed terms in μ_j and μ_k, so that the update step in each voxel is independent of the updates in other voxels. The second order Taylor expansion of $\mathcal{L}$ is given by:

$$\begin{aligned} T_2\left(\vec{\mu}^n, \Delta\vec{\mu}\right) &= \mathcal{L}\left(\vec{\mu}^n\right) + \sum_j \left.\frac{\partial \mathcal{L}\left(\vec{\mu}\right)}{\partial \mu_j}\right|_{\vec{\mu}=\vec{\mu}^n} \Delta\mu_j \\ &\quad + \frac{1}{2}\sum_{j,k} \left.\frac{\partial^2 \mathcal{L}\left(\vec{\mu}\right)}{\partial \mu_j \partial \mu_k}\right|_{\vec{\mu}=\vec{\mu}^n} \Delta\mu_j \Delta\mu_k \end{aligned} \tag{1.11}$$

$$\begin{aligned} &= \mathcal{L}\left(\vec{\mu}^n\right) + \sum_j \left.\frac{\partial \mathcal{L}\left(\vec{\mu}\right)}{\partial \mu_j}\right|_{\vec{\mu}=\vec{\mu}^n} \Delta\mu_j \\ &\quad + \frac{1}{2}\sum_{j,k} \left.\frac{\partial^2 L\left(\vec{\mu}\right)}{\partial \mu_j \partial \mu_k}\right|_{\vec{\mu}=\vec{\mu}^n} \Delta\mu_j \Delta\mu_k \\ &\quad + \frac{\beta}{2}\sum_{j,k} \left.\frac{\partial^2 P_s\left(\vec{\mu}\right)}{\partial \mu_j \partial \mu_k}\right|_{\vec{\mu}=\vec{\mu}^n} \Delta\mu_j \Delta\mu_k. \end{aligned} \tag{1.12}$$

To find $T_S\left(\vec{\mu}^n, \Delta\vec{\mu}\right)$ we need the derivatives of L and P_s:

$$\frac{\partial L\left(\vec{\mu}\right)}{\partial \mu_j} = \sum_i l_{ij}\left(\hat{y}_i - y_i\right), \tag{1.13}$$

$$\frac{\partial^2 L\left(\vec{\mu}\right)}{\partial \mu_j \partial \mu_k} = -\sum_i l_{ij} l_{ik} \hat{y}_i, \tag{1.14}$$

$$\frac{\partial P_s\left(\vec{\mu}\right)}{\partial \mu_j} = -\sum_k w_{jk}\left(\mu_j - \mu_k\right), \tag{1.15}$$

$$\frac{\partial^2 P_s\left(\vec{\mu}\right)}{\partial \mu_j^2} = -\sum_k w_{jk}, \tag{1.16}$$

$$\frac{\partial^2 P_s\left(\vec{\mu}\right)}{\partial \mu_j \partial \mu_{k\neq j}} = w_{jk}, \tag{1.17}$$

and the following inequality:

$$\begin{aligned} \left(\Delta\mu_j - \Delta\mu_k\right)^2 = \Delta\mu_j^2 + \Delta\mu_k^2 - 2\Delta\mu_j\Delta\mu_k \geq 0 \\ \Rightarrow \Delta\mu_j^2 + \Delta\mu_k^2 \geq 2\Delta\mu_j\Delta\mu_k. \end{aligned} \tag{1.18}$$

The term that includes the second derivatives of L can be replaced as follows, with the knowledge that this second derivative is always less than or equal to zero (see equation (1.14)) and by using the inequality in equation (1.18):

$$\begin{aligned} &\frac{1}{2}\sum_{j,k}\frac{\partial^2 L\left(\vec{\mu}\right)}{\partial \mu_j \partial \mu_k}\Delta\mu_j\Delta\mu_k \\ &\quad=\frac{1}{4}\sum_{j,k}\frac{\partial^2 L\left(\vec{\mu}\right)}{\partial \mu_j \partial \mu_k}\left(2\Delta\mu_j\Delta\mu_k\right) \\ &\quad\geq\frac{1}{4}\sum_{j,k}\frac{\partial^2 L\left(\vec{\mu}\right)}{\partial \mu_j \partial \mu_k}\left(\Delta\mu_j^2 + \Delta\mu_k^2\right) \\ &\quad=\frac{1}{2}\sum_{j,k}\frac{\partial^2 L\left(\vec{\mu}\right)}{\partial \mu_j \partial \mu_k}\Delta\mu_j^2. \end{aligned} \tag{1.19}$$

The prior term can be replaced in a similar way, with the knowledge that weights β and w_{jk} are both greater than or equal to zero, and that $w_{jk} = w_{kj}$.

$$
\begin{aligned}
&\frac{\beta}{2}\sum_{j,k}\frac{\partial^2 P_s\left(\vec{\mu}\right)}{\partial\mu_j\partial\mu_k}\Delta\mu_j\Delta\mu_k\\
&=\frac{\beta}{2}\sum_{j}\frac{\partial^2 P_s\left(\vec{\mu}\right)}{\partial\mu_j^2}\Delta\mu_j^2+\frac{\beta}{2}\sum_{j,k\neq j}\frac{\partial^2 P_s\left(\vec{\mu}\right)}{\partial\mu_j\partial\mu_k}\Delta\mu_j\Delta\mu_k\\
&=\frac{\beta}{2}\sum_{j}\left(-\sum_{k}w_{jk}\right)\Delta\mu_j^2+\frac{\beta}{2}\sum_{j,k\neq j}\left(w_{jk}\right)\Delta\mu_j\Delta\mu_k\\
&=-\frac{\beta}{4}\sum_{j,k}w_{jk}\Delta\mu_j^2-\frac{\beta}{4}\sum_{j,k}w_{jk}\Delta\mu_k^2+\frac{\beta}{4}\sum_{j,k\neq j}w_{jk}2\Delta\mu_j\Delta\mu_k \qquad (1.20)\\
&=-\frac{\beta}{4}\sum_{j,k}w_{jk}\left(\Delta\mu_j^2+\Delta\mu_k^2-2\Delta\mu_j\Delta\mu_k\right)\\
&\geq-\frac{\beta}{4}\sum_{j,k}w_{jk}\left(\Delta\mu_j^2+\Delta\mu_k^2+\Delta\mu_j^2+\Delta\mu_k^2\right)\\
&=-\beta\sum_{j,k}w_{jk}\Delta\mu_j^2.
\end{aligned}
$$

By replacing the two last terms in equation (1.12) by the replacements given in equations (1.19) and (1.20) we find $T_S\left(\vec{\mu}^n,\Delta\vec{\mu}\right)$:

$$
\begin{aligned}
T_S\left(\vec{\mu}^n,\Delta\vec{\mu}\right)=&\mathcal{L}\left(\vec{\mu}^n\right)+\sum_{j}\left.\frac{\partial\mathcal{L}\left(\vec{\mu}\right)}{\partial\mu_j}\right|_{\vec{\mu}=\vec{\mu}^n}\Delta\mu_j\\
&+\frac{1}{2}\sum_{j,k}\left.\frac{\partial^2 L\left(\vec{\mu}\right)}{\partial\mu_j\partial\mu_k}\right|_{\vec{\mu}=\vec{\mu}^n}\Delta\mu_j^2-\beta\sum_{j,k}w_{jk}\Delta\mu_j^2.
\end{aligned} \qquad (1.21)
$$

This function is a sum of independent quadratic equations which can be maximized in a single step for each variable $\Delta\mu_j$ by setting the first derivative to zero:

$$\begin{aligned}
&\frac{\partial T_S\left(\vec{\mu}^n, \Delta\vec{\mu}\right)}{\partial \Delta\mu_j} = 0 \\
\Leftrightarrow\ & \left.\frac{\partial \mathcal{L}\left(\vec{\mu}\right)}{\partial \mu_j}\right|_{\vec{\mu}=\vec{\mu}^n} + \sum_k \left.\frac{\partial^2 L\left(\vec{\mu}\right)}{\partial \mu_j \partial \mu_k}\right|_{\vec{\mu}=\vec{\mu}^n} \Delta\mu_j - 2\beta \sum_k w_{jk} \Delta\mu_j = 0 \\
\Leftrightarrow\ & \Delta\mu_j = \frac{- \left.\frac{\partial \mathcal{L}(\vec{\mu})}{\partial \mu_j}\right|_{\vec{\mu}=\vec{\mu}^n}}{\sum_k \left.\frac{\partial^2 L(\vec{\mu})}{\partial \mu_j \partial \mu_k}\right|_{\vec{\mu}=\vec{\mu}^n} - 2\beta \sum_k w_{jk}} \qquad (1.22) \\
\Leftrightarrow\ & \Delta\mu_j = \frac{-\left(\sum_i l_{ij}\left(\hat{y}_i^n - y_i\right) - \beta \sum_k \left(\mu_j^n - \mu_k^n\right)\right)}{-\sum_i l_{ij} \hat{y}_i^n \sum_k l_{ik} - 2\beta \sum_k w_{jk}} \\
\Leftrightarrow\ & \Delta\mu_j = \frac{\sum_i l_{ij}\left(\hat{y}_i^n - y_i\right) - \beta \sum_k \left(\mu_j^n - \mu_k^n\right)}{\sum_i l_{ij} \hat{y}_i^n \sum_k l_{ik} + 2\beta \sum_k w_{jk}}.
\end{aligned}$$

Because

$$\mathcal{L}\left(\vec{\mu}^n\right) = T_2\left(\vec{\mu}^n\right) = T_S\left(\vec{\mu}^n\right) \tag{1.23}$$

and

$$\mathcal{L}\left(\vec{\mu}^n + \Delta\vec{\mu}\right) \approx T_2\left(\vec{\mu}^n, \Delta\vec{\mu}\right) \geq T_S\left(\vec{\mu}^n, \Delta\vec{\mu}\right), \tag{1.24}$$

each update step $\Delta\vec{\mu}$ from equation (1.22) which maximizes T_S will increase T_2 and therefore, provided that T_2 is an adequate approximation of $\mathcal{L}$, also increase the posterior log likelihood.

1.2.2 Alternative Update Steps

The reconstruction methods that are introduced in this work extend a modified version of the MLTR algorithm which includes individual voxel weights $\alpha_j > 0$, analogous to the grouped-coordinate ascent method introduced by Fessler et al. [51]. These can be introduced in the MLTR method by applying the following transformation, with $\alpha_j > 0$, such that $l_{ij}\mu_j = l'_{ij}\mu'_j$:

$$\begin{aligned}
\mu'_j &= \frac{\mu_j}{\alpha_j}, \\
l'_{ij} &= \alpha_j l_{ij}.
\end{aligned} \tag{1.25}$$

This means the forward model in (equation 1.7) and the quadratic prior in equation 1.8 can now be rewritten as follows:

$$\hat{y}_i = b_i e^{-\sum_j l_{ij}\mu_j} = b_i e^{-\sum_j l'_{ij}\mu'_j}, \tag{1.26}$$

$$\begin{aligned}\ln P = \beta P_s &= -\frac{\beta}{4}\sum_{j,k} w_{jk}\left(\mu_j - \mu_k\right)^2 \\ &= -\frac{\beta}{4}\sum_{j,k} w_{jk}\left(\alpha_j \mu'_j - \alpha_k \mu'_k\right)^2,\end{aligned} \tag{1.27}$$

which in its turn leads to these new derivatives of L and P_s:

$$\frac{\partial L}{\partial \mu'_j} = \sum_i l'_{ij}\left(\hat{y}_i - y_i\right), \tag{1.28}$$

$$\frac{\partial^2 L}{\partial \mu'_j \partial \mu'_k} = -\sum_i l'_{ij} l'_{ik} \hat{y}_i, \tag{1.29}$$

$$\frac{\partial P_s}{\partial \mu'_j} = -\sum_k \alpha_j w_{jk}\left(\alpha_j \mu'_j - \alpha_k \mu'_k\right), \tag{1.30}$$

$$\frac{\partial^2 P_s}{\partial \mu'^2_j} = -\alpha_j^2 \sum_k w_{jk}, \tag{1.31}$$

$$\frac{\partial^2 P_s}{\partial \mu'_j \partial \mu'_{k\neq j}} = \alpha_j \alpha_k w_{jk}. \tag{1.32}$$

The transform does not influence the surrogate for the second derivative of the likelihood:

$$\frac{1}{2}\sum_{j,k} \frac{\partial^2 L\left(\vec{\mu}'\right)}{\partial \mu'_j \partial \mu'_k} \Delta\mu'_j \Delta\mu'_k \geq \frac{1}{2}\sum_{j,k} \frac{\partial^2 L\left(\vec{\mu}'\right)}{\partial \mu'_j \partial \mu'_k} \Delta\mu'^2_j, \tag{1.33}$$

and only slightly for the second derivative of the quadratic prior:

$$
\begin{aligned}
&\frac{\beta}{2}\sum_{j,k}\frac{\partial^2 P_s\left(\vec{\mu}'\right)}{\partial\mu'_j\partial\mu'_k}\Delta\mu'_j\Delta\mu'_k\\
&\quad=\frac{\beta}{2}\sum_{j}\frac{\partial^2 P_s\left(\vec{\mu}'\right)}{\partial\mu'^2_j}\Delta\mu'^2_j+\frac{\beta}{2}\sum_{j,k\neq j}\frac{\partial^2 P_s\left(\vec{\mu}'\right)}{\partial\mu'_j\partial\mu'_k}\Delta\mu'_j\Delta\mu'_k\\
&\quad=\frac{\beta}{2}\sum_{j}\left(-\alpha_j^2\sum_k w_{jk}\right)\Delta\mu'^2_j+\frac{\beta}{2}\sum_{j,k\neq j}\left(\alpha_j\alpha_k w_{jk}\right)\Delta\mu'_j\Delta\mu'_k\\
&\quad=-\frac{\beta}{4}\sum_{j,k}w_{jk}\alpha_j^2\Delta\mu'^2_j-\frac{\beta}{4}\sum_{j,k}w_{jk}\alpha_k^2\Delta\mu'^2_k+\frac{\beta}{4}\sum_{j,k\neq j}w_{jk}2\alpha_j\Delta\mu'_j\alpha_k\Delta\mu'_k\\
&\quad=-\frac{\beta}{4}\sum_{j,k}w_{jk}\left(\alpha_j^2\Delta\mu'^2_j+\alpha_k^2\Delta\mu'^2_k-2\alpha_j\Delta\mu'_j\alpha_k\Delta\mu'_k\right)\\
&\quad\geq-\frac{\beta}{4}\sum_{j,k}w_{jk}\left(\alpha_j^2\Delta\mu'^2_j+\alpha_k^2\Delta\mu'^2_k+\alpha_j^2\Delta\mu'^2_j+\alpha_k^2\Delta\mu'^2_k\right)\\
&\quad=-\beta\sum_{j,k}w_{jk}\alpha_j^2\Delta\mu'^2_j.
\end{aligned}
\tag{1.34}
$$

To compute the new update step, we apply the transformation to the Taylor expansion in equation (1.12), and substitute the two last terms by the replacements in equations (1.33) and (1.34) to find $T_S\left(\vec{\mu}'^n,\Delta\vec{\mu}'\right)$:

$$
\begin{aligned}
T_S\left(\vec{\mu}'^n,\Delta\vec{\mu}'\right)=&\mathcal{L}\left(\vec{\mu}'^n\right)+\sum_j\left.\frac{\partial\mathcal{L}\left(\vec{\mu}'\right)}{\partial\mu'_j}\right|_{\vec{\mu}'=\vec{\mu}'^n}\Delta\mu'_j\\
&+\frac{1}{2}\sum_{j,k}\left.\frac{\partial^2 L\left(\vec{\mu}'\right)}{\partial\mu'_j\partial\mu'_k}\right|_{\vec{\mu}'=\vec{\mu}'^n}\Delta\mu'^2_j-\beta\sum_{j,k}w_{jk}\alpha_j^2\Delta\mu'^2_j
\end{aligned}
\tag{1.35}
$$

Now we can again set the derivative to 0 to find the update step $\Delta\mu'_j$, before using it to determine the unmodified update step $\Delta\mu_j$ with individual voxel weights:

$$\begin{aligned}
&\frac{\partial T_S\left(\vec{\mu}'^n, \Delta\vec{\mu}'\right)}{\partial \Delta\mu'_j} = 0 \\
&\Leftrightarrow \left.\frac{\partial \mathcal{L}\left(\vec{\mu}'\right)}{\partial \mu'_j}\right|_{\vec{\mu}'=\vec{\mu}'^n} + \sum_k \left.\frac{\partial^2 L\left(\vec{\mu}'\right)}{\partial \mu'_j \partial \mu'_k}\right|_{\vec{\mu}'=\vec{\mu}'^n} \Delta\mu'_j - 2\beta \sum_k w_{jk}\alpha_j^2 \Delta\mu'_j = 0 \\
&\Leftrightarrow \Delta\mu'_j = \frac{-\left.\frac{\partial \mathcal{L}(\vec{\mu}')}{\partial \mu'_j}\right|_{\vec{\mu}'=\vec{\mu}'^n}}{\sum_k \left.\frac{\partial^2 L(\vec{\mu}')}{\partial \mu'_j \partial \mu'_k}\right|_{\vec{\mu}'=\vec{\mu}'^n} - 2\alpha_j^2 \beta \sum_k w_{jk}} \\
&\Leftrightarrow \Delta\mu'_j = \frac{-\left(\sum_i l'_{ij}\left(\hat{y}_i^n - y_i\right) - \alpha_j \beta \sum_k \left(\alpha_j \mu_j'^n - \alpha_k \mu_k'^n\right)\right)}{-\sum_i l'_{ij}\hat{y}_i^n \sum_k l'_{ik} - 2\alpha_j^2 \beta \sum_k w_{jk}} \\
&\Leftrightarrow \frac{\Delta\mu_j}{\alpha_j} = \frac{\sum_i \alpha_j l_{ij}\left(\hat{y}_i^n - y_i\right) - \alpha_j \beta \sum_k \left(\mu_j^n - \mu_k^n\right)}{\sum_i \alpha_j l_{ij}\hat{y}_i^n \sum_k \alpha_k l_{ik} + 2\alpha_j^2 \beta \sum_k w_{jk}} \\
&\Leftrightarrow \Delta\mu_j = \alpha_j \frac{\sum_i l_{ij}\left(\hat{y}_i^n - y_i\right) - \beta \sum_k \left(\mu_j^n - \mu_k^n\right)}{\sum_i l_{ij}\hat{y}_i^n \sum_k \alpha_k l_{ik} + 2\alpha_j \beta \sum_k w_{jk}}.
\end{aligned} \tag{1.36}$$

The update step in this last equation forms the basis of the reconstruction methods introduced in chapters 4 and 5.

1.2.3 Smoothing Priors

In the remainder of this work, the choice of smoothing prior is not restricted to the quadratic prior presented in equation 1.8 of the MLTR derivation. When dealing with small, high contrast targets such as microcalcifications, edge preserving smoothing priors such as the Huber prior [52] or the total variation (TV) prior [53] are interesting alternatives to the quadratic prior.

The TV prior, in equation 1.37, applies a penalty that increases linearly with increasing attenuation differences between neighboring voxels:

$$\ln P\left(\vec{\mu}\right) = -4\beta_{TV} \sum_{j,k} w_{jk}\left|\mu_j - \mu_k\right|, \tag{1.37}$$

and the Huber prior, in equation 1.38, applies the quadratic penalty when the difference between neighboring attenuation values is smaller than a certain threshold δ, and the linear penalty when the difference is larger:

$$\begin{aligned} |\mu_j - \mu_k| < \delta: \quad \ln P(\vec{\mu}) &= -\beta \sum_{j,k} w_{jk} \frac{(\mu_j - \mu_k)^2}{2\delta^2}, \\ |\mu_j - \mu_k| \geq \delta: \quad \ln P(\vec{\mu}) &= -\beta \sum_{j,k} w_{jk} \frac{|\mu_j - \mu_k| - \delta/2}{\delta}. \end{aligned} \tag{1.38}$$

In both instances this means that larger contrasts are penalized less than for the quadratic prior, and thus sharp edges are preserved. Unfortunately these priors can introduce speckle noise for low values of β and result in unnaturally flat images for high values of β. As an alternative we also introduce and evaluate a combined quadratic + TV prior, by adding the penalties in equations 1.8 and 1.37.

The neighborhood w is always chosen as the first order neighborhood for two dimensional grids defined by Hebert and Leahy [50], which means that the prior is only applied in the directions parallel to the detector, and not in the direction perpendicular to the detector. This was preferred over a three-dimensional neighborhood because of the anisotropic resolution in the reconstructions, where the plane separation is typically an order of magnitude larger than the in-plane resolution.

1.3 System and Simulation Parameters for the Siemens Mammomat Inspiration

Since all patient and phantom data used in this work were acquired on a Siemens Mammomat Inspiration DBT system, we used the same geometry in our simulations, and used the same parameters for the reconstruction volume to allow for easier comparisons. A photograph of the system is shown in figure 1.5 and a schematic in figure 1.6.

In the system, the x-ray source (S) is located 608.5 mm (r_s) above the center of rotation (C), which is used as the center of our coordinate system. During an acquisition, 25 exposures are made at a regular interval when the source rotates from -25° to +25° in 25 seconds. The X-ray tube itself contains two anodes made of molybdenum or tungsten and two filters made of 30 μm of molybdenum or 50 μm of rhodium. In clinical practice only the tungsten anode and rhodium filter are used, with tube voltages typically ranging from 26 kV to 33 kV, depending on the compressed breast thickness of the patient. Before the image acquisition, the breast is placed on top of the support plate (P_s), which is made of 1.8 mm of carbon fibre, and located 30 mm below the center of rotation (C). The compression paddle (P_c), made of 2.5 mm of PMMA, then compresses and immobilizes the

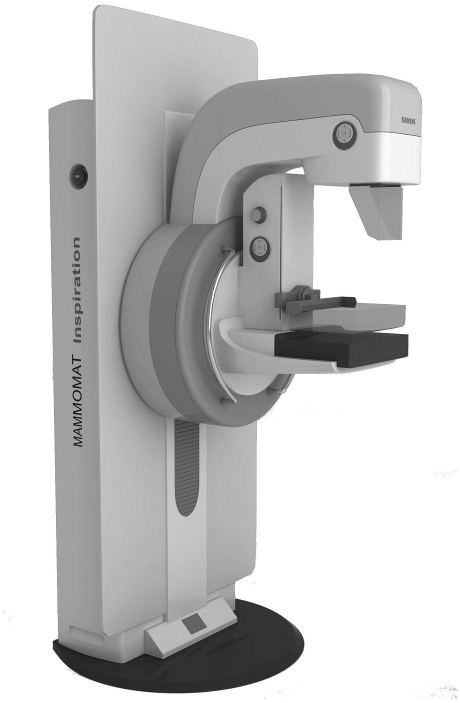

Figure 1.5: The Siemens Mammomat Inspiration tomosynthesis system.

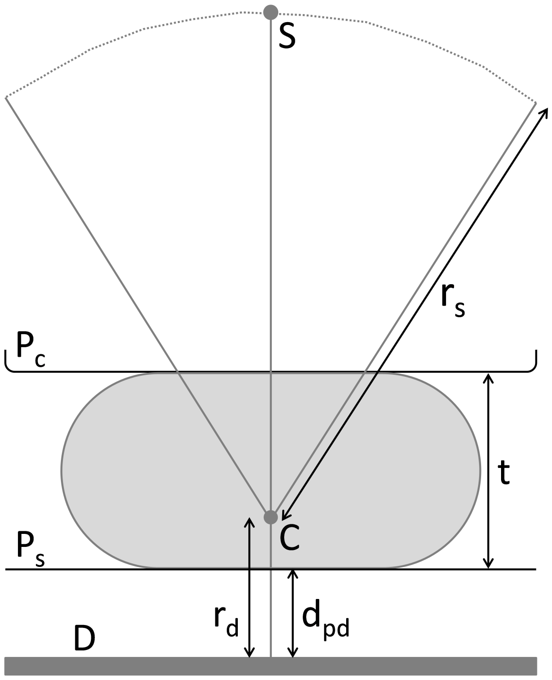

Figure 1.6: Geometry of a tomosynthesis system, reproduced from [54].

breast. The compressed breast thickness t is measured by the system, and used to determine the tube voltage for the exposure and select the number of planes to reconstruct. The x-ray detector is located below the support plate, 47 mm below the center of rotation. It is an amorphous selenium (a-Se) direct-conversion energy-integrating detector [55] with 3584 elements in the tube-travel direction, 2816 elements in the front-back direction, and a pixel spacing of 85 μm.

The default reconstruction is performed using a volume of $3584 \times 2816 \times t$ elements, with an in-plane voxel spacing of 85 μm and a plane separation of 1 mm, although in most instances it will be trimmed in size as much as possible to reduce the processing time and data size. The clinical reconstruction uses a filtered backprojection based on the work of Mertelmeier et al. [56] and Orman et al. [57], and the latest research prototype (SRSAR) includes statistical artifact reduction, super-resolution backprojection and post-reconstruction noise filtering [58], [59]. The iterative reconstructions of clinical data performed in this work are performed on the same grid to allow easier comparisons.

When simulating measurements for this system, the same exposure parameters are used as in the real system, with the following exceptions. The detector is assumed to have a 100% x-ray detection efficiency, and is supersampled by a factor of five (i.e. a single 85×85 μm^2 detector element becomes 25 17×17 μm^2 detector elements) when simulating projections of small features in order to account for partial volume effects. The grid size of the background volume is set to $85 \times 85 \times 85$ μm^3, and contains a slowly varying structure scaled between the attenuation values of adipose and glandular tissue. Microcalcifications are simulated with a grid size of $5 \times 5 \times 5$ μm^3, and assumed to consist of $CaCO_4$.

To simulate the motion of the x-ray tube during the acquisition, we combine projections from multiple stationary subsources at a regular interval over the angular span covered during a single x-ray exposure. The subsources are placed approximately 300 μm apart on the arc, and thus the number of subsources depends on the exposure length that is being simulated. This source spacing results in quarter to half-pixel shifts of the projection data and thus significantly smaller than the detector resolution which was modeled, in a first approximation, by a Gaussian point spread function (PSF) with a full width at half maximum of 90 μm.

1.4 GPU Acceleration

The main disadvantage of iterative reconstruction is its high computational cost, which could be impractical for daily clinical use. Because the same independent operations are repeated for each element of the sinogram $\vec{y}$ or image $\vec{\mu}$, this problem is well suited for parallel execution on a dedicated graphical processing unit (GPU) [60].

Initially GPUs were only programmable by using shading languages such as Cg, HLSL, or GLSL. Since these languages are designed specifically for rendering graphics rather than general purpose computations, such problems need to be adapted to fit the rendering problem. Some examples for image reconstruction can be found in the works of Xu and Mueller [61], [62] and Goddard et al. [63].

The introduction of general purpose GPU programming languages such as CUDA (Nvidia Corporation, Santa Clara, CA, USA) in 2007 and OpenCL (Khronos Group, Beaverton, OR, USA) in 2008 greatly increased the user-friendliness of GPU computing. Comparisons of both languages [64]–[66] indicate that CUDA implementations perform faster than OpenCL implementations on the same hardware, which is not that surprising when considering the nature of both languages: CUDA was designed specifically for Nvidia hardware and is not supported on other hardware, while OpenCL is vendor agnostic and is supported on desktop GPUs and CPUs of AMD, Intel, and Nvidia. This means that while CUDA has the advantage on Nvidia hardware, OpenCL is much more flexible by allowing the same multithreaded code to run on a dedicated GPU and on a computer cluster node with multicore CPU.

To allow maximal flexibility and easy prototyping, only the most computationally expensive part of the reconstruction is implemented in OpenCL, while the remainder of the code was implemented in IDL (Exelis Visual Information Solutions, Boulder, CO, USA), which is used for all high level software in our research group. With this in mind, we implemented the distance driven projector and backprojector [67] for the MLTR reconstruction in OpenCL. These are the operators $\sum_j l_{ij}$ and $\sum_i l_{ij}$ in equations (1.7) and (1.22) respectively.

We performed a comparison between the sequential C and the parallel OpenCL implementations by performing projections with 25 angles for volumes containing between 1 and 64 planes of 3584×2816 voxels each. Projection times were measured for four different systems, listed in table 1.2. The results are plotted in figure 1.7 and show a clear offset for the timings of the GPU and the CPU with 32 threads. This is due to a fixed overhead associated with starting the multithreaded process and the data transfer from host memory to device memory in the case of the GPU, which is the cause of the dependency of the acceleration factor on the data size. In this case the acceleration between the original C implementation on the Einstein server

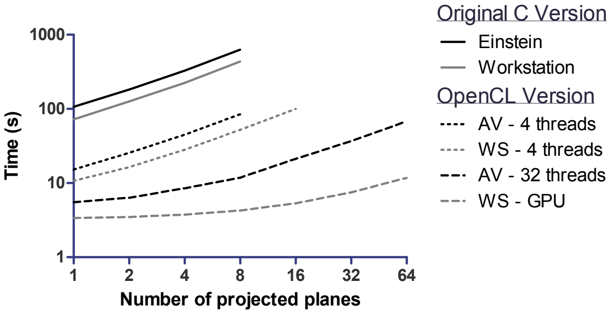

Figure 1.7: Benchmark for the OpenCL version of the distance-driven projector. The CPU and GPU details are listed in table 1.2.

System Name	CPU/GPU	Type
Einstein	Intel Xeon E5440	2.83 GHz (CPU)
Workstation	Intel Xeon E5606	2.13 GHz (CPU)
	Nvidia Tesla C2075	1.15 GHz (GPU)
Avalok	AMD Opteron 6128HE	2.00 GHz (CPU)

Table 1.2: Hardware details of the systems used to compare the projector implementations.

and the Tesla GPU starts at a factor of 32 for a single plane, increases to a factor of 148 for eight planes, and if we then extrapolate the results of the original C version linearly to 64 planes, a factor of 410. When comparing both implementations on the CPU of the workstation, we see an acceleration factor of eight rather than the factor of four which would be expected from the number of threads in the OpenCL implementation. This extra factor of two is related to the geometric constraints in the OpenCL implementation, which assumes a tomosynthesis setup where the detector is flat and parallel to the planes in the reconstruction volume, while the C implementation is more general and makes no assumptions on the system geometry.

With this new implementation, the estimated reconstruction time for 10 iterations of the MLTR algorithm in equation (1.22) with $\beta = 0$ goes from approximately 24 hours when using the C implementation of the projector on the Einstein server to roughly 1 hour when using the OpenCL implementation with 32 threads on the Avalok computer cluster and about 10 minutes on the Tesla C2075 GPU for a typical patient with a compressed breast thickness of 45 mm. This acceleration made it possible to evaluate the methods presented in this work on realistic simulations and clinical datasets.

1.5 Research Objectives and Thesis Overview

To summarize, tomosynthesis is a recent imaging modality gaining acceptance as valuable diagnostic tool for breast imaging. Clinical evaluations have shown that when combined with digital mammography it improves diagnostic accuracy [68], [69] and reduces recall rate [35], and when used on its own, diagnostic accuracy is non-inferior [22]. When looking closer at the different lesion types, evidence points to improved visualization of masses and distortions [14], [70], but potentially worse visualization of microcalcification clusters [15]–[17]. Due to the first-to-market advantage, most of these clinical evaluations were performed on the Hologic Selenia Dimensions system which uses a filtered backprojection reconstruction. With recent technical and task based evaluations [40], [49], [71] indicating that iterative reconstruction might be a better solution for limited angle reconstruction in breast tomosynthesis, it is possible that these studies do not show the full potential of this new modality.

Therefore, the goal of this work was to design, implement, and evaluate a practical maximum a posteriori reconstruction algorithm for digital breast tomosynthesis with a focus on the visualization of microcalcifications.

The work to attain this goal is reported in the next six chapters (of which five have been published or submitted as a paper or conference proceeding), First, we should note that the 'practical' aspect of the goal is interpreted to mean that the reconstruction algorithm should be directly applicable on projection data acquired in clinical practice, and that the reconstruction time remains below one hour for the partially optimized algorithm. The main consequence of this time limitation is that all evaluations are performed after only a few iterations, unless we are specifically examining convergence, and that strength β of each smoothing prior is selected to result in images with acceptable clinical image quality after these few iterations.

In order to be able to reconstruct clinical data, a series of preprocessing steps is presented in chapter 2. These consist of a detector offset correction, an estimation of the blank scan, an estimation of the spatial support of the scanned object, a scatter correction and a beam hardening correction. These preprocessing steps were not available from the start of this work, but were applied in all clinical and phantom reconstruction in chapters 5, 6, and 7.

Chapter 3 then shows the validity of performing the scatter correction as a precorrection instead of including it in the forward model of the iterative reconstruction. Because this correction only modifies low frequency information [72], its effect was evaluated by measuring the signal-difference-to-noise ratio (SDNR) of low contrast spherical masses inserted in patient images. The work in this chapter was presented at the SPIE Medical Imaging Conference (San Diego, 2014), and published in the conference proceedings [73].

In chapter 4 we introduce the first version of our patchwork reconstruction with resolution modeling ($\mathrm{MLTR}_{\mathrm{pr}}$). The forward model in the MLTR algorithm is extended to include a resolution model designed to represent the motion of the x-ray tube during image acquisition which helps reconstruction of microcalcifications. Because this motion creates a height dependent system sharpness [74], we proposed to update the reconstructed volume plane by plane, while the parameters of the resolution model are adjusted for each plane. This update strategy has the advantage of accelerating convergence, but needs to be slowed down in the first iterations to prevent convergence to incorrect solutions in the null space of the limited angle acquisition, resulting in a considerable inefficiency. Since this work was carried out concurrently with the work in chapter 3, it still includes the scatter term in the forward model, rather than as a precorrection. This work was presented at the CT Meeting (Salt Lake City, 2012), published in Medical Physics [75], and patented [76].

In chapter 5, the convergence of the reconstruction algorithm is accelerated by including a multigrid initialization, which is also much more robust against unrealistic null space solutions.The convergence of this updated method was compared to an alternative optimization strategy in the form of ordered subsets and found to produce equivalent results. This work is published in Medical Physics [54].

The best performing method from chapter 5 was then used for all further phantom and patient reconstructions in chapters 6 and 7. Chapter 6 presents the design and validation of a model observer for detecting microcalcification groups in a structured background, and its application on the optimization of a combined quadratic and total variation smoothing prior. The model observer was found to correlate well with human observers, except for the most extreme amounts of smoothing, which were clearly outside of the clinically relevant range. The optimization study found that the detection of microcalcifications was relatively insensitive to the strength of the combined smoothing prior over a large range of settings. This work is partially based on work presented at the SPIE Medical Imaging Conference [77] (Orlando, 2013), and has been submitted for publication in Medical Physics.

The last paper in chapter 7 compares the $\mathrm{MLTR}_{\mathrm{pr}}$ reconstruction introduced in chapter 5 with the Siemens system FBP and the latest Siemens prototype super-resolution filtered backprojection with post reconstruction denoising (SRSAR). The evaluation consisted of a phantom based evaluation of microcalcification and mass detectability and a clinical visual grading study performed by radiologists. For the detection tasks, $\mathrm{MLTR}_{\mathrm{pr}}$ and SRSAR outperformed FBP. However, SRSAR was preferred over $\mathrm{MLTR}_{\mathrm{pr}}$ and FBP in the visual grading study. This work has been accepted for presentation at the European Congress of Radiology (Vienna, 2016).

References

[1] J Ferlay, E Steliarova-Foucher, J Lortet-Tieulent, S Rosso, J. W. W. Coebergh, H Comber, D Forman, and F Bray, "Cancer incidence and mortality patterns in europe: Estimates for 40 countries in 2012", *Eur. J. Cancer*, vol. 49, no. 6, pp. 1374–1403, Apr. 2013.

[2] C. Nickson, K. E. Mason, D. R. English, and A. M. Kavanagh, "Mammographic screening and breast cancer mortality: A case-control study and meta-analysis", *Cancer Epidemiol. Biomarkers Prev.*, vol. 21, no. 9, pp. 1479–1488, Sep. 2012.

[3] Independent UK Panel on Breast Cancer Screening, "The benefits and harms of breast cancer screening: An independent review", *Lancet*, vol. 380, no. 9855, pp. 1778–1786, 2012.

[4] R. E. Bird, T. W. Wallace, and B. C. Yankaskas, "Analysis of cancers missed at screening mammography", *Radiology*, vol. 184, no. 3, pp. 613–617, Sep. 1992.

[5] A. S. Majid, E. S. de Paredes, R. D. Doherty, N. R. Sharma, and X. Salvador, "Missed breast carcinoma: Pitfalls and pearls", *Radiographics*, vol. 23, no. 4, pp. 881–895, Jul. 2003.

[6] D. G. Grant, "Tomosynthesis: A Three-Dimensional radiographic imaging technique", *IEEE Transactions on Biomedical Engineering*, vol. BME-19, no. 1, pp. 20–28, Jan. 1972.

[7] L. T. Niklason, B. T. Christian, L. E. Niklason, D. B. Kopans, D. E. Castleberry, B. H. Opsahl-Ong, C. E. Landberg, P. J. Slanetz, A. A. Giardino, R. H. Moore, D. Albagli, M. C. DeJule, P. F. Fitzgerald, D. F. Fobare, B. W. Giambattista, R. F. Kwasnick, J. Liu, S. J. Lubowski, G. E. Possin, J. F. Richotte, C.-Y. Wei, and R. F. Wirth, "Digital tomosynthesis in breast imaging", *Radiology*, vol. 205, no. 2, pp. 399–406, Nov. 1997.

[8] GE Healthcare, *SenoClaire breast tomosynthesis*, `www3.gehealthcare.com/en/products/categories/mammography/senoclaire_3d`, Accessed: 2015-10-26, 2015.

[9] M. F. Stone, W. Zhao, B. V. Jacak, P. O'Connor, B. Yu, and P. Rehak, "The x-ray sensitivity of amorphous selenium for mammography", *Med. Phys.*, vol. 29, no. 3, pp. 319–324, 2002.

[10] B. Zhao and W. Zhao, "Imaging performance of an amorphous selenium digital mammography detector in a breast tomosynthesis system", *Med. Phys.*, vol. 35, no. 5, pp. 1978–1987, 2008.

[11] C. Ghetti, A. Borrini, O. Ortenzia, R. Rossi, and P. L. Ordonez, “Physical characteristics of GE senographe essential and DS digital mammography detectors”, *Med. Phys.*, vol. 35, no. 2, pp. 456–463, 2008.

[12] M. Åslund, B. Cederström, M. Lundqvist, and M. Danielsson, “Physical characterization of a scanning photon counting digital mammography system based on si-strip detectors”, *Med. Phys.*, vol. 34, no. 6, pp. 1918–1925, 2007.

[13] I. Sechopoulos, “A review of breast tomosynthesis. part i. the image acquisition process”, *Med. Phys.*, vol. 40, no. 1, p. 014 301, 2013.

[14] J. M. Park, E. A. Franken, M. Garg, L. L. Fajardo, and L. T. Niklason, “Breast tomosynthesis: Present considerations and future applications”, *Radiographics*, vol. 27 Suppl 1, S231–S240, Oct. 2007.

[15] S. P. Poplack, T. D. Tosteson, C. A. Kogel, and H. M. Nagy, “Digital breast tomosynthesis: Initial experience in 98 women with abnormal digital screening mammography”, *AJR Am. J. Roentgenol.*, vol. 189, no. 3, pp. 616–623, Sep. 2007.

[16] M. L. Spangler, M. L. Zuley, J. H. Sumkin, G. Abrams, M. A. Ganott, C. M. Hakim, R. Perrin, D. M. Chough, R. Shah, and D. Gur, “Detection and classification of calcifications on digital breast tomosynthesis and 2D digital mammography: A comparison”, *American Journal of Roentgenology*, vol. 196, no. 2, pp. 320–324, Feb. 2011.

[17] A. Tagliafico, G. Mariscotti, M. Durando, C. Stevanin, G. Tagliafico, L. Martino, B. Bignotti, M. Calabrese, and N. Houssami, “Characterisation of microcalcification clusters on 2D digital mammography (FFDM) and digital breast tomosynthesis (DBT): Does DBT underestimate microcalcification clusters? results of a multicentre study”, *Eur. Radiol.*, vol. 25, no. 1, pp. 9–14, Jan. 2015.

[18] J. A. Baker and J. Y. Lo, “Breast tomosynthesis: State-of-the-art and review of the literature”, *Acad. Radiol.*, vol. 18, no. 10, pp. 1298–1310, Oct. 2011.

[19] T. Uematsu, “The emerging role of breast tomosynthesis”, *Breast Cancer*, pp. 1–9, Mar. 2013.

[20] H. R. Peppard, B. E. Nicholson, C. M. Rochman, J. K. Merchant, R. C. Mayo 3rd, and J. A. Harvey, “Digital breast tomosynthesis in the diagnostic setting: Indications and clinical applications”, *Radiographics*, p. 140 204, 2015.

[21] H. J. Teertstra, C. E. Loo, M. A. A. J. Den, H. V. Tinteren, E. J. T. Rutgers, S. H. Muller, and K. G. A. Gilhuijs, “Breast tomosynthesis in clinical practice: Initial results”, *Eur. Radiol.*, vol. 20, no. 1, pp. 16–24, Jan. 2010.

[22] G. Gennaro, A. Toledano, C. Maggio, E. Baldan, E. Bezzon, M. Grassa, L. Pescarini, I. Polico, A. Proietti, A. Toffoli, and P. C. Muzzio, “Digital breast tomosynthesis versus digital mammography: A clinical performance study”, *Eur. Radiol.*, vol. 20, no. 7, pp. 1545–1553, Jul. 2010.

[23] T. M. Svahn, D. P. Chakraborty, D Ikeda, S Zackrisson, Y Do, S Mattsson, and I Andersson, “Breast tomosynthesis and digital mammography: A comparison of diagnostic accuracy”, *Br. J. Radiol.*, vol. 85, no. 1019, e1074–e1082, Jun. 2012.

[24] K. Lång, I. Andersson, A. Rosso, A. Tingberg, P. Timberg, and S. Zackrisson, “Performance of one-view breast tomosynthesis as a stand-alone breast cancer screening modality: Results from the malmö breast tomosynthesis screening trial, a population-based study”, *Eur. Radiol.*, vol. 26, no. 1, pp. 184–190, Jan. 2016.

[25] G. Svane, E. Azavedo, K. Lindman, M. Urech, J. Nilsson, N. Weber, L. Lindqvist, and C. Ullberg, “Clinical experience of photon counting breast tomosynthesis: Comparison with traditional mammography”, *Acta radiol.*, vol. 52, no. 2, pp. 134–142, 2011.

[26] M. G. Wallis, E. Moa, F. Zanca, K. Leifland, and M. Danielsson, “Two-view and single-view tomosynthesis versus full-field digital mammography: High-resolution x-ray imaging observer study”, *Radiology*, vol. 262, no. 3, pp. 788–796, Mar. 2012.

[27] B. M. Haas, V. Kalra, J. Geisel, M. Raghu, M. Durand, and L. E. Philpotts, “Comparison of tomosynthesis plus digital mammography and digital mammography alone for breast cancer screening”, *Radiology*, vol. 269, no. 3, pp. 694–700, Dec. 2013.

[28] E. A. Rafferty, J. M. Park, L. E. Philpotts, S. P. Poplack, J. H. Sumkin, E. F. Halpern, and L. T. Niklason, “Assessing radiologist performance using combined digital mammography and breast tomosynthesis compared with digital mammography alone: Results of a multicenter, multireader trial”, *Radiology*, vol. 266, no. 1, pp. 104–113, Jan. 2013.

[29] S. L. Rose, A. L. Tidwell, L. J. Bujnoch, A. C. Kushwaha, A. S. Nordmann, and R. Sexton Jr, “Implementation of breast tomosynthesis in a routine screening practice: An observational study”, *AJR Am. J. Roentgenol.*, vol. 200, no. 6, pp. 1401–1408, Jun. 2013.

[30] P. Skaane, A. I. Bandos, R. Gullien, E. B. Eben, U. Ekseth, U. Haakenaasen, M. Izadi, I. N. Jebsen, G. Jahr, M. Krager, L. T. Niklason, S. Hofvind, and D. Gur, “Comparison of digital mammography alone and digital mammography plus tomosynthesis in a population-based screening program”, *Radiology*, vol. 267, no. 1, pp. 47–56, Apr. 2013.

[31] A. M. McCarthy, D. Kontos, M. Synnestvedt, K. S. Tan, D. F. Heitjan, M. Schnall, and E. F. Conant, "Screening outcomes following implementation of digital breast tomosynthesis in a general-population screening program", *J. Natl. Cancer Inst.*, vol. 106, no. 11, Nov. 2014.

[32] E. A. Rafferty, J. M. Park, L. E. Philpotts, S. P. Poplack, J. H. Sumkin, E. F. Halpern, and L. T. Niklason, "Diagnostic accuracy and recall rates for digital mammography and digital mammography combined with one-view and two-view tomosynthesis: Results of an enriched reader study", *AJR Am. J. Roentgenol.*, vol. 202, no. 2, pp. 273–281, Feb. 2014.

[33] F. J. Gilbert, L. Tucker, M. G. C. Gillan, P. Willsher, J. Cooke, K. A. Duncan, M. J. Michell, H. M. Dobson, Y. Y. Lim, T. Suaris, S. M. Astley, O. Morrish, K. C. Young, and S. W. Duffy, "Accuracy of digital breast tomosynthesis for depicting breast cancer subgroups in a UK retrospective reading study (TOMMY trial)", *Radiology*, p. 142 566, 2015.

[34] G. Gennaro, R. E. Hendrick, P. Ruppel, R. Chersevani, C. di Maggio, M. La Grassa, L. Pescarini, I. Polico, A. Proietti, E. Baldan, E. Bezzon, F. Pomerri, and P. C. Muzzio, "Performance comparison of single-view digital breast tomosynthesis plus single-view digital mammography with two-view digital mammography", *Eur. Radiol.*, vol. 23, no. 3, pp. 664–672, Mar. 2013.

[35] D. Gur, G. S. Abrams, D. M. Chough, M. A. Ganott, C. M. Hakim, R. L. Perrin, G. Y. Rathfon, J. H. Sumkin, M. L. Zuley, and A. I. Bandos, "Digital breast tomosynthesis: Observer performance study", *AJR Am. J. Roentgenol.*, vol. 193, no. 2, pp. 586–591, Aug. 2009.

[36] F. Thibault, C. Dromain, C. Breucq, C. S. Balleyguier, C. Malhaire, L. Steyaert, A. Tardivon, E. Baldan, and H. Drevon, "Digital breast tomosynthesis versus mammography and breast ultrasound: A multireader performance study", *Eur. Radiol.*, vol. 23, no. 9, pp. 2441–2449, Sep. 2013.

[37] T Svahn, I Andersson, D Chakraborty, S Svensson, D Ikeda, D Förnvik, S Mattsson, A Tingberg, and S Zackrisson, "The diagnostic accuracy of dual-view digital mammography, single-view breast tomosynthesis and a dual-view combination of breast tomosynthesis and digital mammography in a free-response observer performance study", *Radiat. Prot. Dosimetry*, vol. 139, no. 1-3, pp. 113–117, Apr. 2010.

[38] J. Lei, P. Yang, L. Zhang, Y. Wang, and K. Yang, "Diagnostic accuracy of digital breast tomosynthesis versus digital mammography for benign and malignant lesions in breasts: A meta-analysis", *Eur. Radiol.*, vol. 24, no. 3, pp. 595–602, Mar. 2014.

[39] N. Houssami and P. Skaane, “Overview of the evidence on digital breast tomosynthesis in breast cancer detection”, *Breast*, vol. 22, no. 2, pp. 101–108, 2013.

[40] T. Wu, R. H. Moore, E. A. Rafferty, and D. B. Kopans, “A comparison of reconstruction algorithms for breast tomosynthesis”, *Med. Phys.*, vol. 31, no. 9, pp. 2636–2647, 2004.

[41] Y. Zhang, H.-P. Chan, B. Sahiner, J. Wei, M. M. Goodsitt, L. M. Hadjiiski, J. Ge, and C. Zhou, “A comparative study of limited-angle cone-beam reconstruction methods for breast tomosynthesis”, *Med. Phys.*, vol. 33, no. 10, pp. 3781–3795, 2006.

[42] M. J. Willemink, P. A. de Jong, T. Leiner, L. M. de Heer, R. A. J. Nievelstein, R. P. J. Budde, and A. M. R. Schilham, “Iterative reconstruction techniques for computed tomography part 1: Technical principles”, *Eur. Radiol.*, vol. 23, no. 6, pp. 1623–1631, Jun. 2013.

[43] I. Sechopoulos, S. Suryanarayanan, S. Vedantham, C. J. D’Orsi, and A. Karellas, “Scatter radiation in digital tomosynthesis of the breast”, *Med. Phys.*, vol. 34, no. 2, pp. 564–576, 2007.

[44] Y. Zhang, H.-P. Chan, B. Sahiner, J. Wei, M. M. Goodsitt, L. M. Hadjiiski, J. Ge, C. Zhou, M. J. Flynn, and J. Hsieh, “Tomosynthesis reconstruction using the simultaneous algebraic reconstruction technique (SART) on breast phantom data”, in *Medical Imaging 2006: Physics of Medical Imaging*, ser. SPIE Proceedings, vol. 6142, SPIE, 2006, pp. 614 249–614249–9.

[45] E. Y. Sidky, X. Pan, I. S. Reiser, R. M. Nishikawa, R. H. Moore, and D. B. Kopans, “Enhanced imaging of microcalcifications in digital breast tomosynthesis through improved image-reconstruction algorithms”, *Med. Phys.*, vol. 36, no. 11, pp. 4920–4932, 2009.

[46] K. Lange and J. A. Fessler, “Globally convergent algorithms for maximum a posteriori transmission tomography”, *IEEE Trans. Image Process.*, vol. 4, no. 10, pp. 1430–1438, Jan. 1995.

[47] T. Wu, A. Stewart, M. Stanton, T. McCauley, W. Phillips, D. B. Kopans, R. H. Moore, J. W. Eberhard, B. H. Opsahl-Ong, L. T. Niklason, and M. B. Williams, “Tomographic mammography using a limited number of low-dose cone-beam projection images”, *Med. Phys.*, vol. 30, no. 3, pp. 365–380, 2003.

[48] J. Nuyts, B. De Man, P. Dupont, M. Defrise, P. Suetens, and L. Mortelmans, “Iterative reconstruction for helical CT: A simulation study”, *Phys. Med. Biol.*, vol. 43, no. 4, pp. 729–737, Apr. 1998.

[49] J. Zhou, B. Zhao, and W. Zhao, “A computer simulation platform for the optimization of a breast tomosynthesis system”, *Med. Phys.*, vol. 34, no. 3, pp. 1098–1109, 2007.

[50] T. Hebert and R. M. Leahy, “A generalized EM algorithm for 3-D bayesian reconstruction from poisson data using gibbs priors”, *IEEE Trans. Med. Imaging*, vol. 8, no. 2, pp. 194–202, Jun. 1989.

[51] J. A. Fessler, E. P. Ficaro, N. H. Clinthorne, and K. Lange, “Grouped-coordinate ascent algorithms for penalized-likelihood transmission image reconstruction”, *IEEE Trans. Med. Imaging*, vol. 16, no. 2, pp. 166–175, Apr. 1997.

[52] E. Ü. Mumcuoğlu, R. M. Leahy, and S. R. Cherry, “Bayesian reconstruction of PET images: Methodology and performance analysis”, *Phys. Med. Biol.*, vol. 41, no. 9, pp. 1777–1807, Sep. 1996.

[53] V. Y. Panin, G. L. Zeng, and G. T. Gullberg, “Total variation regulated EM algorithm”, *IEEE Trans. Nucl. Sci.*, vol. 46, no. 6, pp. 2202–2210, Dec. 1999.

[54] K. Michielsen and J. Nuyts, “Multigrid reconstruction with block-iterative updates for breast tomosynthesis”, *Med. Phys.*, vol. 42, no. 11, pp. 6537–6548, 2015.

[55] M Bissonnette, M Hansroul, E Masson, S Savard, S Cadieux, P Warmoes, D Gravel, J Agopyan, B Polischuk, W Haerer, T Mertelmeier, J. Y. Lo, Y Chen, J. T. Dobbins III, J. L. Jesneck, S Singh, and M. J. Flynn, “Digital breast tomosynthesis using an amorphous selenium flat panel detector”, in *Medical Imaging 2005: Physics of Medical Imaging*, M. J. Flynn, Ed., ser. SPIE Proceedings, vol. 5745, SPIE, 2005, pp. 529–540.

[56] T. Mertelmeier, J. Orman, W. Haerer, and M. K. Dudam, “Optimizing filtered backprojection reconstruction for a breast tomosynthesis prototype device”, in *Medical Imaging 2006: Physics of Medical Imaging*, M. J. Flynn and J. Hsieh, Eds., ser. SPIE Proceedings, vol. 6142, SPIE, 2006, 61420F–61420F–12.

[57] J. Orman, T. Mertelmeier, and W. Haerer, “Adaptation of image quality using various filter setups in the filtered backprojection approach for digital breast tomosynthesis”, in *Digital Mammography*, ser. Lecture Notes in Computer Science, Springer Berlin Heidelberg, 2006, pp. 175–182.

[58] S. Abdurahman, A. Jerebko, T. Mertelmeier, T. Lasser, and N. Navab, “Out-of-Plane artifact reduction in tomosynthesis based on regression modeling and outlier detection”, in *Breast Imaging*, ser. Lecture Notes in Computer Science, Springer Berlin Heidelberg, 2012, pp. 729–736.

[59] S. Abdurahman, F. Dennerlein, A. Jerebko, A. Fieselmann, and T. Mertelmeier, “Optimizing high resolution reconstruction in digital breast tomosynthesis using filtered back projection”, in *Breast Imaging*, ser. Lecture Notes in Computer Science, Springer International Publishing, 2014, pp. 520–527.

[60] G. Pratx and L. Xing, “GPU computing in medical physics: A review”, *Med. Phys.*, vol. 38, no. 5, pp. 2685–2697, 2011.

[61] F. Xu and K. Mueller, “Accelerating popular tomographic reconstruction algorithms on commodity PC graphics hardware”, *IEEE Trans. Nucl. Sci.*, vol. 52, no. 3, pp. 654–663, Jun. 2005.

[62] ——, “Real-time 3D computed tomographic reconstruction using commodity graphics hardware”, *Phys. Med. Biol.*, vol. 52, no. 12, pp. 3405–3419, Jun. 2007.

[63] I. Goddard, T. Wu, S. Thieret, A. Berman, H. Bartsch, M. J. Flynn, and J. Hsieh, “Implementing an iterative reconstruction algorithm for digital breast tomosynthesis on graphics processing hardware”, in *Medical Imaging 2006: Physics of Medical Imaging*, ser. SPIE Proceedings, vol. 6142, SPIE, 2006, pp. 61424V–61424V–7.

[64] C. Siegl, H. G. Hofmann, B Keck, M Prümmer, J Hornegger, N. J. Pelc, E. Samei, and R. M. Nishikawa, “Opencl: A viable solution for high-performance medical image reconstruction?”, in *Medical Imaging 2011: Physics of Medical Imaging*, N. J. Pelc, E. Samei, and R. M. Nishikawa, Eds., ser. SPIE Proceedings, vol. 7961, SPIE, 2011, 79612Q–79612Q–9.

[65] S. Sawall, L. Ritschl, M. Knaup, and M. Kachelrieß, “Performance comparison of OpenCL and CUDA by benchmarking an optimized perspective backprojection”, in *International Meeting on Fully Three-dimensional Image Reconstruction in Radiology and Nuclear Medicine*, 2011, pp. 15–18.

[66] S Mukherjee, N Moore, J Brock, and M Leeser, “CUDA and OpenCL implementations of 3D CT reconstruction for biomedical imaging”, in *High Performance Extreme Computing (HPEC), 2012 IEEE Conference on*, 2012, pp. 1–6.

[67] B. De Man and S. Basu, “Distance-driven projection and backprojection in three dimensions”, *Phys. Med. Biol.*, vol. 49, no. 11, pp. 2463–2475, 2004.

[68] D. Gur, A. I. Bandos, H. E. Rockette, M. L. Zuley, J. H. Sumkin, D. M. Chough, and C. M. Hakim, “Localized detection and classification of abnormalities on FFDM and tomosynthesis examinations rated under an FROC paradigm”, *AJR Am. J. Roentgenol.*, vol. 196, no. 3, pp. 737–741, Mar. 2011.

[69] M. J. Michell, A Iqbal, R. K. Wasan, D. R. Evans, C Peacock, C. P. Lawinski, A Douiri, R Wilson, and P Whelehan, “A comparison of the accuracy of film-screen mammography, full-field digital mammography, and digital breast tomosynthesis”, *Clin. Radiol.*, vol. 67, no. 10, pp. 976–981, Oct. 2012.

[70] I. Andersson, D. M. Ikeda, S. Zackrisson, M. Ruschin, T. Svahn, P. Timberg, and A. Tingberg, “Breast tomosynthesis and digital mammography: A comparison of breast cancer visibility and BIRADS classification in a population of cancers with subtle mammographic findings”, *Eur. Radiol.*, vol. 18, no. 12, pp. 2817–2825, Dec. 2008.

[71] D. Van de Sompel, S. M. Brady, and J. Boone, “Task-based performance analysis of FBP, SART and ML for digital breast tomosynthesis using signal CNR and channelised hotelling observers”, *Med. Image Anal.*, vol. 15, no. 1, pp. 53–70, 2010.

[72] I. Sechopoulos, K. Bliznakova, and B. Fei, “Power spectrum analysis of the x-ray scatter signal in mammography and breast tomosynthesis projections”, *Med. Phys.*, vol. 40, no. 10, p. 101 905, 2013.

[73] K. Michielsen, A. Fieselmann, L. Cockmartin, and J. Nuyts, “Evaluation of low contrast detectability after scatter correction in digital breast tomosynthesis”, in *SPIE Medical Imaging*, B. R. Whiting and C. Hoeschen, Eds., ser. SPIE Proceedings, vol. 9033, International Society for Optics and Photonics, 2014, pp. 903 313–903313–9.

[74] N. W. Marshall and H. Bosmans, “Measurements of system sharpness for two digital breast tomosynthesis systems”, *Phys. Med. Biol.*, vol. 57, no. 22, pp. 7629–7650, Nov. 2012.

[75] K. Michielsen, K. Van Slambrouck, A. Jerebko, and J. Nuyts, “Patchwork reconstruction with resolution modeling for digital breast tomosynthesis”, *Med. Phys.*, vol. 40, no. 3, p. 031 105, Mar. 2013.

[76] A. Jerebko, K. Michielsen, and J. Nuyts, “Plane-by-plane iterative reconstruction for digital breast tomosynthesis”, pat. 8 594 407, 2013.

[77] K. Michielsen, F. Zanca, N. Marshall, H. Bosmans, and J. Nuyts, “Two complementary model observers to evaluate reconstructions of simulated micro-calcifications in digital breast tomosynthesis”, in *SPIE Medical Imaging*, C. K. Abbey and C. R. Mello-Thoms, Eds., ser. SPIE Proceedings, vol. 8673, International Society for Optics and Photonics, 2013, 86730G–86730G–6.

Chapter 2

A Modular Precorrection for Digital Breast Tomosynthesis Projection Data

Koen Michielsen, Guozhi Zhang, Nicholas Marshall,
and Johan Nuyts

Abstract

Purpose: To implement a sequence of preprocessing steps for tomosynthesis projection data to make them compatible with a mono-energetic and scatter-free forward model for transmission tomography used in iterative maximum likelihood reconstruction.

Methods: The preprocessing starts from a set of 'FOR PROCESSING' DICOM data. To start, an empirical offset correction is applied and a blank scan is fitted to the data. The spatial support for the reconstruction is determined by backprojecting the segmented breast in the projection data. At this point a low resolution reconstruction is performed and the results segmented to create a voxel phantom which is then used in a Monte Carlo simulation to obtain a scatter estimate. After applying the scatter correction, the blank scan is updated and a beam hardening correction is applied.

Results: On average the estimated blank scan overestimated the background values by 2%. A visual inspection of the Monte Carlo voxel phantoms shows that they sufficiently reflect patient data, except for thick glandular breasts, where there is a significant underestimation of glandular content.The scatter estimate itself corresponds well with the scatter estimate produced by the Siemens Mammomat Inspiration PRIME method, except at the breast edge.

A comparison between reconstructions from uncorrected and precorrected data shows that average attenuation values for adipose breasts increase from 0.036 mm^{-1} before correction to 0.045 mm^{-1} after correction, which is close to the expected attenuation of 0.046 mm^{-1} found in literature.

Conclusion: The sequence of steps was successfully implemented using both empirical and model based corrections, and reconstructed attenuation values after these corrections were close to their expected theoretical values.

2.1 Introduction

Iterative reconstruction estimates the image from measured projections by optimizing a cost function that includes a forward model $\hat{y}_i$ of the data acquisition. For the maximum likelihood for transmission tomography (MLTR) algorithm [1] this model can be written as

$$\hat{y}_i = b_i e^{-\sum_j l_{ij}\mu_j}, \tag{2.1}$$

with μ_j the linear attenuation coefficient of voxel j, l_{ij} the intersection length between projection line i and voxel j, and b_i the unattenuated value for projection line i, here referred to as the blank scan.

One of the main assumptions is that models that better reflect reality will result in better reconstructions. A straightforward modification would be to include the polychromatic nature of the x-rays used in the acquisition by introducing a dependency on energy bin k for blank scan b_{ik} and attenuation μ_{jk}, and adding a scatter term s_i:

$$\hat{y}_i = \sum_k b_{ik} e^{-\sum_j l_{ij}\mu_{jk}} + s_i. \tag{2.2}$$

Although this is a much better model of the real measurement, our experience in x-ray computed tomography (CT) indicates that the large increase in complexity and computational cost is not always accompanied by an increase in image quality when compared to a reconstruction with the simple model in equation (2.1) after applying scatter and beam hardening correction to the measured data [2]. The largest improvements in image quality were only apparent in patients with metallic implants, while other improvements, such as the suppression of cupping artifacts caused by beam hardening, were equally well handled by performing a water based beam hardening precorrection on the measured data as by the polychromatic forward model.

Therefore, it is important in practical applications to use these sophisticated forward models only where they can improve image quality, and revert to simpler models or precorrections in the other cases. One possible approach is demonstrated in the work of Van Slambrouck and Nuyts [2] that introduces a patchwork reconstruction that applies region specific forward models in the reconstruction volume, to get most of the gain in image quality while avoiding a large part of the computational cost.

Unlike for CT, where projection data retrieved from the system are fully precorrected and log converted, breast tomosynthesis data are available as DICOM 'for processing', with only the flatfield correction for 2D digital mammography applied. Because these projection data are not compatible with the forward model in equation (2.1) which assumes mono-energetic and scatter free data, we present the precorrection steps needed to resolve this. This allows us to apply the MLTR reconstruction to breast tomosynthesis data before moving towards more advanced models in further work.

2.2 Materials and Methods

The following steps were applied to precorrect the measured data, generate a matching blank scan, and constrain the image support. The details for each step are explained in the referred section.

1. Detector offset correction (section 2.2.1).
2. Initial blank scan estimation (section 2.2.2).
3. Determine spatial support (section 2.2.3).
4. Perform scatter correction (section 2.2.4).
5. Update blank scan estimate (section 2.2.2).
6. Apply beam hardening correction (section 2.2.5).

The offset correction and blank scan estimation are specific for the Siemens Mammomat Inspiration system, and modifying them for other vendors will require system specific measurements. The other steps are more general and can be applied to other tomosynthesis systems after accounting for the acquisition geometry.

2.2.1 Offset Correction

DICOM 'for processing' data typically have an arbitrary constant offset value added to all pixel values (PV) such that a pixel that has not measured any radiation has a PV equal to this constant. This is done to make sure dark-frame subtraction, which corrects for dark noise in the detector, does not result in negative pixel values, or wrap around to very high pixel values in readout to unsigned variables. According to the specifications, this offset should be set to 50 for the Siemens Mammomat Inspiration system. In reality we found a systematic increase for this value as a function of the projection number, as shown in figure 2.1. The points in this figure are the average of 12 measurements performed at the lowest system exposure setting while the detector is shielded by lead. Standard deviations were between 0.1 and 0.4 PV for the repeated measurements.

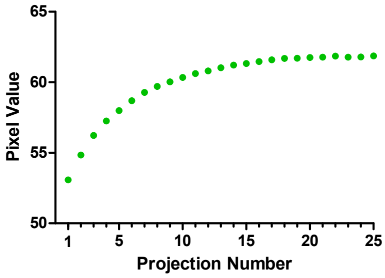

Figure 2.1: Measured offset values for the Siemens Mammomat Inspiration system.

Projection Number	Offset (PV)
1	53
2	55
3	56
4	57
5	58
6–7	59
8–10	60
11–16	61
17–25	62

Table 2.1: Rounded offset correction terms for each projection number.

Because DICOM images only contain integer data values, the measured offset values for each projection number were rounded to the nearest integer value (listed in table 2.1), and then subtracted from the measured data. Any negative pixel values after this operation were set to 0.

2.2.2 Blank Scan Estimation

A patient specific estimate is preferred over a measured blank scan for simplicity, since the model based estimate can account for differences in exposure angles between acquisitions, the use of different x-ray spectra, variations in detector response between systems and after detector calibration during maintenance, and is guaranteed not to introduce additional noise in the reconstruction. In order to use measured blank scans, a set of measurements would be needed for each exposure spectrum on each system and these would need to be updated after each system calibration. Combining the measurements to create a noiseless blank scan would also be challenging due to the variation in exposure angles between repeated acquisitions on the same system.

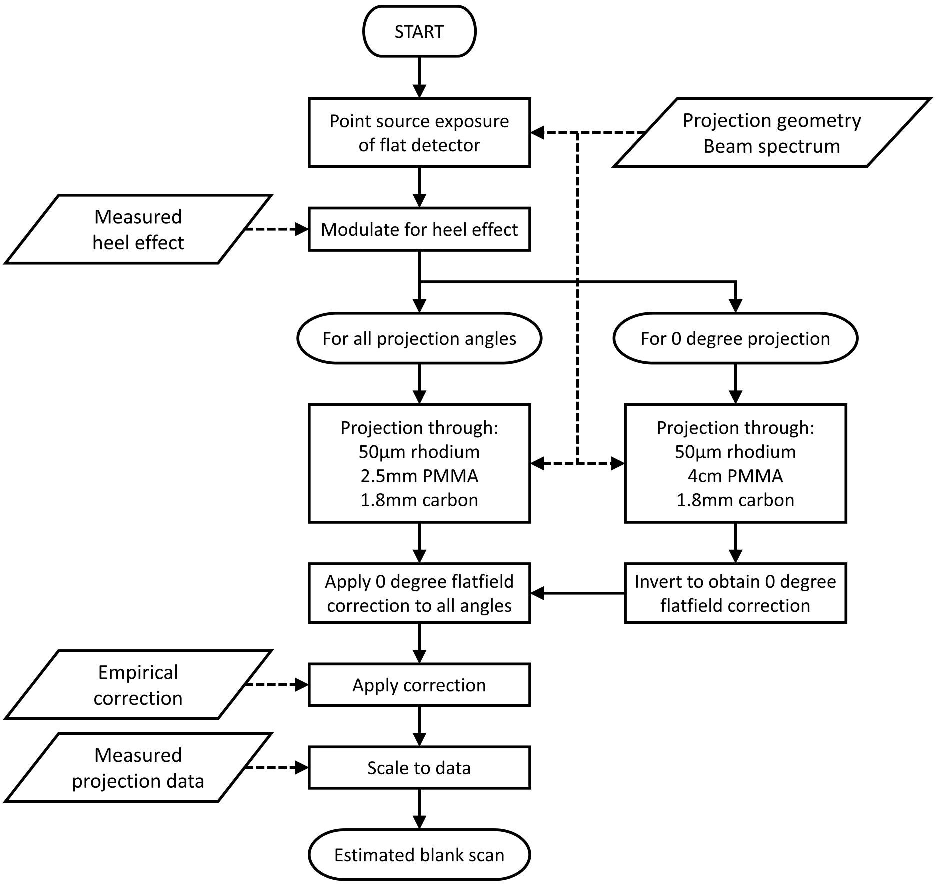

Figure 2.2: Flowchart of the blank scan estimation process.

The blank scans are estimated specifically from each set of acquired patient data starting from the beam spectrum and the measured clinical data, with the general assumption that the flatfield correction for 2D digital mammography with anti-scatter grid, which is only appropriate for the 0° projection, is actually applied to all projections of the tomosynthesis acquisition, which we believe to be the case for the Siemens Mammomat Inspiration system. A flowchart of the steps presented in the following paragraphs is shown in figure 2.2.

The first step was to create a normalization image containing the theoretical measurements for an exposure from a point source at the different exposure angles, accounting for the distance between the source and each detector element ($1/r^2$) and the entry angle in this detector element ($\cos\theta$). This image was then further modified to include the heel effect, which was measured using a storage phosphor cassette for computed radiography (CR). After this, the inverse flatfield correction is determined by performing a poly-

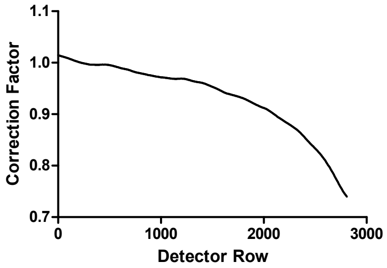

Figure 2.3: Correction factor for the blank scan as a function of detector row starting from the chest side of the detector.

chromatic projection for the 0° position, with equal intensity for each line integral before attenuation by a 50 μm rhodium filter, a flatfield phantom of 4 cm of PMMA, and a 1.8 mm carbon breast support plate, and then multiplying this projection by the 0° normalization image.

The actual blank scan was then created by a polychromatic projection for each source location, with equal intensity for each line integral before attenuation by a 50 μm rhodium filter, a 2.5 mm PMMA compression plate, and a 1.8 mm carbon breast support plate, and then multiplying these projections by the normalization image for each angle. The final step then accounts for the fact that the system applies the 0° flatfield correction at every angle by dividing the normalized projection at each angle by the inverse flatfield correction for the 0° source position.

This image should then differ from the true blank scan only by a scaling factor, but we found that it overestimated values at the back of the detector. Since the cause of this deviation was not clear, and since it was consistent over the full width of the detector and for all angles, an empirical correction (shown in figure 2.3) depending only on the distance from the chest-side of the detector was applied.

The remaining scaling factor can be determined either from the detector response curve, which relates pixel values and exposure, or by directly fitting the blank scan to the projection data. Because the detector response curve can change after a detector calibration, we prefer to use a direct fit to the data.

The scaling factor is determined independently for each projection angle by taking the median of the pixel by pixel proportion between the blank scan and the measured data, after excluding detector pixels covered by the breast, saturated detector values, and the first 256 pixels at the left, right, and back sides of the detector. We prefer the median over the mean (which is the maximum likelihood scale factor) because it is less sensitive to errors in determining which pixels are covered by the breast, and any possible image artifacts.

The blank scan estimation step is performed twice in the precorrection, once after the offset correction for use in the low resolution reconstruction to create the voxel phantom in section 2.2.4, and then again after the scatter correction to account for the scatter that was subtracted in the background area not covered by the breast.

The blank scan estimation was evaluated on a series of 33 artifact-free sets of projection data after all preprocessing steps had been performed. For each set of projection data we calculated the mean proportion between the measured sinogram and the estimated blank scan in the background area next to the breast and the standard deviation of this proportion, and measured the background noise in the sinogram.

2.2.3 Spatial Support

Exact or even partial a priori knowledge of the spatial support, defined as the non-zero attenuation part of the image, can significantly help the reconstruction process, especially in incomplete tomography, as shown by Manduca et al. [3] and Dogandzic et al. [4]. Before implementing this in our reconstruction, we performed an experiment to verify this for the Siemens Mammomat Inspiration system geometry.

We simulated projection data for half of a homogeneous ellipsoid phantom cut on top and bottom by the compression plate and detector cover respectively. These data were then used for three reconstructions of 10 MLTR iterations, the first without spatial support, the second with the spatial support determined by segmenting the projection images, and then excluding all image voxels for which at least one projection line falls outside the segmented area, and the third with the exact spatial support. The results are shown in figures 2.4 and 2.5, and confirm that restricting the reconstruction volume to a predetermined image support can help our reconstruction.

Therefore we include the predetermined segmentation based image support in our reconstructions. A simple thresholding is performed to perform the segmentation, and this worked well in a large range of patients except when artifacts were present in this image. In those cases the segmentation was manually adjusted.

2.2.4 Scatter Correction

In most breast tomosynthesis systems scattered x-rays are included in the measured projection data due to the absence of an anti-scatter grid. We implemented a patient specific Monte Carlo based scatter estimate so that it can be subtracted from the acquired data. For this method we first generate a patient specific voxel phantom, and then use this phantom in a Monte Carlo simulation to estimate the scatter in the measured data.

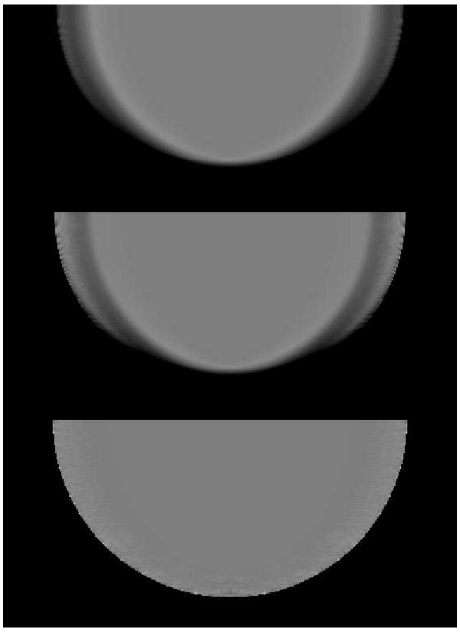

Figure 2.4: Effect of using an image support after 10 MLTR iterations in the central plane of a simulated homogeneous phantom. Top: no image support; middle: segmentation based image support; bottom: exact image support.

Figure 2.5: Difference between 10 MLTR iterations and the true image of a simulated homogeneous phantom. Top: no image support; middle: segmentation based image support; bottom: exact image support.

Voxel Phantom

The voxel phantom is created by classifying each voxel inside the spatial support as either adipose or glandular tissue, using the segmentation of a low resolution (8×8 rebinned) reconstruction with 4 MLTR iterations. No other tissue types are considered in order to reduce complexity. The segmentation is performed by comparing the attenuation in each voxel to the local mean calculated by applying an in-plane 2D Gaussian smoothing with FWHM of 16 voxels to the reconstruction. If the difference between this attenuation value and the local mean is above the threshold T in equation (2.3) then the voxel is classified as glandular tissue, otherwise it is classified as adipose tissue. The variable threshold T (mm^{-1}) was determined empirically by first selecting a separate threshold value for each of four patient cases so that each resulted in a good segmentation, and then performing a linear fit as a function of the compressed breast thickness for the selected values, resulting in the following equation:

$$T = 4 \cdot 10^{-5}\ \text{mm}^{-2} \cdot t - 2 \cdot 10^{-3}\ \text{mm}^{-1}. \tag{2.3}$$

This means the threshold is higher for thicker breast and thus fewer voxels are classified as glandular, following the trend that thinner breasts are on average more glandular than thicker breasts [5].

This voxel phantom is then extended with a 2.5 mm PMMA compression plate and a 1.8 mm carbon breast support plate to form the complete voxel phantom that is used in the Monte Carlo simulation.

Monte Carlo Scatter Estimate

The EGSnrc (Electron Gamma Shower) Monte Carlo package [6] was used with user codes validated in the work of Zhang et al. [7]. The beam spectrum and exposure angles were chosen to match those reported in the DICOM headers. An independent simulation with 10^7 particles was started for each exposure angle, allowing for easy parallelization.

The Monte Carlo simulation includes a 100% efficient energy integrating detector that provided two sets of data: one set containing all detected photons, and a second set containing only the subset of photons that were Compton- or Rayleigh-scattered during transport. The scatter image is first smoothed using total variation image denoising [8] to make sure we do not introduce additional noise in the projection data after scatter correction.

Because the Monte Carlo simulation is setup to generate a homogeneous exposure of the detector when no attenuating objects are present, both images were multiplied by the blank scan to account for the inhomogeneous irradiation of the detector that was not modeled. The scatter image is then rescaled to match the exposure level of the original projection data by multiplying by the ratio of the average of the measured data and the average of the simulated data. This rescaled scatter image is then subtracted from the projection data to get an estimate of the scatter-free projection data.

Evaluation

The accuracy of the voxel phantoms for 54 patient cases was evaluated through visual inspection by the author. The effect of over- or underestimating the amount of glandular tissue in these voxel phantoms on attenuation values was checked by reconstructing the same set of projection data with scatter corrections based on estimates from 5 different segmentations with varying degrees of accuracy.

Since the user codes for the Monte Carlo simulator had been validated [7], we performed a limited evaluation of the new application by comparing the results to the scatter estimate from the Siemens Mammomat Inspiration PRIME product. PRIME uses a deterministic estimation in projection domain using scattering kernels [9]–[11] computed by polychromatic Monte Carlo simulations for different breast models, and the oblique incidence of x-rays from non-zero projection angles is accounted for by a correction factor similar to the work by Wu et al. [12].

2.2.5 Beam Hardening Correction

The final correction to be applied, is a beam hardening correction using the method of Herman [13]. For this method we first log-convert the projection data to get the total measured attenuation along each projection line, using the previously determined blank scan. If we then assume that the attenuating material only consists of water, we can create a lookup table (LUT) relating the attenuation of a poly-energetic measurement to a theoretical mono-energetic acquisition at a reference energy of 20 keV. After this LUT is applied to the log-converted measured data, the data are converted back to pixel values proportional to the measured cumulative photon energy and can now be used with reconstruction models that assume a mono-energetic measurement.

To evaluate the combination of the scatter correction and the beam hardening correction, the reconstructed attenuation was measured in reconstructions of eight patient cases using both uncorrected and precorrected projection data. The eight cases consisted of four thin (<40mm), dense (DY in the Wolfe classification [14]) breasts and four thick (>70mm) adipose (N1) breasts.

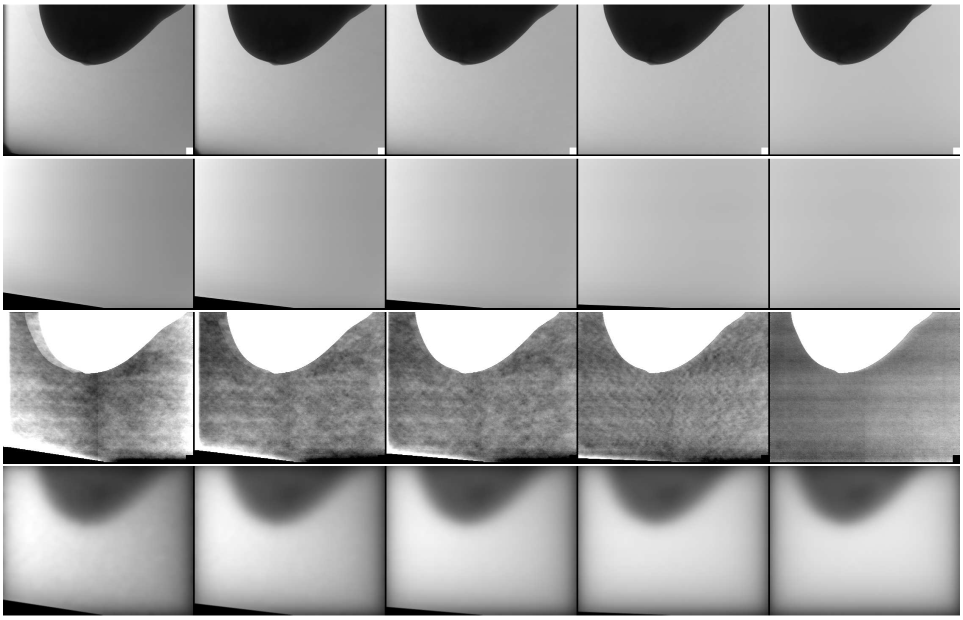

Figure 2.6: Results of the precorrection steps for a single patient, showing projection angles at -25°, -19°, -13°, -6°, and 0° in the five columns. The first row shows the corrected sinogram and the second row the estimated blank scan, both with the window set to [0–2000]. The third row shows the ratio between the estimated blank scan and the corrected sinogram, with the window set to [0.95–1.05], and bottom row shows the scatter estimate with the window set to [0–150].

2.3 Results

Figure 2.6 shows the complete results of the precorrection steps for a single patient. This includes the corrected sinogram, the estimated blank scan, the ratio between the estimated blank scan and the corrected sinogram, and the scatter estimate.

2.3.1 Blank Scan Estimation

Results for the mean ratio between the estimated blank scan and background values in the projection data of 33 patients are shown in figure 2.7. The mean ratio was 1.019 with a 95% confidence interval from 1.016 to 1.021. The smallest mean ratio within this group of cases was 0.993 and the maximum was 1.034. For the individual cases the average standard deviation on the ratio was 0.036 which itself had a standard deviation of 0.018 and ranged from 0.019 to 0.085 (minimum to maximum). The average noise level in the background was 1.52% with a standard deviation of 0.23%, and ranging from 1.10% to 2.30% (minimum to maximum).

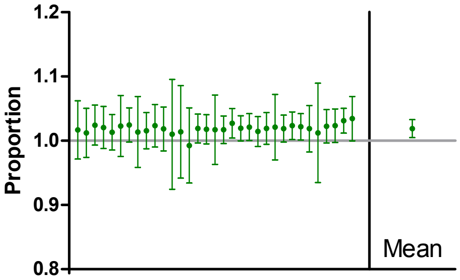

Figure 2.7: Mean ratio between the estimated blank scan and background values in the projection data of 33 patients. Error bars on the individual cases on the left of the divider are standard deviations, the error bar on the mean represents the 95% confidence interval.

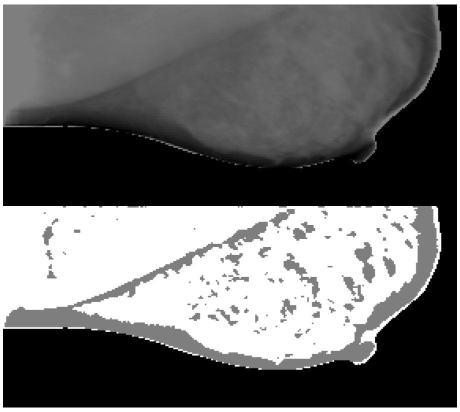

Figure 2.8: Central plane of a low resolution reconstruction and estimated distribution of glandular tissue for a patient with compressed breast thickness of 25 mm.

2.3.2 Scatter Simulation

Visual comparison of 54 voxel phantoms to the patient reconstructions on which they were based, revealed that the glandularity distribution in most phantoms adequately reflected the patient data.

Figures 2.8 and 2.9 show two typical cases, with some overestimation of glandular tissue in figure 2.8 and some underestimation in figure 2.9. The six patient cases that showed the largest deviation were all thick glandular breasts for which the phantom underestimated the glandular content. An example is shown in figure 2.10.

Figure 2.11 shows the case for which we checked the effect of over- or underestimating the amount of glandular tissue on attenuation values. The first estimate simply assumed no scatter was present, the four other scatter estimates are based on Monte Carlo simulations of a fully adipose breast

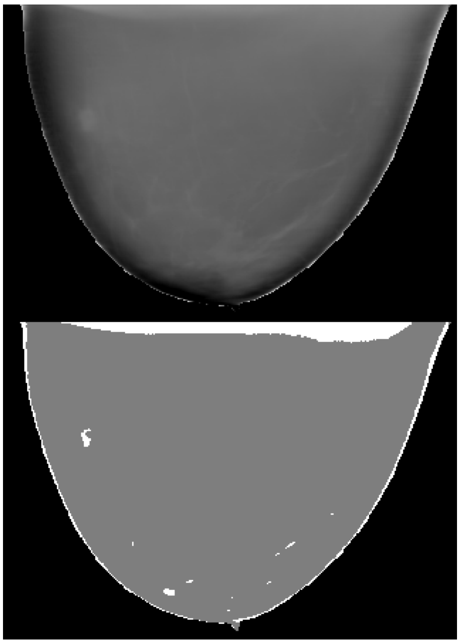

Figure 2.9: Central plane of a low resolution reconstruction and estimated distribution of glandular tissue for a patient with compressed breast thickness of 74 mm.

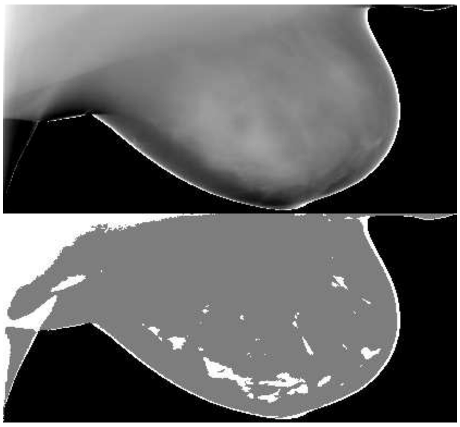

Figure 2.10: Central plane of a low resolution reconstruction and estimated distribution of glandular tissue for a patient with compressed breast thickness of 68 mm.

	Mean Attenuation (mm^{-1})
No correction	0.0405
Only adipose tissue	0.0489
Underestimation of glandular tissue	0.0471
Overestimation of glandular tissue	0.0451
Only glandular tissue	0.0427

Table 2.2: Mean reconstructed attenuation for different scatter corrections.

phantom, breast phantoms that under- and overestimate the glandular content, and a fully glandular breast phantom, as shown in figures 2.11b, 2.11c, 2.11d, and 2.11e respectively. For this patient, our method would produce the voxel phantom in figure 2.11d, with some overestimation of the amount of glandular tissue.

The voxel phantoms in figures 2.8, 2.9, 2.10, and 2.11 are based on reconstructions from rebinned projection data and constrained by a rebinned image support, which causes the high attenuation artifact that can be seen at the breast edge.

The measured mean attenuation for each of the reconstructions is shown in table 2.2. This shows that the limited over- or underestimation in most cases will not have a large influence on the reconstructed attenuation, but that a large underestimation of the glandularity will lead to a large overestimation of the attenuation, and vice versa.

We compared the Monte Carlo and Siemens PRIME scatter estimates and corresponding scatter-to-primary ratios (SPR) for the patients in figures 2.8 (patient A), 2.9 (patient B), and 2.11 (patient C) with compressed breast thicknesses of 25 mm, 74 mm, and 53 mm respectively. Because the PRIME scatter estimation only includes photons scattered in the breast, and not those scattered in the compression plate or the breast support, we performed Monte Carlo simulations both with (MC 1) and without (MC 2) the compression plate and breast support in order to be able to compare the results.

Profiles of the simulation results at projection angles of 0° and 25° are plotted in figures 2.12, 2.14, and 2.16, and the corresponding smoothed SPR profiles, calculated by dividing each scatter estimate by the difference of the measured sinogram and that scatter estimate, are plotted in figures 2.13, 2.15, and 2.17, for patients A, B, and C respectively. One profile is placed parallel to the chestside detector edge, at 22mm, and one perpendicular, in the middle of the detector. For figures 2.12, 2.14, and 2.16 the total intensity (primary + scatter) is plotted on the left Y-axis, and the scatter intensity is plotted on the right Y-axis.

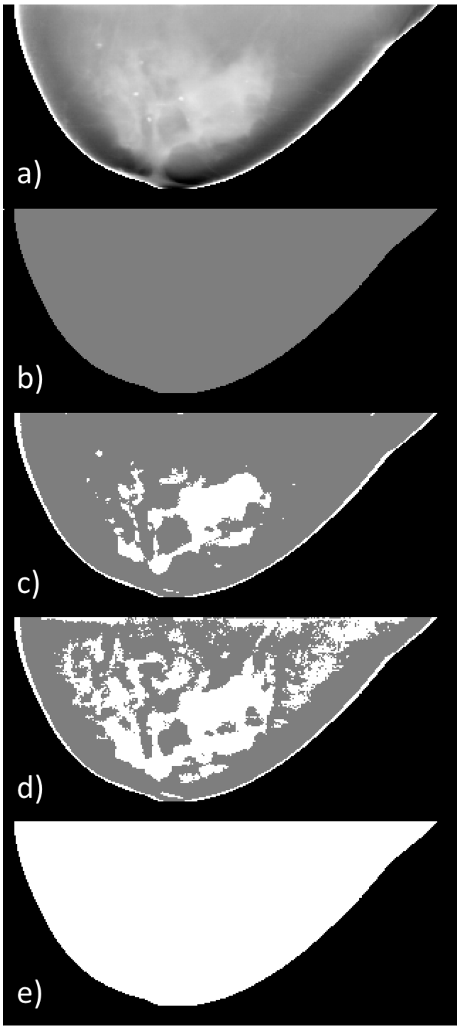

Figure 2.11: Central plane of a low resolution reconstruction for a patient with compressed breast thickness of 53 mm (a) and four examined Monte Carlo voxel phantoms: b) only adipose tissue, c) underestimation of glandular tissue, d) proposed method, with some overestimation of glandular tissue, e) only glandular tissue.

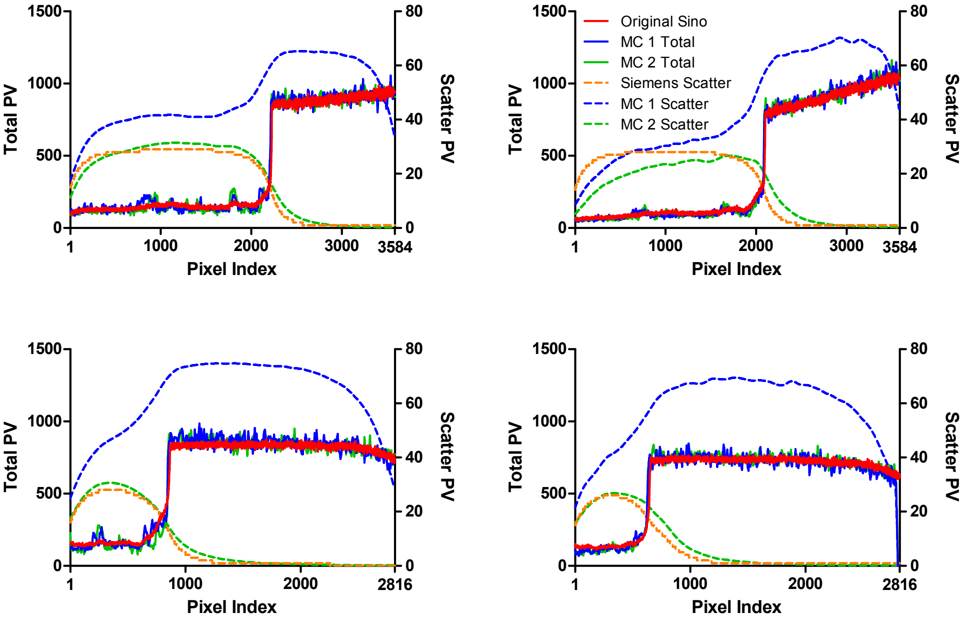

Figure 2.12: Intensity (left axis) and scatter (right axis) profiles at 0° (left column) and 25° (right column) projection angle along the detector width (top row) and depth (bottom row) for patient A, with compressed breast thickness of 25mm.

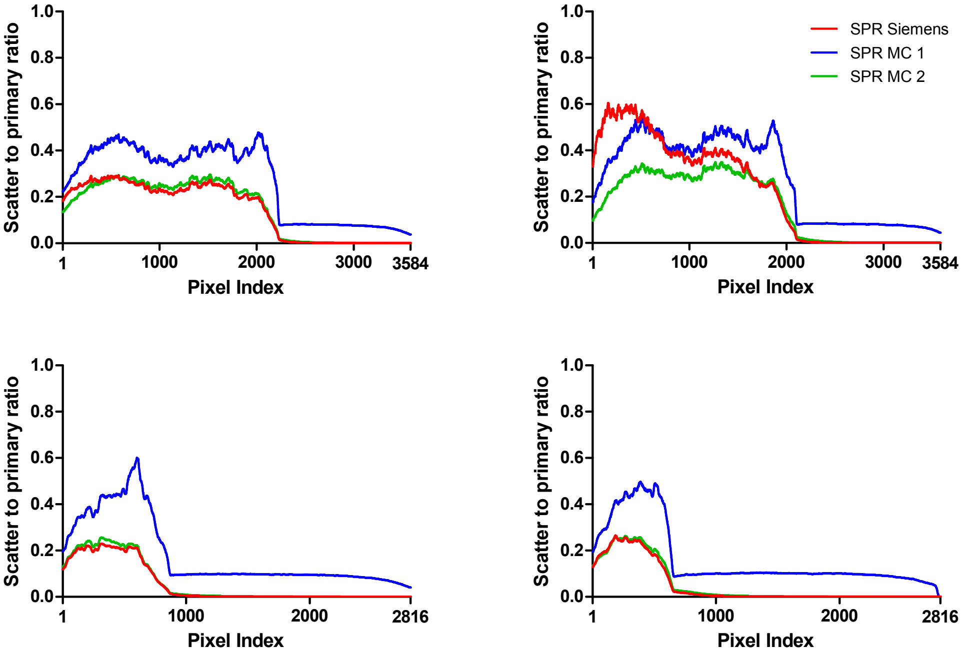

Figure 2.13: SPR profiles at 0° (left column) and 25° (right column) projection angle along the detector width (top row) and depth (bottom row) for patient A, with compressed breast thickness of 25mm.

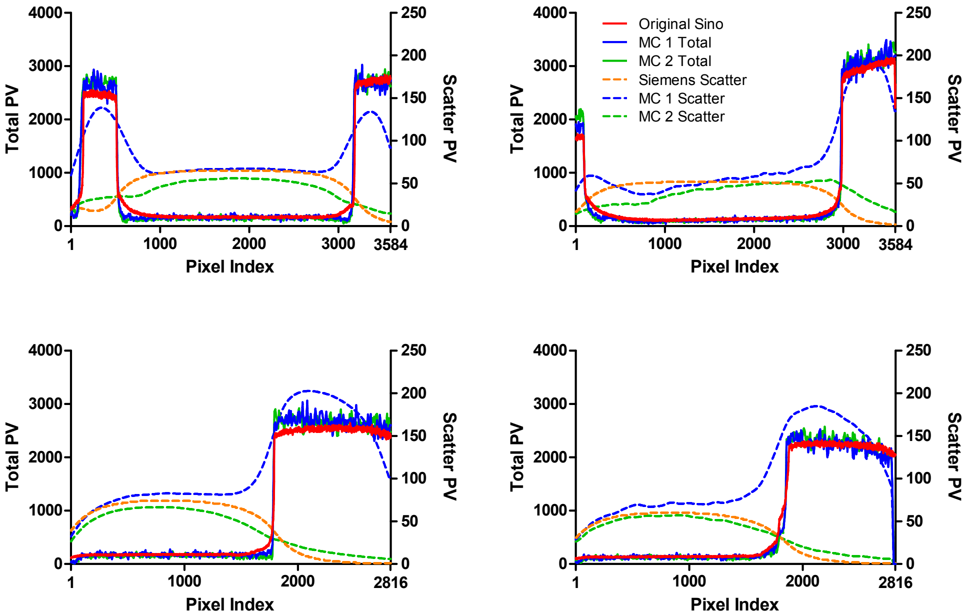

Figure 2.14: Intensity (left axis) and scatter (right axis) profiles at 0° (left column) and 25° (right column) projection angle along the detector width (top row) and depth (bottom row) for patient B, with compressed breast thickness of 74mm.

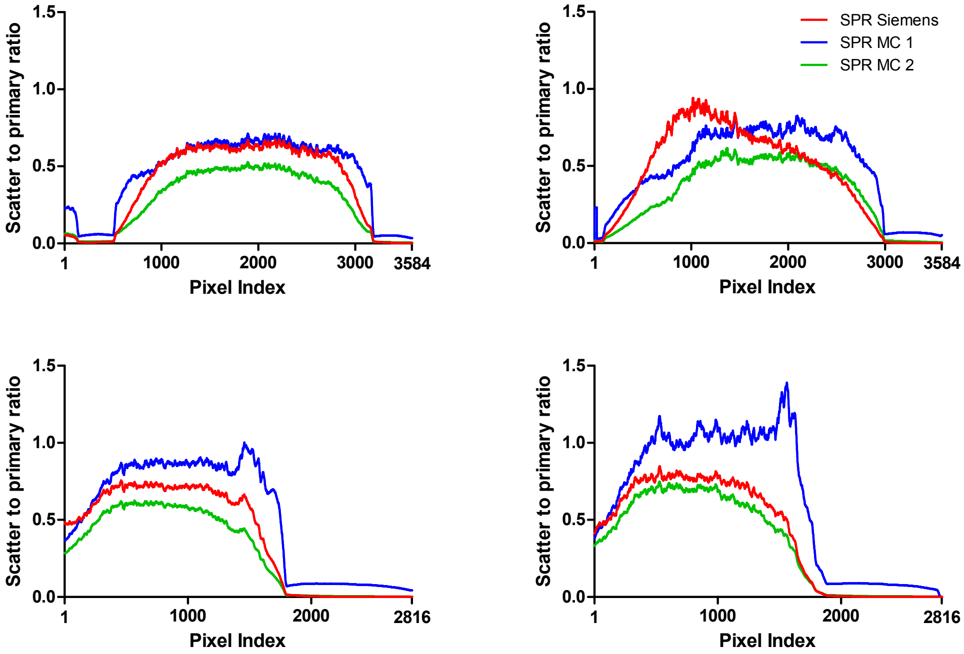

Figure 2.15: SPR profiles at 0° (left column) and 25° (right column) projection angle along the detector width (top row) and depth (bottom row) for patient B, with compressed breast thickness of 74mm.

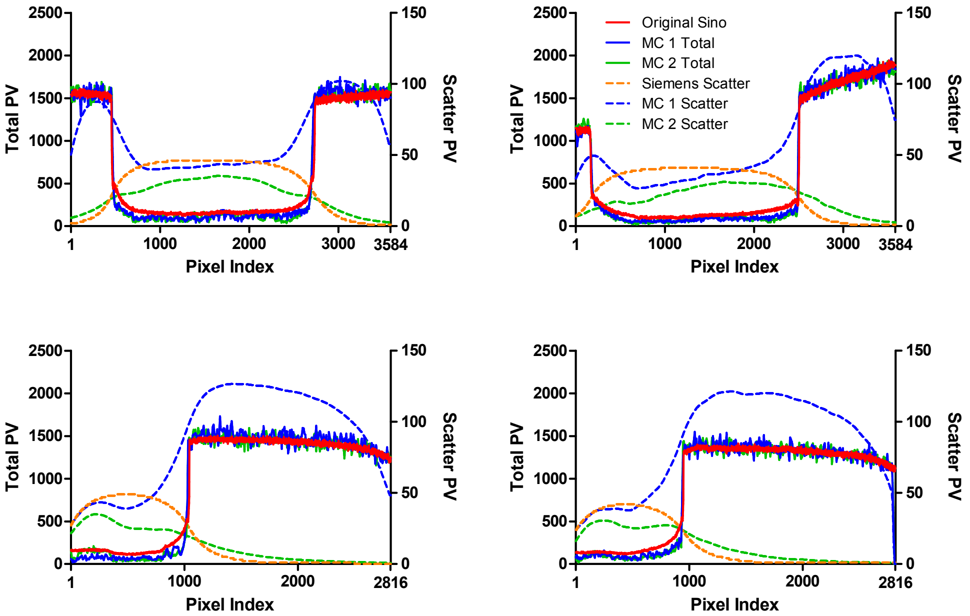

Figure 2.16: Intensity (left axis) and scatter (right axis) profiles at 0° (left column) and 25° (right column) projection angle along the detector width (top row) and depth (bottom row) for patient C, with compressed breast thickness of 53mm.

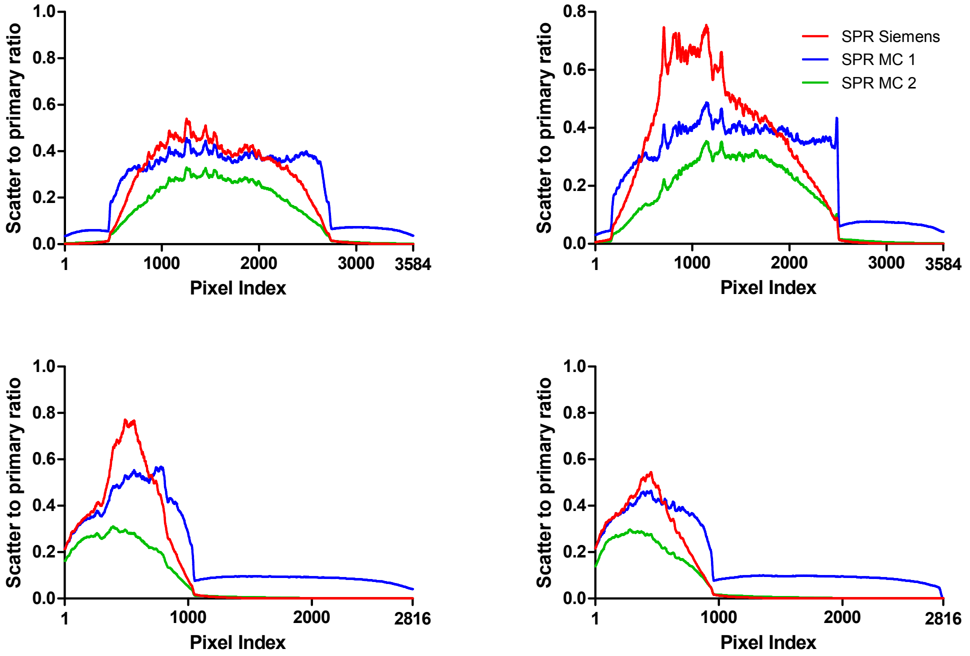

Figure 2.17: SPR profiles at 0° (left column) and 25° (right column) projection angle along the detector width (top row) and depth (bottom row) for patient C, with compressed breast thickness of 53mm.

When comparing the Monte Carlo images to the original sinogram we find an acceptable match for all three patients. The main discrepancy is visible at the breast edge, where the Monte Carlo simulation underestimates the sinogram. This is caused by overestimating the extent of the breast near the top and the bottom of the voxel phantom, due to the limited angular range of the acquisition.

For the scatter estimates themselves, we see that the PRIME and MC 2 scatter estimates match quite well in shape and intensity, with the largest differences seen in patient C which has a more complex distribution of glandular tissue than the other two cases. The difference between the MC 1 and MC 2 scatter profiles clearly shows the influence of including the compression plate and breast support in the Monte Carlo simulation. Because the large amount of scatter in the detector area not covered by the breast does not actually influence the reconstruction, the most important difference is seen at the breast edge where the MC 1 estimate correctly includes scatter which requires additional correction factors in scatter kernel methods that were not included in the PRIME estimate.

SPR values were also measured in a central 128×128 pixel region in the 0° and 25° degree projections, and compared to values calculated according to the formulas of Boone et al. [15] for the 0° projection and Sechopoulos et al. [9] for both projection angles. The 'breast diameter' parameter in the formula of Boone et al. was set to 17cm, 25cm, and 19cm, and glandularity in the formula of Sechopoulos et al. was set to 100%, 0% and 50%, for patients A, B, and C respectively. The results are shown in table 2.3. For patient A, the MC 1 SPR estimate is close to the values from Sechopoulos et al., while the PRIME and MC 2 estimates are close to the value from Boone et al.. This makes sense since the MC 1 simulation and the calculation by Sechopoulos et al. take the compression paddle and breast support into account, while the others do not. For the 0° projection of patient B, the MC 1 SPR estimate corresponds again to the value calculated with the formula given by Sechopoulos et al., but now there is a large deviation for the 25° projection. This very large SPR value seems to be inconsistent with the results shown in figure 17 of the work of Sechopoulos et al. [9]. In that figure, SPR is shown to increase roughly 20% when going from the 0° to the 25° projection for an 80mm breast with 50% glandular content, which is consistent with what we see here for the MC 1 SPR values. Lastly, for patient C, there are large differences for both projection angles. Closer examination of figure 2.16 reveals that the rescaling step of the simulation results in the MC 1 total intensity underestimating the measured data, which means that the scatter estimate itself is also too small.

Patient	A (0°)	A (25°)	B (0°)	B (25°)	C (0°)	C (25°)
PRIME	0.26	0.40	0.73	0.94	0.59	0.84
MC 1	0.43	0.50	0.88	1.07	0.45	0.52
MC 2	0.28	0.32	0.61	0.69	0.29	0.32
Boone et al. [15]	0.28		0.93		0.57	
Sechopoulos et al. [9]	0.42	0.48	0.88	1.82	0.71	1.07

Table 2.3: SPR in a central region of the breast from the scatter simulations of patients A, B, and C, compared to results given by Boone et al. [15] and Sechopoulos et al. [9].

2.3.3 Reconstructed Attenuation

An average attenuation values was measured in a single 256×256×N voxel region in each patient, with N the number of reconstructed planes. For the thick adipose (N1) breasts, a central region was chosen for the ROI, while the most dense region was chosen for the thin glandular (DY) breasts. Results of these measurements from before and after scatter and beam hardening correction are shown in figure 2.18 together with reference attenuation values of adipose and glandular tissue at 20keV measured by Chen et al. [16] and Johns and Yaffe [17], and theoretical values based on ICRU 44 elemental tissue compositions [18] and elemental attenuation coefficients presented by Boone and Chavez [19].

Average attenuation values for the four adipose breasts were similar in both circumstances, and increased by 27% from an average of 0.036 mm^{-1} to 0.045 mm^{-1}, which is still below the expected value of 0.054 mm^{-1} for adipose tissue in ICRU 44, but close to the value of 0.046 mm^{-1} found by both Chen et al. and Johns and Yaffe.

Results for the four dense breast are harder to interpret since these consist of an unknown mixture of adipose and glandular tissue. The average attenuation is at least consistent with the visual impression of the density, since the single case which is visually less dense than the other three also has a lower average attenuation.

2.4 Discussion

The presented preprocessing methods provide the steps needed to use projection data measured on the Siemens Mammomat Inspiration system in an iterative reconstruction algorithm with the basic forward model in equation (2.1). A comparison showed that average attenuation values for adipose breasts were close to the values found by Chen et al. [16] and Johns and Yaffe [17], but remained well below the values calculated for the tissue compositions given in ICRU 44 [18]. We considered the correction to be sufficiently accurate because we were more inclined to trust the attenuation values presented by Chen et al. [16] and Johns and Yaffe [17] as these were both

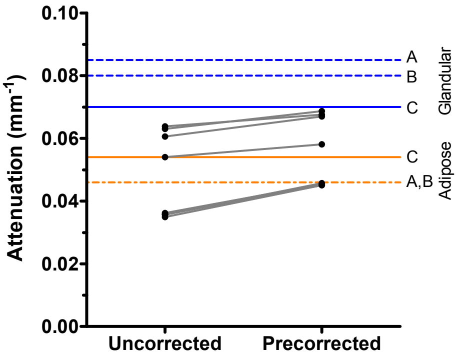

Figure 2.18: Result of precorrection on reconstructed attenuation measured in eight patients, with reference attenuation values from (A) Chen et al. [16], (B) Johns and Yaffe [17], and (C) ICRU 44 [18], [19]

obtained by measuring physical samples. Since quantitative reconstruction was not one of the overall goals for this doctoral thesis, no further work was done to examine the causes of this discrepancy in attenuation values.

The projection dependent offset correction is purely empirical and we have no explanation for this unexpected behavior of the detector. We made some inquiries to the detector manufacturer via Siemens Healthcare, but they could not offer any explanation. Because we did not believe this had any influence on the reconstruction after correction, we did not follow up any further on this topic.

Generating the blank scan is the only necessary step in the preprocessing since it is needed in any forward model. Our model describes the relative measured pixel values for all detector pixels and all source positions which can then be fitted to the part of the detector that is not covered by the patient or phantom being measured. On average, this method results in an average overestimation of 2% near the detector area covered by the breast. Considering the other sources of error in the precorrection steps, this is an acceptable value.

In newer software versions of the Siemens Mammomat Inspiration system the measured pixel values are clipped at 2000, which makes it impossible to rescale the blank scan to the measured data for acquisitions above a certain exposure level. A possible solution would be to rescale the blank scan proportionally to the exposure level as indicated by the current time product (mAs). We did not implement this and only worked with patient cases where the blank scan could be fit to the measured data.

The inclusion of the spatial support serves two purposes. The main reason is to reduce the number of possible solutions from the limited angle acquisition and thereby also reduce some of the edge artifacts in the reconstruction. This effect can be seen in figures 2.4 and 2.5, and these also show that a more accurate estimate of the spatial support will further improve the reconstruction. Any improvements to the current backprojection based estimate would require either a significant additional computational cost by using a discrete tomography reconstruction, or additional hardware to perform an optical measurement to determine the breast shape.

A second reason to include the spatial support is that it allows us to limit the number of voxels that need to be updated in each iteration to the smallest rectangular cuboid that contains the spatial support, and thus reduce the computational cost of the reconstruction. The updates are restricted to this larger rectangular volume rather than the smaller spatial support itself because it was required for operations parallelized in OpenCL (Khronos Group), such as the projector, backprojector, and total variation smoothing prior.

The main source of inaccuracy in our Monte Carlo scatter estimates is the patient specific voxel phantom. Since it starts from the spatial support, it suffers from the same overestimation of the extent of the breast edge near the detector cover and the compression plate. The most difficult aspect is however the segmentation into adipose and glandular tissue. In ideal circumstances this segmentation could be based on a simple threshold in a quantitatively accurate reconstruction, which would depend on a good scatter estimate. Because the initial segmentation depends on a non-quantitative reconstruction, we selected a simple method that puts a threshold on the difference with the local average depending on the breast thickness. This solution works well in the majority of cases because of the inverse correlation between compressed breast thickness and breast glandularity [5], but will result in large over or underestimation of the amount of glandular tissue in thin adipose breasts or thick glandular breast respectively.

The most direct way to improve this segmentation (and thus the Monte Carlo estimate that is based on it) would be to use a more advanced texture based segmentation method such as for example those presented by Shafer et al. [20] or Qin et al. [21]. On the other hand, the work of Boone et al. [15] suggests that a better segmentation might not actually make much difference because the scatter to primary ratio resulting from adipose and glandular tissue is very similar. An alternative point of improvement is linked to obtaining a more accurate image support, since this would result in a more accurate voxel phantom near the breast edge, and lead to a better scatter estimate near the breast edge.

2.5 Conclusion

The sequence of steps was successfully implemented using both empirical and model based corrections and reconstructed attenuation values of adipose tissue after these corrections were close to values found in literature. While substantial additional improvements can be made to the corrections listed above, such as for example in determining the spatial support and the voxel phantom used for the scatter estimate, these were not necessary to evaluate the new reconstruction methods introduced in later chapters on patient data.

The preprocessing sequence that was presented, provides the basic steps needed to make the tomosynthesis projection data compatible with the MLTR forward model. These steps include determination of a blank scan and scatter and beam hardening corrections which are typically performed before all x-ray tomography reconstructions. The additional generation of a spatial support is typically not included, but is useful for limited angle tomography since it reduces the number of possible solutions.

Acknowledgments

This work was supported financially by Siemens Healthcare.

References

[1] J. Nuyts, B. De Man, P. Dupont, M. Defrise, P. Suetens, and L. Mortelmans, “Iterative reconstruction for helical CT: A simulation study”, *Phys. Med. Biol.*, vol. 43, no. 4, pp. 729–737, Apr. 1998.

[2] K Van Slambrouck and J Nuyts, “Metal artifact reduction in computed tomography using local models in an image block-iterative scheme”, *Med. Phys.*, vol. 39, no. 11, pp. 7080–7093, Nov. 2012.

[3] A. Manduca, J. D. Trzasko, and Z. Li, “Compressive sensing of images with a priori known spatial support”, in *SPIE Medical Imaging*, International Society for Optics and Photonics, 2010, pp. 762 223–762223–7.

[4] A Dogandzic, R. Gu, and K. Qiu, “Mask iterative hard thresholding algorithms for sparse image reconstruction of objects with known contour”, in *Signals, Systems and Computers (ASILOMAR), 2011 Conference Record of the Forty Fifth Asilomar Conference on*, Nov. 2011, pp. 2111–2116.

[5] D. R. Dance, C. L. Skinner, K. C. Young, J. R. Beckett, J. C. Kotre, and C. J. Kotre, “Additional factors for the estimation of mean glandular breast dose using the UK mammography dosimetry protocol”, *Phys. Med. Biol.*, vol. 45, no. 11, pp. 3225–3240, Nov. 2000.

[6] I Kawrakow, E Mainegra-Hing, D. W. O. Rogers, F Tessier, and B. R. B. Walters, “The EGSnrc code system: Monte carlo simulation of electron and photon transport”, NRCC, Tech. Rep. 701, 2013.

[7] G Zhang, R Pauwels, N Marshall, E Shaheen, J Nuyts, R Jacobs, and H Bosmans, “Development and validation of a hybrid simulation technique for cone beam CT: Application to an oral imaging system”, *Phys. Med. Biol.*, vol. 56, no. 18, pp. 5823–5843, 2011.

[8] A. Beck and M. Teboulle, “Fast gradient-based algorithms for constrained total variation image denoising and deblurring problems”, *IEEE Trans. Image Process.*, vol. 18, no. 11, pp. 2419–2434, 2009.

[9] I. Sechopoulos, S. Suryanarayanan, S. Vedantham, C. J. D’Orsi, and A. Karellas, “Scatter radiation in digital tomosynthesis of the breast”, *Med. Phys.*, vol. 34, no. 2, pp. 564–576, 2007.

[10] O. Díaz, D. R. Dance, K. C. Young, P. Elangovan, P. R. Bakic, and K. Wells, “A fast scatter field estimator for digital breast tomosynthesis”, in *SPIE Medical Imaging*, N. J. Pelc, R. M. Nishikawa, and B. R. Whiting, Eds., ser. SPIE Proceedings, vol. 8313, International Society for Optics and Photonics, 2012, pp. 831 305–831305–9.

[11] O Diaz, D. R. Dance, K. C. Young, P Elangovan, P. R. Bakic, and K Wells, “Estimation of scattered radiation in digital breast tomosynthesis”, *Phys. Med. Biol.*, vol. 59, no. 15, pp. 4375–4390, 2014.

[12] G. Wu, J. G. Mainprize, J. M. Boone, and M. J. Yaffe, “Evaluation of scatter effects on image quality for breast tomosynthesis”, *Med. Phys.*, vol. 36, no. 10, pp. 4425–4432, 2009.

[13] G. T. Herman, “Correction for beam hardening in computed tomography”, *Phys. Med. Biol.*, vol. 24, no. 1, pp. 81–106, Jan. 1979.

[14] J. N. Wolfe, “Breast patterns as an index of risk for developing breast cancer”, *AJR Am. J. Roentgenol.*, vol. 126, no. 6, pp. 1130–1137, Jun. 1976.

[15] J. M. Boone, K. K. Lindfors, V. N. Cooper, and J Anthony Seibert, “Scatter/primary in mammography: Comprehensive results”, *Med. Phys.*, vol. 27, no. 10, pp. 2408–2416, Oct. 2000.

[16] R. C. Chen, R Longo, L Rigon, F Zanconati, A De Pellegrin, F Arfelli, D Dreossi, R.-H. Menk, E Vallazza, T. Q. Xiao, and E Castelli, “Measurement of the linear attenuation coefficients of breast tissues by synchrotron radiation computed tomography”, *Phys. Med. Biol.*, vol. 55, no. 17, pp. 4993–5005, Sep. 2010.

[17] P. C. Johns and M. J. Yaffe, “X-ray characterisation of normal and neoplastic breast tissues”, *Phys. Med. Biol.*, vol. 32, no. 6, pp. 675–695, Jun. 1987.

[18] International Commision on Radiation Units & Measurements, “Tissue substitutes in radiation dosimetry and measurement”, ICRU, Tech. Rep. 44, 1989.

[19] J. M. Boone and A. E. Chavez, “Comparison of xray cross sections for diagnostic and therapeutic medical physics”, *Med. Phys.*, vol. 23, no. 12, pp. 1997–2005, 1996.

[20] C. M. Shafer, V. L. Seewaldt, and J. Y. Lo, “Segmentation of adipose and glandular tissue for breast tomosynthesis imaging using a 3D hidden-markov model trained on breast MRIs”, in *SPIE Medical Imaging*, International Society for Optics and Photonics, 2011, 79615H–79615H–8.

[21] X. Qin, G. Lu, I. Sechopoulos, and B. Fei, “Breast tissue classification in digital tomosynthesis images based on global gradient minimization and texture features”, in *SPIE Medical Imaging*, International Society for Optics and Photonics, 2014, pp. 90341V–90341V–8.

Chapter 3

Evaluation of Low Contrast Detectability after Scatter Correction in Digital Breast Tomosynthesis

Koen Michielsen, Andreas Fieselmann,
Lesley Cockmartin, and Johan Nuyts

This chapter is based on the conference proceeding published as: K Michielsen, A Fieselmann, L Cockmartin, and J Nuyts, "Evaluation of low contrast detectability after scatter correction in digital breast tomosynthesis," Proc. SPIE vol. 9033, 903313 (2014).

Abstract

Projection images from digital breast tomosynthesis acquisitions can contain a large fraction of scattered x-rays due to the absence of an anti-scatter grid in front of the detector. In order to produce quantitative results, this should be accounted for in reconstruction algorithms. We examine the possible improvement in signal-difference-to-noise ratio (SDNR) for low contrast spherical densities when applying a scatter correction algorithm.

Hybrid patient data were created by combining real patient data with attenuation profiles of spherical masses acquired with matching exposure settings. Scatter in these cases was estimated using Monte-Carlo based scattering kernels. All cases were reconstructed using filtered backprojection (FBP) with and without beam hardening correction and two maximum likelihood methods for transmission tomography, with and without quadratic smoothing prior (MAPTR and MLTR). For all methods, images were re-

constructed without scatter correction, and with scatter precorrection, and for the iterative methods also with an adjusted update step obtained by including scatter in the physics model. SDNR of the inserted spheres was calculated by subtracting the reconstructions with and without inserted template to measure the signal difference, while noise was measured in the image containing the template.

SDNR was significantly improved by 3.5% to 4.5% ($p < 0.0001$) at iteration 10 for both correction methods applied to the MLTR and MAPTR reconstructions. For MLTR these differences disappeared by iteration 100. For regular FBP, SDNR remained the same after correction ($p = 0.60$) while it dropped slightly for FBP with beam hardening correction (-1.4%, $p = 0.028$).

These results indicate that for the iterative methods, application of a scatter correction algorithm has very little effect on the SDNR, it only causes a slight decrease in convergence speed, which is similar for precorrection and correction incorporated in the update step. The FBP results were unchanged because the scatter being corrected is a low frequency component in the projection images, and this information is mostly ignored in the reconstruction due to the high pass filter.

3.1 Introduction

Digital breast tomosynthesis (DBT) is an imaging modality using limited angle tomography to reconstruct thick slices. It is usually implemented as an extension of a regular mammography system, using a partially rotating x-ray tube and a stationary detector. Since the anti-scatter grid in the regular mammography system is focused, it cannot be used in tomosynthesis mode, and thus these projections can contain a significant amount of scatter.

Numerous algorithms have been suggested to mitigate the effect of scattered radiation in x-ray imaging. Rührnschopf and Klingenbeck [1], [2] classify them into deterministic and statistical methods in the projection domain, iterative algorithms that are applied during image reconstruction and image post-processing methods. In general these algorithms produce more quantitative reconstructions, while the effect on image quality seems to be more varied [3]–[5]. Specifically for DBT, Liu et al. [3] found no improvement in SDNR and number of detected image feature targets in a physical phantom when using scatter correction for filtered backprojection (FBP), backprojection (BP), or a proprietary FBP implementation. On the other hand, Feng and Sechopoulos [4] did find that correcting for scatter increased SDNR of low contrast lesions in the CIRS 082 phantom, and improved visualization of lesions in patient cases when using maximum likelihood-expectation maximization (MLEM) reconstruction. A second iterative method, the simultaneous algebraic reconstruction technique

(SART), was also found to improve SDNR in simulated phantom images by Wu et al. [5], but these results can not be directly compared to those of Liu et al. or Feng and Sechopoulos since scatter was removed physically by a grid, which also removes the additional noise introduced by the scatter, something which is not possible when using a post-acquisition digital scatter reduction method.

In this study we will investigate the effect of scatter correction on low contrast detectability in DBT, described by signal difference to noise ratio by using real patient data with inserted spherical masses, and this for several reconstruction methods.

3.2 Materials and Methods

We evaluate the effect of scatter correction on SDNR of inserted low contrast spherical densities in real patient data for different reconstruction methods. In this section we describe the creation of hybrid projection images, scatter estimation, image reconstruction and analysis methods.

3.2.1 Creating Hybrid Projections Images

Cockmartin et al. [6] proposed a technical-clinical method to create attenuation templates of clinically relevant objects, based on the ratio of projections of these objects and the projections of their homogeneous background, for later insertion in patient images. Spheres made of breast tissue simulating material (CIRS, Norfolk VA, USA) and with a diameter of 5 mm were used to represent mass lesions. Three different densities were used, namely 0%, 30% and 50% breast density equivalence. To adequately simulate the surrounding adipose tissue in the breast, the spheres were submersed in vegetable oil. The height of the oil was varied in order to represent a range of compressed breast thicknesses (i.e. 45 mm of oil was used to represent breasts between 40 and 50 mm).

High dose acquisitions with beam qualities as in patient image acquisitions were performed with and without the spheres present in the oil bath on our clinical breast tomosynthesis system (MAMMOMAT Inspiration; Siemens AG, Healthcare Sector, Erlangen, Germany). The tube current-time product (mAs) was set as high as possible (500 mAs) and each image was acquired five times and then averaged into one image. This avoids additional noise in the hybrid patient images after insertion of the templates. The templates were then created based on simple image division of the images with and without the sphere present in the oil bath. Next, the spheres were manually segmented and normalized by the average background signal, measured in four regions of interest in the homogeneous oil closely around the spheres. This normalization was performed to eliminate short term reproducibility errors, which can arise due to small instabilities in the image

Thickness	Number of cases	Lesion density
30 – 39 mm	10	0%
40 – 49 mm	13	0%
50 – 59 mm	11	0%
60 – 69 mm	12	0%, 30%
70 – 79 mm	11	0%

Table 3.1: Overview of patient cases.

acquisition process. These templates, which now capture the properties of the imaging system, were multiplied into unprocessed DBT projection images of patients with corresponding equivalent breast thicknesses in order to obtain hybrid images of spherical densities within anatomical backgrounds.

In this study we selected 57 patient cases with compressed breast thickness between 30 and 79 mm. All acquisitions were used to generate cases which include the lowest density simulated lesion (0%). Cases with thickness between 60 and 69 mm were used to create versions which included densities with contrast of 30% breast density equivalence. The selection is summarized in table 3.1.

3.2.2 Scatter Estimation

For scatter estimation, we use a deterministic method in the projection domain based on scattering kernels [7], [8]. This method can be implemented such that it is computationally fast. Scattering kernels were computed by Monte-Carlo simulations using polychromatic x-ray spectra and the geometry from a breast tomosynthesis system (MAMMOMAT Inspiration) and different kinds of breast tissue models. Oblique incidence of the X-ray from non-zero projection angles was accounted for by a correction factor similar to the work by Wu et al. [5].

Using this estimation method, precorrected projection data were created by subtracting the scatter estimate from the original projection data. This resulted in four sets of projection data for each patient case: with and without an inserted sphere and with and without scatter correction.

3.2.3 Image Reconstruction

The projection data (both with and without scatter precorrection) were reconstructed using an iterative maximum likelihood (ML) method with and without smoothing prior, and filtered backprojection. The data without precorrection were also reconstructed with an ML method (again with and without smoothing prior) that includes a scatter correction in the acquisition model of the algorithm. The iterative ML methods are based on a Poisson model of the image acquisition. Although this noise model is no longer valid after the scatter precorrection, we assume it is still a reasonable approximation because the correction is very smooth within the projected area of the breast, resulting in relatively homogeneous changes to the noise. The Poisson model produces log-likelihood $L = \sum_i y_i \ln \hat{y}_i - \hat{y}_i$, with measured data y_i, and acquisition model $\hat{y}_i$ which includes intersection lengths l_{ij}, a given blank scan b_i, and attenuation distribution $\vec{\mu}$, as shown in equation 3.1. The acquisition model can also include an additive scatter factor s_i, as in equation 3.2.

$$\hat{y}_i = b_i e^{-\sum_j l_{ij}\mu_j} \tag{3.1}$$

$$\hat{y}_i = b_i e^{-\sum_j l_{ij}\mu_j} + s_i \tag{3.2}$$

Log-likelihood L is maximized in order to obtain the measured attenuation distribution $\vec{\mu}$. The optimization is done using the Maximum Likelihood for Transmission (MLTR) algorithm [9], which provides the additive iteration scheme in equation 3.3, with $\Delta\mu_j$ dependent on the acquisition model. The Maximum a Posteriori for Transmission (MAPTR) update steps, which include a smoothing prior P with strength β are shown in equation 3.4 for the acquisition model without scatter, and equation 3.5 for the acquisition model with scatter. Choosing $\beta = 0$ results in the update equation for the original MLTR form. Reconstructions were stopped after 100 iterations.

$$\mu_j^{n+1} = \mu_j^n + \Delta\mu_j^n \tag{3.3}$$

$$\Delta\mu_j = \frac{\sum_i l_{ij}\left(\hat{y}_i - y_i\right) + \beta \sum_k w_{jk} \frac{\partial P(\mu_j,\mu_k)}{\partial \mu_j}}{\sum_i l_{ij}\left(\sum_h l_{ih}\right)\hat{y}_i - 2\beta \sum_k w_{jk} \frac{\partial^2 P(\mu_j,\mu_k)}{\partial \mu_j^2}} \tag{3.4}$$

$$\Delta\mu_j = \frac{\sum_i l_{ij}\left(\hat{y}_i - y_i\right)\frac{\hat{y}_i - s_i}{\hat{y}_i} + \beta \sum_k w_{jk} \frac{\partial P(\mu_j,\mu_k)}{\partial \mu_j}}{\sum_i l_{ij}\left(\sum_h l_{ih}\right)\frac{(\hat{y}_i - s_i)^2}{\hat{y}_i} - 2\beta \sum_k w_{jk} \frac{\partial^2 P(\mu_j,\mu_k)}{\partial \mu_j^2}} \tag{3.5}$$

$$P\left(\mu_j, \mu_k\right) = -\left(\mu_j - \mu_k\right)^2 \tag{3.6}$$

In the MAPTR reconstruction without scatter correction $\beta = 10^5$ was chosen. The value of β needs to be adjusted for the reconstructions with precorrection and with the modified algorithm in equation 3.5 to make sure the smoothing prior has the same strength relative to the likelihood term in the numerator. When using the update step in formula 3.4 with a precorrection, the likelihood term doesn't change since scatter is subtracted from both $\hat{y}_i$ and y_i. The prior term does increase in strength since it depends on the quadratic difference between attenuation values, which change due to the scatter correction. In practice, attenuation values increased by 20%, increasing the weight of the prior term by 44%. To compensate β was set to

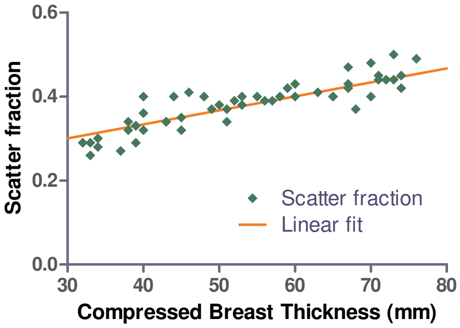

Figure 3.1: Scatter fraction in all patient cases, with linear fit.

$0.7 \cdot 10^5$. For the modified update step, the likelihood term is changed with a factor $(\hat{y}_i - s_i) / \hat{y}_i$ which can be approximated by $1 - \mathrm{SF}$ with SF the scatter fraction in the projection images. The resulting β is then $(1 - \mathrm{SF}) \cdot 0.7 \cdot 10^5$. The scatter fraction used for this calculation was derived from a linear fit to the measured scatter fraction behind the breast for all projection images in all patient cases, as shown in figure 3.1.

The FBP method is adapted to the limited angle cone beam geometry, similar to an FDK [10] type algorithm. It includes a filtering step which performs an approximate inversion of the system modulation transfer function (MTF), a spectral filter and a slice thickness filter [11]. A variant of this method applies a beam hardening correction (BHC) on the projection data before the filtering step.

3.2.4 Data Analysis

After reconstruction, matching cases with and without inserted mass were subtracted in order to obtain an image which contains only the signal difference. The SDNR is then calculated by dividing the mean pixel value inside the lesion in the subtracted image by the root mean square of the standard deviations inside a series of half-overlapping 8×8 pixel regions in the location of the lesion, in the image containing the lesion. The mean signal, standard deviation and SDNR are calculated for each dataset and select comparisons are made between all reconstructions at iterations 10 and 100 using a repeated measures ANOVA analysis followed by Tukey's post test to compare results from both correction methods to the uncorrected reconstruction. The FBP reconstructions with and without scatter correction were compared using a two sided paired t-test.

Comparisons where made at iteration 100 because here reconstructions were approaching convergence while reconstruction time remained feasible for the large datasets. An additional comparison was made at iteration 10 because reconstructions of preliminary experiments with calcifications with

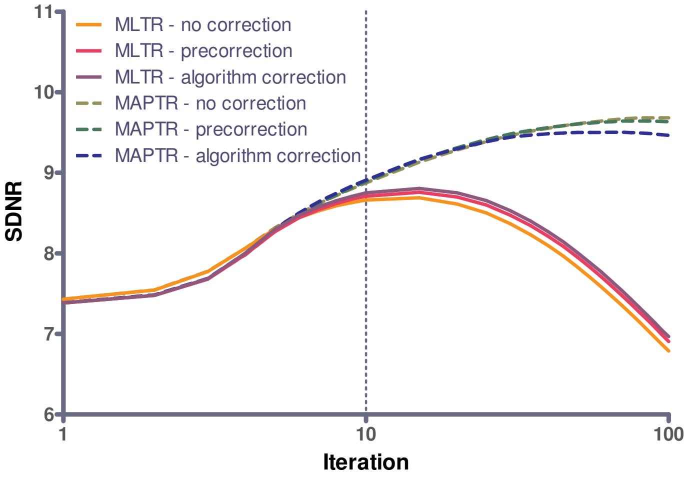

Figure 3.2: Average SDNR values for calcifications with a diameter of 250 μm in a 30 mm breast.

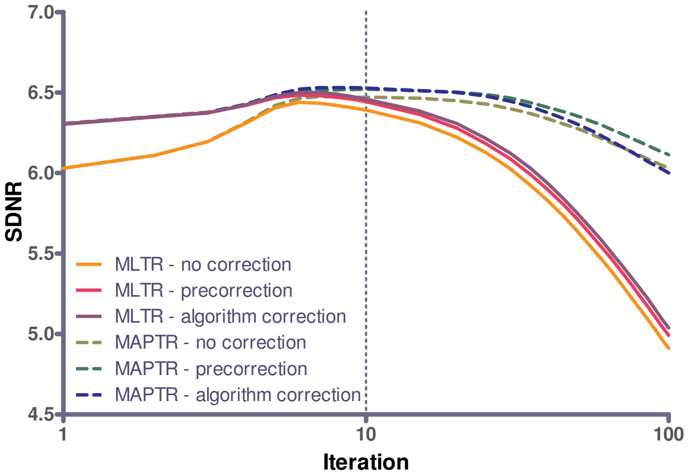

Figure 3.3: Average SDNR values for calcifications with a diameter of 250 μm in a 60 mm breast.

a diameter of 250 μm showed peak SDNR roughly around iteration 10, as shown in figures 3.2 and 3.3 for patients with compressed breast thickness in the range of 30 to 39 mm and 60 to 69 mm.

3.3 Results

Figure 3.4 shows an example of the region around the inserted sphere for a MAPTR reconstruction with and without scatter precorrection. Figures 3.5 and 3.6 show SDNR of the 0% and 30% density contrast spheres as a function of the number of iterations. The results from the reconstructions using the modified update step in equation 3.5 are not shown since they overlap with the results of the reconstruction with precorrection. The result of the FBP reconstructions is shown as a horizontal line in the graph. This line represents both FBP methods with and without scatter correction because they produced overlapping data. It crosses the iterative results between iterations 15 and 20 for both graphs. Figure 3.7 plots the SDNR values of the 0% density contrast sphere at the tenth iteration as a function of compressed breast thickness, with the same overlapping data left out as in the previous graphs.

Statistical test results of the ANOVA analysis with Tukey's post test for the differences in SDNR values at iterations 10 and 100 of the 0% density contrast sphere are listed in table 3.2. Critical q-values for the post test are 3.34 for a 95% confidence interval, and 4.18 for a 99% confidence interval.

Table 3.3 lists signal, noise and SDNR for the patient cases with compressed breast thickness between 60 and 69 mm. The statistical test results for these data can be found in table 3.4. Critical q-values for the post test are 3.47 for a 95% confidence interval, and 4.41 for a 99% confidence interval.

3.4 Discussion

The first conclusion is that the effect of scatter correction in the iterative methods is mainly a change in convergence speed, as can be seen in the MLTR curves in figures 3.5 and 3.6. The differences in SDNR between the methods at iteration 10 almost disappear by iteration 100. Table 3.4 shows that a difference remains for the precorrection, but this is small and only just significant. When combining all thickness groups as in table 3.2, it is the difference between the uncorrected reconstruction and the reconstruction with modified update step that is significant, but again only just and with small actual difference. We suspect these remaining differences are the result of differences in convergence speed.

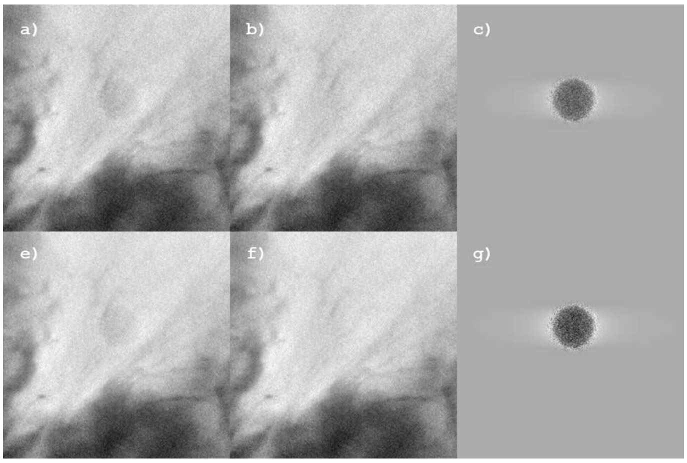

Figure 3.4: MAPTR reconstruction after 10 iterations for one case containing the 0% glandularity density. All subfigures rescaled were to the same minimum and maximum. a) without scatter correction, with density; b) without scatter correction, without density; c) difference between a) and b); e) with scatter precorrection, with density; f) with scatter precorrection, without density; g) difference between e) and f).

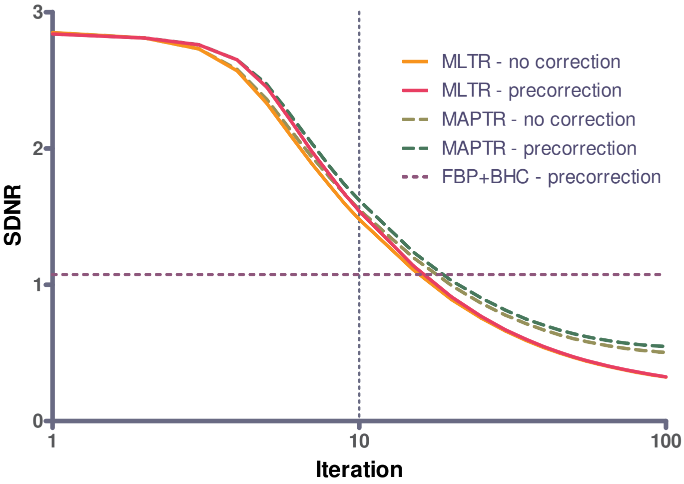

Figure 3.5: SDNR of the 0% density sphere for patients with compressed breast thickness between 60 and 69 mm.

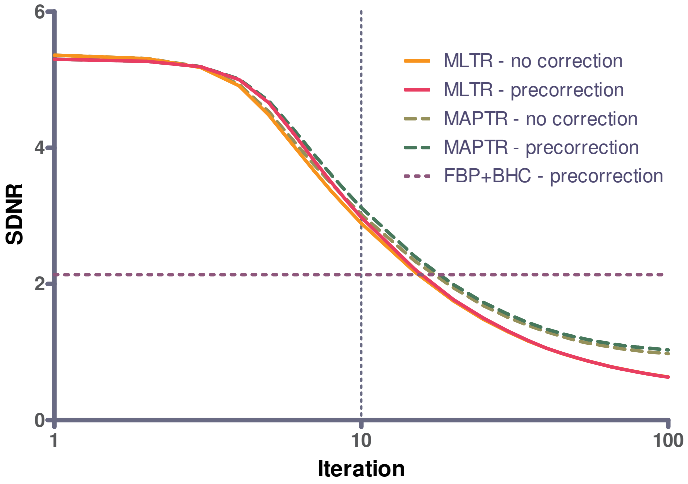

Figure 3.6: SDNR of the 30% density sphere for patients with compressed breast thickness between 60 and 69 mm.

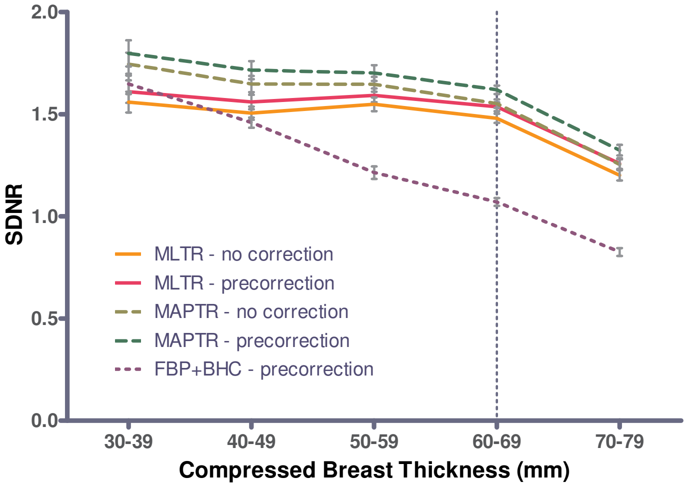

Figure 3.7: SDNR of the 0% density sphere at iteration 10 for all compressed breast thickness groups.

Reconstruction	Precorrection			Algorithm change		
	SDNR change	p-value	q-value	SDNR change	p-value	q-value
MLTR (10it)	+3.6%	<0.0001	26.63	+3.5%	<0.0001	25.74
MLTR (100it)	+0.5%	<0.0001	**3.097**	-0.6%	<0.0001	3.918
MAPTR (10it)	+4.0%	<0.0001	19.90	+4.0%	<0.0001	19.98
MAPTR (100it)	+6.5%	<0.0001	8.918	+7.2%	<0.0001	9.983
FBP	+0.2%	**0.101**				
FBP + BHC	-0.2%	**0.517**				

Table 3.2: Differences, p-values, and q-values for comparing both scatter correction methods to the baseline without scatter correction, for the 0% density contrast sphere in all thickness groups combined. Critical q-values for the post test are 3.34 for a 95% confidence interval, and 4.18 for a 99% confidence interval. Non-significant p- and q-values are printed in bold.

Reconstruction	No scatter correction			Precorrection			Algorithm change		
	Signal	Noise	SDNR	Signal	Noise	SDNR	Signal	Noise	SDNR
MLTR (10it)	.000 976	.000 662	1.48	.001 623	.001 062	1.54	.001 617	.001 060	1.53
MLTR (100it)	.001 429	.004 449	0.32	.002 511	.007 792	0.33	.002 474	.007 784	0.32
MAPTR (10it)	.000 963	.000 623	1.55	.001 594	.000 987	1.62	.001 589	.000 984	1.62
MAPTR (100it)	.001 426	.002 831	0.50	.002 498	.004 537	0.55	.002 463	.004 474	0.55
FBP	162.3	151.7	1.07	214.9	201.2	1.07			
FBP + BHC	232.6	214.8	1.09	298.5	279.6	1.07			

Table 3.3: Mean signal, mean noise and mean SDNR values of the 0% density sphere for patients with compressed breast thickness between 60 and 69 mm.

Reconstruction	Precorrection			Algorithm change		
	SDNR change	p-value	q-value	SDNR change	p-value	q-value
MLTR (10it)	+3.7%	<0.0001	23.99	+3.5%	<0.0001	22.86
MLTR (100it)	+0.3%	0.007	3.637	-1.0%	0.007	**2.763**
MAPTR (10it)	+4.5%	<0.0001	13.94	+4.5%	<0.0001	13.54
MAPTR (100it)	+9.3%	0.0011	5.280	+9.3%	0.0011	5.392
FBP	-0.2%	**0.60**				
FBP + BHC	-1.4%	0.028				

Table 3.4: Differences, p-values, and q-values for comparing both scatter correction methods to the baseline without scatter correction, for all 0% density cases with compressed breast thickness between 60 and 69 mm. Critical q-values for the post test are 3.47 for a 95% confidence interval, and 4.41 for a 99% confidence interval. Non-significant p- and q-values are printed in bold.

A larger difference remains between the SDNR of the corrected and uncorrected MAPTR reconstruction, both for the 60 to 69 mm group and for all data combined, but it is not clear whether this is caused by a true difference, by an incorrect modification of the β parameter applied to ensure the relative strength of likelihood and prior were the same for all reconstructions, or by convergence differences between the MAPTR reconstructions after 100 iterations.

As shown in figure 3.7, the difference in SDNR between methods remains constant for different thickness groups. The SDNR of the iterative methods are less influenced by thickness than the FBP reconstructions.

No effect of scatter correction on the SDNR of the FBP images was observed. This is probably because the scatter being corrected is a low frequency component in the projection images, and this information is mostly ignored in the reconstruction due to the high pass filter. The combination of a beam hardening correction and a scatter correction shows a small negative trend, which might be caused by the fact that the applied beam hardening correction is currently tuned for data that includes scatter and should be adapted for use on scatter corrected data.

3.5 Conclusions

Our results indicate that applying a scatter correction method only has an effect on lesion SDNR in iterative reconstructions due to a small change in convergence speed. The fact that there is barely a difference in the results of both scatter correction methods, allows us to choose the simpler precorrection method when it is necessary to obtain quantitative reconstructed data.

References

[1] E.-P. Rührnschopf and K. Klingenbeck, “A general framework and review of scatter correction methods in x-ray cone-beam computerized tomography. part 1: Scatter compensation approaches”, *Med. Phys.*, vol. 38, no. 7, pp. 4296–4311, 2011.

[2] ——, “A general framework and review of scatter correction methods in cone beam CT. part 2: Scatter estimation approaches”, *Med. Phys.*, vol. 38, no. 9, pp. 5186–5199, 2011.

[3] B. Liu, X. Li, E. Samei, and J. Hsieh, “Effects of scatter radiation on reconstructed images in digital breast tomosynthesis”, in *Medical Imaging 2009: Physics of Medical Imaging*, E. Samei and J. Hsieh, Eds., ser. SPIE Proceedings, vol. 7258, SPIE, 2009, 72585Y–72585Y–13.

[4] S. S. J. Feng and I. Sechopoulos, “A software-based x-ray scatter correction method for breast tomosynthesis”, *Med. Phys.*, vol. 38, no. 12, pp. 6643–6653, 2011.

[5] G. Wu, J. G. Mainprize, J. M. Boone, and M. J. Yaffe, “Evaluation of scatter effects on image quality for breast tomosynthesis”, *Med. Phys.*, vol. 36, no. 10, pp. 4425–4432, 2009.

[6] L. Cockmartin, D. Stalmans, F. Zanca, N. W. Marshall, D. R. Dance, K. C. Young, E. Shaheen, and H. Bosmans, *A new hybrid technical-clinical test demonstrates improved low contrast detectability in tomosynthesis when compared to 2D mammography*, 2012.

[7] I. Sechopoulos, S. Suryanarayanan, S. Vedantham, C. J. D’Orsi, and A. Karellas, “Scatter radiation in digital tomosynthesis of the breast”, *Med. Phys.*, vol. 34, no. 2, pp. 564–576, 2007.

[8] O. Díaz, D. R. Dance, K. C. Young, P. Elangovan, P. R. Bakic, and K. Wells, “A fast scatter field estimator for digital breast tomosynthesis”, in *SPIE Medical Imaging*, N. J. Pelc, R. M. Nishikawa, and B. R. Whiting, Eds., ser. SPIE Proceedings, vol. 8313, International Society for Optics and Photonics, 2012, pp. 831 305–831305–9.

[9] J. Nuyts, B. De Man, P. Dupont, M. Defrise, P. Suetens, and L. Mortelmans, “Iterative reconstruction for helical CT: A simulation study”, *Phys. Med. Biol.*, vol. 43, no. 4, pp. 729–737, Apr. 1998.

[10] L. A. Feldkamp, L. C. Davis, and J. W. Kress, “Practical cone-beam algorithm”, *J. Opt. Soc. Am.*, vol. 1, no. 6, pp. 612–619, Jun. 1984.

[11] T. Mertelmeier, J. Orman, W. Haerer, and M. K. Dudam, “Optimizing filtered backprojection reconstruction for a breast tomosynthesis prototype device”, in *Medical Imaging 2006: Physics of Medical Imaging*, M. J. Flynn and J. Hsieh, Eds., ser. SPIE Proceedings, vol. 6142, SPIE, 2006, 61420F–61420F–12.

Chapter 4

Patchwork Reconstruction with Resolution Modeling for Digital Breast Tomosynthesis

Koen Michielsen, Katrien Van Slambrouck,
Anna Jerebko, and Johan Nuyts

This chapter is based on the paper published as: K Michielsen, K Van Slambrouck, A Jerebko, and J Nuyts, "Patchwork reconstruction with resolution modeling for digital breast tomosynthesis," Med. Phys. 40(3), 031105 (2013).

Abstract

Purpose: Digital breast tomosynthesis is a relatively new diagnostic x-ray modality that allows high resolution breast imaging while suppressing interference from overlapping anatomical structures. However, proper visualization of microcalcifications remains a challenge. For the subset of systems considered in this work, the main cause of deterioration is movement of the x-ray source during exposures. Therefore a modified grouped coordinate ascent algorithm is proposed that includes a specific acquisition model to compensate for this deterioration.

Methods: A resolution model based on the movement of the x-ray source during image acquisition is created and combined with a grouped coordinate ascent algorithm. Choosing planes parallel to the detector surface as the groups enables efficient implementation of the position dependent resolution model. In the current implementation, the resolution model is approximated by a Gaussian smoothing kernel.

The effect of the resolution model on the iterative reconstruction is evaluated by measuring contrast to noise ratio (CNR) of spherical microcalcifications in a homogeneous background. After this, the new reconstruction method is compared to the optimized filtered backprojection method for the considered system, by performing two observer studies: the first study simulates clusters of spherical microcalcifications in a power law background for a free search task; the second study simulates smooth or irregular microcalcifications in the same type of backgrounds for a classification task.

Results: Including the resolution model in the iterative reconstruction methods increases the CNR of microcalcifications. The first observer study shows a significant improvement in detection of microcalcifications ($p = 0.029$), while the second study shows that performance on a classification task remains the same ($p = 0.935$) compared to the filtered backprojection method.

Conclusions: The new method shows higher CNR and improved visualization of microcalcifications in an observer experiment on synthetic data. Further study of the negative results of the classification task showed performance variations throughout the volume linked to the changing noise structure introduced by the combination of the resolution model and the smoothing prior.

4.1 Introduction

Early detection of breast cancers by mammography has been shown to improve patient outcome [1]. However, some lesions, like masses in dense breasts, remain difficult to detect due to the amount of anatomical noise [2]. A three-dimensional imaging technique, such as digital breast tomosynthesis (DBT), may be able to solve this problem by removing interference from overlapping dense tissue [3]. Current experience shows that visualization of masses is much improved [4], but problems remain for microcalcifications [5], [6].

One path to improve visualization of microcalcifications is to optimize the dose and angular distribution of the limited angle set of projections [7]–[9]. These projections are then usually reconstructed with filtered backprojection (FBP) although this reconstruction by FBP is not always optimal [10], [11] because of the limited angular range and low dose acquisitions, especially for small angular range [12]. This while according to Lu et al. [9] a small angular range is actually better for visualizing subtle microcalcifications when using a simultaneous algebraic reconstruction technique (SART), showing that reconstruction technique and acquisition geometry are linked and that an optimal geometry for one reconstruction might not be valid for another method.

The second approach is improving and optimizing the reconstruction algorithm itself. Das et al. [13] show that switching to a penalized maximum likelihood method significantly improves the detection of microcalcifications. Within one iterative method, the precise choice of parameters of the regularization can make a difference [14], both positive and negative. Therefore, Lu et al. [15] create an optimized regularization that preserves the contrast of microcalcifications in DBT and later introduces a multiscale regularization that also preserves details in low contrast lesions [16].

Since iterative reconstruction is most effective when the projection is based on an accurate model of the acquisition process, it might be worth focusing on this aspect in addition to the work on image regularization. Chung et al. [17] improve the model by taking the polychromatic nature of the x-ray spectrum into account. However, we believe that next to the limited angular range, the motion of the x-ray tube focal spot during image formation is the major deteriorating factor in many tomosynthesis systems. Tube motion may contribute blurring on a scale several times larger than the pixel spacing on mammography flat panel detectors (typically ≤ 100 μm). This deterioration can be seen as a large drop of the modulation transfer function (MTF) as a function of the height above the detector plane [18].

Resolution recovery methods have been used successfully in iterative reconstruction methods for single photon emission computed tomography (SPECT) [19], [20], positron emission tomography (PET) [21], [22], and computed tomography (CT) [23], [24]. The general idea behind these methods is that by taking into account the size of the x-ray source, collimation effects, and detector characteristics, the final reconstruction is improved. We will follow the same idea by modeling the combined effect of the x-ray source motion and the finite detector size as a position dependent point spread function (PSF) during reconstruction. Effects from the finite size of the voxels in the reconstructed volume are avoided by using distance driven projection and backprojection [25].

We will combine our resolution model with the noise and acquisition models of the Maximum Likelihood for Transmission (MLTR) algorithm [26], [27], but this algorithm (like all iterative methods) is quite slow in comparison to FBP. Therefore, we try to improve the convergence speed of the algorithm by applying a grouped coordinate ascent (GCA) approach [28], [29], where groups of voxels are updated sequentially instead of simultaneously. By choosing the reconstruction planes parallel to the detector as the groups in the GCA algorithm, we can introduce a resolution model which is dependent on the height above the detector. The adapted MLTR algorithm will also be combined with a regularization term to create a maximum a posteriori algorithm (MAPTR).

4.2 Materials and Methods

4.2.1 Resolution Model

Iterative reconstruction requires a mathematical model of the image acquisition. In the simplest case the estimated transmission scan $\hat{y}_i$ can be written as

$$\hat{y}_i = b_i e^{-\sum_j l_{ij} \mu_j}, \tag{4.1}$$

with μ_j the linear attenuation in voxel j of the reconstruction volume, b_i the blank value for projection line i and l_{ij} the intersection length between projection line i and voxel j. In this case we want to capture resolution effects both from the detector and from the pulsed exposures from a continuously moving x-ray source. Equation (4.2) expands (4.1) to include these effects

$$\hat{y}_{s\theta} = \int_{\theta-\frac{\alpha}{2}}^{\theta+\frac{\alpha}{2}} \sum_n A_{sn} b_n(\phi)\ e^{-\sum_p \sum_k l_{nkp}(\phi)\ \mu_{kp}}\ d\phi. \tag{4.2}$$

The two-dimensional version of this geometry is shown in figure 4.1. Index i of the projection lines has been split in detector coordinate s in the XY plane and angle θ on the arc of projection angles ϕ, with the integral over these angles ϕ representing the tube motion during one of the acquisitions of the tomosynthesis series. Volume coordinate j has been split in plane number p on the Z-axis and inplane coordinate k. The blank value $b_n(\phi)$ now includes the variable intensity (waveform) of the x-ray exposure during each pulse and the smoothing kernel with coefficients A_{sn} represents the intrinsic detector blurring.

It is, however, not feasible to create an update equation from the new acquisition model in equation (4.2). Therefore, we create a simplified version from which to derive the new update equation

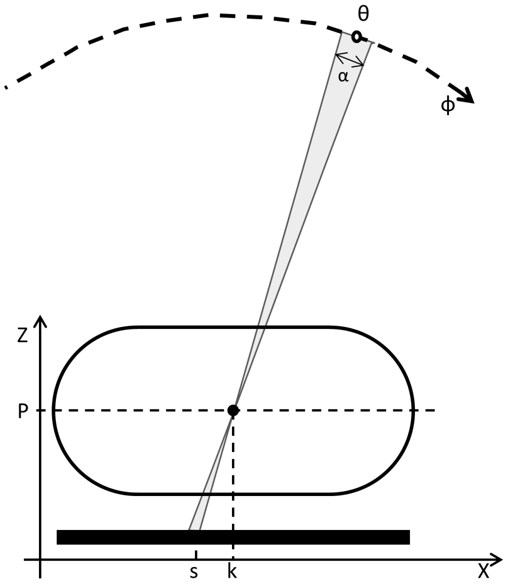

Figure 4.1: Acquisition geometry with moving x-ray source.

$$
\begin{aligned}
\hat{y}_{s\theta} &= \sum_{\phi=\theta-\frac{\alpha}{2}}^{\theta+\frac{\alpha}{2}} \sum_{n} A_{sn} b_{n\phi}\ e^{-\sum_p \sum_k l_{n\phi kp}\ \mu_{kp}}, && (4.3)\\
&= \sum_{\phi=\theta-\frac{\alpha}{2}}^{\theta+\frac{\alpha}{2}} \sum_{n} A_{sn} b_{n\phi}\ e^{-\sum_{p\neq P} \sum_k l_{n\phi kp}\ \mu_{kp}} \\
&\qquad\quad e^{-\sum_k l_{n\phi kP}\ \mu_{kP}}, && (4.4)\\
&\approx b_{s\theta}\ e^{-\sum_{p\neq P} \sum_k l_{s\theta kp}\ \mu_{kp}} \\
&\qquad\qquad \sum_{n} A_{sn} \sum_{\phi=\theta-\frac{\alpha}{2}}^{\theta+\frac{\alpha}{2}} w_{\theta\phi} e^{-\sum_k l_{n\phi kP}\ \mu_{kP}}, && (4.5)\\
&\approx b_{s\theta}\ e^{-\sum_{p\neq P} \sum_k l_{s\theta kp}\ \mu_{kp}} \\
&\qquad\qquad \sum_{n} A_{sn} \sum_{\xi} w_{n\xi}^{P} e^{-\sum_k l_{\xi\theta kP}\ \mu_{kP}}, && (4.6)\\
&= b_{s\theta}\ e^{-\sum_{p\neq P} \sum_k l_{s\theta kp}\ \mu_{kp}} \sum_{n} A_{sn}^{P} e^{-\sum_k l_{n\theta kP}\ \mu_{kP}}. && (4.7)
\end{aligned}
$$

Equation (4.3) is obtained from (4.2) by replacing the integral over ϕ by a sum. In (4.4) we assume that the volume is homogeneous everywhere except for a few high contrast lesions in plane P and thus split out the contribution of attenuation in that plane. The contributions of the homogeneous parts of the volume are then placed outside of the smoothing kernel in equation (4.5), with $b_{s\theta}$ the total blank value for angle θ and $w_{\theta\phi}$ the normalized waveform of the exposure at angle θ. The key approximation is then applied in (4.6) where the sum over the sparsely sampled angles with kernel $w_{\theta\phi}$ is replaced by a sum over the densely sampled detector pixels with kernel $w^P_{n\xi}$, which is combined with kernel A_{sn} to form A^P_{sn} in (4.7).

At this point, we can assume that there are more high contrast lesions in the volume, but that they do not overlap in the projections. Repeating the previous steps for all other planes results in (4.8). Reverting back to index i for the projection lines and index j for the reconstruction volume and including scatter term s_i gives our final approximation of the acquisition process in equation (4.9),

$$\hat{y}_{s\theta} \approx b_{s\theta} \prod_p \sum_n A^p_{sn} e^{-\sum_k l_{n\theta kp}\ \mu_{kp}}, \tag{4.8}$$

$$\hat{y}_i = b_i \prod_p \sum_n A^p_{in} e^{-\sum_{j\in p} l_{nj}\mu_j} + s_i. \tag{4.9}$$

In essence, the motion blur, which is dependent on the height above the detector plane, is combined with the detector blur to form a system resolution model A^p_{in}.

4.2.2 Grouped Coordinate Ascent Algorithm for DBT

In the MLTR algorithm, attenuation distribution $\vec{\mu}$ is obtained by maximizing log-likelihood function L. Assuming that the data are subject to Poisson noise, the log-likelihood can be written as

$$L = \sum_i y_i \ln \hat{y}_i - \hat{y}_i, \tag{4.10}$$

with y_i the measured transmission scan, i the index of the projection line and $\hat{y}_i$ the mathematical model of the transmission scan, such as for example the models in equations (4.1) or (4.9).

With the model in equation (4.1), we can construct the update step of a gradient ascent algorithm [26], [28], [30] using formula (4.11), where $\alpha_j \geq 0$ is a design parameter

$$\Delta\mu_j = \frac{-\alpha_j \frac{\partial L}{\partial \mu_j}}{\sum_k \alpha_k \frac{\partial^2 L}{\partial \mu_j \partial \mu_k}} \tag{4.11}$$

$$= \frac{\alpha_j \sum_i l_{ij}(y_i - \hat{y}_i)}{\sum_i l_{ij}\hat{y}_i \sum_k \alpha_k l_{ik}}. \tag{4.12}$$

Choosing $\alpha_j = 1$ for all j in equation (4.12) results in the MLTR algorithm and $\alpha_j = \mu_j^{\mathrm{old}} + \epsilon$, with ϵ a small positive constant to make sure $\alpha_j > 0$, gives the convex algorithm [31]. The computational cost of this algorithm is dominated by the four (back)projections. If α_j is constant one of the projections can be precomputed, reducing the cost to three (back)projections per iteration.

To create a GCA algorithm, the image is divided into regions (patches) that are updated separately and sequentially [28], [30]. Accelerated convergence is partly due to the sequential updates but mainly due to an increased step size in the update. In equation (4.12), we can consider a patch update as an update with $\alpha_j = 0$ everywhere except in the current group. Therefore, the sum $\sum_h \alpha_h l_{ih}$ in the denominator will be smaller and the step size for updates will be larger for smaller patches. We choose to use each plane (parallel to the detector surface) in the reconstruction volume as a separate patch. This is both the logical choice, since this is how tomosynthesis images are visualized, and close to optimal, since it minimizes the denominator in equation (4.12), indicating that voxels in one plane share little information in the projection. Splitting the updates in this way does not change the computational cost because for each iteration the same number of intersection lengths l_{ij} needs to be calculated. In the real implementation, this introduces some overhead, but the three full (back)projections in each iteration remain dominant.

The MLTR and MAPTR algorithms combined with the plane-by-plane GCA updates will be called $\mathrm{MLTR_p}$ and $\mathrm{MAPTR_p}$ from now on.

According to the central slice theorem, a (parallel beam) projection provides a central slice perpendicular to the projection lines in the Fourier domain. It follows that in tomosynthesis, no samples along the vertical axis in the Fourier domain are obtained. These samples correspond to attenuation distributions that are nearly uniform within the plane, but vary in the direction orthogonal to the plane. As a consequence, the maximum likelihood algorithm has no strong preference about how attenuation components, that are uniform in the plane, should be distributed along the planes. This is very obvious when choosing the groups as planes parallel to the detector surface, where the patchwork algorithm tends to accumulate all low frequency information in the first updated plane. To ensure that low frequency information will be uniformly distributed over all planes, we initialize the reconstruction volume with a rough estimate of the attenuation and divide the update step for each plane in the first two iterations by the number of planes that still need to be updated in the current iteration. This still leaves a limited nonuniformity in the volume, which is largely removed by reversing the update order of the patches in the second iteration. The effects of this initialization on the reconstruction of a homogeneous phantom are shown in figure 4.2.

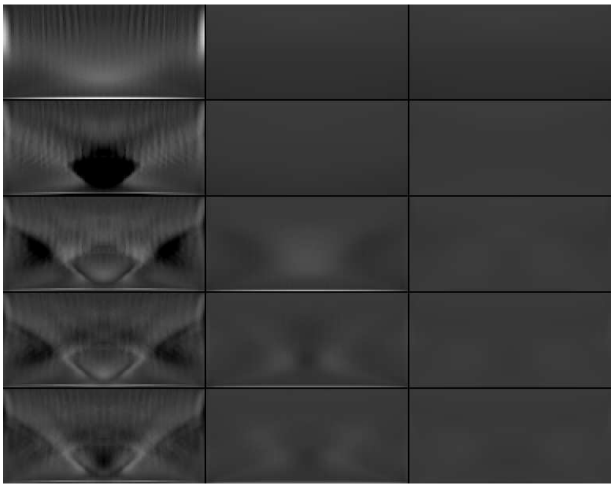

Figure 4.2: Effect of initial updates on the patchwork reconstruction of a homogeneous phantom. Axial slices of the first five iterations (rows) are shown. Left: normal (full weight) updates, going from bottom to top; middle: reduced weight updates in iterations 1 and 2, going from bottom to top; right: reduced weight updates in iterations 1 and 2, going from bottom to top, except for iteration 2, where the update direction is reversed.

4.2.3 Patchwork Reconstruction with Resolution Modeling

To create the full patchwork reconstruction, we combine the resolution model with the grouped coordinate ascent updates so that each group (patch) has its own unique acquisition model determined by the resolution model and is updated separately and sequentially [27].

To derive the update for the new algorithm, we introduce the following definitions that describe the acquisition model:

$$\hat{y}_i = b_i \prod_p \bar{\psi}_i^p + s_i, \tag{4.13}$$

$$\bar{\psi}_i^p = \sum_n A_{in}^p \psi_n^p, \tag{4.14}$$

$$\psi_i^p = e^{-\sum_{j\in p} l_{ij}\mu_j}. \tag{4.15}$$

With this we can calculate the update step using equation (4.11), where $\alpha_j > 0$ inside the current patch and $\alpha_j = 0$ outside. The approximation for the second derivative comes from the assumption that the intersection lengths are smooth on the scale of the kernel A_{in}^p (4.18),

$$-\alpha_j \frac{\partial L}{\partial \mu_j} = \alpha_j \sum_i l_{ij} \psi_i^{p(j)} \sum_n A_{in}^{p(j)} \frac{y_n - \hat{y}_n}{\bar{\psi}_n^{p(j)}} \frac{\hat{y}_n - s_n}{\hat{y}_n}, \tag{4.16}$$

$$\sum_k \alpha_k \frac{\partial^2 L}{\partial \mu_j \partial \mu_k} \approx -\sum_i l_{ij} \psi_i^{p(j)} \cdot \sum_k \alpha_k l_{ik} \cdot \sum_n A_{in}^{p(j)} \frac{\hat{y}_n - s_n}{\bar{\psi}_n^{p(j)}} \left(1 - \frac{y_n s_n}{\hat{y}_n^2}\right), \tag{4.17}$$

$$\sum_n A_{in}^p \psi_n^p \sum_{k \in p} l_{nk} \approx \sum_{k \in p} l_{ik} \sum_n A_{in}^p \psi_n^p. \tag{4.18}$$

If $\alpha_j = \mu_j$ or constant for all j inside the current patch, then this update equation has a computational cost of five (back)projections for each full iteration. The convolution operation adds an additional cost, but this is small in comparison to the additional forward and backprojection needed in this algorithm.

The MLTR$_\mathrm{p}$ and MAPTR$_\mathrm{p}$ algorithms that include the plane-by-plane resolution model will be called MLTR$_\mathrm{pr}$ and MAPTR$_\mathrm{pr}$ from now on.

4.2.4 Determining Smoothing Kernel A_{in}^p

To determine the smoothing kernels A_{in}^p, we assume that the exposure waveform is Gaussian, and the pulse duration in the DICOM header represents its full width at half maximum (FWHM). This FWHM is then projected from the arc on which the focal spot moves onto the detector plane with projection lines crossing in the midpoint of plane p, as shown in figure 4.1. It is clear from the geometry that the projected FWHM will be smaller if plane p is closer to the detector, and wider if p is further from the detector.

Figures 4.3 and 4.5 show that these approximations are appropriate for small calcifications with the relative error in the projection increasing with the diameter (and thus contrast) of the projected object.

Figure 4.3 shows the projections of five calcifications with diameters 100, 125, 150, 175, and 200 μm, located at 60 mm above the detector plane. The left column shows the projections created using a simulation according to the accurate description in formula (4.3) with a rectangular exposure pulse, and the middle column is simulated using the approximated description in formula (4.9). The right column then shows the relative error in the projection by dividing both projections. The profiles of these projections are shown in figure 4.4, and the maximum errors without resolution model (4.1) and with resolution model (4.9) are shown in figure 4.5.

4.2.5 Phantom Simulation and Reconstruction

To test the new reconstruction method, we compare it to other methods by evaluating reconstructions of phantoms containing simulated lesions. The creation and simulation of these phantoms is described in this section, the evaluation methods in section 4.2.6.

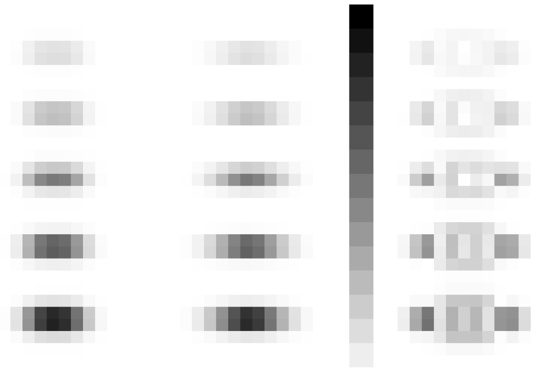

Figure 4.3: Projection of five calcifications (diameters: 100, 125, 150, 175, and 200 μm) located at 60 mm above the detector. Left column: simulation using formula 4.3; middle column: projection using formula 4.9; right column: absolute value of the error in the projection by dividing the left and middle columns. For the projection images, the grayscale runs from 92% (black) to 100% (white) in 16 steps of 0.5%, for the error image, the scale goes from 0% (white) to 1.6% (black) in 16 steps of 0.1%.

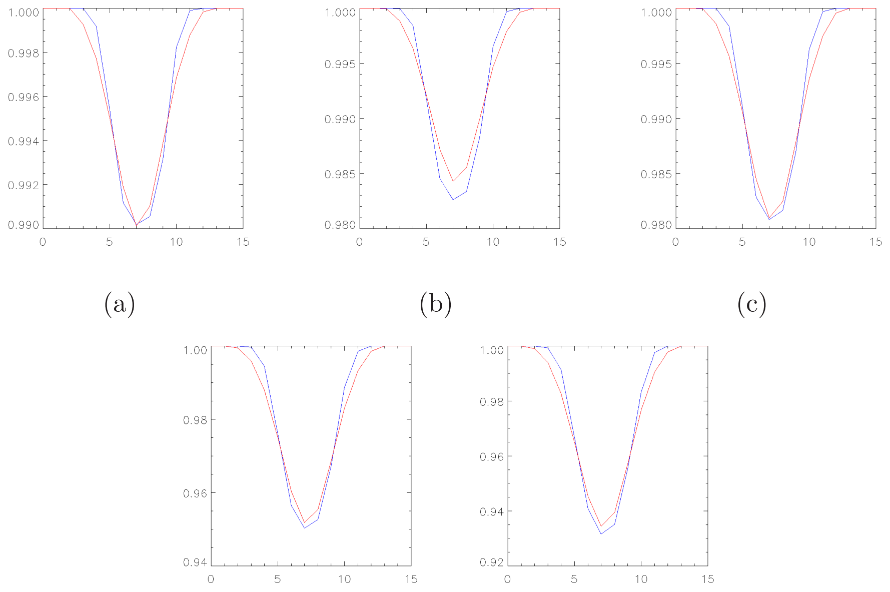

(a) (b) (c)

(d) (e)

Figure 4.4: Profiles of projection of five calcifications (diameters: (a) 100, (b) 125, (c) 150, (d) 175, and (e) 200 μm) located at 60 mm above the detector. The simulation (equation 4.3) is shown in blue, and the approximation (equation 4.9) is shown in red.

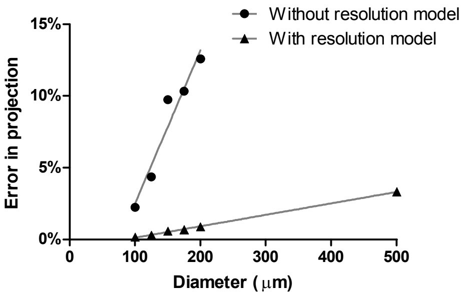

Figure 4.5: Maximum relative error for projections of different diameter calcifications without resolution model (equation (4.1)) and with the approximate model (equation (4.9)).

We simulated two types of background images: a simple homogeneous background with linear attenuation set at a 50-50 mix of adipose and glandular tissue and a background with structured noise created by filtering white noise with a power law filter [32], [33] $f(\nu) = \kappa/\nu^{\beta}$, with ν the frequency, $\beta = 3$ and $\kappa = 10^{-5}$ mm^{-1}. The linear attenuation coefficients of this background were rescaled to values between the attenuation of adipose and glandular tissue. The resulting images were reduced to 500×500×200 isotropic voxels with sides of 85 μm. Figure 4.6 shows some examples of the second type of background. These volumes are then placed in one of three possible locations, always with one side above the chest-side detector edge: central at 27 mm above the detector plane (location 1), central at 67 mm above the detector plane (location 2), and 75 mm off center at a height of 47 mm (location 3). These locations are shown in figure 4.7.

Sixteen spherical microcalcifications were added to the middle plane of the homogeneous background in a 4×4 grid. Separate volumes were created for calcifications with a diameter of 100, 150, and 200 μm.

The structured background images were used to generate two additional data sets: in the first we added a random number of clusters to each background image, Poisson distributed with a mean of 1.0 per image, and placed at a random location within the volume (but not on the edge). Each cluster consisted of a random number of calcifications, with a mean of 2.5 per cluster (again Poisson distributed), but with a minimum of a single calcification per cluster. The individual calcifications were spherical, with a diameter between 100 and 200 μm, spaced 0.5-1.5 mm apart in a random direction and set in a volume with isotropic voxel spacing of 5 μm. Figure 4.8 shows some enlarged examples of the generated clusters.

For the second data set using the structured backgrounds, we created two series of microcalcifications (smooth, corresponding to Le Gal II and irregular, corresponding to Le Gal IV) according to the method of Näppi et

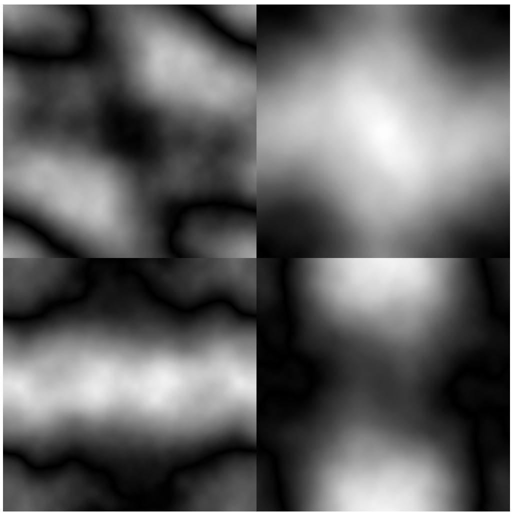

Figure 4.6: Four examples of the power law backgrounds.

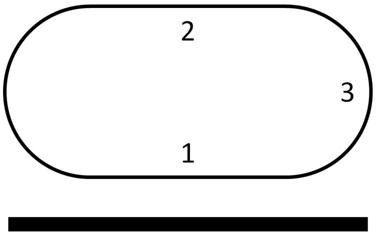

Figure 4.7: Three locations in the breast where the simulated backgrounds are located.

Figure 4.8: Eight examples of simulated clusters consisting of spherical microcalcifications.

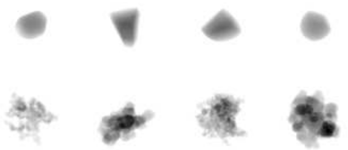

Figure 4.9: Examples of smooth (Le Gal II, top row) and irregular (Le Gal IV, bottom row) microcalcifications.

al. [34]. These microcalcifications were rescaled to a diameter of 200, 300, 400, 500, or 600 μm by changing the voxel spacing of the simulated volume, resulting in isotropic voxel spacings between 6 and 18 μm, depending on the rescaling. Figure 4.9 shows some enlarged examples of the generated calcifications.

Projections of these volumes were simulated according to the acquisition model described in equation (4.3) and with increased detector sampling. Nine source positions were sampled for each exposure angle, corresponding to an exposure time of 120 ms per projection, x-ray energy was set to 20 keV and Poisson noise was generated with a blank scan of 1500 photons per pixel (12.5 μGy detector dose after attenuation).

The geometric blurring parameters for our model were determined for the Mammomat Inspiration system (Siemens, Erlangen, Germany), which is in clinical use on site. Therefore we included the Siemens iFBP method [35] as an additional point of reference next to the iterative methods we described. It was used without detector binning, with slice thickness filter and with a filter designed so that resulting reconstructed slices resemble 2D mammography images.

For the maximum a posteriori methods, the Huber prior [36] [equation (4.19)] was used, with $\beta = 3.0 \times 10^{-4}$ and $\delta = 2.5 \times 10^{-4}$ mm^{-1}. Since the average reconstructed attenuation is about 0.06 mm^{-1}, the prior function is mostly active in linear mode [second line of equation (4.19)],

$$\begin{aligned} |\mu_j - \mu_k| < \delta: \ P(\vec{\mu}) &= -\beta \sum_{j,k} w_{jk} \frac{(\mu_j - \mu_k)^2}{2\delta^2}, \\ |\mu_j - \mu_k| \geq \delta: \ P(\vec{\mu}) &= -\beta \sum_{j,k} w_{jk} \frac{|\mu_j - \mu_k| - \delta/2}{\delta}. \end{aligned} \tag{4.19}$$

Figure 4.10 shows an example of three of these reconstruction methods (iFBP, MLTR$_{\text{pr}}$, and MAPTR$_{\text{pr}}$) for two simulated calcifications.

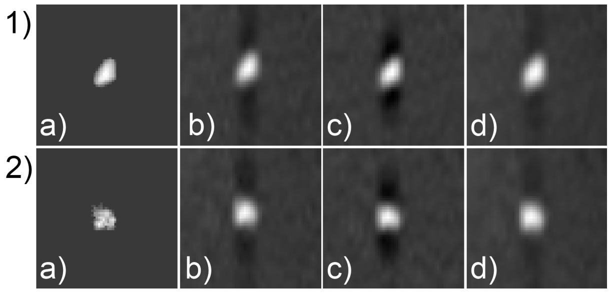

Figure 4.10: Projection and reconstruction of two simulated calcifications. 1) smooth (Le Gal II), 2) irregular (Le Gal IV); a) high resolution projection, b) Siemens iFBP, c) $\mathrm{MLTR_{pr}}$, d) $\mathrm{MAPTR_{pr}}$.

4.2.6 Reconstruction Comparison

The effect of the resolution model on the iterative reconstruction is shown by evaluating peak contrast to noise ratio (pCNR) for 50 iterations of $\mathrm{MLTR_{p}}$, $\mathrm{MLTR_{pr}}$, $\mathrm{MAPTR_{p}}$, and $\mathrm{MAPTR_{pr}}$, using the first simulated phantom described in section 4.2.5. The pCNR was calculated by dividing the difference of the maximum attenuation in the reconstructed calcification and the median attenuation of a surrounding region of 32×32 pixels by the standard deviation in that surrounding region.

We compare the convergence speed of the patchwork iterative methods with and without resolution model ($\mathrm{MLTR_{p}}$, $\mathrm{MLTR_{pr}}$, $\mathrm{MAPTR_{p}}$, and $\mathrm{MAPTR_{pr}}$) with their non-patched equivalents (MLTR and MAPTR) by plotting the difference between the likelihood and the maximum likelihood ($L - L_{max}$) as a function of iteration number for a reconstruction of the pCNR phantom with 150 μm calcification placed in region 3 used for the pCNR measurements described above. Likelihood L is defined in equation (4.10) and the maximum value of the likelihood L_{max} can be calculated by replacing $\hat{y}_i$ with y_i in this equation. These first results were then used to determine the number of iterations to use for our algorithms in further evaluation.

A final, more detailed comparison was limited to the $\mathrm{MLTR_{pr}}$, $\mathrm{MAPTR_{pr}}$, and iFBP reconstructions. It was split in two distinct observer experiments: first, a free search study to check the detectability of small spherical microcalcifications and second, a classification task to check the discrimination between smooth (Le Gal II) and irregular (Le Gal IV) microcalcifications.

For the detection study, 7 readers performed a free search on 120 cases for each reconstruction (with 40 of those cases used for initial training) and scored detected lesions on a 4 point scale as shown in table 4.1. Results were analyzed using the weighted JAFROC method [37].

Score	Description
1	I see a hint of a calcification
2	This might be a calcification
3	This is probably a calcification
4	I am sure this is a calcification

Table 4.1: Evaluation scale for the detection experiment.

For the classification study, 5 readers evaluated 300 cases for each reconstruction (of which 100 cases were used as initial training) by classifying them as smooth or irregular and providing their certainty of this classification (low, medium, or high certainty). These results were transformed to scores from 1 (smooth, high certainty) to 6 (irregular, high certainty) and then analyzed using the DBM MRMC method [38].

Data of the classification study was further split per location and in overlapping size groups (200 – 400, 300 – 500, and 400 – 600 μm) for further analysis using the same methods as the full data set.

4.3 Results

Figure 4.11 shows the mean pCNR for each calcification diameter (100, 150, and 200 μm) and each location (as shown in figure 4.7). The reconstructions that include a resolution model score equal or higher than those without resolution model, and maximal pCNR is achieved by the MAPTR$_{\mathrm{pr}}$ algorithm before iteration 10.

The reconstructions shown in figure 4.12 (iFBP and 50 iterations of both MLTR$_{\mathrm{p}}$ and MLTR$_{\mathrm{pr}}$ on the projections in figure 4.3) illustrate that the resolution model has a significant effect on the FWHM and intensity in the reconstruction. The FWHM and contrast is similar between the iFBP reconstruction and the MLTR$_{\mathrm{p}}$ algorithm, but there are no artifacts visible in the MLTR$_{\mathrm{p}}$ reconstruction. The MLTR$_{\mathrm{pr}}$ reconstruction shows both improved FWHM and contrast.

Figure 4.13 shows $L - L_{max}$ in function of the logarithm of the number of iterations for the MLTR, MLTR$_{\mathrm{p}}$, and MLTR$_{\mathrm{pr}}$ reconstructions. The algorithms that include a regularization term (MAPTR, MAPTR$_{\mathrm{p}}$, and MAPTR$_{\mathrm{pr}}$) are not shown on the graph for clarity, since at this scale the curves would overlap. The MLTR and MLTR$_{\mathrm{p}}$ reconstructions converge to the same likelihood, while the MLTR$_{\mathrm{pr}}$ converges to a different value at a slower pace due to the resolution model. Some concrete comparisons of the convergence speed: MLTR$_{\mathrm{p}}$ only needs 3 iterations to reach the likelihood that MLTR reaches in iteration 25, 7 iterations to reach the likelihood of 100 iterations of MLTR, and 23 iterations to reach 500 iterations of MLTR.

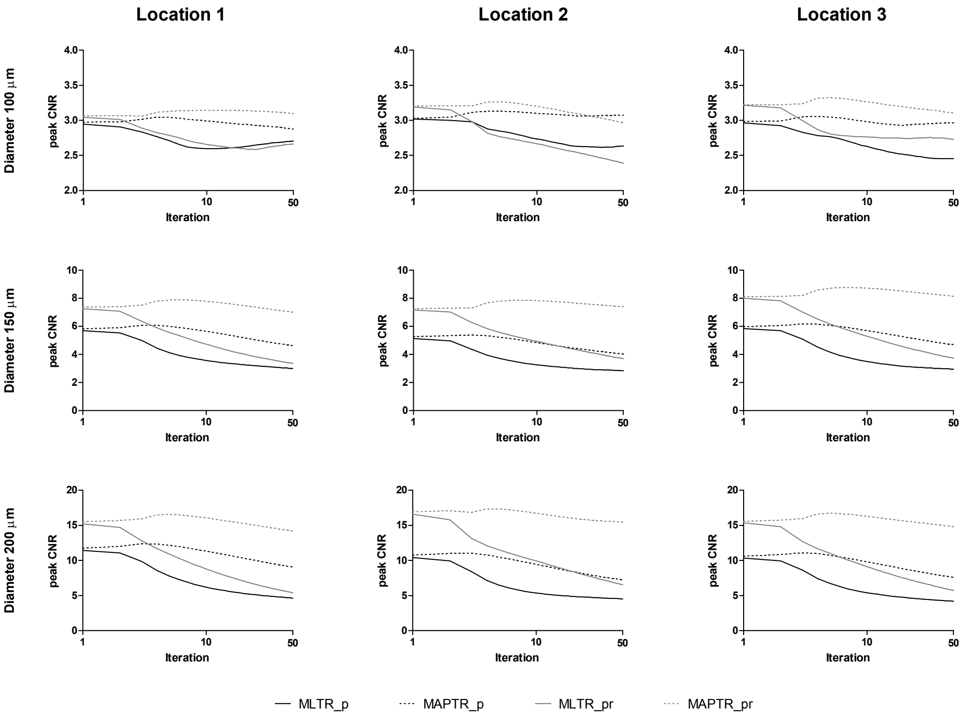

Figure 4.11: Overview of pCNR results.

Figure 4.12: Reconstruction of the simulated projection shown in figure 4.3. Left: Siemens iFBP; middle: 50 iterations of $\mathrm{MLTR_p}$; right: 50 iterations of $\mathrm{MLTR_{pr}}$.

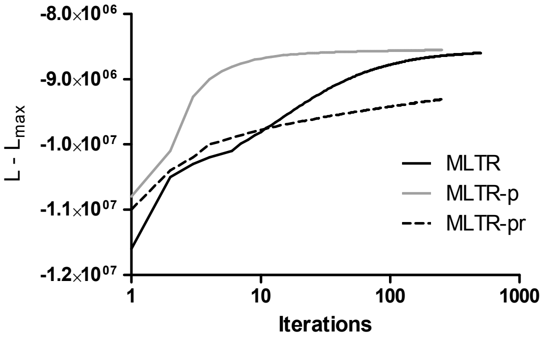

Figure 4.13: Convergence of the MLTR, MLTR$_\mathrm{p}$, and MLTR$_\mathrm{pr}$ algorithms.

Reconstruction	Figure of Merit (95% CI)
Siemens iFBP	0.780 (0.710 – 0.851)
MLTR$_\mathrm{pr}$	0.778 (0.717 – 0.840)
MAPTR$_\mathrm{pr}$	0.819 (0.765 – 0.873)

Table 4.2: AFROC figures of merit from the detection study.

This can also be seen subjectively in figure 4.14. The images on the top row, 20 iterations of MAPTR on the left and 3 iterations of MAPTR$_\mathrm{p}$ on the right are almost alike. The images on the bottom row are 3 iterations of the MAPTR algorithms and show that the image intensities have not yet converged. The image on the left is shown with the same window level setting as the images in the top row, while the window level setting for the image on the right is set from the minimum to the maximum pixel value to show more details.

Tables 4.2 and 4.3 and figure 4.15 show results for the detection study. The extension from the point of the lowest confidence score (1 in table 4.1) is shown in gray. There are significant differences between the iFBP and the MAPTR$_\mathrm{pr}$ reconstruction ($p = 0.029$) and between the MLTR$_\mathrm{pr}$ and MAPTR$_\mathrm{pr}$ reconstructions ($p = 0.022$) for detecting the smallest microcalcifications (<200 μm). There is no difference between the iFBP and the MLTR$_\mathrm{pr}$ reconstruction ($p = 0.893$).

Differences	p-value
Siemens iFBP vs. MLTR$_\mathrm{pr}$	0.893
Siemens iFBP vs. MAPTR$_\mathrm{pr}$	0.029
MLTR$_\mathrm{pr}$ vs. MAPTR$_\mathrm{pr}$	0.022

Table 4.3: P-values for the differences between the figures of merit from the detection study.

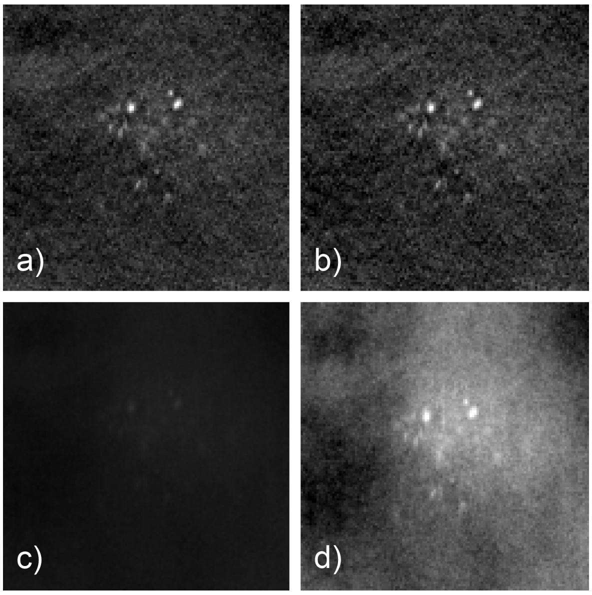

Figure 4.14: A cluster of microcalcifications in the reconstructed ROI to evaluate Convergence. a) 20 iterations of MAPTR; b) 3 iterations of $\mathrm{MAPTR_p}$; c) 3 iterations of MAPTR; d) 3 iterations of MAPTR with adjusted window level.

Reconstruction	Figure of Merit (95% CI)
Siemens iFBP	0.774 (0.733 – 0.815)
$\mathrm{MLTR_{pr}}$	0.773 (0.716 – 0.829)
$\mathrm{MAPTR_{pr}}$	0.769 (0.719 – 0.819)
p-value	0.935

Table 4.4: ROC figures of merit from the classification study.

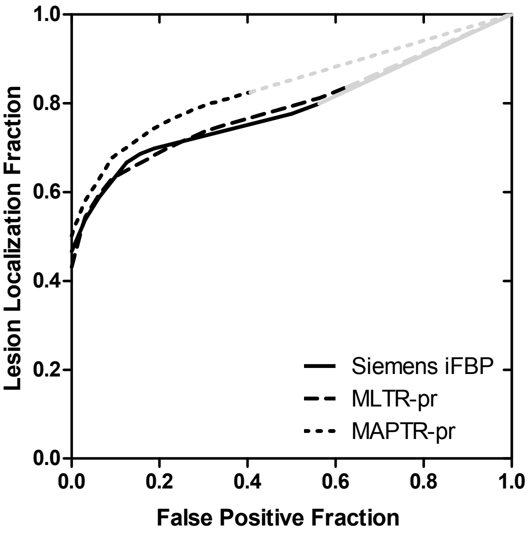

Figure 4.15: AFROC curves from the detection study results.

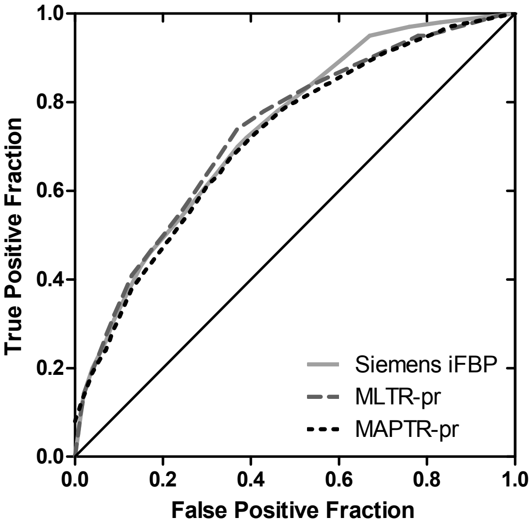

Figure 4.16: ROC curves from the classification study results.

Table 4.4 and figure 4.16 show the results for the shape discrimination study with the area under the ROC curve as the figure of merit. The p-value of 0.935 indicates that the three reconstruction methods have identical performance when considering shape discrimination of small lesions.

The results from the further subanalysis of the classification task are listed in table 4.5. None of the results in this table are statistically significantly different ($p > 0.05$).

Location	Reconstruction	Figure of Merit		
		small	medium	large
1	Siemens iFBP	0.691	0.789	0.842
	$\mathrm{MLTR}_{\mathrm{pr}}$	0.681	0.779	0.839
	$\mathrm{MAPTR}_{\mathrm{pr}}$	0.726	0.803	0.844
2	Siemens iFBP	0.633	0.684	0.796
	$\mathrm{MLTR}_{\mathrm{pr}}$	0.687	0.756	0.822
	$\mathrm{MAPTR}_{\mathrm{pr}}$	0.620	0.702	0.858
3	Siemens iFBP	0.685	0.779	0.870
	$\mathrm{MLTR}_{\mathrm{pr}}$	0.734	0.811	0.859
	$\mathrm{MAPTR}_{\mathrm{pr}}$	0.652	0.754	0.827

Table 4.5: ROC figures of merit of the classification study sub-analyses.

4.4 Discussion

We introduced a resolution model in the grouped coordinate ascent algorithm to improve visualization of microcalcifications. The first evaluation shows the effect of the resolution model on the GCA algorithm ($\mathrm{MLTR}_{\mathrm{pr}}$ and $\mathrm{MAPTR}_{\mathrm{pr}}$ vs $\mathrm{MLTR}_{\mathrm{p}}$ and $\mathrm{MAPTR}_{\mathrm{p}}$). The increased pCNR when applying the resolution model can be explained by the fact that the attenuation of the calcifications is now concentrated in less voxels so that the contrast increases, and that the resolution model causes an additional smoothing of the background, thus reducing the noise. The higher pCNR of the regularized versions of the algorithms is a result of the Huber prior which reduces noise in the background while maintaining the contrast in the calcifications for these reconstructions.

Further evaluations then show that the patchwork reconstruction with resolution modeling and smoothing prior ($\mathrm{MAPTR}_{\mathrm{pr}}$) can improve upon the Siemens iFBP after only three iterations for detecting very small microcalcifications while performing at the same level for classifying slightly larger microcalcifications.

The identical performance of all three reconstruction methods for the classification task was unexpected, so we examined the scores further by splitting up the results per lesion size and location (shown in table 4.5). In

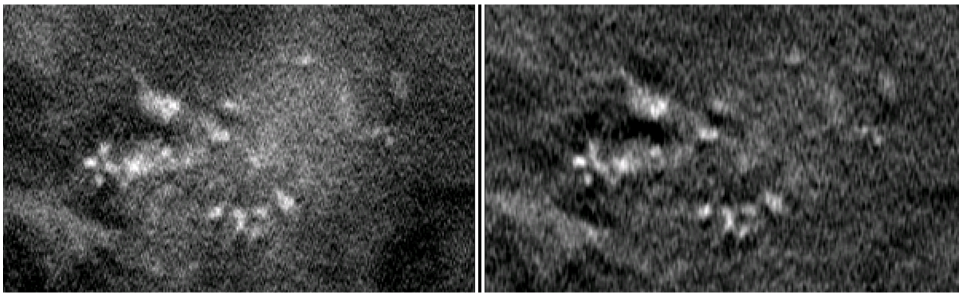

Figure 4.17: A cluster of microcalcifications (left: iFBP, right: three iterations of $\mathrm{MAPTR_{pr}}$).

this table, we can see that for location 1 $\mathrm{MAPTR_{pr}}$ has the highest scores, and for locations 2 and 3 $\mathrm{MLTR_{pr}}$ performs better than the two other reconstructions. We believe this is caused by the smoothing prior, which smooths more in planes further from the detector, because the likelihood provides less information there. A possible solution which we will investigate, is to vary the prior strength as a function of the position, aiming at a more uniform balance between prior and likelihood [39].

A useful feature of the proposed algorithm is the improved convergence speed per iteration that comes from applying a grouped coordinate ascent algorithm, although this effect is reduced by the resolution model. The convergence of the $\mathrm{MLTR_{pr}}$ algorithm towards a lower likelihood than $\mathrm{MLTR_{p}}$ is a consequence of the resolution model which strongly reduces the degrees of freedom of the reconstruction. This reduction limits the propagation of Poisson noise and thus lowers the similarity between the measured data and the estimated transmission scan, and therefore the likelihood of the reconstruction. Nevertheless, convergence of the $\mathrm{MLTR_{pr}}$ and $\mathrm{MAPTR_{pr}}$ algorithms is sufficiently fast to make the computation time acceptable for clinical applications.

From the pCNR results in figure 4.11, we expect that a few more iterations will further improve the results, but we would like to keep reconstruction time as short as possible. Therefore, we will investigate more effective initialization methods, that allow full weight updates in the two first iterations where we now used reduced strength updates to allow for a simple homogeneous initialization.

The new algorithm currently results in a limited improvement on the clinical image quality, as shown in a comparison with iFBP in figure 4.17. This makes sense when considering the fact that the iFBP algorithm has been specifically optimized for the Mammomat Inspiration system. We expect further improvements in our algorithm when including the measured point spread functions of the system in the resolution model instead of a Gaussian approximation.

4.5 Conclusions

The described method greatly increases convergence rate per iteration of DBT reconstruction while including an accurate resolution model. Adding a Huber-prior to the algorithm limits the noise in the image and allows reconstruction of clinical images in only three iterations while increasing detection performance in comparison to iFBP and maintaining the same level of lesion discrimination performance.

Acknowledgments

The authors would like to thank Nicholas Marshall for providing the MTF measurements for the resolution model; Federica Zanca for her advice on designing the observer study; and Joke Bints, Gregory Cieters, Lesley Cockmartin, Annelies Jacobs, Xochitl Lopez Rendon, Ahmadreza Rezaei, Elena Salvagnini, Eman Shaheen and Lin Zhou for their participation in the observer study.

This work is supported by Siemens AG and by SBO project QUANTIVIAM (060819) of the Institute for Promotion of Innovation through Science and Technology in Flanders (IWT-Vlaanderen).

References

[1] L. Nyström, I. Andersson, N. Bjurstam, J. Frisell, B. Nordenskjöld, and L. E. Rutqvist, “Long-term effects of mammography screening: Updated overview of the swedish randomised trials”, *Lancet*, vol. 359, no. 9310, pp. 909–919, Mar. 2002.

[2] R. E. Bird, T. W. Wallace, and B. C. Yankaskas, “Analysis of cancers missed at screening mammography”, *Radiology*, vol. 184, no. 3, pp. 613–617, Sep. 1992.

[3] J. A. Baker and J. Y. Lo, “Breast tomosynthesis: State-of-the-art and review of the literature”, *Acad. Radiol.*, vol. 18, no. 10, pp. 1298–1310, Oct. 2011.

[4] J. M. Park, E. A. Franken, M. Garg, L. L. Fajardo, and L. T. Niklason, “Breast tomosynthesis: Present considerations and future applications”, *Radiographics*, vol. 27 Suppl 1, S231–S240, Oct. 2007.

[5] J. T. Dobbins 3rd, “Tomosynthesis imaging: At a translational crossroads”, *Med. Phys.*, vol. 36, no. 6, pp. 1956–1967, Jun. 2009.

[6] T. M. Svahn, D. P. Chakraborty, D Ikeda, S Zackrisson, Y Do, S Mattsson, and I Andersson, “Breast tomosynthesis and digital mammography: A comparison of diagnostic accuracy”, *Br. J. Radiol.*, vol. 85, no. 1019, e1074–e1082, Jun. 2012.

[7] M. Das, H. C. Gifford, J Michael OConnor, and S. J. Glick, “Evaluation of a variable dose acquisition technique for microcalcification and mass detection in digital breast tomosynthesis”, *Med. Phys.*, vol. 36, no. 6, pp. 1976–1984, 2009.

[8] Y.-H. Hu and W. Zhao, “The effect of angular dose distribution on the detection of microcalcifications in digital breast tomosynthesis”, *Med. Phys.*, vol. 38, no. 5, p. 2455, 2011.

[9] Y. Lu, H.-P. Chan, J. Wei, M. M. Goodsitt, P. L. Carson, L. M. Hadjiiski, A. Schmitz, J. W. Eberhard, and B. E. H. Claus, “Image quality of microcalcifications in digital breast tomosynthesis: Effects of projection-view distributions”, *Med. Phys.*, vol. 38, no. 10, pp. 5703–5712, 2011.

[10] T. Wu, R. H. Moore, E. A. Rafferty, and D. B. Kopans, “A comparison of reconstruction algorithms for breast tomosynthesis”, *Med. Phys.*, vol. 31, no. 9, pp. 2636–2647, 2004.

[11] Y. Zhang, H.-P. Chan, B. Sahiner, J. Wei, M. M. Goodsitt, L. M. Hadjiiski, J. Ge, and C. Zhou, “A comparative study of limited-angle cone-beam reconstruction methods for breast tomosynthesis”, *Med. Phys.*, vol. 33, no. 10, pp. 3781–3795, 2006.

[12] T. Mertelmeier, J. Ludwig, B. Zhao, and W. Zhao, “Optimization of tomosynthesis acquisition parameters: Angular range and number of projections”, in *Digital Mammography*, ser. Lecture Notes in Computer Science, J. Marti, A. Oliver, J. Freixenet, and R. Marti, Eds., vol. 5116, Springer Berlin Heidelberg, 2008, pp. 220–227.

[13] M. Das, H. C. Gifford, J Michael O’Connor, and S. J. Glick, “Penalized maximum likelihood reconstruction for improved microcalcification detection in breast tomosynthesis”, *IEEE Trans. Med. Imaging*, vol. 30, no. 4, pp. 904–914, Apr. 2011.

[14] E. Y. Sidky, X. Pan, I. S. Reiser, R. M. Nishikawa, R. H. Moore, and D. B. Kopans, “Enhanced imaging of microcalcifications in digital breast tomosynthesis through improved image-reconstruction algorithms”, *Med. Phys.*, vol. 36, no. 11, pp. 4920–4932, 2009.

[15] Y. Lu, H.-P. Chan, J. Wei, and L. M. Hadjiiski, “Selective-diffusion regularization for enhancement of microcalcifications in digital breast tomosynthesis reconstruction”, *Med. Phys.*, vol. 37, no. 11, pp. 6003–6014, 2010.

[16] Y. Lu, H.-P. Chan, J. Wei, L. Hadjiiski, C. Zhou, N. J. Pelc, R. M. Nishikawa, and B. R. Whiting, “Multiscale regularized reconstruction for enhancing microcalcification in digital breast tomosynthesis”, in

Medical Imaging 2012: Physics of Medical Imaging, N. J. Pelc, R. M. Nishikawa, and B. R. Whiting, Eds., ser. SPIE Proceedings, vol. 8313, SPIE, 2012, p. 831 322.

[17] J. Chung, J. G. Nagy, and I. Sechopoulos, "Numerical algorithms for polyenergetic digital breast tomosynthesis reconstruction", *SIAM J. Imag. Sci.*, vol. 3, no. 1, pp. 133–152, Jan. 2010.

[18] N. W. Marshall and H. Bosmans, "Measurements of system sharpness for two digital breast tomosynthesis systems", *Phys. Med. Biol.*, vol. 57, no. 22, pp. 7629–7650, Nov. 2012.

[19] B. C. Penney, M. A. King, and K. Knesaurek, "A projector, backprojector pair which accounts for the two-dimensional depth and distance dependent blurring in SPECT", *IEEE Trans. Nucl. Sci.*, vol. 37, no. 2, pp. 681–686, Apr. 1990.

[20] G. L. Zeng, G. T. Gullberg, B. M. W. Tsui, and J. A. Terry, "Three-dimensional iterative reconstruction algorithms with attenuation and geometric point response correction", *IEEE Trans. Nucl. Sci.*, vol. 38, no. 2, pp. 693–702, Apr. 1991.

[21] R. H. Huesman, E. M. Salmeron, and J. R. Baker, "Compensation for crystal penetration in high resolution positron tomography", *IEEE Trans. Nucl. Sci.*, vol. 36, no. 1, pp. 1100–1107, Feb. 1989.

[22] Z. Liang, "Detector response restoration in image reconstruction of high resolution positron emission tomography", *IEEE Trans. Med. Imaging*, vol. 13, no. 2, pp. 314–321, Jan. 1994.

[23] J. A. Browne, J. M. Boone, and T. J. Holmes, "Maximum-likelihood x-ray computed-tomography finite-beamwidth considerations", *Appl. Opt.*, vol. 34, no. 23, pp. 5199–5209, Aug. 1995.

[24] K. Zeng, B. De Man, J.-B. Thibault, Y. Zhou, C. Bouman, K. Sauer, and Z. Yu, "Spatial resolution enhancement in CT iterative reconstruction", in *IEEE Nuclear Science Symposium and Medical Imaging Conference*, IEEE, Oct. 2009, pp. 3748–3751.

[25] B. De Man and S. Basu, "Distance-driven projection and backprojection in three dimensions", *Phys. Med. Biol.*, vol. 49, no. 11, pp. 2463–2475, 2004.

[26] J. Nuyts, B. De Man, P. Dupont, M. Defrise, P. Suetens, and L. Mortelmans, "Iterative reconstruction for helical CT: A simulation study", *Phys. Med. Biol.*, vol. 43, no. 4, pp. 729–737, Apr. 1998.

[27] K Van Slambrouck and J Nuyts, "Metal artifact reduction in computed tomography using local models in an image block-iterative scheme", *Med. Phys.*, vol. 39, no. 11, pp. 7080–7093, Nov. 2012.

[28] J. A. Fessler, E. P. Ficaro, N. H. Clinthorne, and K. Lange, "Grouped-coordinate ascent algorithms for penalized-likelihood transmission image reconstruction", *IEEE Trans. Med. Imaging*, vol. 16, no. 2, pp. 166–175, Apr. 1997.

[29] J. A. Fessler and D. Kim, "Axial block coordinate descent (ABCD) algorithm for x-ray CT image reconstruction", in *International Meeting on Fully Three-dimensional Image Reconstruction in Radiology and Nuclear Medicine*, 2011, pp. 262–265.

[30] K Van Slambrouck and J Nuyts, "Accelerated convergence with image-block iterative reconstruction", in *IEEE Nuclear Science Symposium and Medical Imaging Conference*, IEEE, Oct. 2011, pp. 2576–2580.

[31] K. Lange and J. A. Fessler, "Globally convergent algorithms for maximum a posteriori transmission tomography", *IEEE Trans. Image Process.*, vol. 4, no. 10, pp. 1430–1438, Jan. 1995.

[32] K. G. Metheany, C. K. Abbey, N. Packard, and J. M. Boone, "Characterizing anatomical variability in breast CT images", *Med. Phys.*, vol. 35, no. 10, pp. 4685–4694, 2008.

[33] E. Engstrom, I. Reiser, and R. Nishikawa, "Comparison of power spectra for tomosynthesis projections and reconstructed images", *Med. Phys.*, vol. 36, no. 5, pp. 1753–1758, 2009.

[34] J. Näppi, P. B. Dean, O. Nevalainen, and S. Toikkanen, "Algorithmic 3D simulation of breast calcifications for digital mammography", *Comput. Methods Programs Biomed.*, vol. 66, no. 1, pp. 115–124, Jul. 2001.

[35] J. Ludwig, T. Mertelmeier, H. Kunze, and W. Härer, "A novel approach for filtered backprojection in tomosynthesis based on filter kernels determined by iterative reconstruction techniques", in *Digital Mammography*, ser. Lecture Notes in Computer Science, E. A. Krupinski, Ed., vol. 5116, Springer Berlin Heidelberg, 2008, pp. 612–620.

[36] E. Ü. Mumcuoğlu, R. M. Leahy, and S. R. Cherry, "Bayesian reconstruction of PET images: Methodology and performance analysis", *Phys. Med. Biol.*, vol. 41, no. 9, pp. 1777–1807, Sep. 1996.

[37] D. P. Chakraborty and K. S. Berbaum, "Observer studies involving detection and localization: Modeling, analysis, and validation", *Med. Phys.*, vol. 31, no. 8, pp. 2313–2330, Aug. 2004.

[38] D. D. Dorfman, K. S. Berbaum, and C. E. Metz, "Receiver operating characteristic rating analysis. generalization to the population of readers and patients with the jackknife method", *Invest. Radiol.*, vol. 27, no. 9, pp. 723–731, Sep. 1992.

[39] J. A. Fessler and W. L. Rogers, “Spatial resolution properties of penalized-likelihood image reconstruction: Space-invariant tomographs”, *IEEE Trans. Image Process.*, vol. 5, no. 9, pp. 1346–1358, Jan. 1996.

Chapter 5

Multigrid Reconstruction with Block-Iterative Updates for Breast Tomosynthesis

KOEN MICHIELSEN AND JOHAN NUYTS

This chapter is based on the paper published as: K Michielsen and J Nuyts, "Multigrid reconstruction with block-iterative updates for breast tomosynthesis," Med. Phys. 42(11), 65376548 (2015).

Abstract

Purpose: We wish to evaluate the possible advantages of using a multigrid approach to maximum-a-posteriori reconstruction in digital breast tomosynthesis together with block-iterative updates in the form of either plane-by-plane updates or ordered subsets.

Methods: We previously developed a penalized maximum likelihood reconstruction algorithm with resolution model dedicated to breast tomosynthesis [1]. This algorithm was extended with ordered subsets and multigrid updates, and the effects on the convergence and on limited angle artifact appearance were evaluated on a mathematical phantom and patient data. To ensure a fair comparison, the analysis was performed at the same computational cost for all methods. To assess convergence and artifact creation in the phantom reconstructions, we looked at posterior likelihood, sum of squared residuals, contrast of identical calcifications at different positions, and the standard deviation between the contrasts of these calcifications. For the patient cases we calculated posterior likelihood, measured the signal difference to noise ratio of subtle microcalcifications, and visually evaluated the reconstructions.

Results: We selected multigrid sequences scoring in the best 10% of the four evaluated parameters, except for the reconstructions with subsets where a low standard deviation of the contrast was incompatible with the three other parameters. In further evaluation of phantom reconstructions from noisy data and patient data, we found improved convergence and a reduction in artifacts for our chosen multigrid reconstructions compared to the single grid reconstructions with equivalent computational cost, although there was a diminishing return for an increasing number of subsets.

Conclusions: Multigrid reconstruction improves upon reconstruction with a fixed grid when evaluated at a fixed computational cost. For multigrid reconstruction, using plane-by-plane updates or applying ordered subsets resulted in similar performance.

5.1 Introduction

Digital breast tomosynthesis (DBT) is a recent pseudo three dimensional imaging technique that reconstructs the breast volume as a series of planes (which we define as parallel to the detector, unless specified otherwise), with small in-plane pixel spacing (typically between 50 and 150 μm) and a much larger inter-plane spacing (typically 1 mm). This reduces the effect of overlapping normal tissue structures on the visualization of low contrast lesions, such as masses in dense breasts, which are difficult to detect in projection images [2]. A recent overview of clinical studies examining the effect of DBT on cancer detection rates by Houssami and Skaane [3] concludes that while addition of 2-view DBT to standard mammography improves cancer detection rates, there is still insufficient evidence to justify a change from digital mammography to DBT. It should be noted that all systems included in the referenced studies used filtered backprojection (FBP) for reconstruction, and at this point there have been several studies showing the potential of iterative algebraic and maximum likelihood (ML) methods to improve upon this method [4]–[6].

Reconstruction of DBT projections is a challenging problem since the acquisition process is far away from ideal conditions required for exact inversion. The most important deviation is the limited angle setup, with systems listed by Sechopoulos [7] as currently in clinical use or under development having an angular sampling range between 11° and 50°. This means that in theory an infinite number of tissue distributions could explain the acquired measurement and thus could be considered valid reconstructions. Most of these systems also acquire projection images with a continuously moving x-ray source instead of a step-and-shoot approach, which results in additional blurring of the data in the tube travel direction [8]. These and any other system specific considerations need to be taken into account when adapting a reconstruction algorithm to these systems.

Filtered backprojection is the most common reconstruction method and was adapted for use in DBT by Mertelmeier et al. [9], with further refinement of the filter by Orman et al. [10]. Work by Ludwig et al. [11] and Erhard et al. [12] showed that it is possible to design reconstruction filters to include desirable features from iterative methods and more recent developments by Abdurahman et al. [13] add statistical artifact reduction and super-sampling to further increase image quality. In contrast to the direct inversion in FBP, iterative methods optimize a cost function, typically either to find the least squares solution as in SART [14] or POCS [15], or to find the maximum likelihood solution as for the ML convex algorithm from Lange and Fessler [16] first introduced in DBT by Wu et al. [17].

The main assumptions for iterative methods are that the optimal solution to a cost function with a more accurate forward model and more complete prior knowledge will result in a better reconstruction than the solution to a less accurate model. In addition, when noise suppression is incorporated into the cost function (as in penalized likelihood or maximum-a-posteriori reconstruction), it is assumed that iterating till convergence is beneficial. A distinct disadvantage of the iterative methods is their high computational cost, even if the reconstruction is stopped before convergence. Wu et al. [17] for example find that reconstruction with nonregularized ML resulted in patient images with sufficient feature contrast and detail after eight iterations which is roughly equivalent to 24 times the computational cost of FBP, considering that each ML iteration contains one forward projection and two backprojection operations, and FBP only includes a single backprojection.

This high computational cost can be offset by performing the same calculations more efficiently, for example by parallel execution on a dedicated graphical processing unit (GPU), or alternatively by devising more efficient algorithms that need fewer calculations to perform the same reconstruction. In most instances these two methods will be combined.

Iterative image reconstruction is a problem well suited to parallelization since all operations can be performed independently on all image voxels [18] and practical applications have demonstrated significant acceleration [19]–[21]. The main limitation of GPUs is the small amount of available memory which might limit their use for large datasets. This is one of the reasons why some implementations will only offload the most computationally expensive parts of the algorithm (such as the forward and backprojections) to the GPU, in order to get most of the acceleration while avoiding the memory limitations.

Although memory size and computational power keep growing year after year, the relatively small GPU memory will likely remain the main bottleneck as imaging modalities evolve towards ever larger data sizes at the same time [22]. Therefore methods that perform better for the same computational cost will always be useful. Block-iterative methods (discussed in section 5.2.2) are frequently used for this purpose, whereas multigrid methods (section 5.2.4) are less popular, but we will show their usefulness for DBT reconstruction in this paper. Other options, which we did not explore in this work, can accelerate convergence by using more efficient update steps to optimize the cost function [23]–[26]. New update strategies for DBT were proposed by Sidky et al. [27] and Park et al. [28], and for computed tomography by Ramani and Fessler [29] and Kim et al. [30].

In this work we will examine whether a multigrid approach can accelerate the convergence of our block-iterative maximum likelihood reconstruction which includes an acquisition dependent resolution model and a combined quadratic and total variation regularization. The existing and new variants that we use are first presented separately and then combined with a multigrid algorithm that can use specific acquisition models and update strategies for each grid size. We will find the multigrid sequence with the fasted convergence for each block-iterative method based on reconstructions from simulated projection data, and then further evaluate this selection on simulated data with added noise and a small set of patient data.

5.2 Materials and Methods

5.2.1 Maximum Likelihood Reconstruction

Maximum likelihood reconstruction is formulated as an optimization problem that includes the forward acquisition model. With this approach, the analytic inversion is avoided and replaced by an iterative numerical inversion. The accuracy and complexity of the forward model will determine the properties of the algorithm. A simple form of the estimated transmission scan $\hat{y}_i$ can be written as

$$\hat{y}_i = b_i e^{-\sum_j l_{ij}\mu_j}, \tag{5.1}$$

with μ_j the linear attenuation in voxel j of the reconstruction volume, l_{ij} the intersection length between projection line i and voxel j, and b_i the unattenuated value for projection line i. Using this model and assuming Poisson noise in the measured data, it is possible to calculate the log-likelihood L for the measured projection data y_i:

$$L = \sum_i y_i \ln \hat{y}_i - \hat{y}_i - \ln(y_i!). \tag{5.2}$$

Using equations (5.1) and (5.2), we determine the update step $\Delta\vec{\mu}$ needed to iteratively maximize log-likelihood L starting from image $\vec{\mu}^0$. To this end we approximate L with its second order Taylor expansion at the current reconstruction $\vec{\mu}^n$ and then apply optimization transfer to a separable surrogate function for each voxel j [31]–[34]. This results in the following update equation for reconstruction volume $\vec{\mu}$:

$$\mu_j^{n+1} = \mu_j^n + \frac{-\alpha_j \frac{\partial L}{\partial \mu_j}|_{\vec{\mu}=\vec{\mu}^n}}{\sum_k \alpha_k \frac{\partial^2 L}{\partial \mu_j \partial \mu_k}|_{\vec{\mu}=\vec{\mu}^n}}, \tag{5.3}$$

with k a second index over all image voxels, and $\alpha_j \geq 0$ a design parameter introduced by Fessler et al. [31] that can be chosen freely.

Calculating the derivatives of L for model $\hat{y}_i$ in equation (5.1) results in the following expression for the update in every iteration:

$$\Delta\mu_j = \frac{\alpha_j \sum_i l_{ij} \left(\hat{y}_i - y_i\right)}{\sum_i l_{ij}\hat{y}_i \sum_k l_{ik}\alpha_k}. \tag{5.4}$$

In this equation we can see that the specific choice of α_j influences the convergence speed of individual voxels j. Choosing a high value for a particular voxel j will increase the convergence speed in that voxel at the expense of other voxels that are influenced by the increase of α_j in the denominator. For uniform convergence we can choose $\alpha_j = 1$ for all j which produces the maximum likelihood for transmission (MLTR) update from our previous work [32]. Another frequent choice is setting $\alpha_j = \mu_j^n$, creating an update step proportional to the current attenuation estimate and thus increasing convergence speed for high attenuation regions and slowing it down elsewhere. This is equivalent to the ML convex algorithm of Lange and Fessler [16].

Like all Bayesian methods, the cost function in equation (5.2) can be extended with prior information [35], allowing for additional constraints, which is a definite advantage in DBT where reconstruction is an ill-posed problem due to the limited angular range of the projections. In this work we use both the quadratic [36] and total variation TV_{l_1} [37], [38] smoothing priors.

The quadratic prior can be added as a penalty to the log-likelihood in equation (5.2):

$$L = \sum_i y_i \ln \hat{y}_i - \hat{y}_i - \ln\left(y_i!\right) - \frac{\beta_Q}{4} \sum_{j,k} w_{jk}(\mu_j - \mu_k)^2, \tag{5.5}$$

with quadratic penalty strength β_Q, and symmetric neighbor weights $w_{jk} = w_{kj}$. This modification is compatible with the optimization transfer to surrogate functions, and results in the following update:

$$\Delta\mu_j = \frac{\alpha_j \sum_i l_{ij} \left(\hat{y}_i - y_i\right) + \alpha_j \beta_Q P'(\vec{\mu})}{\sum_i l_{ij}\hat{y}_i \sum_k l_{ik}\alpha_k + \alpha_j \beta_Q P''}, \tag{5.6}$$

with

$$P'(\vec{\mu}) = \sum_k w_{jk}(\mu_j - \mu_k), \tag{5.7}$$

$$P'' = -2 \sum_k w_{jk}. \tag{5.8}$$

The total variation prior is implemented as an additional smoothing step after each update of the reconstruction volume. At that point we apply the GP algorithm derived by Beck and Teboulle [38], with the regularization parameter λ chosen as the desired strength β_{TV} of the prior divided by the denominator of the update step that was just applied:

$$\lambda = \frac{\beta_{TV}}{\sum_i l_{ij}\hat{y}_i \sum_k l_{ik}\alpha_k + \alpha_j \beta_Q P''}. \tag{5.9}$$

Which gives a combined cost function of:

$$\begin{aligned} L = &\sum_i y_i \ln \hat{y}_i - \hat{y}_i - \ln(y_i!) \\ &- \frac{\beta_Q}{4}\sum_{j,k} w_{jk}(\mu_j - \mu_k)^2 - 4\beta_{TV}\sum_{j,k} w_{jk}\left|\mu_j - \mu_k\right| \end{aligned} \tag{5.10}$$

We set the prior strengths $\beta_Q = 10^4$ and $\beta_{TV} = 2$, and choose a $3 \times 3 \times 3$ element neighborhood w where only the four direct neighbors in the plane parallel to the detector are set to 0.25 and all other elements are set to 0. This combination of priors yielded a good compromise between resolution and noise on realistic data and was chosen in consultation with an experienced radiologist after evaluating a range of settings on a small set of patient cases. The accelerated reconstruction reported on in this paper facilitates further task based optimization of the prior parameters, which is ongoing work but outside the scope of this paper.

5.2.2 Block-Iterative Methods

One of the main disadvantages of ML iterative reconstruction methods is the high number of iterations and corresponding computation time that is needed to produce high quality images. For this reason algorithms are typically modified to include accelerated update strategies such as ordered subsets [39]–[42], or image-block updates [31], [34], [43]–[45].

The MLTR update with subsets (OSTR) can be implemented by limiting the sum over projection rays i in equation (5.4) to only include rays from the selected projection angles in subset S. When including a smoothing prior, the backprojections need to be reweighed with the proportion of the total number of projection angles N_A and the number of projection angles in the current subset N_S to preserve the relative strength between the data and prior:

$$\Delta\mu_j = \frac{\alpha_j \frac{N_A}{N_S} \sum_{i \in S} l_{ij}\left(\hat{y}_i - y_i\right) + \alpha_j \beta_Q P'(\vec{\mu})}{\frac{N_A}{N_S} \sum_{i \in S} l_{ij}\hat{y}_i \sum_k l_{ik}\alpha_k + \alpha_j \beta_Q P''}. \tag{5.11}$$

	Subsets S
2	(1, 3, 5, 7, 9, 11, 13, 15, 17, 19, 21, 23, 25); (2, 4, 6, 8, 10, 12, 14, 16, 18, 20, 22, 24)
5	(1, 6, 11, 16, 21); (5, 10, 15, 20, 25); (3, 8, 13, 18, 23); (2, 7, 12, 17, 22); (4, 9, 14, 19, 24)
12	(1, 13, 25); (12, 24); (6, 18); (9, 21); (3, 15); (8, 20); (2, 14); (7, 19); (11, 23); (5, 17); (10, 22); (4, 16)
25	1; 25; 13; 7; 19; 4; 16; 10; 22; 9; 21; 8; 20; 6; 18; 5; 17; 3; 15; 2; 14; 24; 11; 23; 12

Table 5.1: Subset update ordering.

No attempt was made to optimize the order of the subsets, which were ordered such that each subset had maximum angular difference with its predecessor, and if possible also with all previous subsets, following the advice of Hudson and Larkin [39]. The chosen angles for each subset are listed in table 5.1.

The image-block version of the MLTR algorithm, where the blocks are chosen as planes parallel to the detector (MLTR$_\mathrm{p}$) can be implemented by limiting the voxels μ_j we will update in equation (5.3) to those within a single plane, i.e. choosing $\alpha_j = 1$ for the voxels inside that plane and $\alpha_j = 0$ for the voxels outside that plane, and repeating this for all planes in the reconstruction volume. The update equation for plane P then becomes

$$\Delta\mu_j = \frac{\sum_i l_{ij}\,(\hat{y}_i - y_i) + \beta_Q P'(\vec{\mu})}{\sum_i l_{ij}\hat{y}_i \sum_{k\in P} l_{ik} + \beta_Q P''} : j \in P. \tag{5.12}$$

In this equation, the accelerated convergence can be understood by analyzing the denominator. The sum over all voxels k, $\sum_k l_{ik}$ in equations (5.4) and (5.6), is reduced to a sum over the voxels in a single plane P, $\sum_{k\in P} l_{ik}$. This means the update step will increase by a factor roughly equal to the number of planes in the reconstruction volume, which is typically between 20 and 80 for breast tomosynthesis, depending on the patient. Splitting the updates in this way does not actually change the computational cost of one update of the complete volume, since for each full iteration the same number of intersection lengths l_{ij} need to be calculated. Because the voxels that are updated simultaneously are only weakly coupled, convergence should not be adversely affected by this simultaneous update [45].

5.2.3 Reconstruction with Resolution Recovery

It is possible to use different reconstruction models for each of the image blocks [46], which we did in previous work [1] by including a resolution model with plane-dependent point spread function, to compensate for blur caused by the motion of the x-ray tube during the image acquisition [8]. This required replacing the model in equation (5.1) by the model in equation (5.13), with p the plane index in the reconstruction volume, and A^p the smoothing kernel that models the resolution in plane p:

$$\hat{y}_i = b_i \prod_p \sum_n A_{in}^p e^{-\sum_{j \in p} l_{nj} \mu_j}. \tag{5.13}$$

We can then calculate the update step for this model from equation (5.3), again with $\alpha_j = 1$ for the voxels inside the updated plane, and $\alpha_j = 0$ for the voxels outside that plane. Relying on the assumption that the intersection lengths vary little over the range of smoothing kernel A_{in}^P results in the MLTR$_{\mathrm{pr}}$ update step [1]:

$$\Delta\mu_j = \frac{\sum_i l_{ij} \psi_i^P \sum_n A_{in}^P \frac{\hat{y}_n - y_n}{\bar{\psi}_n^P} + \beta_Q P'(\vec{\mu})}{\sum_i l_{ij} \psi_i^P \sum_{k \in P} l_{ik} \sum_n A_{in}^P \frac{\hat{y}_n}{\bar{\psi}_n^P} + \beta_Q P'(\vec{\mu})}, \tag{5.14}$$

for $j \in P$, and with:

$$\psi_i^p = e^{-\sum_{j \in p} l_{ij} \mu_j}, \tag{5.15}$$

$$\bar{\psi}_i^p = \sum_n A_{in}^p \psi_n^p. \tag{5.16}$$

Using the resolution model in equation (5.13) instead of the model in equation (5.1) improved the detectability of simulated microcalcifications [1], but required a good initialization to counteract limited angle artifacts.

In a preliminary study for this work we examined the effect of the update order when starting from a good initialization, and found that it is more efficient to apply the image updates consistently from bottom to top rather than alternating the order. Since this good initialization is one of the motivations to use the multigrid method, we used the bottom to top updates for all MLTR$_{\mathrm{r}}$ and MLTR$_{\mathrm{pr}}$ methods in this work.

Instead of the plane-by-plane updates, it is equally possible to use subsets by sequentially calculating the updates for each plane without updating transmission scan $\hat{y}$, using $\sum_k l_{ik}$ instead of $\sum_{k \in P} l_{ik}$ in the denominator, and reweighing the backprojection by ${}^{N_A}/_{N_S}$ as for the OSTR update in equation (5.11). This gives us the OSTR$_{\mathrm{r}}$ update:

$$\Delta\mu_j = \frac{\frac{N_A}{N_S} \sum_{i \in S} l_{ij} \psi_i^{p(j)} \sum_n A_{in}^{p(j)} \frac{\hat{y}_n - y_n}{\bar{\psi}_n^{p(j)}} + \beta_Q P'(\vec{\mu})}{\frac{N_A}{N_S} \sum_{i \in S} l_{ij} \psi_i^{p(j)} \sum_k l_{ik} \sum_n A_{in}^{p(j)} \frac{\hat{y}_n}{\bar{\psi}_n^{p(j)}} + \beta_Q P''}, \tag{5.17}$$

with S the currently selected subset and $p(j)$ the plane containing voxel j.

5.2.4 Multigrid Reconstruction

Multigrid reconstruction, which was first introduced by Ranganath et al. [47] in PET imaging, can accelerate convergence by starting with a coarse grid in the reconstruction volume and then decreasing the voxel spacing in multiple steps during the iterations, initializing the volume with the interpolated values from the previous grid. Further experiments by Pan and Yagle [48] found that this method only accelerates convergence of high frequency components compared to a fixed grid when the volume is locally smooth. Changing the pixel spacing in the projection data together with the grid changes in the image domain, further reduces the computational cost of each iteration [49], and was successfully applied in tomosynthesis reconstruction by Chen and Barner [50].

These methods use the same acquisition model and optimization strategy for all grid sizes, which is sufficient for simple models, but not optimal for more complex models such as equation (5.13), where the smoothing kernel will be negligible at coarse grid sizes. Next to this, the typical reconstruction grid in DBT is anisotropic, with in-plane voxel spacing identical to the pixels spacing of the detector, and a patient dependent number of 1 mm planes, so that resizing the grid equally in all directions is not practical.

There is a lot of freedom in a multigrid algorithm with regard to when to switch to a finer grid or another update step. Due to the different cost functions in each step, and the non-linearity of iterative methods it is hard to predict which sequence will result in the best reconstruction. Therefore we examine a selection of the parameter space and evaluate the reconstructions to find the schemes that result in the best convergence, measured by: a) the likelihood calculated from equations (5.10) and (5.13), b) good and artifact-free convergence in image domain, measured by the sum of squared residuals (SSR) between the reconstructed image and the original phantom image, and c) good and uniform convergence resulting in position independent visualization of the microcalcifications, which is measured by the contrast and the standard deviation of the contrast measured in different locations.

We set the following constraints when searching the parameter space:

a) A sequence will either use plane-by-plane MLTR updates or ordered subsets, but not both since our simulation experiments indicated that combining them adversely affects convergence.

b) We want to fix the total computational cost of the reconstruction to the equivalent of four full resolution $\mathrm{MLTR}_{\mathrm{pr}}$ updates and the reconstruction should finish with at least two full resolution $\mathrm{MLTR}_{\mathrm{pr}}$ or $\mathrm{OSTR}_{\mathrm{r}}$ updates.

c) Reconstructions start at 8×8 rebinning with at least four MLTR iterations before switching to the $\mathrm{MLTR_p}$ and $\mathrm{MLTR_{pr}}$ updates, or can start with any number of MLTR or OSTR updates before switching to $\mathrm{OSTR_r}$ updates.

d) The resolution model should not be used in grids rebinned coarser than 2×2 since the width of the convolution mask in the resolution model is typically less than two pixels at 4×4 rebinning, and once the switch is made to use the resolution model, it should be used for all following updates.

We decided to determine the theoretical computational cost of the algorithms at different grid sizes instead of measuring real calculation times because the implementations of the different update steps are not optimized to the same degree. The relative computational cost is proportional to the total number of projections and backprojections, and the number of projection lines in each projection or backprojection. For each of the algorithms, switching to a coarser grid, with 2×2 rebinning in both projection data and reconstruction volume, reduces the number of projection lines, and thus the computational cost, by a factor of four.

The number of projections and backprojections for each of the algorithms is as follows: the MLTR update in equation (5.4) contains two backprojections ($\sum_i l_{ij}$), and two projections ($\sum_j l_{ij}$). The first projection is used to calculate forward model $\hat{y}$ and the second one to calculate the projection weights $\sum_j l_{ij}\alpha_j$, which are the same in every iteration and can thus be precalculated. This results in a total of three forward or backprojection operations for each iteration.

The $\mathrm{MLTR_p}$ update in equation (5.12) has the same number of forward and backprojections as the MLTR update, although they are split between the different planes. Here it is not feasible to precalculate the weighs $\sum_{j\in p} l_{ij}\alpha_j$ since this needs to be done separately for all planes p and requires keeping too much data in computer memory. Thus each iteration has four forward or backprojection operations. Switching to the $\mathrm{MLTR_{pr}}$ updates in equation (5.14) adds another projection to calculate each ψ^p and $\bar{\psi}^p$, resulting in a total of five forward or backprojection operations.

The OSTR update in equation (5.11) has the same number of forward and backprojections as MLTR, and can also precalculate projection weights $\sum_j l_{ij}\alpha_j$, resulting in a total cost of three forward or backprojections for a full iteration over all subsets. The cost of the $\mathrm{OSTR_r}$ updates in equation (5.17) is the same as the $\mathrm{MLTR_{pr}}$ updates, except for the fact that the projection weights can be precalculated, resulting in a total cost of four instead of five forward or backprojections.

We should note that for the subset updates the smoothing prior is now applied to the entire volume after each subset. This means that this cost can become significant when using many subsets. Therefore we add an extra

rebinning factor	iteration cost		
	MLTR OSTR	MLTR$_\mathrm{p}$ OSTR$_\mathrm{r}$	MLTR$_\mathrm{pr}$
1 × 1	192	256	320
2 × 2	48	64	80
4 × 4	12	16	20
8 × 8	3	4	5

Table 5.2: Relative computational cost of one iteration of the included algorithms (without smoothing prior).

cost of $^1/_{25^\mathrm{th}}$ of a projection (roughly corresponding to one operation on the reconstruction volume) for each subset when using 5, 12, or 25 subsets. All relative computational costs for the five updates and four grid sizes that will be used are shown in table 5.2.

5.2.5 Phantom & Simulation

Since evaluating all possible multigrid iterations schemes on full sized data would not be feasible, we perform the optimization and evaluation on a simulated acquisition of a three dimensional phantom. This simulation was performed using the geometry in figure 5.1. The X-axis is placed at chest side of the detector, going left to right, the Y-axis goes front-to-back along the detector, and the Z-axis goes from the detector to the 0° position of the x-ray source. The center of rotation was set 608.5 mm below the x-ray source ($\mathrm{r_s}$) and 47 mm above the detector ($\mathrm{r_d}$). The phantom was placed 17 mm above the detector ($\mathrm{d_{pd}}$).

The phantom was created by taking a region of 2048 × 48 × 600 cubic voxels (85 μm) out of an ellipsoid with axes of 1024, 1024, and 640 voxels, and filling this area with white noise filtered by a power law filter [51], [52] $f(\nu) = \kappa/\nu^\beta$, with frequency ν, $\beta = 3$ and $\kappa = 10^{-5}$ mm^{-1}. The values inside the phantom were then rescaled between the attenuation of fat and glandular breast tissue. Three sets of 15 high contrast calcifications modeled as spheres with 150 μm diameter were created in a $5 \times 5 \times 5$ μm^3 grid and inserted at 10 mm, 25 mm, and 40 mm above the bottom of the phantom. One slice in the X-Z plane of the phantom is shown in figure 5.2.

Scatterfree projection data were generated for 25 angles distributed equally between -25° and 25° from the vertical axis, with a photon energy of 20 keV. For each source position α, nine subsources were simulated between $\alpha - 0.115°$ and $\alpha + 0.115°$ to represent the pulsed exposures from a continuously moving x-ray source. The detector consisted of 3584 × 64 pixels of 85×85 μm^2, which were supersampled by a factor of five during the simulation, and then rebinned to the original size. Blank scan value b_i was set

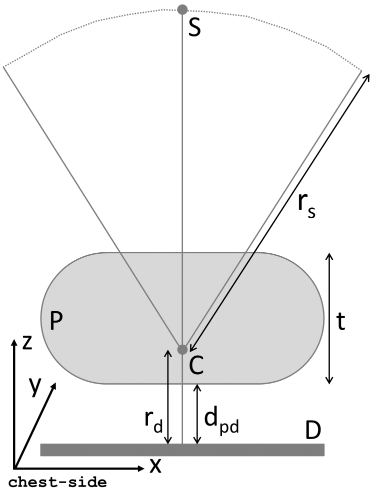

Figure 5.1: The simulation geometry (not to scale), with x-ray source S, detector D, phantom P, and center of rotation C.

Figure 5.2: Slice of the optimization phantom with the locations of the inserted calcifications, shown with exaggerated contrast.

to 2000 for all projection lines i. No noise was added to the projections unless specified otherwise. In those cases Poisson noise is generated in each detector pixel using the pixel value in the noiseless projection data as mean for the Poisson distribution. This noise level is roughly 20% higher than in the patient cases we used in the evaluation. With these projection data, the phantom was reconstructed to a final volume of $2048 \times 48 \times 51$ voxels for all methods, with an in-plane pixel size of 85×85 $\mu\mathrm{m}^2$ and 1 mm plane separation.

5.2.6 Phantom & Patient Evaluation

After the parameter search, we compare the best $\mathrm{MLTR_{pr}}$ and $\mathrm{OSTR_r}$ multigrid sequences to 4 iterations of the $\mathrm{MLTR_{pr}}$ algorithm with underrelaxation in the first two iterations [1] and 4 full iterations of $\mathrm{OSTR_r}(25)$ ($\mathrm{OSTR_r}$ with 25 subsets) or 5 full iterations of $\mathrm{OSTR_r}(5)$ or $\mathrm{OSTR_r}(12)$.

For the phantom data, we use the same criteria for the parameter search (section 5.2.4) for comparison, with the addition of the signal difference to noise ratio (SDNR) of the calcifications in reconstructions from noisy data.

After the phantom evaluation, we reconstruct data from five patient cases using the same methods. Here we calculate the likelihood, measure SDNR for a selection of microcalcifications, and perform a visual evaluation. Because the reconstruction model in equation (5.13) assumes a mono-energetic acquisition without scatter, all patient data were corrected for scatter [53] and beam hardening [54] before reconstruction.

5.3 Results

5.3.1 Convergence of Ordered Subsets in DBT

We evaluated the four choices of subsets listed in table 5.1 together with MLTR and $\mathrm{MLTR_p}$ by reconstructing the phantom described in section 5.2.5 with 1000 iterations, after initialization by 10 MLTR iterations. The difference between the upper bound of the likelihood, defined as

$$L_{max} = \sum_i y_i \ln y_i - y_i - \ln(y_i!), \tag{5.18}$$

and the posterior likelihood L from equation (5.10), is plotted in figure 5.3 to compare the convergence of the six methods. For less than 100 iterations, using more subsets increases the speed of convergence, and $\mathrm{MLTR_p}$ performs similarly to OSTR(5) (OSTR with 5 subsets). The value of $L_{max} - L$ after 1000 iterations is listed in table 5.3, where $\mathrm{MLTR_p}$ shows the best convergence, followed by OSTR(5), OSTR(2), MLTR, OSTR(12), and OSTR(25).

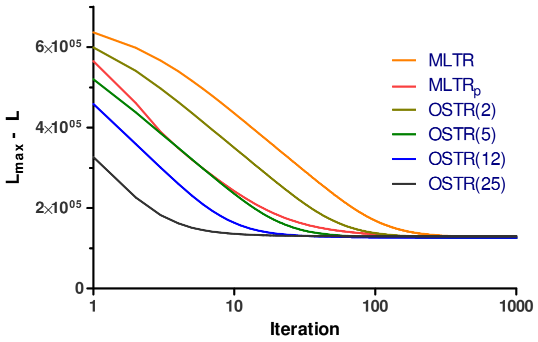

Figure 5.3: Difference between the upper bound of the log-likelihood L_{max} and posterior log-likelihood L as a function of iterations for the MLTR, $\mathrm{MLTR_p}$, and OSTR algorithms.

Algorithm	$L_{max} - L$
MLTR	$1.261{\cdot}10^5$
$\mathrm{MLTR_p}$	$1.255{\cdot}10^5$
OSTR(2)	$1.256{\cdot}10^5$
OSTR(5)	$1.255{\cdot}10^5$
OSTR(12)	$1.264{\cdot}10^5$
OSTR(25)	$1.295{\cdot}10^5$

Table 5.3: $L_{max} - L$ for MLTR, $\mathrm{MLTR_p}$, and OSTR after 1000 iterations.

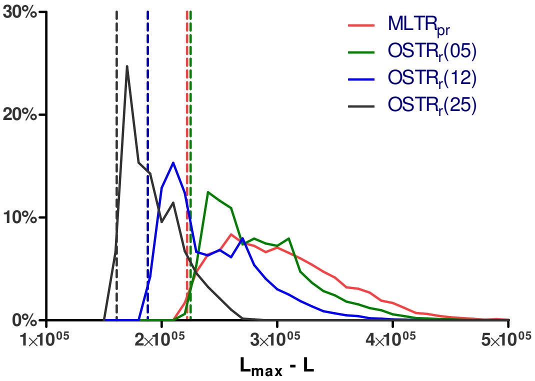

Figure 5.4: Histogram of $L_{max} - L$ from phantom reconstructions using all multigrid sequences. The vertical lines indicate the selected sequences from table 5.4.

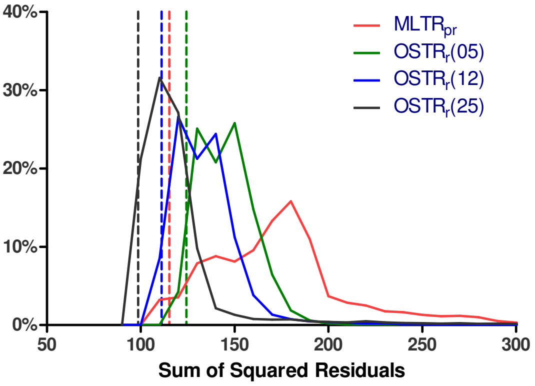

Figure 5.5: Histogram of the sum of squared residuals from phantom reconstructions using all multigrid sequences. The vertical lines indicate the selected sequences from table 5.4.

5.3.2 Choice of the Multigrid Sequence

Following the restrictions listed in section 5.2.4, we evaluated 8041 multigrid sequences for $\mathrm{MLTR_{pr}}$, 6339 for $\mathrm{OSTR_r}(5)$, 4383 for $\mathrm{OSTR_r}(12)$, and 2613 for $\mathrm{OSTR_r}(25)$. Figures 5.4, 5.5, 5.6, and 5.7 show the histograms of: the difference between the upper bound of the log-likelihood L_{max} and posterior log-likelihood L; the sum of squared residuals between the reconstruction and the original phantom; the mean contrast of the calcifications in the phantom; and the standard deviation of the mean contrast of calcifications in three locations in the phantom respectively.

The selected multigrid sequences for $\mathrm{MLTR_{pr}}$ and for $\mathrm{OSTR_r}$ with 5, 12, and 25 subsets are shown as vertical lines in figures 5.4, 5.5, 5.6, and 5.7, and are listed in table 5.4. The chosen $\mathrm{MLTR_{pr}}$ scores in the top 10% for the

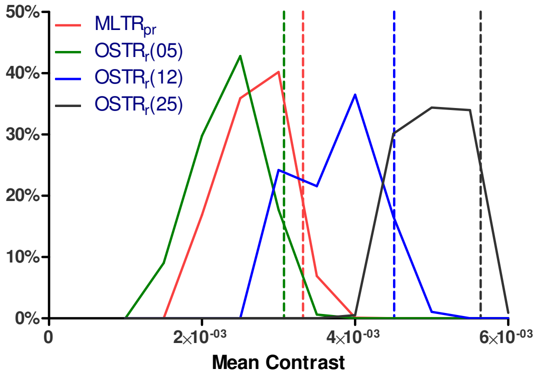

Figure 5.6: Histogram of the mean contrast of the calcifications in the phantom from reconstructions using all multigrid sequences. The vertical lines indicate the selected sequences from table 5.4.

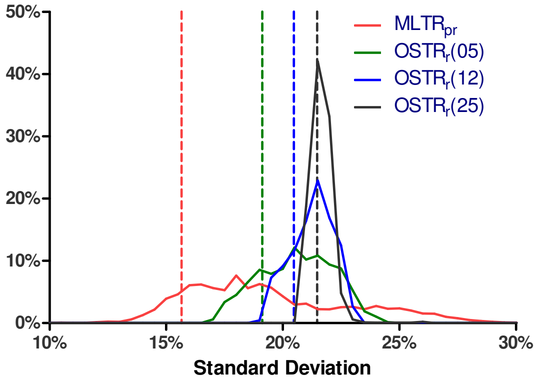

Figure 5.7: Histogram of the standard deviation of the mean contrast of calcifications in three locations in the phantom from reconstructions using all multigrid sequences. The vertical lines indicate the selected sequences from table 5.4.

Binning	Multigrid Sequences							
8×8	5×	MLTR	19×	OSTR(5)	9×	OSTR(12)	4×	OSTR(25)
4×4	11×	MLTR$_{p}$	9×	OSTR(5)	4×	OSTR(12)	3×	OSTR(25)
2×2	7×	MLTR$_{p}$	7×	OSTR(5)	7×	OSTR(12)	5×	OSTR(25)
1×1			1×	OSTR(5)	1×	OSTR(12)	1×	OSTR(25)
1×1	2×	MLTR$_{pr}$	2×	OSTR$_{r}$(5)	2×	OSTR$_{r}$(12)	2×	OSTR$_{r}$(25)

Table 5.4: Overview of the selected multigrid sequences, shown as vertical lines in figures 5.4, 5.5, 5.6, and 5.7.

four examined parameters, but for $\mathrm{OSTR_r}$ there were no sequences where all four examined parameters were in the top 10%, so the standard deviation of the mean contrast was not taken into account when selecting the sequence.

To make sure these choices remained valid for noisy data, we repeated the analysis for a selection of sequences using 10 noise realizations of the projection data, and found that the average likelihood, sum of squared residuals, and mean contrast from the noise realizations correlated well ($R > 0.95$) with the results from the noiseless reconstructions. This was not the case when looking at the standard deviation between the means of the three groups of calcifications. Here we found correlations of 0.94 for $\mathrm{MLTR_{pr}}$, and 0.73, 0.48, and -0.06 for $\mathrm{OSTR_r}$ with 5, 12, and 25 subsets respectively.

5.3.3 Phantom Evaluation

Now we compare the selected multigrid (MG) reconstructions to the original single grid (SG) versions. Table 5.5 lists the parameters used to choose the multigrid sequence and the signal difference to noise ratio (SDNR) for reconstructions with noise. In these reconstructions we see that the noise level increases from 3.1% for MG $\mathrm{MLTR_{pr}}$ to 3.3%, 4.6%, and 5.4% for MG $\mathrm{OSTR_r}$ with 5, 12, and 25 subsets respectively. Therefore we add an extra set of OSTR reconstructions with adjusted β_Q and β_{TV} to create reconstructions with matching noise levels.

In table 5.5 we see that $L_{max} - L$ and the sum of squared residuals consistently score better for the multigrid version of the algorithms, with the largest gains for the $\mathrm{MLTR_{pr}}$ method, and reduced benefits for an increasing number of subsets in the $\mathrm{MLTR_r}$ methods. The mean contrast of the included calcifications improves in the noiseless multigrid reconstructions, except for 25 subsets, where the contrast remains unchanged. For reconstructions with noise, contrast improves when using 5 subsets, and changes of 2% or less for the other methods. The standard deviation between the mean contrast of the calcifications in different locations in the phantom are all very similar, with only MG $\mathrm{MLTR_{pr}}$ scoring much lower with 15.7%. Average signal difference to noise ratio (SDNR) was calculated for the calcifications in the reconstructions with noise. Only $\mathrm{MLTR_{pr}}$ shows a noticeable change with an increase of 15% when switching to multigrid. For the $\mathrm{OSTR_r}$ methods SDNR is lowered with 3% or less when switching to multigrid reconstruction.

The tabulated residuals are indicative of the strength of reconstruction artifacts, but not their distribution. Figure 5.8 shows part of a coronal slice of a reconstruction from a sinogram with noise for the single and multigrid versions of the $\mathrm{MLTR_{pr}}$ and $\mathrm{OSTR_r}(5)$ methods. Here we see that SG $\mathrm{MLTR_{pr}}$ overestimates the attenuation close to the detector, which is much reduced in the multigrid variant and not present in the $\mathrm{OSTR_r}(5)$ images. The main difference between $\mathrm{MLTR_{pr}}$ and $\mathrm{OSTR_r}(5)$ can be seen in the

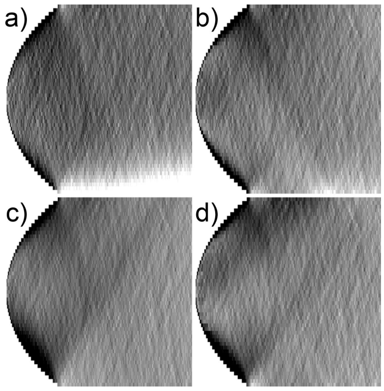

Figure 5.8: Artifacts in the coronal plane (the XZ plane in figure 5.1) for one noise realization of the phantom reconstructions. a) SG MLTR$_{\mathrm{pr}}$, b) MG MLTR$_{\mathrm{pr}}$, c) SG OSTR$_{\mathrm{r}}$(5), d) MG OSTR$_{\mathrm{r}}$(5).

bottom left of the phantom where OSTR$_{\mathrm{r}}$(5) underestimates the attenuation close to the phantom edge to a greater degree than MLTR$_{\mathrm{pr}}$. There were almost no visual differences between the artifacts shown for MG OSTR$_{\mathrm{r}}$(5) and those in MG OSTR$_{\mathrm{r}}$(12) and MG OSTR$_{\mathrm{r}}$(25) which were not shown. The structure of the artifacts for SG OSTR$_{\mathrm{r}}$(12) and SG OSTR$_{\mathrm{r}}$(25) is similar to that in SG OSTR$_{\mathrm{r}}$(5) but with decreasing intensity.

5.3.4 Patient Evaluation

We continue the evaluation of the multigrid methods by reconstructing five patient cases with the four single-grid methods and the four selected multigrid methods in table 5.4. The average of the difference between the upper bound of the likelihood and the posterior likelihood is listed in table 5.6 and shows that switching from single to multigrid improves convergence for these patient cases. The average SDNR from 14 subtle microcalcifications (between 2 and 5 in each patient case) is listed in table 5.7. MLTR$_{\mathrm{pr}}$ shows the largest gain, with a decreasing advantage for multigrid reconstruction with an increasing number of subsets.

Figures 5.9 and 5.10 show an irregular opacity and a cluster of microcalcifications respectively. Here we see switching to multigrid improves contrast most for MLTR$_{\mathrm{pr}}$ and OSTR$_{\mathrm{r}}$(5), and that there is little visual difference between single and multigrid versions of OSTR$_{\mathrm{r}}$(12) and OSTR$_{\mathrm{r}}$(25). Figure 5.11 illustrates the reconstruction artifacts for the different methods. The largest difference can be seen between the single and multigrid versions of MLTR$_{\mathrm{pr}}$ where the attenuation in the single grid reconstruction is underestimated in most of the volume due to the overestimation close to the detector. The differences between single and multigrid are much smaller for the OSTR$_{\mathrm{r}}$ reconstructions, but the improvement for multigrid is clear

	$L_{max} - L$		Residuals		Mean Contrast		Standard Deviation		Mean SDNR	
Algorithm	SG	MG	SG	MG	SG	MG	SG	MG	SG	MG
Results from reconstructions without noise:										
MLTR$_{\mathrm{pr}}$	$8.66{\cdot}10^5$	$2.22{\cdot}10^5$	339	117	$2.10{\cdot}10^{-3}$	$3.32{\cdot}10^{-3}$	21.4%	15.7%		
OSTR$_{\mathrm{r}}$(5)	$5.99{\cdot}10^5$	$2.25{\cdot}10^5$	181	124	$2.16{\cdot}10^{-3}$	$3.07{\cdot}10^{-3}$	21.8%	19.1%		
OSTR$_{\mathrm{r}}$(12)	$4.61{\cdot}10^5$	$1.88{\cdot}10^5$	144	111	$4.07{\cdot}10^{-3}$	$4.51{\cdot}10^{-3}$	21.7%	20.5%		
OSTR$_{\mathrm{r}}$(25)	$3.46{\cdot}10^5$	$1.61{\cdot}10^5$	113	98.6	$5.65{\cdot}10^{-3}$	$5.64{\cdot}10^{-3}$	21.1%	21.5%		
Results from reconstructions with noise:										
MLTR$_{\mathrm{pr}}$	$3.33{\cdot}10^6$	$2.98{\cdot}10^6$	412	134	$2.74{\cdot}10^{-3}$	$2.69{\cdot}10^{-3}$	22.0%	21.8%	1.31	1.50
OSTR$_{\mathrm{r}}$(5)	$3.17{\cdot}10^6$	$2.99{\cdot}10^6$	193	140	$2.49{\cdot}10^{-3}$	$2.68{\cdot}10^{-3}$	23.0%	21.9%	1.43	1.43
OSTR$_{\mathrm{r}}$(12)	$3.04{\cdot}10^6$	$2.95{\cdot}10^6$	174	142	$3.72{\cdot}10^{-3}$	$3.65{\cdot}10^{-3}$	23.9%	23.7%	1.41	1.39
OSTR$_{\mathrm{r}}$(25)	$2.96{\cdot}10^6$	$2.94{\cdot}10^6$	155	144	$4.30{\cdot}10^{-3}$	$4.31{\cdot}10^{-3}$	25.1%	25.2%	1.39	1.38
Results from reconstructions with noise and modified β_Q and β_{TV}:										
OSTR$_{\mathrm{r}}$(5)	$3.20{\cdot}10^6$	$3.01{\cdot}10^6$	194	140	$2.31{\cdot}10^{-3}$	$2.60{\cdot}10^{-3}$	22.6%	21.5%	1.45	1.44
OSTR$_{\mathrm{r}}$(12)	$3.21{\cdot}10^6$	$3.13{\cdot}10^6$	164	139	$2.80{\cdot}10^{-3}$	$2.73{\cdot}10^{-3}$	20.5%	20.7%	1.55	1.51
OSTR$_{\mathrm{r}}$(25)	$3.28{\cdot}10^6$	$3.25{\cdot}10^6$	138	134	$2.66{\cdot}10^{-3}$	$2.67{\cdot}10^{-3}$	19.7%	21.0%	1.50	1.48

Table 5.5: Comparison between the single grid (SG) and the selected multigrid (MG) versions of the reconstruction algorithms.

	$L_{max} - L$ ($\times 10^8$)			
Algorithm	SG	SG$_\beta$	MG	MG$_\beta$
MLTR$_{\mathrm{pr}}$	1.904		1.755	
OSTR$_{\mathrm{r}}$(5)	1.804	1.809	1.758	1.759
OSTR$_{\mathrm{r}}$(12)	1.797	1.823	1.783	1.805
OSTR$_{\mathrm{r}}$(25)	1.851	1.883	1.843	1.874

Table 5.6: Average $L_{max} - L$ from 5 patients for single and multigrid reconstructions with fixed β (SG and MG) and with adjusted β (SG$_\beta$ and MG$_\beta$).

	Mean SDNR			
Algorithm	SG	SG$_\beta$	MG	MG$_\beta$
MLTR$_{\mathrm{pr}}$	3.27		3.84	
OSTR$_{\mathrm{r}}$(5)	3.22	3.37	3.62	3.66
OSTR$_{\mathrm{r}}$(12)	3.35	3.65	3.50	3.83
OSTR$_{\mathrm{r}}$(25)	3.28	3.69	3.28	3.74

Table 5.7: Average SDNR of 14 subtle calcifications from 5 patients for single and multigrid reconstructions with fixed β (SG and MG) and with adjusted β (SG$_\beta$ and MG$_\beta$).

from visual evaluation. While the artifacts in the MG OSTR$_{\mathrm{r}}$ images are visually similar, but with varying intensity, there are clear differences with the MG MLTR$_{\mathrm{pr}}$ reconstruction, shown by the arrows in figure 5.11. Closer to the detector side (top row), the breast edge is better represented for MG MLTR$_{\mathrm{pr}}$, while the reverse is true closer to the top of the reconstruction volume (bottom row). In the center of the volume (middle row), the differences are relatively small, with one artifact appearing for increasing number of subsets near the top of the image.

Next to the changes in contrast and artifacts, we also see a difference in noise levels between the reconstructions in figures 5.9, 5.10, and 5.11. The average noise levels in the five patient cases are 4.1%, 3.9%, 4.3%, and 4.4% for MLTR$_{\mathrm{pr}}$, OSTR$_{\mathrm{r}}$(5), OSTR$_{\mathrm{r}}$(12), and OSTR$_{\mathrm{r}}$(25) respectively when using the modified prior strength that resulted in equal noise levels in the phantom reconstructions.

The patient reconstructions with adjusted β were also evaluated by an experienced radiologist specialized in breast imaging. She found the SG OSTR$_{\mathrm{r}}$(12), SG OSTR$_{\mathrm{r}}$(25), MG OSTR$_{\mathrm{r}}$(12) and MG OSTR$_{\mathrm{r}}$(25) reconstructions to be identical from a diagnostic point of view, but all containing too much noise, making it harder to spot microcalcifications. The multigrid versions of MLTR$_{\mathrm{pr}}$ and OSTR$_{\mathrm{r}}$(5) did improve the contrast of soft tissue structures and microcalcifications while maintaining a manageable amount

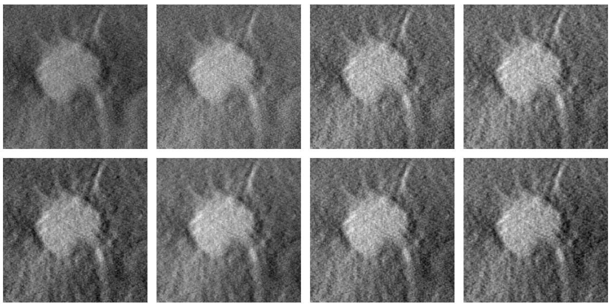

Figure 5.9: Irregular opacity for single (top row) and multigrid (bottom row) variants of (from left to right) $\mathrm{MLTR}_{\mathrm{pr}}$, $\mathrm{OSTR}_{\mathrm{r}}(5)$, $\mathrm{OSTR}_{\mathrm{r}}(12)$, and $\mathrm{OSTR}_{\mathrm{r}}(25)$.

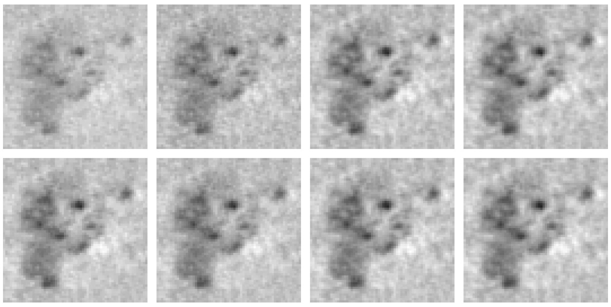

Figure 5.10: Microcalcification cluster for single (top row) and multigrid (bottom row) variants of (from left to right) $\mathrm{MLTR}_{\mathrm{pr}}$, $\mathrm{OSTR}_{\mathrm{r}}(5)$, $\mathrm{OSTR}_{\mathrm{r}}(12)$, and $\mathrm{OSTR}_{\mathrm{r}}(25)$, with inverted grayscale.

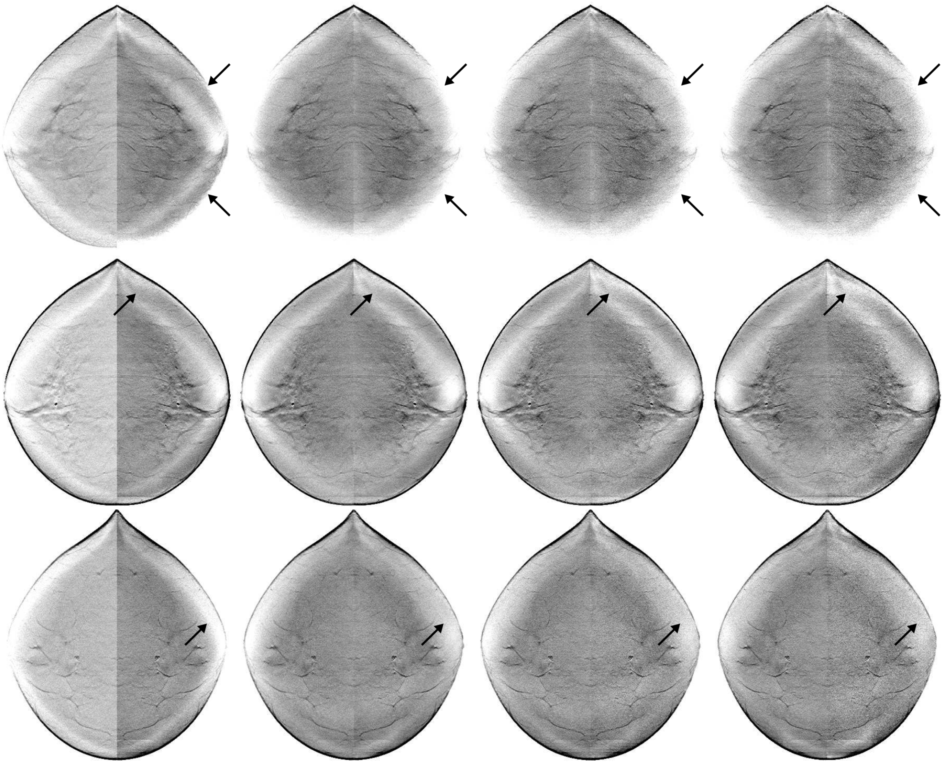

Figure 5.11: Reconstruction planes at 15 (top row), 30 (middle row), and 45 mm (bottom row) from the detector cover for single (left facing) and multigrid (right facing) variants of (from left to right) MLTR$_{\mathrm{pr}}$, OSTR$_{\mathrm{r}}$(5), OSTR$_{\mathrm{r}}$(12), and OSTR$_{\mathrm{r}}$(25). The window is set from 0.03 to 0.06 mm^{-1} with inverted grayscale.

of noise. These two multigrid reconstructions were also considered diagnostically equal and were preferred over the other methods. The image artifacts were not considered a fundamental problem since the information in those areas can still be examined by changing the window settings, but there is a strong preference not to have to do this because it significantly increases the time needed to read each reconstruction volume.

5.4 Discussion

We started our evaluation of multigrid reconstruction for DBT by comparing the relative convergence speed of $\mathrm{MLTR_p}$ and OSTR (figure 5.3). Although only $\mathrm{MLTR_p}$ was guaranteed to converge, differences after 1000 iterations were very small thanks to the addition of the smoothing priors that strongly reduce the limit cycle solution for the OSTR reconstructions. Even though these methods converge to slightly different solutions, we do not expect this to be noticeable when stopping after a few iterations.

The selected multigrid sequences in table 5.4 seem like logical choices, with several iterations at each grid level before moving to the next size. When looking at the full data, we see that suboptimal sequences concentrate too many iterations at a single grid size rather than using a more equal distribution. This type of sequences would not be considered when setting a performance measure to decide when to switch grids as in the original work of Ranganath et al. [47]. By fixing the computational cost instead, we could compare all methods on an equal footing but at the cost of including many suboptimal possibilities in the first step of our analysis.

This computational cost was chosen to allow an $\mathrm{MLTR_{pr}}$ reconstruction within 5 minutes if fully implemented on current hardware (e.g. nVidia Tesla C2075), which is reasonable for the current clinical use where images are evaluated before the patient leaves. This cost will of course need to be re-evaluated when the tomosynthesis system changes, the reconstruction workstation is upgraded with a new CPU or GPU, or for other clinical settings, such as for example a screening environment where images are read in batches several days after the examination.

While we used reconstructions from noiseless data to choose the multigrid sequences, we found good correlations between these parameters and the average of the same parameters calculated from multiple reconstructions from noisy data, with the exception of the standard deviation of the mean contrast of the calcifications in three different locations in the phantom. Here we found good correlation for MG $\mathrm{MLTR_{pr}}$, which produces a large range of values, both in reconstructions from noiseless data (figure 5.7) and in reconstructions from noisy data (histogram not shown). The MG $\mathrm{OSTR_r}$ reconstructions also show the same behavior in the noiseless and noisy reconstructions, with results getting more clumped together for increasing subsets. This makes the lack of correlation less of a problem, since the exact choice of multigrid sequence will only have a small effect on the resulting value of the standard deviation. We found that there were no examined multigrid sequences for $\mathrm{OSTR_r}$ that scored in the lowest 10% of values for this standard deviation while at the same time scoring in the best 10% for the other parameters, and we decided to ignore this parameter when choosing the multigrid sequence. In the end this doesn't seem like a bad choice when we compare the scores of the standard deviation for multigrid $\mathrm{MLTR_{pr}}$ and $\mathrm{OSTR_r}$ with modified beta in table 5.5, where the values lie in a small range from 20.7% to 21.8%. From these results it appears that the choices we examined in this paper had little influence on this standard deviation, but despite this we think it is a valid performance measure to expect identical calcifications in different parts of the phantom to be reconstructed with the same contrast.

If we compare the histograms in figures 5.4, 5.5, and 5.6 it seems that the chosen multigrid sequence with 25 subsets will easily outperform the $\mathrm{MLTR_{pr}}$ sequence and those with 5 and 12 subsets. After introducing noise in the projection data and adjusting the prior weights to produce similar noise levels in the reconstructions, only small differences remain. With different values of β_Q and β_{TV}, the algorithms are optimizing different cost functions and it is no longer possible to directly compare the posterior likelihood. The results indicate that even with the multigrid acceleration, the convergence is still incomplete, and more so if fewer subsets are used. Since high frequencies are slower to converge, this early stopping of the iterations has a smoothing effect. Since MG $\mathrm{OSTR_r}(25)$ has the strongest convergence, it needs more smoothing by the prior to obtain a matched noise level.

In general we find the same conclusions when looking at the patient data, with only relatively small differences between the four multigrid sequences with adjusted prior strength. On closer examination there are some noticeable differences such as the ranking of the average posterior likelihood for the multigrid sequences with the original fixed prior strength (third column in table 5.6) which shows that $\mathrm{MLTR_{pr}}$ has reached better convergence than the three $\mathrm{OSTR_r}$ reconstructions, and that convergence decreases with an increasing number of subsets, which is opposite to the results for the phantom. We also find that the modified prior strength is not entirely effective for the patient cases. The range of the average noise levels is reduced from 4.1%–6.9% to 3.9%–4.4%, but this difference is clearly visible in the patient images, where the $\mathrm{OSTR_r}(12)$ and $\mathrm{OSTR_r}(25)$ reconstructions are considered too noisy for easy diagnosis.

We suspect that the reason for this discrepancy between phantom and patient reconstructions is due to the differences in noise composition and data consistency. The simulated projection data contain pure Poisson noise and are fully consistent, while the patient projection data contain other noise contributions from the detector and possible data inconsistencies from imperfect scatter and beam hardening corrections and possible patient motion.

5.5 Conclusions

In this work we examined the combination of a multigrid reconstruction strategy with block-iterative updates both in the form of plane-by-plane updates and subsets while optimizing a likelihood cost function with a position dependent resolution model. We found improved convergence and a reduction in artifacts for our chosen multigrid reconstructions compared to the single grid reconstructions with equivalent computational cost, although there was a diminishing return for an increasing number of subsets. Ordered subsets provided a stronger acceleration, but when comparing the multigrid reconstructions at matched noise levels, plane-by-plane updating and using ordered subsets produced very similar performance.

Acknowledgments

The authors would like to thank Prof. Dr. C. Van Ongeval for her help in evaluating the patient reconstructions, the reviewers for their helpful comments, and Siemens Healthcare for their financial support.

References

[1] K. Michielsen, K. Van Slambrouck, A. Jerebko, and J. Nuyts, “Patchwork reconstruction with resolution modeling for digital breast tomosynthesis”, *Med. Phys.*, vol. 40, no. 3, p. 031 105, Mar. 2013.

[2] R. E. Bird, T. W. Wallace, and B. C. Yankaskas, “Analysis of cancers missed at screening mammography”, *Radiology*, vol. 184, no. 3, pp. 613–617, Sep. 1992.

[3] N. Houssami and P. Skaane, “Overview of the evidence on digital breast tomosynthesis in breast cancer detection”, *Breast*, vol. 22, no. 2, pp. 101–108, 2013.

[4] T. Wu, R. H. Moore, E. A. Rafferty, and D. B. Kopans, “A comparison of reconstruction algorithms for breast tomosynthesis”, *Med. Phys.*, vol. 31, no. 9, pp. 2636–2647, 2004.

[5] Y. Zhang, H.-P. Chan, B. Sahiner, J. Wei, M. M. Goodsitt, L. M. Hadjiiski, J. Ge, and C. Zhou, “A comparative study of limited-angle cone-beam reconstruction methods for breast tomosynthesis”, *Med. Phys.*, vol. 33, no. 10, pp. 3781–3795, 2006.

[6] D. Van de Sompel, S. M. Brady, and J. Boone, “Task-based performance analysis of FBP, SART and ML for digital breast tomosynthesis using signal CNR and channelised hotelling observers”, *Med. Image Anal.*, vol. 15, no. 1, pp. 53–70, 2010.

[7] I. Sechopoulos, “A review of breast tomosynthesis. part i. the image acquisition process”, *Med. Phys.*, vol. 40, no. 1, p. 014 301, 2013.

[8] N. W. Marshall and H. Bosmans, “Measurements of system sharpness for two digital breast tomosynthesis systems”, *Phys. Med. Biol.*, vol. 57, no. 22, pp. 7629–7650, Nov. 2012.

[9] T. Mertelmeier, J. Orman, W. Haerer, and M. K. Dudam, “Optimizing filtered backprojection reconstruction for a breast tomosynthesis prototype device”, in *Medical Imaging 2006: Physics of Medical Imaging*, M. J. Flynn and J. Hsieh, Eds., ser. SPIE Proceedings, vol. 6142, SPIE, 2006, 61420F–61420F–12.

[10] J. Orman, T. Mertelmeier, and W. Haerer, “Adaptation of image quality using various filter setups in the filtered backprojection approach for digital breast tomosynthesis”, in *Digital Mammography*, ser. Lecture Notes in Computer Science, Springer Berlin Heidelberg, 2006, pp. 175–182.

[11] J. Ludwig, T. Mertelmeier, H. Kunze, and W. Härer, “A novel approach for filtered backprojection in tomosynthesis based on filter kernels determined by iterative reconstruction techniques”, in *Digital Mammography*, ser. Lecture Notes in Computer Science, E. A. Krupinski, Ed., vol. 5116, Springer Berlin Heidelberg, 2008, pp. 612–620.

[12] K. Erhard, M. Grass, S. Hitziger, A. Iske, and T. Nielsen, “Generalized filtered back-projection for digital breast tomosynthesis reconstruction”, in *Medical Imaging 2012: Physics of Medical Imaging*, ser. SPIE Proceedings, vol. 8313, International Society for Optics and Photonics, 2012, pp. 831 320–831320–7.

[13] S. Abdurahman, F. Dennerlein, A. Jerebko, A. Fieselmann, and T. Mertelmeier, “Optimizing high resolution reconstruction in digital breast tomosynthesis using filtered back projection”, in *Breast Imaging*, ser. Lecture Notes in Computer Science, Springer International Publishing, 2014, pp. 520–527.

[14] Y. Zhang, H.-P. Chan, B. Sahiner, J. Wei, M. M. Goodsitt, L. M. Hadjiiski, J. Ge, C. Zhou, M. J. Flynn, and J. Hsieh, “Tomosynthesis reconstruction using the simultaneous algebraic reconstruction technique (SART) on breast phantom data”, in *Medical Imaging 2006: Physics of Medical Imaging*, ser. SPIE Proceedings, vol. 6142, SPIE, 2006, pp. 614 249–614249–9.

[15] E. Y. Sidky, X. Pan, I. S. Reiser, R. M. Nishikawa, R. H. Moore, and D. B. Kopans, "Enhanced imaging of microcalcifications in digital breast tomosynthesis through improved image-reconstruction algorithms", *Med. Phys.*, vol. 36, no. 11, pp. 4920–4932, 2009.

[16] K. Lange and J. A. Fessler, "Globally convergent algorithms for maximum a posteriori transmission tomography", *IEEE Trans. Image Process.*, vol. 4, no. 10, pp. 1430–1438, Jan. 1995.

[17] T. Wu, A. Stewart, M. Stanton, T. McCauley, W. Phillips, D. B. Kopans, R. H. Moore, J. W. Eberhard, B. H. Opsahl-Ong, L. T. Niklason, and M. B. Williams, "Tomographic mammography using a limited number of low-dose cone-beam projection images", *Med. Phys.*, vol. 30, no. 3, pp. 365–380, 2003.

[18] G. Pratx and L. Xing, "GPU computing in medical physics: A review", *Med. Phys.*, vol. 38, no. 5, pp. 2685–2697, 2011.

[19] F. Xu and K. Mueller, "Accelerating popular tomographic reconstruction algorithms on commodity PC graphics hardware", *IEEE Trans. Nucl. Sci.*, vol. 52, no. 3, pp. 654–663, Jun. 2005.

[20] I. Goddard, T. Wu, S. Thieret, A. Berman, H. Bartsch, M. J. Flynn, and J. Hsieh, "Implementing an iterative reconstruction algorithm for digital breast tomosynthesis on graphics processing hardware", in *Medical Imaging 2006: Physics of Medical Imaging*, ser. SPIE Proceedings, vol. 6142, SPIE, 2006, pp. 61424V–61424V–7.

[21] D. Matenine, Y. Goussard, and P. Després, "GPU-accelerated regularized iterative reconstruction for few-view cone beam CT", *Med. Phys.*, vol. 42, no. 4, pp. 1505–1517, Apr. 2015.

[22] A. Eklund, P. Dufort, D. Forsberg, and S. M. LaConte, "Medical image processing on the GPU – past, present and future", *Med. Image Anal.*, vol. 17, no. 8, pp. 1073–1094, Dec. 2013.

[23] J. Barzilai and J. M. Borwein, "Two-Point step size gradient methods", *IMA J. Numer. Anal.*, vol. 8, no. 1, pp. 141–148, 1988.

[24] Y. Nesterov, "Smooth minimization of non-smooth functions", *Math. Program.*, vol. 103, no. 1, pp. 127–152, 2005.

[25] T. Goldstein and S. Osher, "The split bregman method for L1-Regularized problems", *SIAM J. Imag. Sci.*, vol. 2, no. 2, pp. 323–343, Jan. 2009.

[26] A. Chambolle and T. Pock, "A First-Order Primal-Dual algorithm for convex problems with applications to imaging", *J. Math. Imaging Vis.*, vol. 40, no. 1, pp. 120–145, 2010.

[27] E. Sidky, J. Jorgensen, and X. Pan, “Convergence of iterative image reconstruction algorithms for digital breast tomosynthesis”, in *Nuclear Science Symposium and Medical Imaging Conference (NSS/MIC), 2012 IEEE*, ieeexplore.ieee.org, Oct. 2012, pp. 3394–3396.

[28] Y. Park, H. Cho, U. Je, D. Hong, M. Lee, C. Park, H. Cho, S. Choi, and Y. Koo, “Compressed-sensing (CS)-based digital breast tomosynthesis (DBT) reconstruction for low-dose, accurate 3D breast x-ray imaging”, *J. Korean Phys. Soc.*, vol. 65, no. 4, pp. 565–571, 2014.

[29] S. Ramani and J. A. Fessler, “A splitting-based iterative algorithm for accelerated statistical x-ray CT reconstruction”, *IEEE Trans. Med. Imaging*, vol. 31, no. 3, pp. 677–688, Mar. 2012.

[30] D. Kim, S. Ramani, and J. A. Fessler, “Combining ordered subsets and momentum for accelerated x-ray CT image reconstruction”, *IEEE Trans. Med. Imaging*, vol. 34, no. 1, pp. 167–178, Jan. 2015.

[31] J. A. Fessler, E. P. Ficaro, N. H. Clinthorne, and K. Lange, “Grouped-coordinate ascent algorithms for penalized-likelihood transmission image reconstruction”, *IEEE Trans. Med. Imaging*, vol. 16, no. 2, pp. 166–175, Apr. 1997.

[32] J. Nuyts, B. De Man, P. Dupont, M. Defrise, P. Suetens, and L. Mortelmans, “Iterative reconstruction for helical CT: A simulation study”, *Phys. Med. Biol.*, vol. 43, no. 4, pp. 729–737, Apr. 1998.

[33] K. Lange, D. R. Hunter, and I. Yang, “Optimization transfer using surrogate objective functions”, *J. Comput. Graph. Stat.*, vol. 9, no. 1, pp. 1–20, 2000.

[34] K Van Slambrouck and J Nuyts, “Reconstruction scheme for accelerated maximum likelihood reconstruction: The patchwork structure”, *Nuclear Science, IEEE Transactions on*, vol. 61, no. 1, pp. 173–181, Feb. 2014.

[35] T. Hebert and R. M. Leahy, “A generalized EM algorithm for 3-D bayesian reconstruction from poisson data using gibbs priors”, *IEEE Trans. Med. Imaging*, vol. 8, no. 2, pp. 194–202, Jun. 1989.

[36] E. Ü. Mumcuoğlu, R. M. Leahy, and S. R. Cherry, “Bayesian reconstruction of PET images: Methodology and performance analysis”, *Phys. Med. Biol.*, vol. 41, no. 9, pp. 1777–1807, Sep. 1996.

[37] A. Sawatzky, C. Brune, F. Wubbeling, T. Kosters, K Schafers, and M Burger, “Accurate EM-TV algorithm in PET with low SNR”, in *Nuclear Science Symposium Conference Record, 2008. NSS ’08. IEEE*, Oct. 2008, pp. 5133–5137.

[38] A. Beck and M. Teboulle, “Fast gradient-based algorithms for constrained total variation image denoising and deblurring problems”, *IEEE Trans. Image Process.*, vol. 18, no. 11, pp. 2419–2434, 2009.

[39] H. M. Hudson and R. S. Larkin, “Accelerated image reconstruction using ordered subsets of projection data”, *IEEE Trans. Med. Imaging*, vol. 13, no. 4, pp. 601–609, 1994.

[40] H Erdogan and J. A. Fessler, “Ordered subsets algorithms for transmission tomography”, *Phys. Med. Biol.*, vol. 44, no. 11, pp. 2835–2851, Nov. 1999.

[41] C Kamphuis and F. J. Beekman, “Accelerated iterative transmission CT reconstruction using an ordered subsets convex algorithm”, *IEEE Trans. Med. Imaging*, vol. 17, no. 6, pp. 1101–1105, Dec. 1998.

[42] G. Wu, J. G. Mainprize, and M. J. Yaffe, “Characterization of a constrained paired-view technique in iterative reconstruction for breast tomosynthesis”, *Med. Phys.*, vol. 40, no. 10, p. 101 901, 2013.

[43] K Sauer and C Bouman, “A local update strategy for iterative reconstruction from projections”, *Signal Processing, IEEE Transactions on*, vol. 41, no. 2, pp. 534–548, Feb. 1993.

[44] J. Fessler and A. Hero, “Space-alternating generalized expectation-maximization algorithm”, *Signal Processing, IEEE Transactions on*, vol. 42, no. 10, pp. 2664–2677, Oct. 1994.

[45] J. A. Fessler and D. Kim, “Axial block coordinate descent (ABCD) algorithm for x-ray CT image reconstruction”, in *International Meeting on Fully Three-dimensional Image Reconstruction in Radiology and Nuclear Medicine*, 2011, pp. 262–265.

[46] K Van Slambrouck and J Nuyts, “Metal artifact reduction in computed tomography using local models in an image block-iterative scheme”, *Med. Phys.*, vol. 39, no. 11, pp. 7080–7093, Nov. 2012.

[47] M. V. Ranganath, A. P. Dhawan, and N Mullani, “A multigrid expectation maximization reconstruction algorithm for positron emission tomography”, *IEEE Trans. Med. Imaging*, vol. 7, no. 4, pp. 273–278, Jan. 1988.

[48] T.-S. Pan and A. E. Yagle, “Numerical study of multigrid implementations of some iterative image reconstruction algorithms”, *IEEE Trans. Med. Imaging*, vol. 10, no. 4, pp. 572–588, Jan. 1991.

[49] A. Raheja, T. Doniere, and A. P. Dhawan, “Multiresolution expectation maximization reconstruction algorithm for positron emission tomography using wavelet processing”, *Nuclear Science, IEEE Transactions on*, vol. 46, no. 3, pp. 594–602, Jun. 1999.

[50] P. Chen and K. E. Earner, “Three-dimensional multi-resolution statistical reconstruction for tomosynthesis”, in *Biomedical Imaging: Nano to Macro, 2004. IEEE International Symposium on*, vol. 2, IEEE, Apr. 2004, 559–562 Vol. 1.

[51] K. G. Metheany, C. K. Abbey, N. Packard, and J. M. Boone, "Characterizing anatomical variability in breast CT images", *Med. Phys.*, vol. 35, no. 10, pp. 4685–4694, 2008.

[52] E. Engstrom, I. Reiser, and R. Nishikawa, "Comparison of power spectra for tomosynthesis projections and reconstructed images", *Med. Phys.*, vol. 36, no. 5, pp. 1753–1758, 2009.

[53] B. Liu, T. Wu, R. H. Moore, and D. B. Kopans, "Monte carlo simulation of x-ray scatter based on patient model from digital breast tomosynthesis", in *Medical Imaging*, International Society for Optics and Photonics, 2006, 61421N–61421N–9.

[54] G. T. Herman, "Correction for beam hardening in computed tomography", *Phys. Med. Biol.*, vol. 24, no. 1, pp. 81–106, Jan. 1979.

Chapter 6

A Model Observer to Evaluate Calcification Detectability in Breast Tomosynthesis

Koen Michielsen, Lesley Cockmartin, Nicholas Marshall, Hilde Bosmans, and Johan Nuyts

This chapter is based on the paper submitted for publication as: K Michielsen, L Cockmartin, N Marshall, H Bosmans, and J Nuyts, "A Model Observer to Optimize Calcification Detection in Breast Tomosynthesis," Med. Phys. (submitted November 19, 2015).

Abstract

Purpose: In this work we design and validate a model observer that can detect groups of microcalcifications in a four alternative forced choice (4-AFC) experiment and use it to optimize a smoothing prior for detectability of microcalcifications.

Methods: A channelized Hotelling observer (CHO) with eight Laguerre-Gauss channels was designed to detect groups of five microcalcifications in a background of acrylic spheres by adding the CHO log-likelihood ratios calculated at the expected locations of the five calcifications.

This model observer is then applied to optimize the detectability of the microcalcifications as a function of the smoothing prior. We examine the quadratic and total variation (TV) priors, and a combination of both. A selection of these reconstructions was then evaluated by human observers to validate the correct working of the model observer.

Results: We found a clear maximum for the detectability of microcalcifications when using the total variation prior with weight $\beta_{TV} = 35$. Detectability only varied over a small range for the quadratic and combined quadratic-TV priors when weight β_Q of the quadratic prior was changed by two orders of magnitude.

Spearman correlation with human observers was good except for the highest value of β for the quadratic and TV priors. Excluding those, we found $\rho = 0.93$ when comparing detection fractions, and $\rho = 0.86$ for the fitted detection threshold diameter.

Conclusions: We successfully designed a model observer that was able to predict human performance over a large range of settings of the smoothing prior, except for the highest values of β which were outside the useful range for good image quality.

Since detectability only depends weakly on the strength of the combined prior, it is not possible to pick an optimal smoothness based only on this criterion. On the other hand, such choice can now be made based on other criteria without worrying about calcification detectability.

6.1 Introduction

Digital breast tomosynthesis (DBT) is a recent three dimensional (3D) breast imaging technique with increasing clinical use. Compared to 2D mammography, reconstruction of the breast's anatomy in thick slices with high in-plane resolution allows better visualization of low contrast lesions due to the removal of interference from overlapping tissues. According to the meta-analysis by Lei et al. [1] single view DBT results in better sensitivity and specificity than two view digital mammography for diagnosing benign and malignant breast lesions, even though there remains a risk of underclassifying malignant lesions that present as microcalcifications [2].

Despite being commercially available for a few years already, current breast tomosynthesis systems [3] show a large variety in reconstruction methods and acquisition parameters such as angular range and number of projections, indicating that there is no obvious optimal practical implementation of a breast tomosynthesis system. Further optimization within the constraints of existing hardware could therefore potentially increase the clinical performance of these devices, but this process requires relevant quality metrics and efficient methods to evaluate them. A good candidate is the detection performance of simple geometric shapes in a structured background, because for this task human performance can be estimated by model observers [4]–[8].

When model observers are applied in breast tomosynthesis, they are typically used to evaluate either the projection geometry or the 3D reconstruction technique. In many instances a channelized Hotelling observer (CHO) is used to evaluate detectability of low contrast mass-type lesions. Chawla et al. [9] used this method to examine the effect of the number of projection images and the total angular range of those projections on detectability in both the projection and the reconstructed image domains. Possible sources of discrepancies between different model observer implementations were examined by Young et al. [10] who showed the need to take inter-projection correlations into account when applying the CHO in the projection domain and by Park et al. [11] who demonstrated that the choice of different 2D and 3D observer channels resulted in different preferences in system geometry. Focusing on the evaluation of 3D reconstruction techniques, Van de Sompel et al. [12] used the CHO to compare variants of filtered backprojection (FBP), the simultaneous algebraic reconstruction technique (SART), and maximum likelihood (ML) reconstruction, while Zeng et al. [13] found that the choice of reconstruction method did not influence the ranking of different acquisition geometries.

Some authors used alternative model observers to the CHO, such as the channelized non-prewhitening (CNPW) observer from the works of Gifford et al. [14] and Lau et al. [15] which they used to examine the effect of the number of projection views on detectability. This observer was shown to predict human observer performance when combined with a separate holistic search step [15].

In cases where the background structure and noise are stationary, it is possible to use frequency domain observers instead of the CHO and CNPW which are applied in the image domain. Reiser and Nishikawa [16] presented a prewhitening observer which was used to evaluate detectability of low contrast masses as a function of the number of projections, scan angle, and quantum noise. Wang et al. [17] used the same observer type to optimize a slice thickness filter in FBP and Gang et al. [18] evaluated performance of five frequency domain model observers for a wide range of scan angles and found reasonable correspondence with human observers.

While most authors focus on the detection of mass-like lesions, a few also concentrate on the detection of microcalcifications, an area where current tomosynthesis implementations do not have an advantage over digital mammography [19]. Das et al. used the same visual search CNPW as Lau et al. [15] and applied it to compare the detectability of microcalcifications in FBP and penalized ML reconstructions [20] and to evaluate the effect of the cutoff frequency of a Butterworth filter in FBP reconstruction [21]. Hu and Zhao [22] applied a frequency domain prewhitening observer to demonstrate the effects of angular dose distribution on the detection of microcalcifications, and Sidky et al. [23] used the same type of model observer and task to optimize a total variation smoothing prior.

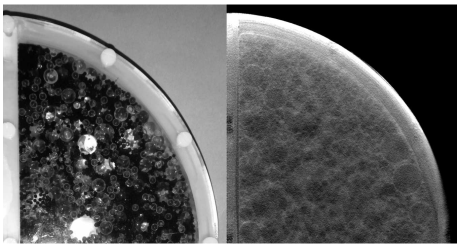

Figure 6.1: A photograph (left) and reconstructed slice (right) of the spheres-phantom.

Here we focus on this last task by designing a channelized Hotelling observer that can predict human observer performance in a microcalcification detection task, and then apply this model observer to optimize the smoothing prior in the model based ML iterative reconstruction we presented previously [24].

6.2 Materials and Methods

6.2.1 Phantom & Reconstruction

We used a prototype phantom designed to compare the performance of 2D full-field digital mammography and digital breast tomosynthesis systems [25]. The phantom is a half cylinder with a radius of 100 mm and a height of 58 mm. It contains 3D printed masses and microcalcification particles ($CaCO_3$) embedded within a structured background consisting of acrylic (PMMA) spheres in water that shows statistical properties close to these of patient images [26]. A photograph and a reconstructed slice of the phantom are shown in figure 6.1. In this work we only consider the microcalcification targets.

The phantom includes five microcalcification groups, each consisting of five calcifications arranged such that four lie in the corners of a square (side 7.1 mm), with the fifth at the center, as shown in figure 6.2. The different groups contain calcifications with diameters in the following ranges: 90–100 μm, 112–125 μm, 140–160 μm, 180–200 μm, and 224–250 μm.

Images acquired from this phantom can then be used to evaluate the detectability threshold of these groups of calcifications for a specific combination of system settings by means of a four-alternative forced choice (4-AFC) study with human observers. In such a study each observer is shown four 3D regions of interest (ROI), one of which contains a group of microcalcifications, and then selects the ROI thought to contain the lesion. By repeating this experiment for different cases and calcification diameters, we can determine the smallest diameter for which at least 62.5% of the microcalcification groups remain visible by a two parameter psychometric curve fit [25], [27]

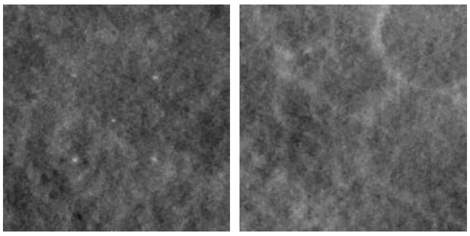

Figure 6.2: Two 20×20 mm^2 regions from the phantom, one with the microcalcification target, and one without.

to the correctly detected fractions $d(\phi)$ for each target diameter ϕ:

$$d(\phi) = 0.25 + \frac{0.75}{1 + \left(\frac{\phi}{\phi_{tr}}\right)^{-f}}. \tag{6.1}$$

The free parameters are the 62.5% detection threshold diameter ϕ_{tr}, and the slope of the curve f.

Fifteen sets of projection data were acquired on the Siemens Mammomat Inspiration tomosynthesis system for each of three exposure settings: the one determined by the automatic exposure control (AEC), and at half and double the AEC dose level. The detector has a pixel spacing of 85 μm and each acquisition consists of 25 projections spread over 50°. Between every set of three acquisitions at the different dose levels, the phantom was shaken and placed back on the detector in order to generate a different background structure with the same statistical properties by displacing the spheres in the phantom.

Phantom images for all three dose levels were reconstructed using the Siemens system filtered backprojection (FBP), based on the work of Mertelmeier et al. [28] and Orman et al. [29]. Images for the AEC dose level were also reconstructed with the $\mathrm{MLTR_{pr}}$ method [24], [30].

$\mathrm{MLTR_{pr}}$ is an iterative reconstruction algorithm that maximizes the posterior likelihood L in equation (6.2). It depends on the measured data y_i, the forward model $\hat{y}_i$ which includes an acquisition dependent resolution model to compensate for blur introduced by the motion of the x-ray tube during image acquisition, and includes additional constraints in the form of a quadratic [31] smoothing prior with weight β_Q and a total variation TV_{l_1} [32], [33] smoothing prior with weight β_{TV}. The two smoothing priors further depend on the reconstruction volume $\vec{\mu}$ (indexed by j and k) and neighbor weights w_{jk}.

$$L = \sum_i y_i \ln \hat{y}_i - \hat{y}_i - \frac{\beta_Q}{4} \sum_{j,k} w_{jk}(\mu_j - \mu_k)^2 - 4\beta_{TV} \sum_{j,k} w_{jk} \left|\mu_j - \mu_k\right| \tag{6.2}$$

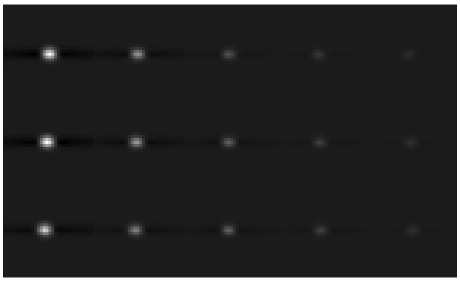

Figure 6.3: Templates of the five target diameters for an FBP reconstruction, showing the focus plane in the middle together with the planes above (top) and below (bottom).

All reconstructions were performed with voxel sizes of 85×85×1000 μm^3 and the ROI sizes that were extracted from these reconstructions for the 4-AFC studies were set to 236×236×30 voxels, roughly corresponding to 20×20×30 mm^3.

6.2.2 Model Observer Design

Templates and Channels

The first task in setting up the model observer is generating a set of signal templates for the reconstructed microcalcification targets in the phantom. Because the target sizes were chosen in order to create a wide range of detection levels (from non-visible to subtle to obvious), it was not feasible to get good signal templates from the measured data. Therefore simulated projection data were used to create the signal templates.

Using the system geometry of the Siemens Mammomat Inspiration tomosynthesis system, we simulated noise- and scatter-free projection data of the microcalcification targets in a homogeneous background, and of the same homogeneous background without the targets. The targets were simulated at an isotropic voxel size of 5 μm, and the background at 85 μm. The detector pixels were supersampled by a factor of 5 to model partial volume effects, and eight source positions were simulated to model the tube motion during the 120 ms exposure time. The target templates were then obtained by subtracting the reconstruction of the background from the reconstruction with the target included. Examples are shown in figures 6.3 and 6.4 for FBP and MLTR$_{\mathrm{pr}}$ with $\beta_Q = 2 \cdot 10^4$ and $\beta_{TV} = 2$ respectively.

Starting from these signal templates, we selected the first eight Laguerre-Gauss channels [34] with the width σ of the Gaussian part set to 187 μm (2.2 pixels of 85 μm). These settings create the channels that are shown in figure 6.5, which is at the same scale as figures 6.3 and 6.4 so that the relative sizes of the channels and targets can be compared.

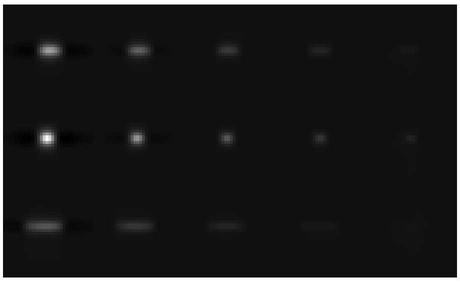

Figure 6.4: Templates of the five target diameters for an $\mathrm{MLTR}_{\mathrm{pr}}$ reconstruction, showing the focus plane in the middle together with the planes above (top) and below (bottom).

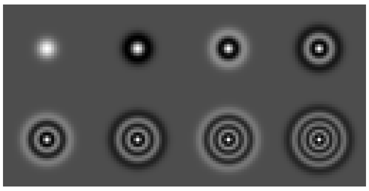

Figure 6.5: Laguerre-Gauss channels with $\sigma = 187\ \mu$m, at the same scale as figures 6.3 and 6.4.

Since the targets all have diameters of 250 μm or less, and reconstructions have a typical plane separation of 1 mm we chose to use a single-plane observer on the in-focus reconstructed plane rather than a multi-plane observer. With this implementation we also avoid problems that would be caused by the different appearance of the out-of-plane artifacts of the calcifications in the different reconstruction types. This can be seen in the top and bottom rows of figure 6.3 and 6.4: the center of the out-of-plane artifact is shifted slightly compared to the central plane target with the direction of the shift depending on the location of the target in the phantom. Additionally the out-of-plane artifacts look very different in both reconstruction techniques. These two observations are the reason why the same channels, centered at the same location in the planes above and below the focus plane, cannot be used.

The 4-AFC Experiment

With these signal templates and channels, we can apply a channelized Hotelling observer (CHO) to the individual calcifications in each group. This is however not the approach adopted by the human observers, who examined the image for the entire group of five calcifications, rather than each calcification individually. In order to perform the same 4-AFC experiment as the human observers, the model observer has to calculate a single likelihood ratio for the presence of five calcifications c_i at locations ℓ_i with $i \in \{1, 2, 3, 4, 5\}$

for each presented ROI. This means calculating $p(L_1, L_2, L_3, L_4, L_5|c_i{=}0)$ and $p(L_1, L_2, L_3, L_4, L_5|c_i{=}1)$, with $c_i{=}0$ shorthand for $c_1{=}c_2{=}c_3{=}c_4{=}c_5{=}0$ and L_i the 8-element channels output of image location ℓ_i.

Because the five locations are independent and there are either five calcifications present or none, we can say:

$$\begin{aligned}
&p(L_1, L_2, L_3, L_4, L_5|c_i{=}1) && (6.3)\\
&\quad = p(L_1|c_i{=}1) \cdot p(L_2|c_i{=}1) \ldots \cdot p(L_5|c_i{=}1) && (6.4)\\
&\quad = p(L_1|c_1{=}1) \cdot p(L_2|c_2{=}1) \ldots \cdot p(L_5|c_5{=}1), && (6.5)
\end{aligned}$$

which means we can add the log-likelihood ratios of the five locations to obtain the log-likelihood ratio $q(A)$ for region of interest A.

$$\begin{aligned}
q(A) &= \ln \frac{p(A|\bar{A}_1)}{p(A|\bar{A}_0)} && (6.6)\\
&= \ln \frac{p(L_1, L_2, L_3, L_4, L_5|c_i{=}1)}{p(L_1, L_2, L_3, L_4, L_5|c_i{=}0)} && (6.7)\\
&= \ln \frac{p(L_1|c_1{=}1)}{p(L_1|c_1{=}0)} + \ldots + \ln \frac{p(L_5|c_5{=}1)}{p(L_5|c_5{=}0)}. && (6.8)
\end{aligned}$$

Each individual log-likelihood ratio q was then calculated as follows [35]:

$$q(L) = \left(\bar{L}_1 - \bar{L}_0\right)' C_A^{-1} L - \frac{1}{2}\left(\bar{L}_1' C_A^{-1} \bar{L}_1 - \bar{L}_0' C_A^{-1} \bar{L}_0\right), \qquad (6.9)$$

with L the channel output of location ℓ in ROI A for which the score is being calculated, $\bar{L}_1$ the template of signal present, $\bar{L}_0$ the template for signal absent, and C_A^{-1} the inverse of the background covariance calculated specifically in the evaluated ROI A. The background covariance matrix itself was calculated from the channel outputs of approximately 10 000 partially overlapping regions of 32×32 voxels, distributed equally through the selected ROI (with a size of 236×236×30 voxels).

Calcification Group Geometry

In ideal circumstances, when the exact location of each calcification is known, scores for those five locations could just be added to get the score of each ROI. However, in reality the exact location of each calcification in the phantom was not known because the targets in this prototype phantom were positioned by hand. Therefore the target regions for the 4-AFC study were extracted by using their relative position to the location of the largest calcification group, which was clearly visible in all images.

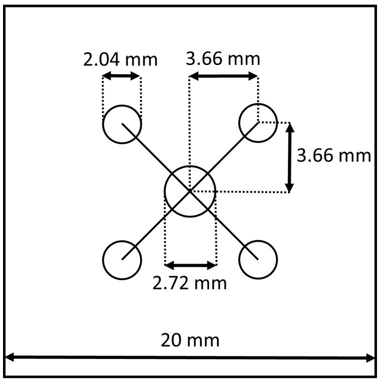

Figure 6.6: Calcification group geometry.

To account for inaccuracies due to deviations from the expected target geometry described in section 6.2.1, the model observer performs a search through five planes centered around the expected position of the calcifications in each ROI. The central target is searched for in a disk with a diameter of 32 pixels (2.72 mm). The search regions for the four calcifications on the corner positions were then determined relative to this variable position of the central calcification. The peripheral microcalcifications are allowed to be within a disc with diameter of 24 pixels (2.04 mm) centered at their expected locations 43 pixels (3.66 mm) to the left or right and 43 pixels to top or bottom from the central calcification, as shown in figure 6.6. All five calcifications also need to be contained within two adjacent planes at most. The final score for each image stack is now the maximum score that falls within these geometric constraints.

Reference Data

Before applying the model observer to its intended task of optimizing a smoothing prior as described in the next section, we compared it to a small set of reference data to make sure the model observer was working as intended. This dataset consisted of the three FBP reconstructions of the low, AEC, and high dose level phantom acquisitions, which had been evaluated by five human observers [25], and one additional MLTR$_{\mathrm{pr}}$ reconstruction with $\beta_Q = 2 \cdot 10^4$ and $\beta_{TV} = 2$ of the AEC dose level acquisition which was evaluated by a different group of five observers.

By comparing the results from the 4-AFC evaluations performed by the model observer to those of the human observers, we found that using a global covariance matrix for the CHO resulted in a large mismatch, which was solved by using a local covariance matrix, as in equation (6.9), and we were able to use this comparison to guide the choice of the geometric constraints in section 6.2.2. From this point of view, these constraints can

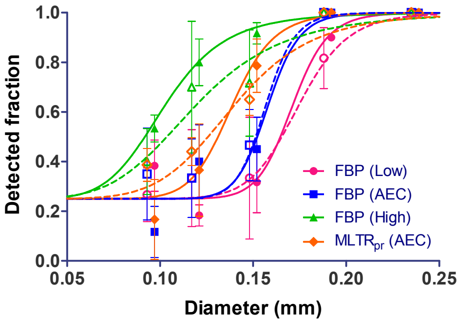

Figure 6.7: 4-AFC results and fitted psychometric curves for human (hollow symbols & dashed lines) and model (full symbols & lines) observers. The symbols are slightly shifted for better visibility.

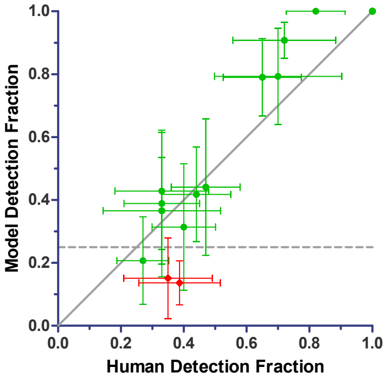

Figure 6.8: Detection fractions from 20 4-AFC experiments evaluated by human and model observers, with 7 overlapping points at (1,1). The scores of the 90–100 μm targets for AEC dose level FBP and MLTR$_{pr}$ are shown in red. The error bars represent 95% confidence intervals.

actually be seen as a type of internal noise that can be tuned to match the human observer results since allowing more flexibility will result in higher average scores from random noise in ROIs without signal.

Figure 6.7 shows the 4-AFC scores and psychometric curves for the human observer and the final implementation of the model observer. Because it is relatively hard to compare the results from both observers, a direct comparison of the 20 detected fractions (5 diameters for 4 reconstructions) from the 4-AFC evaluations is shown in figure 6.8, and the comparison of the fitted detection threshold diameters ϕ_{tr} is shown in figure 6.9.

Figure 6.8 shows that the detected fraction of the smallest microcalcification group (90–100 μm) in the FBP and MLTR$_{pr}$ reconstructions of the AEC dose acquisition are underestimated by the model observer, with one of the points even scoring significantly below the guessing level of 25%. Because the reference dataset was too small to examine this behavior further,

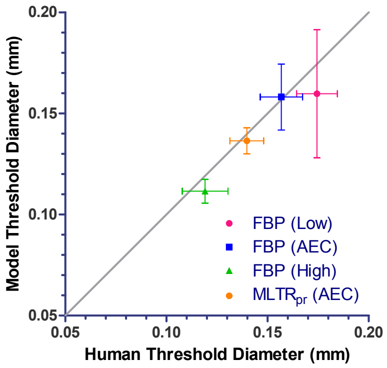

Figure 6.9: The fitted detection threshold diameter ϕ_{tr} for human and model observers. The error bars represent 95% confidence intervals.

the performance of the smallest target size (90–100 μm) was examined in more detail in the results of the application of the model observer on the smoothing prior optimization task.

6.2.3 Smoothing Prior Optimization & Model Observer Validation

We applied the model observer presented in section 6.2.2 to the optimization of the smoothing prior weights β_Q and β_{TV} in the MLTR$_{\text{pr}}$ reconstruction of the AEC dose level phantom measurements. For this task, we examine the quadratic smoothing prior for strength β_Q between $2 \cdot 10^3$ and $5 \cdot 10^5$, the total variation with ℓ_1 norm for strength β_{TV} between 1 and 50, and the combined prior with β_Q between $2 \cdot 10^3$ and $2 \cdot 10^5$ for $\beta_{TV} = 2$, and β_Q between $2 \cdot 10^4$ and $2 \cdot 10^5$ for $\beta_{TV} \in \{4, 6, 8\}$. With these ranges of the prior weight, the reconstructed images vary from noisier to smoother than the images used in clinical practice.

After finishing the optimization study, nine prior settings were selected for evaluation by human observers in order to validate the results obtained by the model observer. The 4-AFC experiments for the selected reconstructions were performed by five human observers. Spearman's ρ, which does not make assumptions on the variable distributions, is used to calculate the correlations between human and model observer detection fractions and fitted threshold diameters.

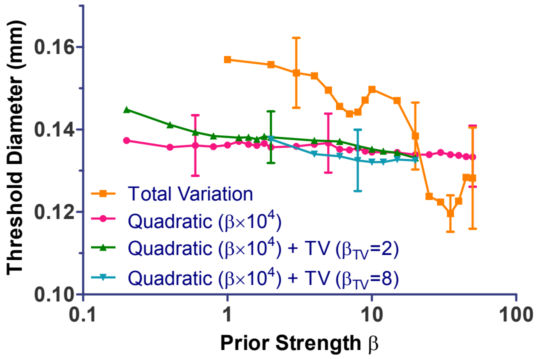

Figure 6.10: Fitted threshold diameter from model observer results for the quadratic, total variation, and combined priors, with 95% confidence intervals for the cases selected for human reading.

Prior Type	Prior Strength (β_Q, β_{TV})
Quadratic	$(6 \cdot 10^3, 0); (5 \cdot 10^4, 0); (5 \cdot 10^5, 0)$
Combined	$(2 \cdot 10^4, 2); (8 \cdot 10^4, 8)$
Total Variation	$(0, 3); (0, 20); (0, 35); (0, 50)$

Table 6.1: Prior settings selected for verification by human readers.

6.3 Results

6.3.1 Smoothing Prior Optimization

Figure 6.10 shows the fitted threshold diameter to the 4-AFC experiment results for the quadratic, total variation, and combined priors. The smallest threshold diameter of 120 μm was reached for the total variation prior with $\beta_{TV} = 35$. Threshold diameters only decrease slowly with increasing prior strength for the quadratic and combined smoothing priors, with threshold diameters between 133 μm and 138 μm for $\beta_Q > 10^4$. Results of the combined prior with $\beta_{TV} = 4$ and $\beta_{TV} = 6$ are not shown because they overlap with the results of the quadratic other two combined priors.

6.3.2 Model Observer Validation

The nine prior settings that were selected for validation by human observers are listed in table 6.1. Figure 6.11 shows a calcification group with 180–200 μm targets for each of these priors and for the low, AEC, and high dose level FBP reconstruction to illustrate the wide range of settings that was chosen.

Human and model observer detection scores for these reconstruction settings are shown in figure 6.12, with the two outliers shown in red: the scores of the 112–125 μm target for $\beta_Q = 5 \cdot 10^5$ and the 140–160 μm target for

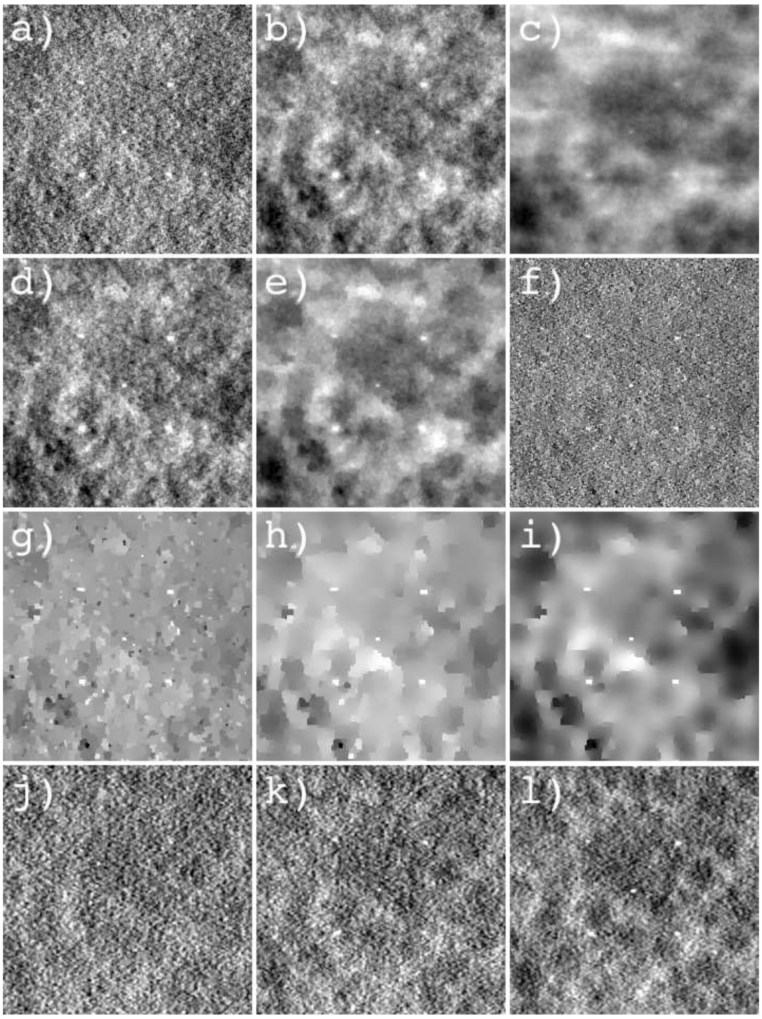

Figure 6.11: Iterative reconstructions of the 180–200 μm targets with: a) $\beta_Q = 6 \cdot 10^3$, b) $\beta_Q = 5 \cdot 10^4$, c) $\beta_Q = 5 \cdot 10^5$, d) $\beta_Q = 2 \cdot 10^4$ and $\beta_{TV} = 2$, e) $\beta_Q = 8 \cdot 10^4$ and $\beta_{TV} = 8$, f) $\beta_{TV} = 3$, g) $\beta_{TV} = 20$, h) $\beta_{TV} = 35$, and i) $\beta_{TV} = 50$, and FBP reconstructions of the j) low, k) AEC, and l) high dose level projection data.

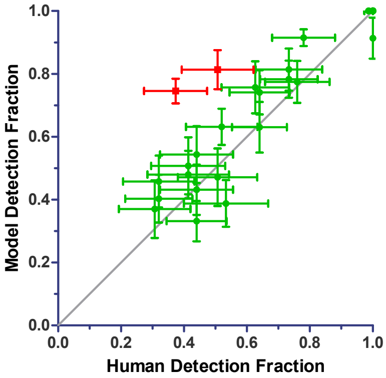

Figure 6.12: Model observer detection fraction as a function of the human detection fraction for all target diameters except 90–100 μm. Two outliers (112–125 μm for $\beta_Q = 5 \cdot 10^5$ and 140–160 μm for $\beta_{TV} = 50$) are shown in red. The error bars represent 95% confidence intervals.

$\beta_{TV} = 50$, i.e. the highest values for β for the quadratic and total variation priors respectively. The scores of the 90–100 μm targets are not included, and examined separately in section 6.3.3. Correlation coefficients (Spearman ρ) and corresponding 95% confidence intervals between human and model observers for these scores were 0.917 [0.844–0.956] and 0.928 [0.862–0.963] with and without the outliers respectively and these are significant in both instances ($p<0.001$).

Figures 6.13 and 6.14 show the fitted detection threshold diameter ϕ_{tr} for human and model observers, with the same two outliers ($\beta_Q = 5 \cdot 10^5$ and $\beta_{TV} = 50$) as in figure 6.12. Correlation coefficients (Spearman ρ) between human and model observers for these thresholds were 0.857 ($p=0.024$) without the outliers, and 0.550 ($p=0.133$) with outliers included. There were too few points to calculate a reliable confidence interval.

6.3.3 Evaluation of the 90–100 μm Target

Scatter plots of the detection fraction of the nine prior settings listed in table 6.1 are shown in figure 6.15 for human and model observers and for the smallest target size. Our assumption for this target is that it is too small to be seen in DBT reconstructions, which means we expect a detection fraction equal to the theoretical guess of 0.25 in a 4-AFC experiment for this target size. However, we find that the average detection fraction of the smallest target is 0.36 for human readers, which is significantly ($p<0.001$) above the guess level. The model observer on the other hand scores 18% correct, significantly below the guess level ($p=0.004$).

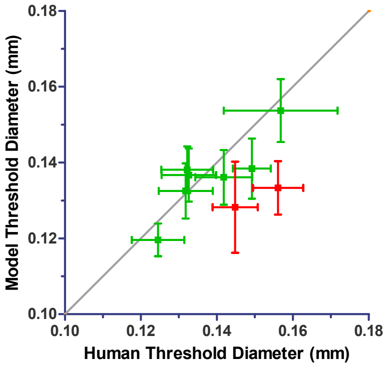

Figure 6.13: The fitted detection threshold diameter ϕ_{tr} for human and model observers. Two outliers ($\beta_Q = 5 \cdot 10^5$ and $\beta_{TV} = 50$) are shown in red. The error bars represent 95% confidence intervals.

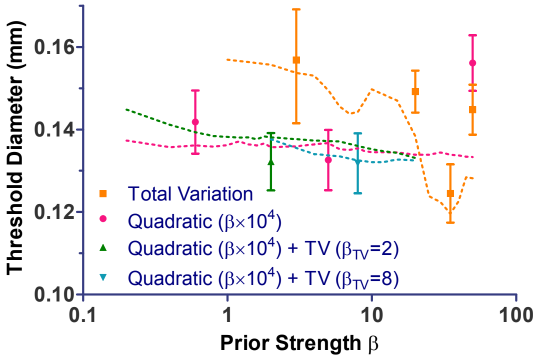

Figure 6.14: Fitted threshold diameter from human observer results for the quadratic, total variation, and combined priors, with 95% confidence intervals. The dashed lines are the corresponding model observer results from figure 6.10.

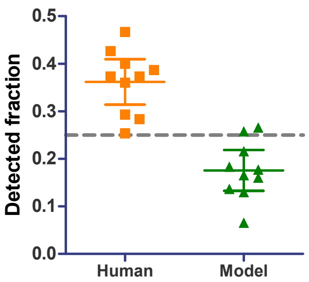

Figure 6.15: Scatter plot with mean and 95% confidence interval of the human and model observer scores of the 90–100 μm targets for the reconstructions listed in table 6.1.

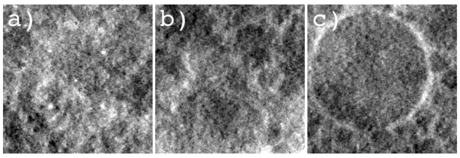

Figure 6.16: Different phantom backgrounds: a) with target present, b) without target, but resembling target background, c) without target, not resembling target background.

Feedback from the observers indicated that the guess rate might have increased because some background types were correctly assumed to never have a target present. This can be seen in figure 6.16: 6.16a shows the signal in its typical background, and 6.16b and 6.16c show two types of normal backgrounds. Because the microcalcification targets in the phantom are mounted on a thin PMMA plate, the presence of the sphere in 6.16c means that there cannot be a microcalcification group at the same locations. Thus if the background in 6.16c appeared in the 4-AFC experiment, it would be rightly discarded as a candidate, and the observer would then choose between the three remaining images, resulting in a higher chance of guessing correctly.

With this information we performed an additional experiment to check if the background types that were quickly discarded by the human observers might have a reversed effect on the model observer, resulting in the lower than expected performance. For this we selected one of the nine reconstructions ($\beta_Q = 2 \cdot 10^4$, $\beta_{TV} = 2$) and visually inspected all background images to see if there was a single large sphere visible in the central plane. Images where no sphere was clearly in focus (as in figure 6.16b) were included in group A, images where such a sphere was clearly visible (as in figure 6.16c) were included in group B.

The model observer log-likelihood ratios q for these groups are plotted in figure 6.17. The mean scores are 11.49 for the abnormal cases, 11.52 for background cases in group A, and 11.92 for background cases in group B. Restricting the normal cases in the 4-AFC experiment to cases from group A results in a detection fraction of 0.22 (95% CI:[0.11–0.33]), up from 0.14 (95% CI:[0.06–0.21]). The new score of 0.22 is not significantly different from 0.25 (p=0.550), while the old score of 0.14 was significantly lower (p=0.006).

6.4 Discussion

In this work we set out to accomplish two main goals: design a model observer that can predict human observer performance in a calcification detection task, and apply this model observer to maximize calcification detectability by optimizing the weights of the smoothing prior. This optimum

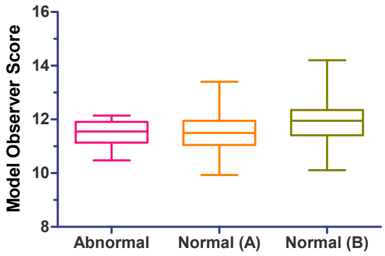

Figure 6.17: Boxplot with whiskers from minimum to maximum of the model observer log-likelihood ratio of the smallest diameter targets, normal cases with background similar to target backgrounds, and normal cases with background not similar to target backgrounds.

was found for the total variation prior with sharp peaks in detection threshold diameter and detected fraction at $\beta_{TV} = 35$. Figure 6.14 shows that this optimum was found for both human and model observers, and that the ranking of the different settings was the same for both observer types. Threshold diameters for the quadratic and combined quadratic and total variation prior only changed by a small amount over the examined range, with the threshold improving slowly with β_Q increasing two orders of magnitude, and images ranging from too noisy to too smooth (as in figures 6.11a and 6.11c).

The sharp minimum at $\beta_{TV} = 35$, rather than a more gradual change is probably a consequence of the non-linear behavior of the total variation prior. Since the threshold diameter is most strongly influenced by the detectability of the 140–160μm target, this value of beta results in the largest possible noise suppression that does not suppress the targets at this crucial diameter. Below this strength, irregular speckle noise (as seen in figure 6.11g) still confounds detectability, while at this specific prior strength, the background is reduced to a featureless piecewise-constant area, with few noise specks that could be confused with the calcification targets, while the targets themselves are not yet suppressed by the prior. Above this strength both noise and targets are suppressed, and thus the threshold diameter increases again.

Unfortunately the prior with the highest detection produces reconstructions that are not clinically useful since most small scale and low contrast information has been removed from the image. This means that the presented optimization process would not have been successful in choosing an appropriate setting for our smoothing prior if the goal had been to select a clinically acceptable reconstruction. Although the detection of small calcifications is a necessary condition for choosing a good smoothing prior, that addresses a weaker point of current tomosynthesis systems, it seems it is not a sufficient condition to guarantee overall optimal performance.

This means we would need either a replacement task or an additional task in the optimization process that would be more sensitive to oversmoothing than the current detection task. Possible options could be distinguishing between different orientations of a capital letter 'E' or 'C', i.e. the tumbling E or Landolt C used to measure visual acuity, or more applied to mammography, distinguishing between smooth and irregular microcalcifications. With these alternative or additional tasks, it seems more likely that the quadratic or mixed smoothing prior will provide the best compromise, since the detection performance remains stable over a large range of β, unlike the total variation prior, where a relatively small change in β would result in performance worse than the quadratic prior.

Even though the chosen detection task was not well suited to the clinical optimization of a smoothing prior, the model observer itself managed to predict human observer results accurately over a large range of prior settings, except for the highest β_Q and β_{TV} values. Considering that these highest prior strengths are clearly not clinically relevant, we find that the model observer is a useful tool in the evaluation of the microcalcification detection task specified in this phantom, and can in fact be used instead of human observers.

When evaluating the detectability for the smallest target diameter of 90–100μm we found that the conflicting performance between human and model observers was caused by scoring differences for two types of backgrounds. Human observers correctly considered the backgrounds that contained a large in focus sphere (as in figure 6.16c) unlikely to contain the target, while the model observer scored these as more likely to contain the target. This behavior results in a performance increase for the human observers, and a decrease for the model observer, both of which are probably present for all target diameters, but most clearly seen for the smallest target.

These results mean that we should make sure that all backgrounds presented during the 4-AFC study have an equal difficulty level. Although this is possible by visual inspection, we believe a better solution would be to adapt the phantom in such a way that all backgrounds resemble the ones in figures 6.16a and 6.16b.

6.5 Conclusion

We successfully designed a model observer that was able to predict human performance over a large range of settings of the smoothing prior, except for the highest values of β which were outside the useful range for good image quality.

Based on the model observer results, we were able to choose a smoothing prior that optimizes the detection of microcalcifications in our iterative reconstruction and a human observer study confirmed that this prior yielded good results for the calcification detection task. Unfortunately, this 'optimal' prior applies strong smoothing, and tends to erase small scale and low contrast information in the reconstructed images, which makes it unsuitable in a clinical setting. Therefore we must also conclude that this detection task lacks the complexity or subtlety required to optimize for the task of reading clinical images.

When focusing on the combined quadratic and total variation prior, we find detectability only changes slightly for different amounts of smoothing, and thus an optimal strength for this prior can be selected based on other criteria without worrying about calcification detectability.

Acknowledgments

The authors would like to thank Esmaeel Rangraz, Ahmadreza Rezaei, Georg Schramm, Tao Sun, and Anna Turco for participating in the 4-AFC experiment, and Siemens Healthcare for their financial support.

References

[1] J. Lei, P. Yang, L. Zhang, Y. Wang, and K. Yang, "Diagnostic accuracy of digital breast tomosynthesis versus digital mammography for benign and malignant lesions in breasts: A meta-analysis", *Eur. Radiol.*, vol. 24, no. 3, pp. 595–602, Mar. 2014.

[2] A. Tagliafico, G. Mariscotti, M. Durando, C. Stevanin, G. Tagliafico, L. Martino, B. Bignotti, M. Calabrese, and N. Houssami, "Characterisation of microcalcification clusters on 2D digital mammography (FFDM) and digital breast tomosynthesis (DBT): Does DBT underestimate microcalcification clusters? results of a multicentre study", *Eur. Radiol.*, vol. 25, no. 1, pp. 9–14, Jan. 2015.

[3] I. Sechopoulos, "A review of breast tomosynthesis. part i. the image acquisition process", *Med. Phys.*, vol. 40, no. 1, p. 014 301, 2013.

[4] H. H. Barrett, J. Yao, J. P. Rolland, and K. J. Myers, "Model observers for assessment of image quality", in *Proceedings of the National Academy of Sciences of the United States of America*, vol. 90, National Academy of Sciences, Nov. 1993, pp. 9758–9765.

[5] J. Beutel, H. L. Kundel, and R. L. Van Metter, *Handbook of Medical Imaging: Physics and psychophysics*. SPIE Press, 2000, vol. 1.

[6] C. K. Abbey and H. H. Barrett, "Human- and model-observer performance in ramp-spectrum noise: Effects of regularization and object variability", *J. Opt. Soc. Am. A*, vol. 18, no. 3, pp. 473–488, 2001.

[7] A. E. Burgess, “Visual perception studies and observer models in medical imaging”, *Semin. Nucl. Med.*, vol. 41, no. 6, pp. 419–436, Nov. 2011.

[8] X. He and S. Park, “Model observers in medical imaging research”, *Theranostics*, vol. 3, no. 10, pp. 774–786, 2013.

[9] A. S. Chawla, J. Y. Lo, J. A. Baker, and E. Samei, “Optimized image acquisition for breast tomosynthesis in projection and reconstruction space”, *Med. Phys.*, vol. 36, no. 11, pp. 4859–4869, 2009.

[10] S. Young, S. Park, S. K. Anderson, A. Badano, K. J. Myers, and P. Bakic, “Estimating breast tomosynthesis performance in detection tasks with variable-background phantoms”, in *Medical Imaging 2009: Physics of Medical Imaging*, E. Samei and J. Hsieh, Eds., ser. SPIE Proceedings, vol. 7258, SPIE, 2009, 72580O–72580O–9.

[11] S. Park, G. Z. Zhang, R. Zeng, and K. J. Myers, “Comparing observer models and feature selection methods for a task-based statistical assessment of digital breast tomsynthesis in reconstruction space”, in *Medical Imaging 2014: Image Perception, Observer Performance, and Technology Assessment*, C. R. Mello-Thoms and M. A. Kupinski, Eds., ser. SPIE Proceedings, SPIE, 2014, pp. 90370M–90370M–11.

[12] D. Van de Sompel, S. M. Brady, and J. Boone, “Task-based performance analysis of FBP, SART and ML for digital breast tomosynthesis using signal CNR and channelised hotelling observers”, *Med. Image Anal.*, vol. 15, no. 1, pp. 53–70, 2010.

[13] R. Zeng, S. Park, P. Bakic, and K. J. Myers, “Evaluating the sensitivity of the optimization of acquisition geometry to the choice of reconstruction algorithm in digital breast tomosynthesis through a simulation study”, *Phys. Med. Biol.*, vol. 60, no. 3, pp. 1259–1288, 2015.

[14] H. C. Gifford, C. S. Didier, M. Das, and S. J. Glick, “Optimizing breast-tomosynthesis acquisition parameters with scanning model observers”, in *Medical Imaging 2008: Image Perception, Observer Performance, and Technology*, B. Sahiner and D. J. Manning, Eds., ser. SPIE Proceedings, SPIE, 2008, 69170S–69170S–9.

[15] B. A. Lau, M. Das, and H. C. Gifford, “Towards visual-search model observers for mass detection in breast tomosynthesis”, in *Medical Imaging 2013: Physics of Medical Imaging*, R. M. Nishikawa and B. R. Whiting, Eds., ser. SPIE Proceedings, vol. 8668, SPIE, 2013, p. 86680X.

[16] I. S. Reiser and R. M. Nishikawa, “Task-based assessment of breast tomosynthesis: Effect of acquisition parameters and quantum noise”, *Med. Phys.*, vol. 37, no. 4, pp. 1591–1600, 2010.

[17] X. Wang, J. G. Mainprize, G. Wu, and M. J. Yaffe, “Task-Based evaluation of image quality of filtered back projection for breast tomosynthesis”, in *Digital Mammography*, ser. Lecture Notes in Computer Science, Springer Berlin Heidelberg, 2010, pp. 106–113.

[18] G. J. Gang, J. Lee, J Webster Stayman, D. J. Tward, W. Zbijewski, J. L. Prince, and J. H. Siewerdsen, “Analysis of fourier-domain task-based detectability index in tomosynthesis and cone-beam CT in relation to human observer performance”, *Med. Phys.*, vol. 38, no. 4, pp. 1754–1768, 2011.

[19] J. A. Baker and J. Y. Lo, “Breast tomosynthesis: State-of-the-art and review of the literature”, *Acad. Radiol.*, vol. 18, no. 10, pp. 1298–1310, Oct. 2011.

[20] M. Das and H. C. Gifford, “Comparison of model-observer and human-observer performance for breast tomosynthesis: Effect of reconstruction and acquisition parameters”, in *Medical Imaging 2011: Physics of Medical Imaging*, N. J. Pelc, E. Samei, and R. M. Nishikawa, Eds., ser. SPIE Proceedings, vol. 7961, SPIE, 2011, pp. 796 118–796118–9.

[21] M. Das, C. Connolly, S. J. Glick, and H. C. Gifford, “Effect of postreconstruction filter strength on microcalcification detection at different imaging doses in digital breast tomosynthesis: Human and model observer studies”, in *Medical Imaging 2012: Physics of Medical Imaging*, N. J. Pelc, R. M. Nishikawa, and B. R. Whiting, Eds., ser. SPIE Proceedings, SPIE, 2012, pp. 831 321–831321–8.

[22] Y.-H. Hu and W. Zhao, “The effect of angular dose distribution on the detection of microcalcifications in digital breast tomosynthesis”, *Med. Phys.*, vol. 38, no. 5, p. 2455, 2011.

[23] E. Sidky, Y Duchin, I Reiser, C Ullberg, and X. Pan, “Optimizing algorithm parameters based on a model observer detection task for image reconstruction in digital breast tomosynthesis”, in *Nuclear Science Symposium and Medical Imaging Conference (NSS/MIC), 2011 IEEE*, Oct. 2011, pp. 4230–4232.

[24] K. Michielsen and J. Nuyts, “Multigrid reconstruction with block-iterative updates for breast tomosynthesis”, *Med. Phys.*, vol. 42, no. 11, pp. 6537–6548, 2015.

[25] L. Cockmartin, N. W. Marshall, G Zhang, K. Lemmens, E Shaheen, C. Van Ongeval, E Fredenberg, D. R. Dance, E. Salvagnini, K. Michielsen, and H. Bosmans, “A structured phantom for detection performance comparison between breast tomosynthesis and digital mammography”, *Med. Phys.*, submitted, 2015.

[26] L Cockmartin, H Bosmans, and N. W. Marshall, "Comparative power law analysis of structured breast phantom and patient images in digital mammography and breast tomosynthesis", *Med. Phys.*, vol. 40, no. 8, p. 081 920, Aug. 2013.

[27] N Karssemeijer and M. Thijssen, "Determination of contrast-detail curves of mammography systems by automated image analysis", *Digital Mammography*, vol. 96, pp. 155–160, 1996.

[28] T. Mertelmeier, J. Orman, W. Haerer, and M. K. Dudam, "Optimizing filtered backprojection reconstruction for a breast tomosynthesis prototype device", in *Medical Imaging 2006: Physics of Medical Imaging*, M. J. Flynn and J. Hsieh, Eds., ser. SPIE Proceedings, vol. 6142, SPIE, 2006, 61420F–61420F–12.

[29] J. Orman, T. Mertelmeier, and W. Haerer, "Adaptation of image quality using various filter setups in the filtered backprojection approach for digital breast tomosynthesis", in *Digital Mammography*, ser. Lecture Notes in Computer Science, Springer Berlin Heidelberg, 2006, pp. 175–182.

[30] K. Michielsen, K. Van Slambrouck, A. Jerebko, and J. Nuyts, "Patchwork reconstruction with resolution modeling for digital breast tomosynthesis", *Med. Phys.*, vol. 40, no. 3, p. 031 105, Mar. 2013.

[31] E. Ü. Mumcuoğlu, R. M. Leahy, and S. R. Cherry, "Bayesian reconstruction of PET images: Methodology and performance analysis", *Phys. Med. Biol.*, vol. 41, no. 9, pp. 1777–1807, Sep. 1996.

[32] A. Sawatzky, C. Brune, F. Wubbeling, T. Kosters, K Schafers, and M Burger, "Accurate EM-TV algorithm in PET with low SNR", in *Nuclear Science Symposium Conference Record, 2008. NSS '08. IEEE*, Oct. 2008, pp. 5133–5137.

[33] A. Beck and M. Teboulle, "Fast gradient-based algorithms for constrained total variation image denoising and deblurring problems", *IEEE Trans. Image Process.*, vol. 18, no. 11, pp. 2419–2434, 2009.

[34] B. D. Gallas and H. H. Barrett, "Validating the use of channels to estimate the ideal linear observer", *J. Opt. Soc. Am.*, vol. 20, no. 9, pp. 1725–1738, Sep. 2003.

[35] K. J. Myers and H. H. Barrett, "Addition of a channel mechanism to the ideal-observer model", *J. Opt. Soc. Am.*, vol. 4, no. 12, pp. 2447–2457, Dec. 1987.

Chapter 7

Phantom and Visual Grading Analysis of Three Breast Tomosynthesis Reconstruction Methods

Koen Michielsen, Chantal Van Ongeval,
Andre Van Steen, Machteld Keupers, Julie Soens,
Hadeel Ghunaim, Lesley Cockmartin, Dimitar Petrov,
Hilde Bosmans, and Johan Nuyts

Abstract

Purpose: We compare three reconstruction techniques for breast tomosynthesis: super-resolution filtered backprojection with post-reconstruction denoising (SRSAR), model based iterative reconstruction (MLTR_{pr}), and regular filtered backprojection (FBP), in terms of target detectability and visual grading analysis.

Methods: Detection threshold diameters of calcification and mass models placed in a phantom with structured background were determined from a four-alternative forced-choice experiment. Clinical image quality was scored based on eight criteria for clinical mammography quality assessment and evaluated by four radiologists on 56 patients with similar distribution in four density groups (N1, P1, P2, DY) and four thickness groups (<40 mm, 40–54 mm, 55–69 mm, and >70 mm). Reader scores were evaluated by visual grading characteristics (VGC) analysis.

Results: Detection thresholds for calcifications and masses are significantly better ($p=0.003$, $p<0.001$) for MLTR_{pr} (137 μm, 2.33 mm) and SRSAR (144 μm, 2.51 mm) than FBP (159 μm, 3.15 mm), but not different between MLTR_{pr} and SRSAR ($p=0.154$, $p=0.125$).

VGC analysis finds an overall trend that prefers SRSAR over FBP, and FBP over MLTR_{pr}. Significant differences were found for the following criteria: increased noise in SRSAR compared to FBP, more artifacts in MLTR_{pr} than in SRSAR, better skin line visualization in SRSAR compared to FBP and MLTR_{pr}, and better overall image quality in SRSAR than in MLTR_{pr}.

Conclusions: Both SRSAR and MLTR_{pr} improved performance on the detection tasks, but resulted in significantly different overall appreciation of image quality. Considering both detection and visual grading evaluations, SRSAR improves most upon current FBP, although adjustment of the denoising might be needed.

7.1 Introduction

Digital breast tomosynthesis (DBT) reconstructions are typically compared by using technical measures such as the artifact spread function (ASF) and signal difference or contrast to noise ratios (SDNR or CNR) [1]–[5], or task based detectability indexes calculated from human [6], [7] or model [6], [8], [9] observers.

Most clinical evaluations of breast tomosynthesis images compare one or two-view tomosynthesis and two-view mammography images on systems from a single manufacturer [10]–[15] or the combination of tomosynthesis and two-view mammography versus two-view mammography alone [16]–[18]. Although these studies, performed on systems from GE, Hologic, Philips and Siemens, agree on the benefits of tomosynthesis, it is worth studying whether performance could be further improved for specific parameter settings [19]. Such comparisons between systems could for example be performed by evaluating microcalcification and mass detection in a physical phantom [7].

Once breast tomosynthesis becomes a more established imaging modality, we would expect more clinical evaluations of different reconstruction algorithms, as in computed tomography (CT) where new low dose iterative reconstruction algorithms are now regularly evaluated in clinical setting [20]–[26].

In this work we will compare three reconstruction methods for breast tomosynthesis by a task-based phantom evaluation and a visual evaluation of a series of patient cases by experienced radiologists.

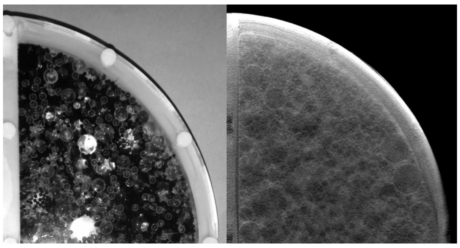

Figure 7.1: A photograph (left) and reconstructed slice (right) of the phantom.

7.2 Materials and Methods

7.2.1 Reconstruction Methods

We compare the following three reconstruction methods in this work: a.) FBP: the Siemens VB30L product reconstruction, based on the work of Mertelmeier et al. [27] and Orman et al. [28], b.) SRSAR: the latest Siemens research prototype, a filtered backprojection with super resolution backprojection and noise filtering, as presented by Abduruhman et al. [29], but without the statistical artifact reduction, and c.) MLTR_{pr}: a multigrid maximum likelihood algorithm that includes an acquisition dependent resolution model to compensate for blur introduced by the motion of the x-ray tube during image acquisition and includes additional constraints in the form of quadratic ($\beta_Q = 2 \cdot 10^4$) and total variation TV_{ℓ_1} ($\beta_{TV} = 4$) smoothing priors [30], [31]. All patient and phantom data were reconstructed in 1 mm planes with an in-plane pixel spacing of 85 μm.

7.2.2 Phantom Evaluation

The phantom we use is designed to evaluate the performance of both 2D full-field digital mammography and digital breast tomosynthesis systems [7]. It contains 3D printed masses and microcalcification particles ($CaCO_3$) embedded within a structured background consisting of acrylic (PMMA) spheres in water that resembles the statistical properties of patient images [32]. A photograph and a reconstructed slice of the phantom are shown in figure 7.1. In this work we evaluated the microcalcification groups and the non-spiculated masses, shown in figure 7.2.

The phantom includes five non-spiculated masses and five microcalcification groups, with each consisting of five calcifications placed on the corners and in the center of a square. The masses have average diameters of 1.6 mm, 2.3 mm, 3.3 mm, 4.6 mm, and 6.2 mm. Each calcification group contains particles with diameters in one of the following ranges: 90–100 μm, 112–125 μm, 140–160 μm, 180–200 μm, and 224–250 μm.

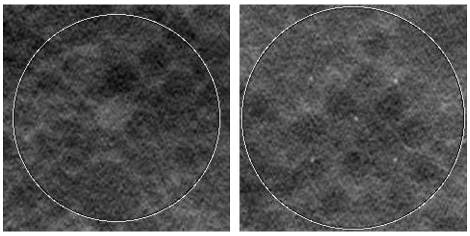

Figure 7.2: FBP reconstruction of a non-spiculated mass (left) and a microcalcification group (right).

Fifteen sets of projection data were acquired under automatic exposure control (AEC) on the Siemens Mammomat Inspiration tomosynthesis system. Between every acquisition, the phantom was shaken and placed back on the detector in order to generate different background structures by displacing the spheres in the phantom. Each set of projections was reconstructed with the FBP, SRSAR, and MLTR_{pr} methods.

Reconstructed images were then used to evaluate the detectability threshold of these targets by setting up a four-alternative forced choice (4-AFC) study. In this study the observer is shown four regions of interest (ROI), each an image stack of 30 planes of 20×20 mm^2 and one of which contains a mass or group of microcalcifications. The reader then selects the ROI which he thinks contains the target. By repeating this experiment for different cases and target diameters, we can find the detection threshold diameter ϕ_{tr} by a two parameter psychometric curve fit [7], [33], [34] to the correctly detected fractions $d(\phi)$ for each target diameter ϕ:

$$d(\phi) = 0.25 + \frac{0.75}{1 + \left(\frac{\phi}{\phi_{tr}}\right)^{-f}}. \tag{7.1}$$

The free parameters are the detection threshold diameter ϕ_{tr}, which is specific for each reconstruction, and f which determines the slope of the curve and is shared between the fits for the three reconstructions.

The 4-AFC observer study to evaluate detection performance for the non-spiculated masses was performed by six human observers. Results for the FBP reconstruction were taken from the study evaluating the application of the phantom [7], and results for the SRSAR and MLTR_{pr} reconstructions were obtained in a follow-up experiment with three observers who had participated in the first study, and three new observers.

The microcalcifications were evaluated by a model observer developed and validated with a human observer study in previous work [35]. This observer combines the scores of a channelized Hotelling observer on each of the five targets in each microcalcification group, while taking into account the relative position of the calcifications in the group.

7.2.3 Visual Grading Study

For the second part of the evaluation a visual grading study was performed on the three reconstruction methods. All cases were selected from a database of 409 tomosynthesis scans of 232 individual patients who had undergone tomosynthesis imaging after suspicious findings in 2D digital mammography or ultrasound imaging, resulting in an enriched dataset. From this group, patients were chosen to represent four glandularity groups described by Wolfe [36] (N1, P1, P2, DY) and four thickness groups (<40 mm, 40–54 mm, 55–69 mm, and >70 mm). Four patients were selected for each combination of glandularity and thickness group, with the exception of the two low glandularity groups (N and P1) for thin breasts (<40 mm) which were not represented. This resulted in a total of 56 image sets from 51 patients that were included in the study: 28 cranio-caudal (CC) views, 1 medio-lateral (ML) view, and 27 medio-lateral oblique (MLO) views. A set of five patient cases from this study is shown in section 7.3.3.

The image quality evaluation criteria were selected from the list presented by Van Ongeval et al. [37] for 2D mammography and included the following criteria:

1. No disturbing noise present.
2. No disturbing artifacts present.
3. Visualization of the skin line.
4. Sharp visualization of Coopers ligaments and vascular structures.
5. Visualization of microcalcifications.
6. Visualization of opacities.
7. Adequate image contrast.
8. General impression of image quality.

Each criterion was given a score between -2 and 2:

-2 Poor quality.

-1 Restricted quality.

0 Sufficient quality.

1 Good quality.

2 Excellent quality.

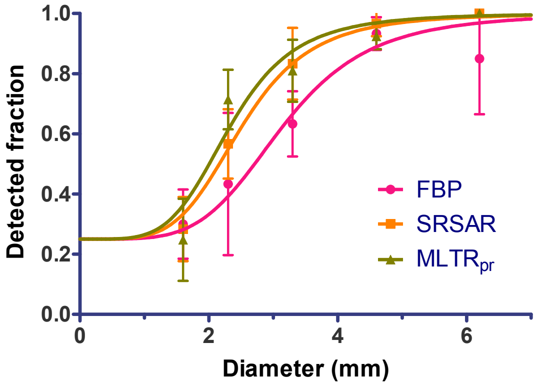

Figure 7.3: Psychometric curve fit for the detection of non-spiculated masses by human observers. Error bars indicate 95% confidence intervals on the detected fractions.

Questions 5 and 6 also included the answer option 'Not applicable' in case no microcalcifications or opacities were present in the image.

The results of the study were analyzed using the visual grading characteristics (VGC) method from Båth and Månsson [38], which compares the modalities two by two. In this method, the reader scores are analyzed similar to a receiver operating characteristics (ROC) analysis by interpreting the criterion scores as confidence thresholds and thus creating a VGC curve. The area under the curve (AUC) is then a measure of the difference in image quality between the compared modalities, with significant differences resulting in AUCs significantly different from 0.5. Because reader scores are reduced to ROC curves, we can use the OR-DBM MRMC 2.50 software package [39]–[43] to perform the multireader-multicase ANOVA analysis to calculate the confidence intervals on the AUCs with trapezoidal fitting. In this evaluation an AUC greater than 0.5 when comparing 'A vs. B' indicates that method A was preferred to method B, and a score of less than 0.5 means method B was preferred over method A. These differences can be considered significant when the confidence interval of the AUC does not include 0.5.

7.3 Results

7.3.1 Phantom Evaluation

Results of the human observer evaluation of non-spiculated masses are shown in figure 7.3 and the fitted threshold diameters are listed in table 7.1. The threshold diameters of the SRSAR and MLTR$_{pr}$ reconstructions are significantly smaller than the FBP threshold diameter ($p<0.001$), but not different between SRSAR and MLTR$_{pr}$ ($p=0.125$).

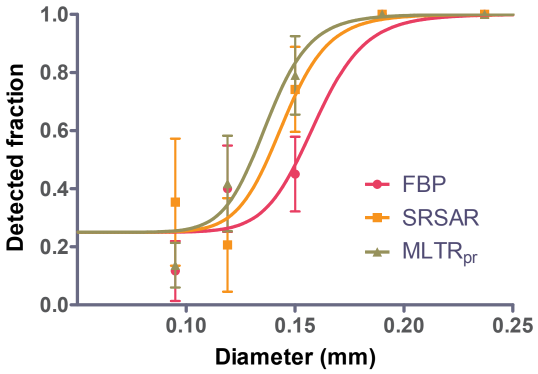

Figure 7.4: Psychometric curve fit for the detection of microcalcification groups by a model observer. Error bars indicate 95% confidence intervals on the detected fractions.

Reconstruction	Masses (mm)	Calcifications (μm)
FBP	3.15 (2.86 – 3.44)	159 (147 – 171)
SRSAR	2.51 (2.31 – 2.71)	144 (138 – 151)
MLTR$_{\text{pr}}$	2.33 (2.13 – 2.53)	137 (130 – 144)

Table 7.1: Fitted threshold diameters ϕ_{tr} with 95% confidence interval.

Results of the model observer evaluation of the microcalcification groups are shown in figure 7.4 and the fitted threshold diameters are listed in table 7.1. The threshold diameters of the SRSAR and MLTR$_{\text{pr}}$ reconstructions are significantly smaller than the FBP threshold diameter (p=0.003), but not different between SRSAR and MLTR$_{\text{pr}}$ (p=0.154).

7.3.2 Visual Grading Study

Individual reader scores, averages and confidence intervals for all criteria are listed in table 7.2. Significant differences are printed in bold. The significant differences are:

- More disturbing noise in SRSAR than in FBP.
- More disturbing artifacts in MLTR$_{\text{pr}}$ than in SRSAR.
- Better visualization of the skin line in SRSAR.
- Better overall image quality in SRSAR than in MLTR$_{\text{pr}}$.

	reader 1	reader 2	reader 3	reader 4	Mean	95% CI
1. Absence of disturbing noise						
SRSAR vs. FBP	0.438	0.399	0.474	0.436	**0.437**	0.385 – 0.489
MLTR$_{\mathrm{pr}}$ vs. FBP	0.551	0.806	0.411	0.373	0.535	0.229 – 0.842
SRSAR vs MLTR$_{\mathrm{pr}}$	0.393	0.125	0.555	0.567	0.410	0.089 – 0.731
2. Absence of disturbing artifacts						
SRSAR vs. FBP	0.524	0.623	0.515	0.461	0.531	0.432 – 0.630
MLTR$_{\mathrm{pr}}$ vs. FBP	0.274	0.581	0.342	0.332	0.382	0.172 – 0.593
SRSAR vs MLTR$_{\mathrm{pr}}$	0.740	0.534	0.660	0.641	**0.644**	0.517 – 0.770
3. Visualization of the skin line						
SRSAR vs. FBP	0.563	0.723	0.624	0.675	**0.646**	0.540 – 0.752
MLTR$_{\mathrm{pr}}$ vs. FBP	0.217	0.575	0.202	0.453	0.362	0.073 – 0.651
SRSAR vs MLTR$_{\mathrm{pr}}$	0.816	0.670	0.866	0.732	**0.771**	0.635 – 0.907
4. Visualization of Coopers ligaments and vascular structure						
SRSAR vs. FBP	0.594	0.785	0.544	0.442	0.591	0.367 – 0.816
MLTR$_{\mathrm{pr}}$ vs. FBP	0.521	0.504	0.479	0.385	0.472	0.384 – 0.561
SRSAR vs MLTR$_{\mathrm{pr}}$	0.559	0.787	0.564	0.558	0.617	0.443 – 0.791
5. Visualization of microcalcifications						
SRSAR vs. FBP	0.601	0.568	0.506	0.577	0.563	0.474 – 0.652
MLTR$_{\mathrm{pr}}$ vs. FBP	0.485	0.472	0.458	0.538	0.488	0.403 – 0.574
SRSAR vs MLTR$_{\mathrm{pr}}$	0.612	0.601	0.544	0.537	0.574	0.489 – 0.659
6. Visualization of opacities						
SRSAR vs. FBP	0.574	0.601	0.497	0.460	0.533	0.423 – 0.643
MLTR$_{\mathrm{pr}}$ vs. FBP	0.539	0.485	0.503	0.424	0.488	0.395 – 0.581
SRSAR vs MLTR$_{\mathrm{pr}}$	0.537	0.618	0.494	0.530	0.544	0.446 – 0.644
7. Image contrast						
SRSAR vs. FBP	0.745	0.762	0.547	0.447	0.625	0.389 – 0.862
MLTR$_{\mathrm{pr}}$ vs. FBP	0.523	0.583	0.522	0.375	0.501	0.372 – 0.629
SRSAR vs MLTR$_{\mathrm{pr}}$	0.691	0.714	0.526	0.570	0.625	0.490 – 0.760
8. General image quality						
SRSAR vs. FBP	0.651	0.718	0.521	0.478	0.592	0.425 – 0.759
MLTR$_{\mathrm{pr}}$ vs. FBP	0.472	0.520	0.406	0.362	0.440	0.338 – 0.542
SRSAR vs MLTR$_{\mathrm{pr}}$	0.673	0.719	0.611	0.613	**0.654**	0.577 – 0.731

Table 7.2: Visual grading results. Significant differences are shown in bold.

Figure 7.5: Irregular mass lesion with distortion and spiculation (left: FBP, middle: SRSAR, right: $\mathrm{MLTR_{pr}}$).

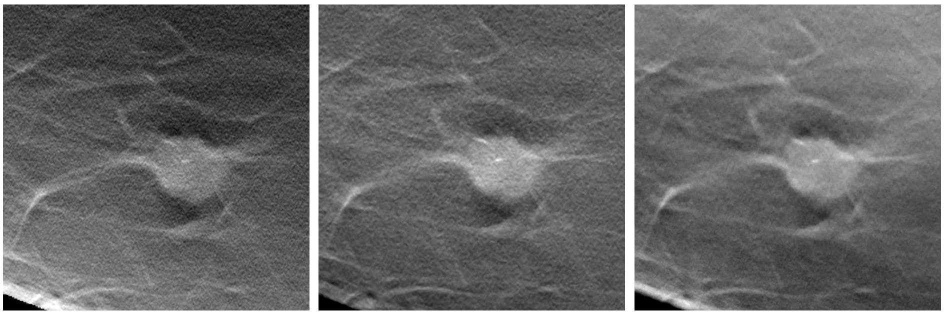

Figure 7.6: Irregular circumscribed opacity with fine spicules in the border (left: FBP, middle: SRSAR, right: $\mathrm{MLTR_{pr}}$).

7.3.3 Patient Images

This appendix shows a few images from the observer study to illustrate the differences between the three reconstruction methods. Figures 7.5, 7.6, and 7.7 show regions of interest from three different patients, each with a mass lesion that contains one or more microcalcifications. Figures 7.8 and 7.9 each show a single full reconstructed plane containing a mass lesion. The window and level was set individually for each image in order to get the best representation, however some loss of image contrast and detail was unavoidable in order to present the images here.

7.4 Discussion

In the evaluation of the phantom-based detection task we find a clear improvement when using the two newer reconstruction methods compared to the default system FBP, and this both for the high contrast microcalcifications and low contrast masses. Analysis of the visual grading results shows a different picture. Except for an increase in noise, SRSAR generally scores

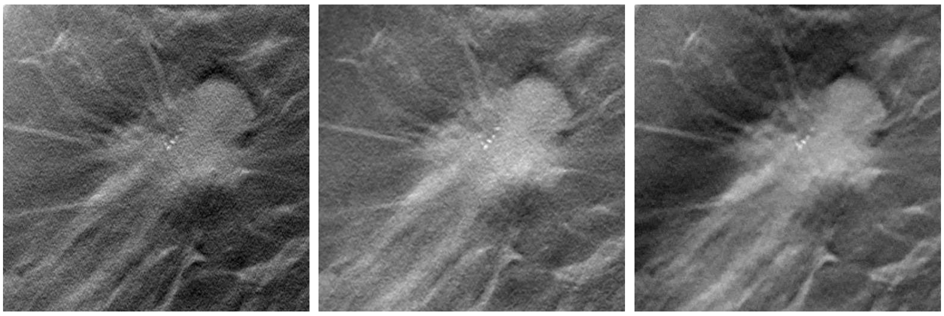

Figure 7.7: Irregular mass lesion with microcalcifications in the center (left: FBP, middle: SRSAR, right: $\mathrm{MLTR}_{\mathrm{pr}}$).

better than FBP, but only the improved visualization of the skin line was significant. $\mathrm{MLTR}_{\mathrm{pr}}$ on the other hand trends towards lower scores than FBP although none of the differences are significant.

It should be noted that the VGC method of Båth and Månsson [38] results in paired comparisons, even though each case in the visual grading study was evaluated individually. This makes it harder for the observers since they need to evaluate each case based on previous experience rather than against a reference image, which is especially difficult for less experienced readers. The strong advantage of the VGC method is that it correctly handles the ordinal data and allows the use of well known statistical methods developed for ROC analysis such as the OR-DBM MRMC software package.

When evaluating the results in table 7.2, there are some noticeable inter-reader differences. There is for example the strong preference of reader 2 for the $\mathrm{MLTR}_{\mathrm{pr}}$ reconstruction noise level, which was not completely unexpected because the $\mathrm{MLTR}_{\mathrm{pr}}$ smoothing prior settings were selected in consultation with this reader. The large variation between the readers might also be explained by the fact that noise is not an anatomical feature, and as such is harder to evaluate consistently between different observers. Two other results that stand out are the scores of readers 1 and 2 for criteria 7 and 8 (image contrast and general image quality). Here we see that the two most experienced readers show a stronger preference for the SRSAR method over the FBP reconstructions, while the two less experienced readers have no strong preference for either of the methods. Although the higher image contrast in SRSAR is somewhat preferred over the low contrast $\mathrm{MLTR}_{\mathrm{pr}}$ images, we believe this to be a matter of taste rather than a problem with the reconstructions, similar to a radiologists preference for viewing either high or low contrast images in digital mammography.

In general, we can conclude that the evaluation methods do not disagree when comparing between SRSAR and FBP although the visual grading evaluation was less sensitive to differences. However, some disagreement was found between the comparisons of $\mathrm{MLTR}_{\mathrm{pr}}$ and FBP. In the phantom

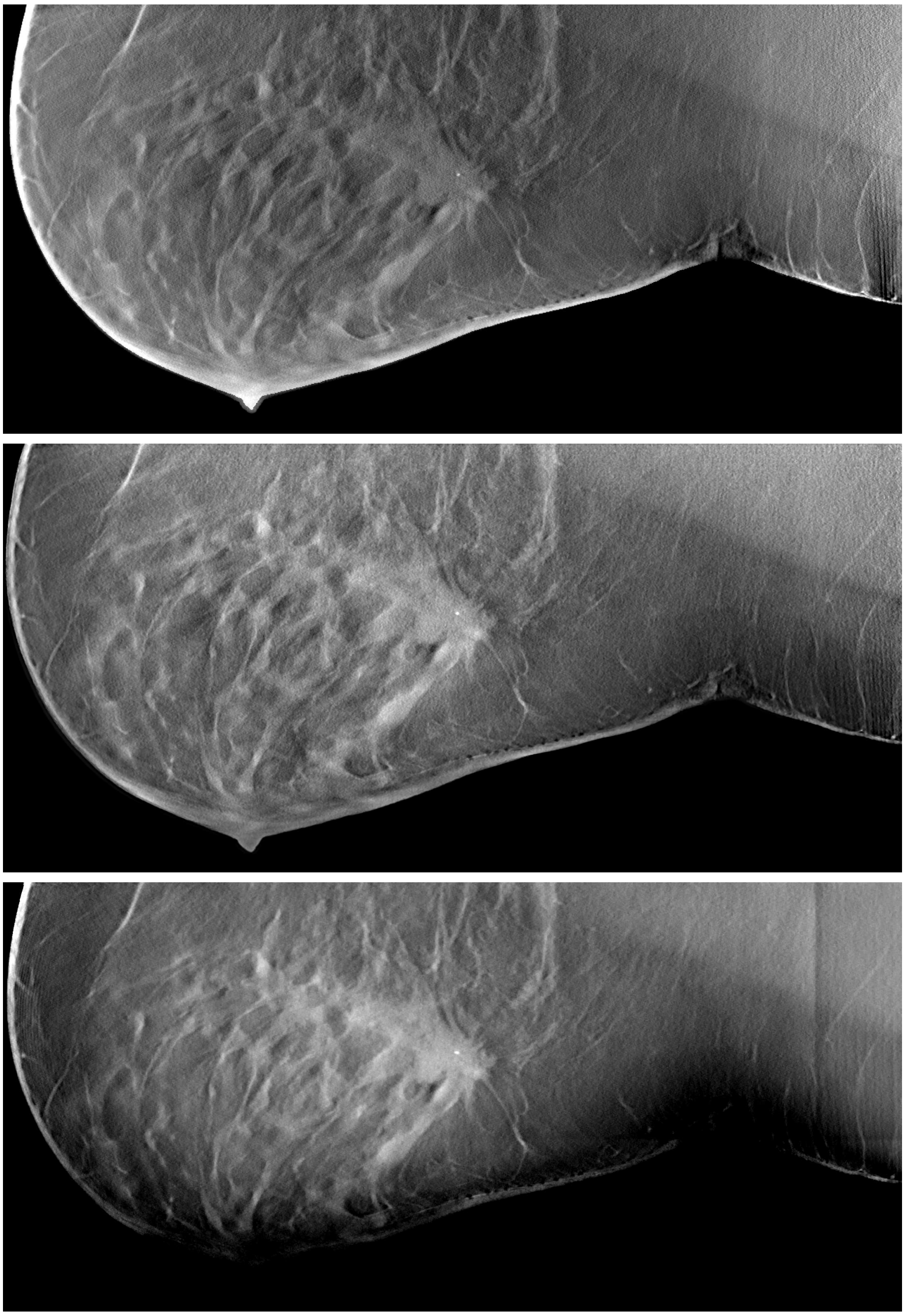

Figure 7.8: Irregular mass lesion with microcalcifications in the center (top: FBP, middle: SRSAR, bottom: MLTR$_{\mathrm{pr}}$).

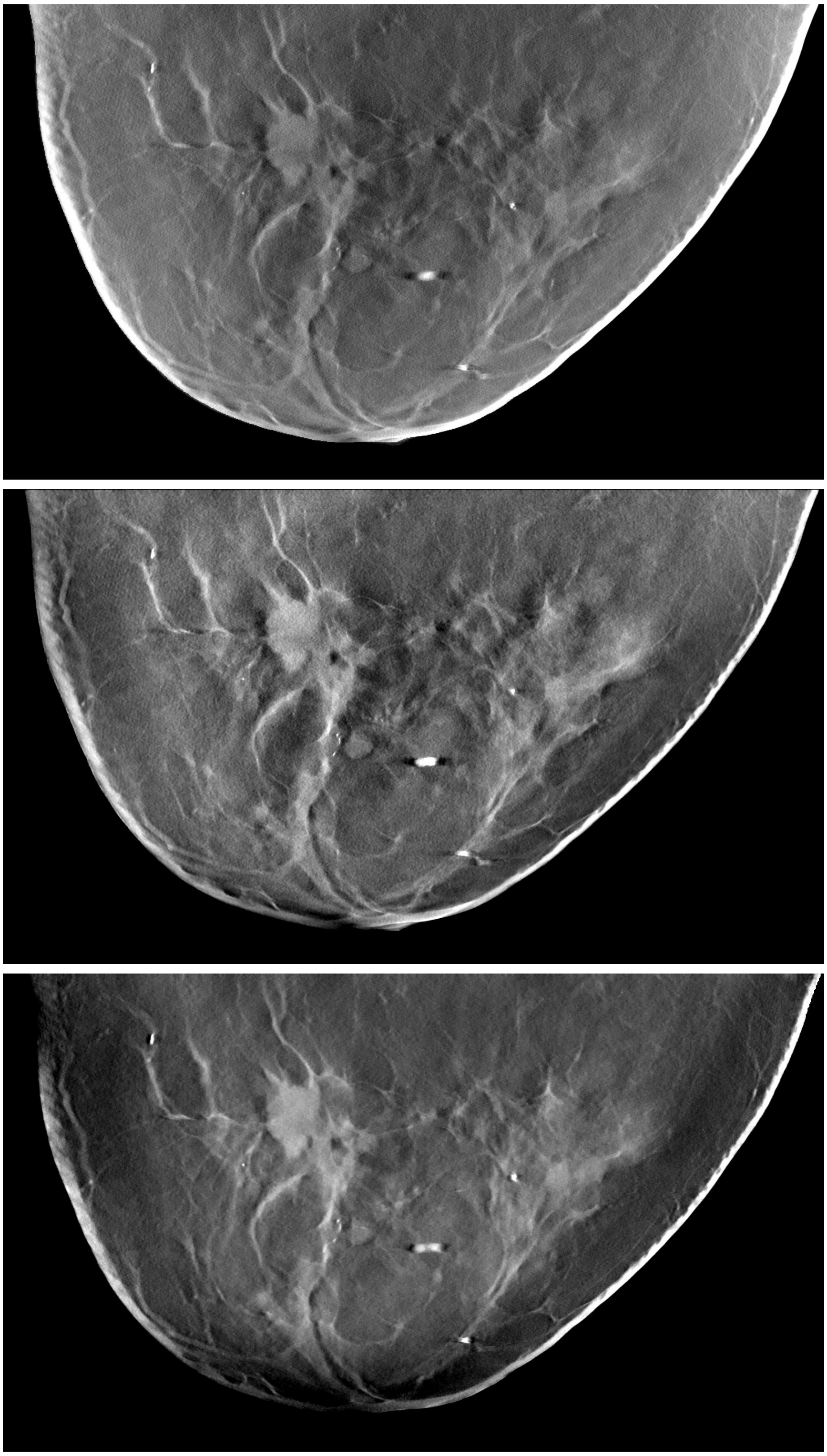

Figure 7.9: Polylobulated mass with irregular borders and fine spiculations (top: FBP, middle: SRSAR, bottom: MLTR$_{\mathrm{pr}}$).

study MLTR$_{\mathrm{pr}}$ scored better than FBP while in the clinical study MLTR$_{\mathrm{pr}}$ was rated at the same level as FBP, with a trend towards worse scores. This discrepancy might be the consequence of a greater focus on technical measures during the development of the MLTR$_{\mathrm{pr}}$ method with relatively little clinical feedback, and is in line with the observation that radiologists usually prefer familiar looking images. This gives another advantage to SRSAR which is an evolution of the FBP method relative to the unfamiliar look of the iterative MLTR$_{\mathrm{pr}}$ method.

7.5 Conclusion

With these results and the feedback from the observers from the visual grading study, we believe SRSAR can replace the current FBP in the clinic, although some finetuning of the denoising step in the algorithm would be useful. The MLTR$_{\mathrm{pr}}$ method will need more work before it reaches this stage. Although the detection performance is at least as good as SRSAR, further development should focus on artifact reduction and improving image contrast, and could gain from clinical input to obtain a more familiar look and feel for the radiologists.

Acknowledgments

The authors would like to thank Siemens Healthcare for their financial support.

References

[1] T. Wu, R. H. Moore, E. A. Rafferty, and D. B. Kopans, “A comparison of reconstruction algorithms for breast tomosynthesis”, *Med. Phys.*, vol. 31, no. 9, pp. 2636–2647, 2004.

[2] Y. Zhang, H.-P. Chan, B. Sahiner, J. Wei, M. M. Goodsitt, L. M. Hadjiiski, J. Ge, and C. Zhou, “A comparative study of limited-angle cone-beam reconstruction methods for breast tomosynthesis”, *Med. Phys.*, vol. 33, no. 10, pp. 3781–3795, 2006.

[3] J. T. Rakowski and M. J. Dennis, “A comparison of reconstruction algorithms for c-arm mammography tomosynthesis”, *Med. Phys.*, vol. 33, no. 8, pp. 3018–3032, 2006.

[4] K Bliznakova, Z Kolitsi, R. D. Speller, J. A. Horrocks, G Tromba, and N Pallikarakis, “Evaluation of digital breast tomosynthesis reconstruction algorithms using synchrotron radiation in standard geometry”, *Med. Phys.*, vol. 37, no. 4, pp. 1893–1903, 2010.

[5] Y.-S. Kim, H.-S. Park, H.-H. Lee, Y.-W. Choi, J.-G. Choi, H. H. Kim, and H.-J. Kim, “Comparison study of reconstruction algorithms for prototype digital breast tomosynthesis using various breast phantoms”, *Radiol. Med.*, 2015.

[6] M. Das and H. C. Gifford, “Comparison of model-observer and human-observer performance for breast tomosynthesis: Effect of reconstruction and acquisition parameters”, in *Medical Imaging 2011: Physics of Medical Imaging*, N. J. Pelc, E. Samei, and R. M. Nishikawa, Eds., ser. SPIE Proceedings, vol. 7961, SPIE, 2011, pp. 796 118–796118–9.

[7] L. Cockmartin, N. W. Marshall, G Zhang, K. Lemmens, E Shaheen, C. Van Ongeval, E Fredenberg, D. R. Dance, E. Salvagnini, K. Michielsen, and H. Bosmans, “A structured phantom for detection performance comparison between breast tomosynthesis and digital mammography”, *Med. Phys.*, submitted, 2015.

[8] D. Van de Sompel, S. M. Brady, and J. Boone, “Task-based performance analysis of FBP, SART and ML for digital breast tomosynthesis using signal CNR and channelised hotelling observers”, *Med. Image Anal.*, vol. 15, no. 1, pp. 53–70, 2010.

[9] R. Zeng, S. Park, P. Bakic, and K. J. Myers, “Evaluating the sensitivity of the optimization of acquisition geometry to the choice of reconstruction algorithm in digital breast tomosynthesis through a simulation study”, *Phys. Med. Biol.*, vol. 60, no. 3, pp. 1259–1288, 2015.

[10] H. J. Teertstra, C. E. Loo, M. A. A. J. Den, H. V. Tinteren, E. J. T. Rutgers, S. H. Muller, and K. G. A. Gilhuijs, “Breast tomosynthesis in clinical practice: Initial results”, *Eur. Radiol.*, vol. 20, no. 1, pp. 16–24, Jan. 2010.

[11] G. Gennaro, A. Toledano, C. Maggio, E. Baldan, E. Bezzon, M. Grassa, L. Pescarini, I. Polico, A. Proietti, A. Toffoli, and P. C. Muzzio, “Digital breast tomosynthesis versus digital mammography: A clinical performance study”, *Eur. Radiol.*, vol. 20, no. 7, pp. 1545–1553, Jul. 2010.

[12] G. Svane, E. Azavedo, K. Lindman, M. Urech, J. Nilsson, N. Weber, L. Lindqvist, and C. Ullberg, “Clinical experience of photon counting breast tomosynthesis: Comparison with traditional mammography”, *Acta radiol.*, vol. 52, no. 2, pp. 134–142, 2011.

[13] M. J. Michell, A Iqbal, R. K. Wasan, D. R. Evans, C Peacock, C. P. Lawinski, A Douiri, R Wilson, and P Whelehan, “A comparison of the accuracy of film-screen mammography, full-field digital mammography, and digital breast tomosynthesis”, *Clin. Radiol.*, vol. 67, no. 10, pp. 976–981, Oct. 2012.

[14] T. M. Svahn, D. P. Chakraborty, D Ikeda, S Zackrisson, Y Do, S Mattsson, and I Andersson, “Breast tomosynthesis and digital mammography: A comparison of diagnostic accuracy”, *Br. J. Radiol.*, vol. 85, no. 1019, e1074–e1082, Jun. 2012.

[15] F. Thibault, C. Dromain, C. Breucq, C. S. Balleyguier, C. Malhaire, L. Steyaert, A. Tardivon, E. Baldan, and H. Drevon, “Digital breast tomosynthesis versus mammography and breast ultrasound: A multireader performance study”, *Eur. Radiol.*, vol. 23, no. 9, pp. 2441–2449, Sep. 2013.

[16] S. P. Poplack, T. D. Tosteson, C. A. Kogel, and H. M. Nagy, “Digital breast tomosynthesis: Initial experience in 98 women with abnormal digital screening mammography”, *AJR Am. J. Roentgenol.*, vol. 189, no. 3, pp. 616–623, Sep. 2007.

[17] D. Gur, G. S. Abrams, D. M. Chough, M. A. Ganott, C. M. Hakim, R. L. Perrin, G. Y. Rathfon, J. H. Sumkin, M. L. Zuley, and A. I. Bandos, “Digital breast tomosynthesis: Observer performance study”, *AJR Am. J. Roentgenol.*, vol. 193, no. 2, pp. 586–591, Aug. 2009.

[18] E. A. Rafferty, J. M. Park, L. E. Philpotts, S. P. Poplack, J. H. Sumkin, E. F. Halpern, and L. T. Niklason, “Assessing radiologist performance using combined digital mammography and breast tomosynthesis compared with digital mammography alone: Results of a multicenter, multireader trial”, *Radiology*, vol. 266, no. 1, pp. 104–113, Jan. 2013.

[19] I. Sechopoulos, “A review of breast tomosynthesis. part i. the image acquisition process”, *Med. Phys.*, vol. 40, no. 1, p. 014 301, 2013.

[20] Y. Sagara, A. K. Hara, W. Pavlicek, A. C. Silva, R. G. Paden, and Q. Wu, “Abdominal CT: Comparison of low-dose CT with adaptive statistical iterative reconstruction and routine-dose CT with filtered back projection in 53 patients”, *AJR Am. J. Roentgenol.*, vol. 195, no. 3, pp. 713–719, Sep. 2010.

[21] S. Singh, M. K. Kalra, J. Hsieh, P. E. Licato, S. Do, H. H. Pien, and M. A. Blake, “Abdominal CT: Comparison of adaptive statistical iterative and filtered back projection reconstruction techniques”, *Radiology*, vol. 257, no. 2, pp. 373–383, Nov. 2010.

[22] A. Moscariello, R. A. P. Takx, U. J. Schoepf, M. Renker, P. L. Zwerner, T. X. O’Brien, T. Allmendinger, S. Vogt, B. Schmidt, G. Savino, C. Fink, L. Bonomo, and T. Henzler, “Coronary CT angiography: Image quality, diagnostic accuracy, and potential for radiation dose reduction using a novel iterative image reconstruction technique-comparison with traditional filtered back projection”, *Eur. Radiol.*, vol. 21, no. 10, pp. 2130–2138, Oct. 2011.

[23] A Korn, M Fenchel, B Bender, S Danz, T. K. Hauser, D Ketelsen, T Flohr, C. D. Claussen, M Heuschmid, U Ernemann, and H Brodoefel, “Iterative reconstruction in head CT: Image quality of routine and low-dose protocols in comparison with standard filtered backprojection”, *AJNR Am. J. Neuroradiol.*, vol. 33, no. 2, pp. 218–224, Feb. 2012.

[24] L. M. Mitsumori, W. P. Shuman, J. M. Busey, O. Kolokythas, and K. M. Koprowicz, “Adaptive statistical iterative reconstruction versus filtered back projection in the same patient: 64 channel liver CT image quality and patient radiation dose”, *Eur. Radiol.*, vol. 22, no. 1, pp. 138–143, Jan. 2012.

[25] F. Pontana, S. Henry, A. Duhamel, J.-B. Faivre, N. Tacelli, J. Pagniez, J. Remy, and M. Remy-Jardin, “Impact of iterative reconstruction on the diagnosis of acute pulmonary embolism (PE) on reduced-dose chest CT angiograms”, *Eur. Radiol.*, vol. 25, no. 4, pp. 1182–1189, Apr. 2015.

[26] J. S. Kriegshauser, S. G. Naidu, R. G. Paden, M. He, Q. Wu, and A. K. Hara, “Feasibility of ultra-low radiation dose reduction for renal stone CT using model-based iterative reconstruction: Prospective pilot study”, *Clin. Imaging*, vol. 39, no. 1, pp. 99–103, Jan. 2015.

[27] T. Mertelmeier, J. Orman, W. Haerer, and M. K. Dudam, “Optimizing filtered backprojection reconstruction for a breast tomosynthesis prototype device”, in *Medical Imaging 2006: Physics of Medical Imaging*, M. J. Flynn and J. Hsieh, Eds., ser. SPIE Proceedings, vol. 6142, SPIE, 2006, 61420F–61420F–12.

[28] J. Orman, T. Mertelmeier, and W. Haerer, “Adaptation of image quality using various filter setups in the filtered backprojection approach for digital breast tomosynthesis”, in *Digital Mammography*, ser. Lecture Notes in Computer Science, Springer Berlin Heidelberg, 2006, pp. 175–182.

[29] S. Abdurahman, F. Dennerlein, A. Jerebko, A. Fieselmann, and T. Mertelmeier, “Optimizing high resolution reconstruction in digital breast tomosynthesis using filtered back projection”, in *Breast Imaging*, ser. Lecture Notes in Computer Science, Springer International Publishing, 2014, pp. 520–527.

[30] K. Michielsen, K. Van Slambrouck, A. Jerebko, and J. Nuyts, “Patchwork reconstruction with resolution modeling for digital breast tomosynthesis”, *Med. Phys.*, vol. 40, no. 3, p. 031 105, Mar. 2013.

[31] K. Michielsen and J. Nuyts, “Multigrid reconstruction with block-iterative updates for breast tomosynthesis”, *Med. Phys.*, vol. 42, no. 11, pp. 6537–6548, 2015.

[32] L Cockmartin, H Bosmans, and N. W. Marshall, “Comparative power law analysis of structured breast phantom and patient images in digital mammography and breast tomosynthesis”, *Med. Phys.*, vol. 40, no. 8, p. 081 920, Aug. 2013.

[33] N Karssemeijer and M. Thijssen, “Determination of contrast-detail curves of mammography systems by automated image analysis”, *Digital Mammography*, vol. 96, pp. 155–160, 1996.

[34] F. A. Wichmann and N. J. Hill, “The psychometric function: I. fitting, sampling, and goodness of fit”, *Percept. Psychophys.*, vol. 63, no. 8, pp. 1293–1313, Nov. 2001.

[35] K. Michielsen, L. Cockmartin, N. Marshall, H. Bosmans, and J. Nuyts, “A model observer to optimize calcification detection in breast tomosynthesis”, *Med. Phys.*, submitted, 2016.

[36] J. N. Wolfe, “Breast patterns as an index of risk for developing breast cancer”, *AJR Am. J. Roentgenol.*, vol. 126, no. 6, pp. 1130–1137, Jun. 1976.

[37] C. Van Ongeval, A. Van Steen, C. Geniets, F. Dekeyzer, H. Bosmans, and G. Marchal, “Clinical image quality criteria for full field digital mammography: A first practical application”, *Radiat. Prot. Dosimetry*, vol. 129, no. 1-3, pp. 265–270, 2008.

[38] M Båth and L. G. Månsson, “Visual grading characteristics (VGC) analysis: A non-parametric rank-invariant statistical method for image quality evaluation”, *Br. J. Radiol.*, vol. 80, no. 951, pp. 169–176, Mar. 2007.

[39] D. D. Dorfman, K. S. Berbaum, and C. E. Metz, “Receiver operating characteristic rating analysis. generalization to the population of readers and patients with the jackknife method”, *Invest. Radiol.*, vol. 27, no. 9, pp. 723–731, Sep. 1992.

[40] N. A. Obuchowski Jr and H. E. Rockette Jr, “Hypothesis testing of diagnostic accuracy for multiple readers and multiple tests an anova approach with dependent observations”, *Communications in Statistics-*, 1995.

[41] S. L. Hillis, N. A. Obuchowski, K. M. Schartz, and others, “A comparison of the Dorfman–Berbaum–Metz and Obuchowski–Rockette methods for receiver operating characteristic (ROC) data”, *Stat. Interface*, 2005.

[42] S. L. Hillis, “A comparison of denominator degrees of freedom methods for multiple observer ROC analysis”, *Stat. Med.*, 2007.

[43] S. L. Hillis, K. S. Berbaum, and C. E. Metz, “Recent developments in the Dorfman-Berbaum-Metz procedure for multireader ROC study analysis”, *Acad. Radiol.*, 2008.

Chapter 8

General Discussion

In this work we sought to design, implement, and evaluate a practical maximum a posteriori reconstruction algorithm for digital breast tomosynthesis with a focus on the visualization of microcalcifications, and the results of this project were presented in the previous six chapters.

Preprocessing of Projection Data

After the introduction, the first two chapters concentrated on preparing measured data for reconstruction with the methods developed in the later chapters. This preparation included estimating the blank scan and the image support, and correcting the data for scatter and beam hardening. The scatter term was the most challenging to determine because a good patient-specific phantom was needed in order to perform the Monte Carlo scatter simulation, and it is difficult to create such a phantom without a well reconstructed image to start from. In circumstances where the need for quantitative results outweighs time constraints, a logical solution would be to use an iterative process that updates the Monte Carlo phantom using the final reconstruction from the previous iteration. This would also allow further constraints on the image support, and together with the better scatter correction suppress some of the artifacts seen in the patient reconstructions in the final evaluation. Since these corrections were not relevant to the goal to improve the detectability of microcalcification clusters, the presented implementation was considered sufficient as it allowed us to reconstruct all measured phantom and patient data with the methods described in the later chapters.

Because there were only minimal differences between applying the scatter estimate as a precorrection to the measured data and including the correction in the forward model of the reconstruction, the simpler precorrection was preferred. This lack of differences between the two correction methods was anticipated, since both correct for the expected amount of energy deposited by the scattered x-rays, but neither can undo the added noise.

Reconstruction with Resolution Modeling

Based on an analysis of the system sharpness [1], the forward model of the new MLTR$_{\mathrm{pr}}$ method was designed to include the motion of the x-ray tube during image acquisition. By modeling the system blur in the acquisition, part of the resolution loss can be reversed in the reconstruction. Due to the relatively large amount of motion blur in the Siemens Inspiration system, our new reconstruction method could clearly show the gain in contrast to noise ratio from this method. The advantage of modeling the system resolution will diminish when less blur occurs, as for example by using a step-and-shoot acquisition that completely avoids motion blur, as is done in the GE SenoClaire system, or by shortening the x-ray pulses during an acquisition with continuous motion of the x-ray tube as is now being implemented for the Siemens Mammomat Inspiration. Depending on the desired resolution in the reconstructed images, it would also be possible to keep the motion blur constant and increase the rotation speed of the x-ray tube to get a shorter examination time, therefore reducing the time that the patient's breast needs to be compressed, which improves patient comfort and reduces the chance of patient motion during the examination.

The initial resolution model described in this chapter assumed a Gaussian waveform for the exposure. Before starting the work in chapter 5, the waveform of the exposure was measured and found to be rectangular, and the model was adjusted to reflect this. In practice the difference between the two models was very small, and therefore these results were not included in the papers.

In general, modeling the system resolution can be useful in any application and it is most efficient when this resolution is lower than the detector pixel size. The actual benefit of the resolution model in task based image quality will depend on the application and will need to be weighted against added complexity and computational cost. The fact that the reconstruction planes are parallel to the detector for the typical breast tomosynthesis geometry means that the convolution kernels from the tube motion resolution model are approximately stationary for each reconstruction plane. This is a significant advantage in computational cost compared to more general implementations with non-stationary convolution kernels that would be needed for other modalities such as (cone beam) CT. Since the width of the convolution kernels that model the tube motion varied depending on the height of the reconstructed plane, the most practical implementation involved calculating the updates sequentially for each plane. This type of image block iterative updates has the added advantage of accelerating convergence [2]. Unfortunately the combination of this acceleration with a limited angle acquisition was found to result in a very inhomogeneous attenuation distribution. Because almost no information is available on how the attenuation is distributed perpendicular to the detector, most of the low frequency attenuation is assigned to the plane that is updated first. This possibility to end up with a very inhomogeneous attenuation distribution explains the need for a good initialization, which may not have been stressed enough in this paper. The principle behind the diminishing relaxation factor was very simple: e.g. in a case with three planes, the first plane would receive a third of the full update, the second plane half, and the last plane a full update, and thus the low frequency attenuation would be spread out equally among the planes, at the cost of slower convergence. This slow convergence speed motivated us to find a faster initialization method, which resulted in the multigrid method presented in chapter 5.

Multigrid Reconstruction

The multigrid approach started from the observation that methods which update the entire volume in a single step suffer much less from the null space problem, but since this is related to large scale variations rather than small details, these updates could just as well be performed at lower resolution. This resulted in the multigrid reconstruction method presented in chapter 5, which starts with full volume updates at low resolution, and then switches to plane-by-plane updates at higher resolutions. In this method, the low frequency attenuation is spread out homogeneously over the different planes before the plane-by-plane updates add higher frequency information in the reconstructions, resulting in a more effective suppression of the artifact and a significantly faster convergence than the original implementation with an underrelaxation factor.

Although the primary reason to include the multigrid approach was to avoid the unrealistic null space solutions, the combination of multigrid and plane-by-plane updates resulted in a further convergence speedup. Because of this focus shift towards acceleration, a comparison with ordered subset updates, which are frequently applied in iterative CT reconstruction, was added. From previous experience in accelerating CT reconstruction [3], we had expected the speedup of the plane-by-plane updates to be proportional to the number of planes in the volume, but this turned out to be too optimistic when considering only a few iterations.

Within the fixed computational constraints both update methods were found to be roughly equivalent for convergence and image artifacts. When considering the practical implementation rather than only the theoretical computational cost, the patchwork method is preferred due to its more elegant implementation and because smoothing priors only need to be applied to the plane that is being updated in the $\mathrm{MLTR}_{\mathrm{pr}}$ method, while the prior needs to be applied to the entire reconstruction volume after each subset update. When relaxing the computational constraints, the $\mathrm{MLTR}_{\mathrm{pr}}$ method gains further advantage because with more iterations, the full acceleration proportional to the number of planes can be achieved, and in almost all cases the number of planes in the reconstruction is greater than the number of projection angles that can be used for the ordered subsets. This advantage remains even if the reconstruction time is unlimited, since convergence is guaranteed for $\mathrm{MLTR}_{\mathrm{pr}}$, unlike the ordered subset method, which will end in a limit cycle. This non-converged solution is not necessarily a low quality reconstruction, but from a theoretical point of view convergence is preferred. It should be noted that comparing image quality in this chapter can always be considered somewhat unfair. When evaluating convergence at a fixed computational cost for a single cost function, the most converged algorithm will result in sharper but noisier images, while less converged algorithms will be less noisy and less sharp. And on the other hand, when evaluating the same algorithms with modified cost functions such that the resulting images have the same noise level, it is no longer possible to directly compare convergence.

A Model Observer for Microcalcifications

The channelized Hotelling observer presented and validated in chapter 6 was designed to evaluate the calcification detection task efficiently and consistently. The model observer successfully predicted the optimum for the total variation prior, and the lack of optimum for the quadratic and combined priors, as obtained in the study with human observers. Unfortunately this result also indicated that the detection task is not sufficient for optimizing these last two priors, since although detection by human observers was not sensitive to the priors for this talk, it is believed that the priors will affect their performance on real data. A specific strength of the model observer is its ability to work on real measured data, where the exact location of the calcification targets inside the phantom might not be known. This makes sure the evaluation takes into account all possible aspects of the data acquisition and reconstruction. Therefore the need to generate the signal templates for the model observer from simulated data rather than being able to rely exclusively on measured data is a definite disadvantage. An alternative solution would be to use very high dose acquisitions to generate the templates, but this might not be practical in reality. It is likely that the required dose level cannot be achieved in a single acquisition due to detector saturation or power limitations on the generator, and repeated measurements cannot be easily combined because the exposure angles will be slightly different between acquisitions and result in additional blurring in the reconstruction. This means that the model observer is currently constrained to systems for which both geometry and reconstruction method are well known. Because the phantom that was used in these evaluations can also be used for digital mammography, it would be useful to expand the model observer to work for projection data. In practice almost no changes would be necessary since the observer is already restricted to a single plane. The main difference is that the 8×8 covariance matrix would now need to be estimated from far fewer samples available in the selected ROI and it remains to be seen whether this is sufficient for a stable estimate. It might also be possible to use a global covariance matrix, estimated from samples of the entire projection image because the detector response is expected to be stationary.

Smoothing Priors

The MLTR$_{\mathrm{pr}}$ reconstruction presented in chapters 4 and 5 always included a smoothing prior to prevent excessive noise propagation in the reconstructed images. The ideal smoothing prior would reduce noise while retaining the contrast of small microcalcifications, but in practice it is very hard to distinguish between both. The initial choice was the Huber prior which applies a quadratic penalty for attenuation differences below a certain threshold and a linear penalty above, thereby preserving contrast above the selected threshold. However, a side effect was found in the appearance of undesirable speckle noise. After this, reconstructions were performed using a combined quadratic and total variation smoothing prior which was able to retain sharpness and present an acceptable image texture without disturbing noise. Instead of a threshold between signal and noise, the current prior depends on the relative weight of the quadratic and total variation components. When examining the optimal choice for these weights with regards to calcification detectability in chapter 6, it turned out that this detectability was more or less constant for different weights, while the image appearance ranged from unacceptably noisy to very smooth. This means that the calcification detection task was insufficient to optimize this smoothing prior, but also that any choice made according to other criteria will not result in worse detectability. It remains to be seen whether simply selecting a setting for the smoothing prior that results in visually pleasing reconstructions is a sufficient criterion, or if a more suitable task needs to be found, since 'visually pleasing' is a subjective evaluation that can vary between observers, as seen in the results of chapter 7, and such visually pleasing image representation is not necessarily the best for diagnostic purposes [4].

One aspect of the smoothing priors that might require further evaluation is their non uniform response in the MLTR$_{\mathrm{pr}}$ reconstruction. Due to the resolution model in the reconstruction, the likelihood contains more information in planes close to the detector, resulting in relatively less smoothing, and less information in planes far from the detector, resulting in relatively more smoothing. By using voxel specific weights for the smoothing prior, it might be possible to achieve a more uniform response [5], although it remains uncertain how this would influence lesion detectability.

Phantom and Visual Grading Analysis

The last chapter brings together all elements in the thesis in a comparison of three reconstruction algorithms: the default FBP for the Siemens Mammomat Inspiration system, the latest Siemens research prototype SRSAR [6], and the $\mathrm{MLTR_{pr}}$ method presented in chapters 4 and 5 combined with the precorrections described in chapters 2 and 3. The first part consisted of a phantom based evaluation of calcification and mass detectability. The calcification detection task was evaluated by the model observer presented in chapter 6 while the mass detection task was presented to human observers. In the second part of the study a series of patient images was evaluated by radiologists in a visual grading study. The phantom based evaluations showed a significantly improved detection performance of $\mathrm{MLTR_{pr}}$ relative to the system FBP, but no differences were found by radiologists in a visual grading study with eight image quality criteria. With these results the goal of improving on the Siemens product FBP was measurable in the technical evaluation, while these differences were not seen in the visual grading, although that does not necessarily mean they were not there [4]. In the same evaluations the detection performance of the SRSAR method scored only slightly below that of $\mathrm{MLTR_{pr}}$, while it was perceived as superior to the FBP method for two image quality criteria, and superior to $\mathrm{MLTR_{pr}}$ for three.

Future Work

Future work on the $\mathrm{MLTR_{pr}}$ reconstruction algorithm depends on the desired goals. One possible goal is to advance the reconstruction with respect to technical measures such as the phantom based detectability in order to show what level of performance is achievable with a certain set of acquisition parameters. This can then be seen as a performance target for advanced FBP type reconstructions such as SRSAR. In this approach the next steps in developing the algorithm should include the implementation of an adaptive voxel grid [7], further acceleration of the convergence, and modifying the smoothing prior such that detectability of lesions is constant through the entire reconstruction volume. Alternatively, future work could be more applied towards introducing the reconstruction in clinical practice. In this instance the current technical quality could be considered as good enough, and modifications can focus on artifact reduction and clinical appearance. This could be achieved by improving the data precorrections in order to reduce inconsistencies between the forward model and reality, and by improving the image support for the reconstruction volume, for example by performing additional optical measurements. In this instance modifications of the smoothing prior can focus on fine-tuning the visual appearance to obtain a familiar noise pattern. This approach could also include post processing steps in the reconstruction domain, similar to the image processing performed in digital mammography on the measured 'FOR PROCESSING' data to generate the 'FOR PRESENTATION' data used in diagnosis. The result of the iterative reconstruction would then be considered as raw data that accurately describe the attenuation distribution, and these data would serve as input for a post processing step that optimizes the image contents for diagnostic visualization. This two step method would allow a clear division between two reconstruction goals that sometimes come in conflict, namely the accurate reconstruction of physical reality, and the optimal clinical visualization of this physical reality.

With these possible improvements, we believe it remains useful to continue the development of iterative maximum a posteriori reconstruction methods that can improve on the new SRSAR method in the same way as the current $\mathrm{MLTR}_{\mathrm{pr}}$ method improved on the system FBP. Even if the resulting algorithms are not selected for clinical implementation, we believe that showing which performance can be achieved from a certain set of projection data is a valuable contribution in itself.

Conclusion

In final conclusion, we successfully implemented a maximum a posteriori algorithm for breast tomosynthesis which is able to reconstruct clinical data efficiently. Phantom evaluations found a significant improvement in detectability of microcalcifications and masses compared to the default system reconstruction, but these improvements were not reflected in the scores in a subsequent visual grading study on clinical data. Therefore, the current reconstruction can be considered as a good starting point for further refinements focusing on artifact reduction and clinical image impression.

References

[1] N. W. Marshall and H. Bosmans, “Measurements of system sharpness for two digital breast tomosynthesis systems”, *Phys. Med. Biol.*, vol. 57, no. 22, pp. 7629–7650, Nov. 2012.

[2] J. A. Fessler, E. P. Ficaro, N. H. Clinthorne, and K. Lange, “Grouped-coordinate ascent algorithms for penalized-likelihood transmission image reconstruction”, *IEEE Trans. Med. Imaging*, vol. 16, no. 2, pp. 166–175, Apr. 1997.

[3] K Van Slambrouck and J Nuyts, “Reconstruction scheme for accelerated maximum likelihood reconstruction: The patchwork structure”, *Nuclear Science, IEEE Transactions on*, vol. 61, no. 1, pp. 173–181, Feb. 2014.

[4] F. Zanca, C. V. Ongeval, F Claus, J. Jacobs, R. Oyen, and H. Bosmans, “Comparison of visual grading and free-response ROC analyses for assessment of image-processing algorithms in digital mammography”, *Br. J. Radiol.*, vol. 85, no. 1020, e1233–e1241, Jul. 2012.

[5] J. A. Fessler and W. L. Rogers, “Spatial resolution properties of penalized-likelihood image reconstruction: Space-invariant tomographs”, *IEEE Trans. Image Process.*, vol. 5, no. 9, pp. 1346–1358, Jan. 1996.

[6] S. Abdurahman, F. Dennerlein, A. Jerebko, A. Fieselmann, and T. Mertelmeier, “Optimizing high resolution reconstruction in digital breast tomosynthesis using filtered back projection”, in *Breast Imaging*, ser. Lecture Notes in Computer Science, Springer International Publishing, 2014, pp. 520–527.

[7] B. Claus and H.-P. Chan, “Digital breast tomosynthesis reconstruction with an adaptive voxel grid”, in *Medical Imaging 2014: Physics of Medical Imaging*, B. R. Whiting and C. Hoeschen, Eds., ser. SPIE Proceedings, vol. 9033, International Society for Optics and Photonics, 2014, 90335A–90335A–7.

Curriculum Vitae

Koen Michielsen was born on February 5th in 1982 in Ekeren, Belgium. He obtained the degree of Bachelor in Physics (Kandidaat Natuurkunde) at the University of Hasselt in 2003, and continued his education at KU Leuven where he graduated cum laude in 2005 with the degree of Master in Physics (Licenciaat Natuurkunde), with a thesis on "Determining the time delays of lensed quasar J1155+635 from a series of CCD images" ("Het bepalen van het lichtvertraginseffect van de gelensde quasar J1155+635 aan de hand van een tijdreeks van CCD beelden").

After receiving a second Master degree in 2007, this time in Medical Radiation Physics (GGS en GAS Medische Stralingsfysica) and with a thesis titled "Automated data collection strategies and results for patient dosimetry in mammography", he started working as a certified medical physics expert at the department of radiology of the University Hospitals in Leuven. He worked there until December 2010, when he started his PhD project at the department of Imaging and Pathology at KU Leuven on the topic "Maximum a Posteriori Reconstruction of Limited Angle Tomography".

Peer Reviewed Articles

- **K. Michielsen** and J. Nuyts, "Multigrid reconstruction with block-iterative updates for breast tomosynthesis," Med. Phys. 42, 6537 (2015).
- J.-Y. Wielandts, S. De Buck, **K. Michielsen**, R. Louw, C. Garweg, J. Nuyts, J. Ector, F. Maes, and H. Heidbuchel, "Multi-phase rotational angiography of the left ventricle to assist ablations: feasibility and accuracy of novel imaging," Eur. Heart J. Cardiovasc. Imaging (2015).
- G. Maleux, **K. Michielsen**, D. Timmerman, W. Poppe, S. Heye, J. Vaninbroukx, and H. Bosmans, "2D versus 3D roadmap for uterine artery catheterization: impact on several angiographic parameters", Acta Radiologica 55, 62–70 (2014).

- **K. Michielsen**, K. Van Slambrouck, A. Jerebko, and J. Nuyts, "Patchwork reconstruction with resolution modeling for digital breast tomosynthesis," Med. Phys. 40, 031105 (2013).
- R. Pauwels, H. Stamatakis, G. Manousaridis, A. Walker, **K. Michielsen**, H. Bosmans, R. Bogaerts, R. Jacobs, K. Horner, K. Tsiklakis, and SEDENTEXCT Project Consortium, "Development and applicability of a quality control phantom for dental cone-beam CT," J. Appl. Clin. Med. Phys. 12, 245-260 (2011).
- P. Pittayapat, C. Oliveira-Santos, P. Thevissen, **K. Michielsen**, N. Bergans, G. Willems, D. Debruyckere, and R. Jacobs, "Image quality assessment and medical physics evaluation of different portable dental X-ray units," Forensic Sci. Int. 201, 112117 (2010).
- F. Zanca, C. Van Ongeval, N. Marshall, T. Meylaers, **K. Michielsen**, G. Marchal, and H. Bosmans, "The relationship between the attenuation properties of breast microcalcifications and aluminum," Phys. Med. Biol. 55, 10571068 (2010).
- **K. Michielsen**, J. Jacobs, K. Lemmens, J. Nens, J. Zoetelief, K. Faulkner, and H. Bosmans, "Results of a European dose survey for mammography," Radiat. Prot. Dosimetry 129, 199203 (2008).

Patents

- A. Jerebko, **K. Michielsen**, and J. Nuyts, "Plane-by-plane iterative reconstruction for digital breast tomosynthesis", US Patent 8,594,407 (2013).

Conference Proceedings

- **K. Michielsen**, A. Fieselmann, L. Cockmartin, and J. Nuyts, "Evaluation of low contrast detectability after scatter correction in digital breast tomosynthesis," Proc. SPIE 9033-13, SPIE Medical Imaging Conference, San Diego (2014).
- **K. Michielsen**, F. Zanca, N. Marshall, H. Bosmans, and J. Nuyts, "Two complementary model observers to evaluate reconstructions of simulated micro-calcifications in digital breast tomosynthesis," Proc. SPIE 8673-0G, SPIE Medical Imaging Conference, Orlando (2013).
- **K. Michielsen**, K. Van Slambrouck, A. Jerebko, and J. Nuyts, "Patchwork reconstruction with resolution modeling for digital breast tomosynthesis," The Second International Conference on Image Formation in X-Ray Computed Tomography, Salt Lake City (2012).

- F. Zanca, **K. Michielsen**, M. Depuydt, J. Jacobs, J. Nens, K. Lemmens, R. Oyen, and H. Bosmans, "Longitudinal tube modulation for chest and abdominal CT examinations: impact on effective patient doses calculations," Proc. SPIE 7961-3E, SPIE Medical Imaging Conference, Orlando (2011).

- **K. Michielsen**, J. Jacobs, N. Marshall, and H. Bosmans, "Analysis of Mammography Quality Control Results: Evidence for a Change in Test Frequency?," Proc. IWDM 6136 pp. 371-377, 10th International Workshop on Digital Mammography (IWDM), Girona (2010).

- F. Zanca, H. Bosmans, J. Jacobs, **K. Michielsen**, F. Sisini, J. Nens, K.C. Young, E. Shaheen, A. Jacobs, and G. Marchal, "Contrast-detail comparison between unprocessed and processed CDMAM images," Proc. SPIE 7258-4Y, SPIE Medical Imaging Conference, Orlando (2009).

- H. Bosmans, K. Lemmens, J. Jacobs, D. Vandenbroucke, F. Zanca, **K. Michielsen**, B. Verbrugge, K. Smans, and G. Marchal, "Can the evaluation of a simple test object be used to predict the performance of a contrast-detail analysis in digital mammography?, Proc. SPIE 7263-19, SPIE Medical Imaging Conference,(Orlando (2009).

- J. Jacobs, K. Lemmens, J. Nens, **K. Michielsen**, G. Marchal, and H. Bosmans, "One Year of Experience with Remote Quality Assurance of Digital Mammography Systems in the Flemish Breast Cancer Screening Program," Proc. IWDM 5116 pp. 703–710, 10th International Workshop on Digital Mammography (IWDM), Tucson (2008).

- H. Bosmans, K. Lemmens, J. Jacobs, B. Verbrugge, **K. Michielsen**, F. Zanca, J. Nens, C. Van Ongeval, and G. Marchal, "Comparative Technical Study of Two Generations of CR Plates for Digital Mammography," Proc. IWDM 5116 pp. 724–731, 10th International Workshop on Digital Mammography (IWDM), Tucson (2008).

- **K. Michielsen**, J. Jacobs, and H. Bosmans, "Patient Dosimetry for Mammography," AIP Conf. Proc 958 pp. 292–293, Fourth International Summer School on Nuclear Physics Methods and Accelerators in Biology and Medicine, Prague (2007).

Presentations without Proceedings

- E. Salvagnini, C. Van Ongeval, N. Marshall, L. Cockmartin, **K. Michielsen**, A. Van Steen, L. Struelens, and H. Bosmans, ”A new AEC set-up achieves constant lesion detectability for different breast thicknesses in digital mammography,” Conference of the Radiological Society of North America (RSNA), Chicago (2015).
- E. Salvagnini, H. Bosmans, C. Van Ongeval, A. Van Steen, **K. Michielsen**, L. Cockmartin, L. Struelens, and N.W. Marshall, ”A FROC study on the influence of breast thickness on simulated lesion detection,” Conference of the Medical Imaging Perception Society (MIPS), Ghent (2015).
- E. Salvagnini, H. Bosmans, C. Van Ongeval, A. Van Steen, **K. Michielsen**, L. Cockmartin, L. Struelens, and N.W. Marshall, ”Impact of compressed breast thickness on detectability of simulated lesions: a clinical trial,” European Congress of Radiology (ECR), Vienna (2015).
- J.-Y. Wielandts, S. De Buck, **K. Michielsen**, R. Louw, C. Garweg, J. Nuyts, J. Ector, F. Maes, and H. Heidbuchel, ”Left ventricular 4D rotational angiography in biplane EP setting,” Belgian Hearth Rhythm Meeting, Brussels (2014).
- **K. Michielsen** and J. Nuyts, ”Parallel data processing on GPU and CPU using OpenCL,” DROITE Workshop, Grenoble (2013).
- E. Salvagnini, L. Cockmartin, **K. Michielsen**, J. Jacobs, N.W. Marshall, L. Struelens, and H. Bosmans, ”Can a color representation of grey-scale images improve object detectability in mammography?,” European Congress of Radiology (ECR), Vienna (2013).
- **K. Michielsen** and J. Nuyts, ”Resolution modeling for digital breast tomosynthesis,” DROITE Workshop, Lyon (2012).
- **K. Michielsen**, J. Jacobs, K. Lemmens, J. Nens, J. Zoetelief, K. Faulkner, and H. Bosmans, ”Results of a European dose survey for mammography,” SENTINEL Workshop, Delft (2007).

Submitted Works

- **K. Michielsen**, L. Cockmartin, N. Marshall, H. Bosmans, and J. Nuyts, ”A model observer to evaluate calcification detectability in breast tomosynthesis,” submitted for publication in Medical Physics.

- **K. Michielsen**, C. Van Ongeval, A. Van Steen, M. Keupers, J. Soens, H. Ghunaim, L. Cockmartin, D. Petrov, and J. Nuyts, ”Phantom and visual grading analysis of three breast tomosynthesis reconstruction methods,” accepted for presentation at the European Congress of Radiology (ECR), Vienna (2016).

- L. Cockmartin, N. Marshall, G. Zhang, K. Lemmens, E. Shaheen, C. Van Ongeval, E. Fredenberg, D.R. Dance, E. Salvagnini, **K. Michielsen**, and H. Bosmans, ”A structured phantom for detection performance comparison between breast tomosynthesis and digital mammography,” submitted for publication in Medical Physics.

- E. Salvagnini, H. Bosmans, C. Van Ongeval, A. Van Steen, **K. Michielsen**, L. Cockmartin, L. Struelens, and N. Marshall,”Impact of thickness and dose on lesion detectability in digital mammography: A FROC study with simulated lesions in real mammograms,” submitted for publication in Medical Physics.